Ultrasonic Characterization of Bitumen with Pressure and Temperature: Implications for seismic monitoring of the Grosmont Formation

by

Arif Rabbani

A thesis submitted in partial fulfillment of the requirements for the degree of

Doctor of Philosophy

in

GEOPHYSICS

Department of Physics
University of Alberta

Abstract

The vastly untapped carbonate Grosmont Formation in north-eastern Alberta may hold in excess of a couple of hundred billion barrels initial volume of bitumen in place. Bitumen, an ultra-heavy hydrocarbon oil, possesses a density comparable to water, but a dynamic shear viscosity million times higher than that of water. Thermal recovery processes, e.g., steam-assisted gravity drainage, are necessary to reduce its extremely high viscosity to make it mobile for the production. During steam injections, the physical properties of the reservoirs change due to the combined effects of increased temperature, pressure, and fluid substitutions. Time-lapse seismic reflection surveys can be used to monitor the alterations, but the proper interpretations require a solid understanding of the host rock's behaviour and most importantly, the pore fluids properties exposed to such environment. Therefore, we have studied the physical properties of bitumen-saturated carbonates and naturally produced bitumen with temperature and pressure using various ultrasonic methods. The bulk and shear moduli in bitumen hosting carbonates derived from the measured compressional and shear wave speeds see a significant drop with the increase of temperature, but the observations cannot be modelled using standard fluid substitutions theories. Bitumen's properties are expected to be the most influential factors for such divergences. Next, studies of compressional wave propagation in bitumen reveal a discrepancy between the conventional bulk and longitudinal moduli, particularly at a lower temperature. The complex longitudinal moduli indicate the importance of bulk viscosity in bitumen in addition to the high shear viscosities. The shear properties studies afterward show that bitumen possesses substantial shear moduli and hence, shear wave speed. It also reveals that viscoelastic relaxation and, most importantly, the shear thinning phenomena in a highly viscous material significantly influence the high-frequency viscosity results. The results, in

combination with the knowledge of the various phase transitions in bitumen through the compositional and thermophysical characteristics, can be implemented to have a better interpretation of seismic surveys, although further studies at seismic frequency are highly recommended.

Preface

This thesis is an original work by Arif Rabbani and submitted for the degree of Doctor of Philosophy in Geophysics at the University of Alberta.

The work of this thesis is either published or under revisions for publications. I was responsible for the system design, data acquisitions, analyses, and manuscript compositions. Prof. Douglas R. Schmitt, the supervisory author, helped in manuscript editing in all the publications.

Chapter 3 is a published paper in Geophysics with Jason Nycz and Ken Gray as the co-authors. They helped with concept formations and improving the manuscript.

This thesis is dedicated to my daughter –

Sehrish Aniya Rabbani

The real happiness is seeing her smile!

Acknowledgements

Words cannot describe the gratitude to my supervisor, Dr. Douglas R. Schmitt. He was a true mentor who not only helped me to become a researcher that I'm today but also to grow as a person. His unabated enthusiasm, proper guidance, and relentless patience had inspired me to explore the area of rock physics even more, and the environment in the lab was so perfect to do that. I promise him that I will slow down myself on jumping into various thoughts too early.

I want to express my special gratitude to my supervisory committee members, Dr. David Potter and Dr. Frank Hegmann for imparting their knowledge and expertise in this work. At the same time, I am deeply grateful to Dr. John Beamish, one of the final committee members, for his time for several valuable discussions. Many thanks to Dr. Mathieu Dumberry and Dr. Maxim Lebedev for reading my thesis. A special thanks to Prof Maxim to wake up 3 o'clock in the morning to participate my final exam through skype!

I am exceedingly obliged to Jason Nycz and Ken Gray for their continued cooperation as well as providing necessary information regarding this research and also their support to complete this endeavour. I would also like to thank our industry partners Laricina Energy Ltd and Osum Oil Sands Corp, and also NSERC for their financial support.

I owe many thanks to my colleagues – Randy, Nam, Tariq, Micah, Chris, Xiwei, Gautier, and Mizan. I still miss the packed office and the busy lab! It's been a great experience spending time with them and I must agree that I have learned a lot from them. It would somewhat have been an everyday journey without all my friends here. Thank you guys for making me smile even when nothing was working in the lab.

The happy faces of my parents for even a little success in my life that I can't see from here but to feel only are what inspire me to overcome the hurdles in following a dream. Deepest gratitude goes to them. Special thanks to my brother and in-laws for having faith in me.

It was a long journey, and I genuinely believe that without having my wife's sacrifices and continuous encouragement this thesis would not have come into existence. I owe you a lot, Jakia! Thank you for being by my side during all the hardships.

Finally, I would like to express my most profound gratitude to Almighty God for giving me the opportunity to complete the degree successfully.

Table of Contents

List of Tables

List of Figures

Chapter 1: Introduction

1.1 Background: Grosmont Bitumen Formation

The vast global reserves of heavy oils and bitumen still remain economically attractive but yet to be exploited despite the increase of hydrocarbon production from tight formations and/or the recent technological advances in efficient extraction. This is even more relevant for Alberta, home of one of the world's largest unconventional hydrocarbon reserves, which contains primary in-place resources of crude bitumen estimated to be about 293.13 billion m^3 (1.84 trillion barrels). Of the total, however, only 5% has so far been produced over the last 40 years (Burrowes et al., 2011) . Most of the reserve lies in oil sands deposits, but a significant fraction resides in nearby untouched carbonate reservoirs. Of this, the carbonate Grosmont Formation in north-eastern Alberta may hold more than 64.5 billion m^3 of (406 billion barrels) initial volume of bitumen in place. The extensive scale of the available resource makes the Grosmont formation a still largely untapped resource and motivates researchers to study the area further.

The bitumen saturating the carbonates is virtually immobile, like the oil sands, at the ambient in situ temperature of 10-14°C (Rassenfoss, 2013). It possesses an extremely high viscosity which is million times higher than that of water (Yang et al., 2014). Therefore, as with the oil sands, recovery necessitates that the viscosity of the bitumen be reduced so that it can flow for production. For this, the reservoir will be sufficiently heated to more than 100°C using thermal recovery methods such as cyclic steam stimulation (CSS) or steam assisted gravity drainage (SAGD) (Jiang et al., 2010; Mohebati et al., 2014; Butler, 1991). These processes of steam injections lead to changes in the physical properties of the reservoirs. A proper geophysical observation, e.g., time-

lapse seismic survey, can play a role to reduce the economic risk of the by-passed reserves and the environmental risk to undesired loss of the injected fluids outside of the intended target zone (Bianco et al., 2008; Kato et al., 2008).

1.2. Motivations: Seismic Monitoring

During SAGD, for example, the combined effects of increased temperature, pore pressure and effective stress changes, and the substitution of bitumen with water and steam impose a significant influence seismic wave speeds and attenuation in the bitumen reservoirs (Schmitt, 2004). This temporal changes will be echoed the seismic reflectivity, and a repetitive seismic survey can be used to observe and understand the changes (Schmitt, 1999; Zadeh et al., 2010; Isaac and Lawton, 2006). However, it is imperative to have a solid understanding of the subsurface properties as the seismic response depends on the velocity, density, stresses, and physical state of the reservoir rocks and saturating fluids (Nycz et al., 2016).

Conventional time lapse seismic surveys, for example, illustrate an acoustic impedance (AI) difference along the injection wells during the steaming over a period of time (Rabbani et al., 2016; Kelly and Lawton, 2012). The acoustic impedance map is an effective method of estimating the movement of the steam front. Nevertheless, as mentioned earlier, a number of factors contribute to the changes in AI. Therefore, a rock physics model is necessary to invert the survey results further to dissect it in terms of e.g., compressional and shear velocities or impedances, attenuations and density. However, there are two questions remain very important to be addressed:

i. Which specific property of the rock or the fluid governs the overall seismic responses, particularly in an ultra-heavy oil saturated reservoirs?

ii. Moreover, why do the conventional fluid substitution models have a tendency to fail to predict the experimental observations in these samples, particularly at the lower temperature?

The first concern can be addressed through the laboratory measurements of seismic properties of the host rock and the fluid independently. A detailed characterization of the saturating fluid could, therefore, also improve the rock physics models – the central theme of this thesis.

As such, our first phase of measurements was with the bitumen saturated carbonates from the Grosmont formation (Rabbani et al., 2017). We observe that ultrasonic P- and S-wave velocities decrease with the temperature significantly, but the standard rock physics models, e.g., the Gassmann-Biot family cannot predict the modulus change with the temperature. The intricate properties of bitumen are expected to be the dominating factor (Rabbani et al., 2017; Yuan et al., 2017). Many researchers, e.g., (Eastwood, 1993; Spencer, 2013) have also observed significant drops in the longitudinal (P-wave) velocities in bitumen saturated sands with increasing temperature at both high and low frequencies, respectively. In contrast, the shear (S-wave) velocity varies slightly. They both emphasize that drop in P-velocity be mostly due to the change in fluid bulk modulus with temperature.

These lead us to characterize bitumen with pressure and temperature, particularly at a lower temperature. This may also be an improvement on most of the earlier studies which typically begin at room temperature, whereas the virgin reservoir temperature in this reservoir is only about 10°C to 14°C. This is also necessary to assist seismic monitoring of the Grosmont bitumen-saturated carbonate Formation.

To achieve the goals, we choose an ultrasonic technique as the primary method of our experiments because of their ease of implementation. The application of an ultrasonic technique for the extremely viscous material might not be the best approach to study the complex moduli and rheology, but it is indeed the most straightforward method to examine the overall response of the bulk and shear behavior of the fluid over a period of temperature, pressure, and frequency.

1.3. Thesis outline

Our primary interest lies in carrying out experiments on bitumen to investigate how much of the observed seismic effects on bitumen-saturated carbonates are due solely to bitumen property changes. Therefore, in **Chapter 2**, the theory of sound wave propagation and absorption in viscous fluids is briefly reviewed. Although there are several mechanisms of acoustic absorption, e.g., thermal conduction and molecular relaxation, attenuation due to viscosity will be focused here due to the apparent reason that for instance, bitumen is million time viscous than water at ambient condition. Bitumen is considered as a Newtonian fluid at low viscosity or higher temperature, while at high viscosity or lower temperature, it is modeled as a viscoelastic material. Therefore, somewhat simplified mechanical linear viscoelastic models are also discussed here.

Chapter 3 presents the temperature and pressure dependence acoustic wave speeds of bitumen hosted carbonates from the Grosmont formation. The measurements were necessary due to the sparsity of the studies on heavy oil hosted carbonates although a significant amount of studies has been completed on the physical rock properties of the oil sands. This chapter reviews the previous laboratory and theoretical works on oil sands and rocks. A brief description of the geological formation of the Grosmont platform is also included here. We test a variety of theoretical models against the experimental

observations. We also explore how seismic responses might be expected to evolve during heating of the reservoir through simple modeling. This chapter is published in a peer-reviewed journal (Rabbani et al., 2017) and a part of it is also presented in conferences such as CSEG (Rabbani et al., 2014) and SEG (Rabbani et al., 2016).

In **Chapter 4,** we study the ultrasonic p-wave transmission through viscous bitumen using an adapted version of the technique that consists two receivers placed at unequal length from the transmitter. As such, we are able to calculate the signal attenuation which also helps us derive the complex longitudinal moduli. We first review the literature as to knowledge of the constituents of bitumen and how temperature dependent phase transitions of these various components influence bitumen's microscopic colloidal structure. We then describe the composition and thermophysical characteristics of our particular bitumen sample using a variety of different techniques. This leads to the tests of the wave speed temperature and pressure dependencies that we interpret regarding the P-wave, or longitudinal modulus. We discuss the results in light of current knowledge of the complex phase transition behaviour in bitumen and what implications this may have to time lapse seismic investigations. A version of this chapter is submitted to Geophysics (Rabbani and Schmitt 2018).

Understanding the rheological behavior of bitumen and how it changes with temperature and pressure is key to the design of efficient extraction processes and also to properly interpret the surface time-lapse geophysical data. **Chapter 5**, hence, describes the construction of an ultrasonic shear wave reflectometer to calculate shear properties of the viscoelastic bitumen. This chapter begins with a brief overview of the theory of extracting shear properties from the complex shear wave reflection coefficient. This is followed a detailed description of our bitumen sample and measurements that incorporate a novel signal processing scheme. We interpret the observed complex shear moduli of bitumen and comment on the meaning of the measurements given that the

analysis relies on the assumed rheological behaviour of the material. A version of this chapter is currently in revision in FUEL (Rabbani and Schmitt 2018).

The last, **Chapter 6**, summarizes the studies with some direction of the future works. That includes studying the complex dynamic bulk moduli of bitumen and -saturated rocks at lower (~100 Hz) frequency which, to some extent, will be more appropriate to characterize seismic surveys.

The author apologizes in advance for unavoidable replication of some material that will appear within the three paper-based chapters. Further, each chapter includes its own independent reference list; no comprehensive bibliography is included.

References

Bianco, E., S. Kaplan, and D. Schmitt. 2008, Seismic rock physics of steam injection in bituminous oil reservoirs. The Leading Edge, **27**, no. 9,1132-1137. doi: 10.1190/1.2978975.

Burrowes, A., M. Teare, R. Marsh, and AAA. 2011, Alberta's Energy Reserves 2011 and Supply/Demand Outlook 2012-2021. . Annual Report ST98-2011, Energy Resources Conservation Board, Calgary, Alberta (June 2011).

Butler, R. 1991, Thermal recovery of oil and bitumen: Prentice Hall.

Eastwood, J. 1993, Temperature-dependent propagation of p-waves and s-waves in cold lake oil sands - comparison of theory and experiment. Geophysics, **58**, no. 6,863-872. doi: 10.1190/1.1443470.

Isaac, J. H., and D. C. Lawton. 2006, A case history of time-lapse 3D seismic surveys at Cold Lake, Alberta, Canada. Geophysics, **71**, no. 4,B93-B99. doi: 10.1190/1.2211027.

Jiang, Q., B. Thornton, J. Russel-Houston, and S. Spence. 2010, Review of Thermal Recovery Technologies for the Clearwater and Lower Grand Rapids Formations in the Cold Lake Area in Alberta. Canadian J. Petroleum Technology, **49**, no. 9,57-68. doi: 10.2118/140118-PA.

Kato, A., S. Onozuka, and T. Nakayama. 2008, Elastic property changes in a bitumen reservoir during steam injection. The Leading Edge, **27**, no. 9,1124-1131. doi: 10.1190/1.2978974.

Kelly, B., and D. C. Lawton. 2012, Processing and interpretation of time-lapse seismic data from a heavy oil field , Alberta , Canada (a) (b) 4D Processing and Interpretation (a) (b).1-5.

Mohebati, M. H., D. Yang, and J. MacDonald. 2014, Thermal Recovery of Bitumen From the Grosmont Carbonate Formation-Part 1: The Saleski Pilot. Journal of Canadian Petroleum Technology, **53**, no. 4,200-211.

Nycz, J., D. Yang, and D. Schmitt. 2016, Analysis of 4D time-lapse seismic responses integrated with 3D data products, production information, and laboratory data to characterize a bitumen-bearing carbonate reservoir, SEG Technical Program Expanded Abstracts 2016. 2951-2955.

Rabbani, A., O. Ong*, X. Chen, D. Schmitt, J. Nycz, and K. Gray. 2016, Rock physics laboratory experiments on bitumen-saturated carbonates from the Grosmont

Formation, Alberta, SEG Technical Program Expanded Abstracts 2016. 3464-3467.

Rabbani, A., D. R. Schmitt, R. Kofman, and J. Nycz. 2014, Laboratory Studies of the Seismic Properties of Bitumen Saturated Grosmont Carbonates. GeoConvention 2014:Focus, Calgary, AB, Canada.

Rabbani, A., D. R. Schmitt, J. Nycz, and K. Gray. 2017, Pressure and temperature dependence of acoustic wave speeds in bitumen-saturated carbonates: Implications for seismic monitoring of the Grosmont Formation. GEOPHYSICS, **82**, no. 5,MR133-MR151. doi: 10.1190/geo2016-0667.1.

Rabbani, A. and D. R. Schmitt. 2018, Ultrasonic Shear Wave Reflectometry Applied to the Determination of the Shear Moduli and Viscosity of a Viscoelastic Bitumen. FUEL (under revision).

Rassenfoss, S. 2013, Finding Pathways to Produce Heavy Oil From Canadian Carbonates. JPT, **65**, no. 08.

Schmitt, D. 2004, Rock Physics of Heavy Oil Deposits. CSEG National Convention - Great Explorations - Canada and Beyond,1-4.

Schmitt, D. R. 1999, Seismic attributes for monitoring of a shallow heated heavy oil reservoir: A case study. Geophysics, **64**, no. 2,368-377. doi: 10.1190/1.1444541.

Spencer, J. W. 2013, Viscoelasticity of Ells River bitumen sand and 4D monitoring of thermal enhanced oil recovery processes. Geophysics, **78**, no. 6,D419-D428. doi: 10.1190/geo2012-0535.1.

Yang, D., M. H. Mohebati, S. Brand, and C. Bennett. 2014, Thermal recovery of bitumen from the grosmont carbonate formation - Part 2: Pilot interpretation and development strategy. Journal of Canadian Petroleum Technology, **53**, no. 4,212-223. doi: 10.2118/171561-PA.

Yuan, H., D.-h. Han, H. Li, and W. Zhang. 2017, A comparison of bitumen sands and bitumen carbonates: Measured data. GEOPHYSICS, **82**, no. 1,MR39-MR50. doi: 10.1190/geo2015-0657.1.

Zadeh, H. M., R. P. Srivastava, N. Vedanti, and M. Landro. 2010, Seismic monitoring of in situ combustion process in a heavy oil field. Journal of Geophysics and Engineering, **7**, no. 1,16-29. doi: 10.1088/1742-2132/7/1/002.

Chapter 2: Theoretical and Phenomenological Background

The theory of sound wave propagation and absorption in viscous fluids is briefly reviewed here. Bitumen is considered as a viscoelastic material at lower temperature. Therefore, simplified mechanical linear viscoelastic models will also be covered in this chapter.

2.1 Wave propagation in viscous materials

A sound wave propagating in a fluid consists of periodical variations of the density, pressure, and temperature of a given fluid element with time. If the variations in pressure and density take place reversibly and adiabatically, a plane harmonic wave will travel through an ideal fluid unattenuated. However, a sound wave passing through a viscous fluid (any real fluid but especially bitumen) partially losses its energy. Numerous mechanisms cause this attenuation, but the viscous attenuation or absorption is the primary 'internal friction' that results in a conversion of mechanical energy into heat.

The acoustic wave propagation in viscous fluids is described by the Navier-Stokes equation (Bhatia and Singh, 1986),

$$\rho_0 \frac{\partial^2 \vec{v}}{\partial t^2} = \rho_0 V_0^2 \vec{\nabla}(\vec{\nabla}.\vec{v}) + \frac{\partial}{\partial t}\left[\left(\eta_B + \frac{1}{3}\eta\right)\vec{\nabla}(\vec{\nabla}.\vec{v}) + \eta\nabla^2\vec{v}\ \right] \quad (1)$$

where $V_0 = (\delta p/\delta\rho)^{1/2}$ is the speed of sound in fluid, p is pressure, ρ and ρ_0 are the perturbed and unperturbed fluid mass density, $\vec{v}$ is the particle velocity, t is time, η is the shear viscosity, and η_B is the bulk viscosity.

The viscosity of the fluid is a major theme in this study, and it is worthwhile to describe it in more detail. The shear viscosity coefficient η is a measure of momentum diffusion by molecules from higher velocities fluid regions to adjacent regions of lower velocities; therefore produces absorption even in pure longitudinal motion.

The bulk or volume viscosity η_B is a measure of the mechanical energy lost by a fluid subjected to pure compression and rarefaction. For a perfect monoatomic gases $\eta_B = 0$ but is generally nonzero for fluids associated with rotational and vibrational degrees of molecular motion, in contrast with the dynamic shear viscosity (η) which only reflects the translational motion (Kinsler, 1982). The bulk viscosity is a dynamic parameter that depends on the time rate of change of the density of the fluid as it is perturbed by the wave; it therefore very difficult to measure directly and one must infer the magnitude of η_B from ultrasonic wave attenuation (Bhatia and Singh, 1986).

In a viscous fluid, as shown in equation (1), shear waves can also, in principle, propagate like longitudinal waves although it remains difficult to observe in practice even in the high viscous fluid because of the extreme attenuation. Being a vector function of position, the particle velocity $\vec{v}$ can be decomposed into the sum of a longitudinal (or irrotational) component $\vec{\phi}$ for which $\vec{\nabla} \times \vec{\phi} = 0$, and a transverse (or rotational) component $\vec{\psi}$ for which $\vec{\nabla}.\vec{\psi} = 0$. Thus ϕ and $\vec{\psi}$ can be represented as a scalar (velocity) and a vector potential respectively (Trusler, 1991; Bouzidi, 2003). Equation (1) can now be uncoupled as,

$$\rho_0 \frac{\partial^2 \phi}{\partial t^2} = \left[\rho_0 V_0^2 + \left(\eta_B + \frac{4}{3}\eta\right)\frac{\partial}{\partial t}\right]\nabla^2 \phi \tag{2}$$

for longitudinal waves (i) and

$$\rho_0 \frac{\partial^2 \vec{\psi}}{\partial t^2} = \eta \frac{\partial}{\partial t}\nabla^2 \vec{\psi} \tag{3}$$

for transverse waves (ii).

(i) First, let's consider the propagation of the **longitudinal wave** — a plane wave in $\hat{x}$ with particle velocity in the same direction (velocities are zero along $\hat{y}$ and $\hat{z}$). Therefore, equation (2) becomes

$$\rho_0 \frac{\partial^2 \phi}{\partial t^2} = \left[\rho_0 V_0^2 + \left(\eta_B + \frac{4}{3}\eta\right)\frac{\partial}{\partial t}\right]\frac{\partial^2 \phi}{\partial x^2} \tag{4}$$

Considering a plane wave solution $\phi = \phi_0 e^{i(\omega t - kx)}$ with k as the wave number and ω as the angular frequency, we get the dispersion relation

$$k^2 = \frac{\rho_0 \omega^2}{\left[\rho_0 V_0^2 + i\omega\left(\eta_B + \frac{4}{3}\eta\right)\right]} \tag{5}$$

Unlike perfect fluids, equation (5) is a complex ω-k relation and requires a complex wave number for interpretation, i.e., $k = k_1 - ik_2$, where the real part, k_1, determines the velocity of propagation and the imaginary part, k_2, is a measure of absorption or attenuation. The scalar potential now becomes $\phi = \phi_0 e^{-k_2 x} e^{i(\omega t - k_1 x)}$.

Rewriting equation (5) with complex wavenumber yields phase velocity and attenuation as

$$k_1^2 - k_2^2 - 2ik_1k_2 = \frac{\omega^2}{V_0^2}\frac{1}{1 + i\frac{\omega}{\omega_\eta}} \tag{6}$$

where $\omega_\eta = \frac{\rho_0 V_0^2}{\eta_B + \frac{4}{3}\eta}$ is known as the viscosity relaxation frequency (Bhatia and Singh, 1986).

For $\omega \ll \omega_\eta$ and $k_2 \ll k_1$ equation (6) can be expressed as

$$k_1^2 - 2ik_1k_2 \cong = \frac{\omega^2}{V_0^2}(1 - i\frac{\omega}{\omega_\eta}) \tag{7}$$

Therefore, separating real part provides propagation velocity in the frequency limit (e.g., $\omega \sim 10^7$ Hz)

$$V = {}^{\omega}/_{k} = V_0 \tag{8}$$

It tells that there is no dispersion in the phase velocity of longitudinal waves (V remains constant).

On the other hand, imaginary parts of equation (7) yield the attenuation of the wave energy due to the viscosity at low frequency limit,

$$k_2(\omega) = \frac{\omega^2}{2\rho_0 V_0^3}\left(\eta_B + \frac{4}{3}\eta\right) = \alpha \tag{9}$$

Equation (9) can be utilized to infer the bulk viscosity η_B using the experimentally observed attenuation (α). The equation also depicts that the attenuation of the wave energy is proportional to the square of the sound frequency — more attenuation for larger wave energy (larger amplitude).

However, in the absence of bulk viscosity, equation (9) reduces merely to Stokes attenuation formula,

$$\alpha^{Stokes} = \frac{2\omega^2\eta}{3\rho_0 V_0^3} \tag{10}$$

(ii) Now consider the **transverse waves** propagating in the $\hat{x}$ direction and the particle motion be in the $\hat{y}$ direction, so equation (3) becomes

$$\rho_0 \frac{\partial^2 \psi_y}{\partial t^2} = \eta \frac{\partial}{\partial t}\frac{\partial^2 \psi_y}{\partial x^2} \tag{11}$$

Using a plane wave solution $\vec{\psi} = \hat{y}\psi_0 e^{i(\omega t - kx)}$, equation (11) yields the dispersion relations,

$$k^2 = -i\omega\frac{\rho_0}{\eta} \tag{12}$$

Letting complex wavenumber $k = k_1 - ik_2$, we get

$$k_1^2 - k_2^2 - 2ik_1k_2 = -i\omega\frac{\rho_0}{\eta} \tag{13}$$

which yields $k_1 = k_2 \; and \; k_1k_2 = {}^{\omega\rho_0}/_{\eta}$. The phase velocity and the attenuation of the viscous waves are then given by,

$$V(\omega) = \left(\frac{2\eta\omega}{\rho_0}\right)^{\frac{1}{2}} \tag{14}$$

$$k_2(\omega) = \left(\frac{\omega\rho_0}{2\eta}\right)^{\frac{1}{2}} = \alpha \tag{15}$$

The above equations show that for transverse waves both the phase velocity and the attenuation depend on frequency. However, the phase velocity increases whereas the attenuation decreases with increasing viscosity.

2.2 Highly viscous liquids

Attenuation and dispersion in highly viscous liquids may be, however, explicable with the assumption that the viscous forces arise from relaxation type of processes involving shear deformations and, therefore, a relaxing shear modulus (Bhatia, 1985). Thus the terms proportional to the dynamic viscosity (η) will get a rise in the same way as a relaxing compressibility or bulk modulus (η_B) gives rise to terms proportional to bulk viscosity.

For highly viscous fluid, e.g., bitumen with viscosity~10^6 cP at 20°C, the viscosity relaxation frequency $\omega_\eta = (\rho_0 V_0^2)/(\eta_B + \frac{4}{3}\eta)$ becomes smaller or of the order of the angular frequency (ω). In such case, the condition of $\omega \ll \omega_\eta$ in equation (7) does not hold and the subsequent attenuation formula (equation (9)) can no longer be used. Therefore, an exact solution of equation (6) provides us phase velocity and attenuation as (Bhatia and Singh, 1986),

$$V^2(\omega) = 2V_0^2 \frac{1 + (\omega/\omega_\eta)^2}{1 + \sqrt{1 + (\omega/\omega_\eta)^2}} \tag{16}$$

$$k_2(\omega) = \frac{\omega V}{2V_0^2} \frac{\omega/\omega_\eta}{1 + (\omega/\omega_\eta)^2} \tag{17}$$

Bhatia and Singh (1986) plotted these functions for glycerol, V/V_o & K_2 vs. ω/ω_η, and found a discrepancy with the experimental observations. The disagreements may underline the built-in limitation of Navier-Stokes equation. For instance, the right hand side of equation (4) consists of a viscosity independent first term but viscosity dependent second term with higher order derivatives of particle velocity. Nevertheless, all higher order derivatives of $\vec{v}$ were neglected in the first case to consider the viscosity stress tensor. This assumption, therefore, refers to smaller second term than the first one in right hand side of equation (4), which then yields that $\omega \ll \omega_\eta$. Therefore, Navier-Stokes equation might not be adequate to describe the complex physics of highly viscous liquids where $\omega \gg \omega_\eta$. All of the above discussion also assumes that ultrasonic scattering is not important in the fluid, which might not the case for bitumen.

2.3 Viscoelasticity

Bitumen is considered as a Newtonian fluid at low viscosity or higher temperature, while at high viscosity or lower temperature, it is modeled as a viscoelastic

material (Wolf et al., 2008). In reality, most materials exhibit a behaviour between that of a purely viscous and of a purely elastic to be considered as viscoelastic. The deformation (strain) is referred to as elastic if the strain can be recovered entirely without no loss of energy when the applied stress is removed. But, if the deformation is permanent once the applied force is removed it is called as inelastic or viscous behaviour. However, for a viscoelastic material, the deformation or strain (ε) varies sinusoidally with the applied stress (σ) but lags in phase (δ), Figure 2.1.

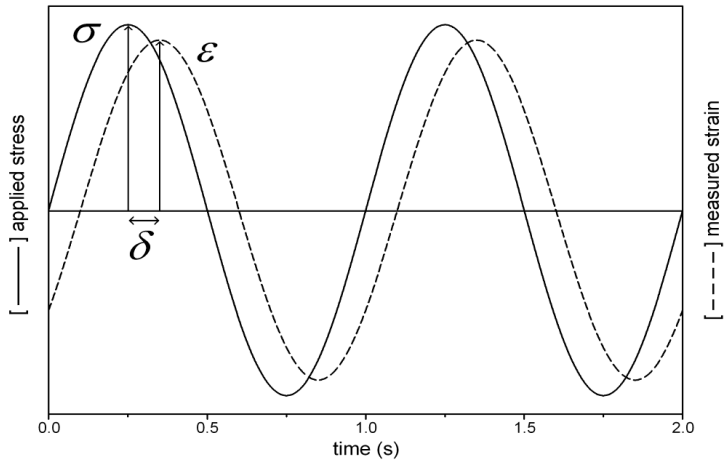

Figure 2.1. The phase lag between the applied stress and the strain as a function of time (Ward and Hadley, 1993; Lakes, 2009)

Some of the unique phenomena in the viscoelastic materials are (Lakes, 2009; Yam, 2011; Chowdhury, 2014; Haddadi et al., 2008):

i. *Creep response:*

Creep, time and temperature dependent phenomena occurs under load control and is a combination of behaviours of viscous liquid and elastic solids, as shown in Figure 2.2.

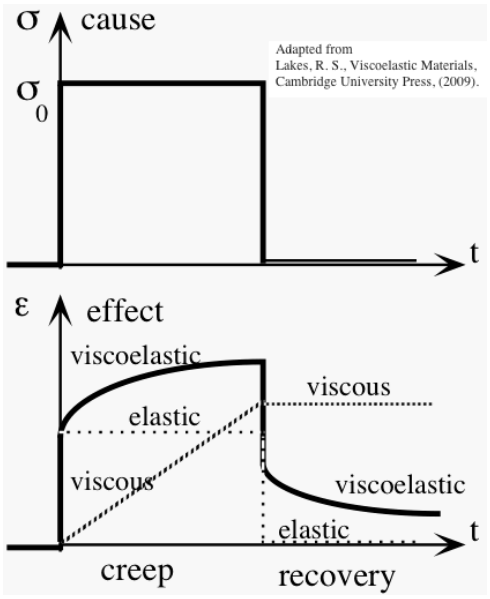

Figure 2.2. Creep and recovery responses of a viscoelastic material (Lakes 2009)

ii. Relaxation or recovery:

The stress relaxation or recovery occurs for a viscoelastic material in order to keep the strain constant with time, as shown in Figure 2.3.

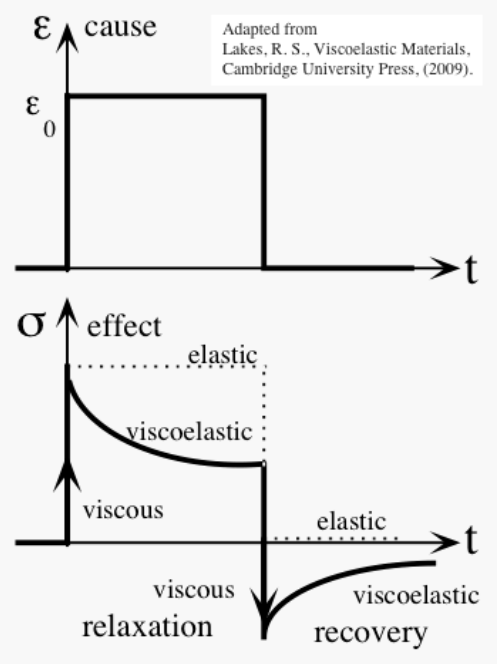

Figure 2.3. Relaxation and recovery response of a viscoelastic material experiencing a step strain (Lakes, 2009).

iii. Dissipation of energy:

Dissipations of mechanical energy happen under cyclic loading. The dissipation factor, storage modulus, and loss modulus vary with the frequency of loading (ω), as shown in Fig 2.4. The real part or storage modulus (E') describes the elastic portion of the material or the resistance to the deformation. The viscous behavior, on the other hand, is represented by the imaginary part or loss modulus (E''). It reflects the loss of useful mechanical energy through dissipation as heat. The loss tangent is essentially the tangent of the phase and is represented by the ratio of the loss to storage moduli, $tan\,\delta = \frac{E''}{E'}$.

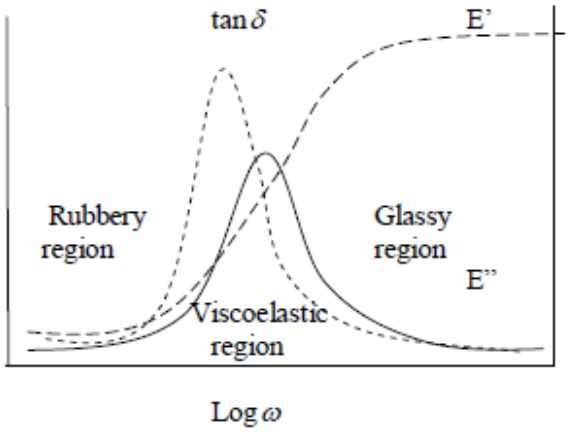

Figure 2.4. The complex modulus of the viscoelastic medium as a function of frequency (Ward and Hadley, 1993).

2.3.1 Relaxation and dynamic approach: Complex moduli

The moduli and viscosities are assumed to be frequency independent in Navier Stokes equations which are not adequate to describe the laboratory observations even with the introduction of bulk viscosity. Therefore, it is now more convenient to express sound

attenuation and dispersion in highly viscous fluids in terms of appropriate elastic stiffness constant (bulk modulus and shear modulus). This approach fundamentally differs from the previous one by assuming that the moduli are frequency dependent (Ferry, 1980). The moduli and viscosities essentially take a complex form in the frequency domain for a harmonic vibration.

The propagation of sound waves is now defined from the equations of isotropic solid but with complex longitudinal modulus $M(i\omega)$ (Litovitz and Davis, 1965; Kono, 1961),

$$M(i\omega) = M'(\omega) + iM''(\omega) = K'(\omega) + \frac{4}{3}G'(\omega) + i[K''(\omega) + \frac{4}{3}G''(\omega)] \tag{18}$$

where, K and G are the bulk and shear modulus, respectively. Moreover, the complex modulus $M(i\omega)$ is not restricted to any particular type of deformation e.g., shear, bulk or tensile. This idea will be implemented in **chapter 4**.

The compressional wave velocity and attenuation can be defined by (Bhatia, 1985),

$$V_p^2 = M'/\rho \tag{19}$$

$$\alpha_{\lambda p} = \pi M''/\left(\rho V_p^2\right) \tag{20}$$

where $V = {}^{\omega}/_{k_1}$ and $\alpha_\lambda = {}^{2\pi k_2}/_{k_1}$

Similarly, shear wave velocity and associated attenuation coefficients are,

$$V_s^2 = G'/\rho \tag{21}$$

$$\alpha_{\lambda s} = \pi G''/(\rho V_s^2) \tag{22}$$

Equations (19) and (20) show that observed values of V_p and $\alpha_{\lambda p}$ can be used to determine M' and M'' in which the effects of shear and dilatational relaxations occur additively as shown in equation (18). A separate measurement of either $K',\ K''$ or $G',\ G''$ is required to determine individual relaxation effects. Moreover, V_s and $\alpha_{\lambda s}$ are very

difficult to measure experimentally to determine $G'and\ G''$ through equations (21) and (22).

However, in principle V_s and $\alpha_{\lambda s}$ can be determined by studying reflections of shear waves at a liquid-solid boundary (details are in **chapter 5**) and thus provide the following relations in case of low viscosity ($\omega\tau_s \ll 1$),

$$V_s^2 = 2\omega G_\infty \tau_s/\rho = 2\omega\eta/\rho \tag{23}$$

$$\alpha_{\lambda s} = 2\pi \tag{24}$$

These are the similar relations with that of Navier-Stokes equations (14) and (15).

And at high viscosity, where $\omega\tau_s \gg 1$, shear wave velocity and attenuation law can be reduced to,

$$V_s^2 = G_\infty/\rho \tag{25}$$

$$\alpha_{\lambda s} \approx \pi/(\omega\tau_s) \tag{26}$$

where G_∞ is the unrelaxed shear modulus and $\tau_s = \eta/G_\infty$ is relaxation time for the shear process at high frequency. For $\omega\tau_s \gg 1$, $G_\infty = G' = G''$, which can be measured from the shear impedance as $Z_{liq,s} = (\rho G_\infty)^{\frac{1}{2}}$ (Greenwood and Bamberger, 2002). Thus the attenuation is small at high frequency due to the liquid's solid like properties, where both the longitudinal and shear waves can propagate. However, these formulations are still over simplified to describe the experimental observations.

Whorlow (1980) introduces **a rheological approach** to characterizing viscoelastic properties of liquids. The "storage modulus" $G'$and imaginary component "loss modulus" G'' in the complex shear modulus of equation (18) can be defined as (Dukhin and Goetz, 2009),

$$G'(\omega) = \rho\omega^2 V^2 \frac{\omega^2 - \alpha_s^2 V^2}{[\omega^2 + \alpha_s^2 V^2]^2} = \frac{\rho\omega^2 \left(\frac{4\pi^2}{\lambda^2} - \frac{1}{z_s^2}\right)}{\left(\frac{4\pi^2}{\lambda^2} + \frac{1}{z_s^2}\right)^2} \tag{27}$$

$$G''(\omega) = 2\rho\omega^3 V^2 \frac{\alpha_s V}{[\omega^2 + \alpha_s^2 V^2]^2} = \frac{\rho\omega^2 \frac{4\pi}{\lambda z_s}}{\left(\frac{4\pi^2}{\lambda^2} + \frac{1}{z_s^2}\right)^2} \tag{28}$$

where α_s is essentially the attenuation associated with shear wave (equation (15)), $z_s = 1/\alpha_s \approx (\eta/\rho\omega)^{0.5}$ is the shear penetration depth, and λ is the wavelength.

In a similar manner, complex longitudinal modulus $K^* = K' + iK''$ can be introduced; where "longitudinal storage modulus" K' and longitudinal loss modulus K'' possess identical formulation of $G' and\ G''$. The longitudinal penetration depth $z_l = 1/\alpha_l \approx \rho V^3/\omega^2\eta$ is associated with stokes attenuation coefficient (equation (10)).

$$K'(\omega) = \rho\omega^2 V^2 \frac{\omega^2 - \alpha_p^2 V^2}{\left[\omega^2 + \alpha_p^2 V^2\right]^2} = \frac{\rho\omega^2 \left(\frac{4\pi^2}{\lambda^2} - \frac{1}{z_p^2}\right)}{\left(\frac{4\pi^2}{\lambda^2} + \frac{1}{z_p^2}\right)^2} \tag{29}$$

$$K''(\omega) = 2\rho\omega^3 V^2 \frac{\alpha_p V}{\left[\omega^2 + \alpha_p^2 V^2\right]^2} = \frac{\rho\omega^2 \frac{4\pi}{\lambda z_p}}{\left(\frac{4\pi^2}{\lambda^2} + \frac{1}{z_p^2}\right)^2} \tag{30}$$

2.3.2 Linear mechanical models

As mentioned earlier, the Navier-Stokes equation with the bulk viscosity can not still satisfactorily account for the complex nature of bitumen. Higher order approximation of stress tensor may improve the equations, but it is too complicated to carry on here. Therefore, a simplified and popular mechanical approach, linear viscoelastic model, is also adapted here to deal with the viscoelastic materials. It is occasionally called as

spring-dashpots model (Özkaya et al., 2017; Lakes, 2009; Gutierrez-Lemini, 2014). The springs and dashpots respectively can represent the elastic and viscous part of the viscoelastic material (Figure 2.5).

(a) (b)

Figure 2.5. (a) A Hookean spring represents the elastic and (b) a Newtonian dashpot represents the viscous material responses (Özkaya et al., 2017). The deformation is recoverable in the spring but permanent for the dashpot with the removal of applied stress.

The manner of deformations, recovery, and storing potential energy of an elastic material bears a resemblance to that of spring and obeys Hooke's law. The stress (σ) or force (F) is proportional to the strain (ε) or displacement (x), as $\sigma=E\varepsilon$ or $F=kx$. Both E *(elastic constant)* and k *(spring constant)* are mainly the measures of stiffness.

A dashpot is a simple piston-cylinder or a syringe type arrangement which is used to emulate the viscous behaviour. The applied stress produces a rate of strain, not strain and the proportionality constant is called the coefficient of viscosity, as $\sigma = \eta \frac{d\varepsilon}{dt}$.

If the two segments 'Hookean spring' and 'Newtonian dashpot' are connected in series, as shown in Figure 2.6, the combination is known as **Maxwell model**.

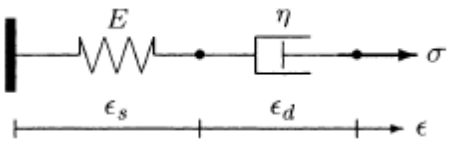

Figure 2.6. The Maxwell viscoelastic model, a series connection of spring and dashpot (Özkaya et al., 2017).

The stress is applied equally on the spring and dashpot ($\sigma = \sigma_S = \sigma_D$) but produces individual strain for the segments ($\varepsilon = \varepsilon_S + \varepsilon_D$). Therefore, the stress and strain for the Maxwell model are related as,

$$\eta \frac{d\sigma}{dt} + E\sigma = E\eta \frac{d\varepsilon}{dt} \tag{31}$$

On the other hand, the configuration with the parallel connection of the spring and dashpot, as shown in Figure 2.7, is known as a **Kelvin-Voight model**.

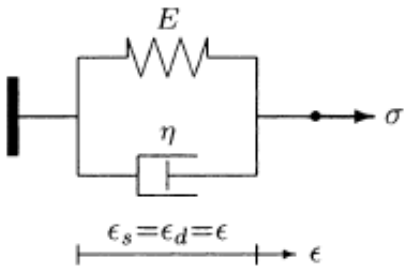

Figure 2.7. The Kelvin – Voight viscoelastic model, a parallel connection of spring and dashpot (Özkaya et al., 2017).

In this case, the two segments – spring and dashpot – share the total applied stress ($\sigma = \sigma_S + \sigma_D$), but the corresponding deformations will be same ($\varepsilon = \varepsilon_S = \varepsilon_D$). The constitutive relation is described as,

$$\sigma(t) = E\varepsilon(t) + \eta \frac{d\varepsilon(t)}{dt}$$

It is important to note that, the Maxwell and Kelvin – Voight models are extensively used as the basic viscoelastic models, but they often fail to deal with a complex viscoelastic material, such as bitumen. Although we do not have the scope to discuss the details here, few more useful mechanical models are also available in the literature. Few of the examples are generalized Burger model, Huet model, DBN model, standard solid model, and so forth (Behzadfar and Hatzikiriakos, 2013; Özkaya et al., 2017). These new configurations are essentially some modified connections of the

Maxwell and Kelvin – Voight models. However, none of the models can alone represent the complete rheological behaviours of bitumen but may only model one type of experimental observation. So, its imperative to study the properties of bitumen extensively.

The next chapter will discuss the rock physics studies with bitumen hosting carbonates, followed by longitudinal and shear properties measurements in raw bitumen.

References

Behzadfar, E., and S. G. Hatzikiriakos. 2013, Viscoelastic properties and constitutive modelling of bitumen. Fuel, **108**, no. Supplement C,391-399. doi: https://doi.org/10.1016/j.fuel.2012.12.035.

Bhatia, A. B. 1985, Ultrasonic absorption : an introduction to the theory of sound absorption and dispersion in gases, liquids and solids: New York : Dover Publications, 1985, c1967.

Bhatia, A. B., and R. N. Singh. 1986, Mechanics of deformable media, Graduate student series in physics: Bristol : Hilger, c1986.

Bouzidi, Y. 2003, The acoustic reflectivity and transmissivity of liquid saturated porous media : experimental tests of theoretical concepts: 2003.

Chowdhury, M. M. H. 2014, Effects of CO2 on seismic wave speed in Fontainebleau sandstone.

Dukhin, A. S., and P. J. Goetz. 2009, Bulk viscosity and compressibility measurement using acoustic spectroscopy. The Journal of Chemical Physics, **130**, no. 12,124519. doi: doi:http://dx.doi.org/10.1063/1.3095471.

Ferry, J. D. 1980, Viscoelastic Properties of Polymers. 3rd ed: Wiley, New York.

Greenwood, M. S., and J. A. Bamberger. 2002, Measurement of viscosity and shear wave velocity of a liquid or slurry for on-line process control. Ultrasonics, **39**, no. 9,623-630. doi: 10.1016/S0041-624X(02)00372-4.

Gutierrez-Lemini, D. 2014, Fundamental Aspects of Viscoelastic Response, Engineering Viscoelasticity: Springer US. 1-21.

Haddadi, S., E. Ghorbel, and N. Laradi. 2008, Effects of the manufacturing process on the performances of the bituminous binders modified with EVA. Construction and Building Materials, **22**, no. 6,1212-1219. doi: https://doi.org/10.1016/j.conbuildmat.2007.01.028.

Kinsler, L. E. 1982, Fundamentals of acoustics: New York : Wiley, 1982. 3rd ed.

Kono, R. 1961, The Dynamic Bulk and Shear Viscosity of High Polymers, 1. Journal of the Physical Society of Japan, **16**, no. 8,1580-1586. doi: 10.1143/JPSJ.16.1580.

Lakes, R. 2009, Viscoelastic Materials: Cambridge University Press.

Litovitz, T. A., and C. M. Davis. 1965, Structural and Shear Relaxation in Liquids. Vol. 2: ACADEMIC PRESS INC.

Özkaya, N., D. Leger, D. Goldsheyder, and M. Nordin. 2017, Mechanical Properties of Biological Tissues, Fundamentals of Biomechanics: Equilibrium, Motion, and Deformation: Springer International Publishing. 361-387.

Trusler, J. P. M. 1991, Physical Acoustics and Metrology of Fluids, The Adam Hilger Series on Measurement Science and Technology: Adam Hilger.

Ward, I. M., and D. W. Hadley. 1993, An introduction to the mechanical properties of solid polymers: John Wiley and Sons Ltd, New York.

Whorlow, R. W. 1980, Rheological techniques, Ellis Horwood physics in medicine and biology series: Chichester [Eng.] : E. Horwood ; New York : Wiley, 1980.

Wolf, K., T. Vanorio, and G. Mavko. 2008, Measuring and monitoring heavy-oil reservoir properties. The Leading Edge, **27**, no. 9,1138-1147. doi: 10.1190/1.2978976.

Yam, H. 2011, CO2 rock physics: a laboratory study.

Chapter 3: Pressure and temperature dependence of acoustic wave speeds in bitumen saturated carbonates: Implications for seismic monitoring of the Grosmont Formation*

*A version of this chapter is published in Geophysics. Rabbani, A., D. R. Schmitt, J. Nycz, and K. Gray. 2017, GEOPHYSICS, **82**, no. 5, MR133-MR151.

Recent time-lapse seismic observations in carbonate reservoirs subject to steam assisted enhanced oil recovery display substantial changes in seismic reflectivity due to the combined effects of saturation, pressure, and temperature. Understanding these field seismic observations requires knowledge of the effects on the seismic wave speeds in bitumen saturated carbonates. We have conducted ultrasonic measurements of compressional (P) and shear (S) wave velocities in bitumen-saturated dolomite taken from the Grosmont Formation in northern Alberta. Wave speeds were measured under a variety of conditions of constant pore pressure, constant effective pressure, and with varying temperature in order to map the various controlling factors. The temperature dependent declines of 12% and 9% for the P- and S-wave speeds, respectively, with temperatures from 10°C to 102°C are most notable. Unlike oil sands, at times the dolomite retains its structure upon removal of the bitumen allowing for measurement of the dry and water saturated frame properties and their subsequent use in substitutional modelling. None of the standard bounding, inclusion, or Biot-Gassmann family models adequately describe the observations in the heated sample. The deviations may be in part due to the inability of these models to properly incorporate the complex bitumen non-Newtonian rheology including a bulk viscosity.

3.1 Introduction

Large bituminous oil resources are available worldwide (Meyer et al., 2007). They are an important component of global hydrocarbon energy reserves and with the development of increasingly efficient technologies for extraction it is expected they will continue to increase in importance in the future. Most of Canada's bitumen resource lies in the well-known oil sand deposits. It is not so generally known, however, that a large fraction of the total Canadian resource resides in carbonate reservoirs that still remain essentially untouched (Ardakani et al., 2014) . Much of the potential supply rests in the Grosmont Formation of north-eastern Alberta (Figure 3.1) containing initial volumes in excess of 64.5 billion m^3 (406 billion barrels) in place (AER, 2016).

In Situ bitumen is not so easily recovered. It is a particularly heavy oil characterized by specific gravities less than 10° API (American Petroleum Institute) that equate to mass densities exceeding that of water (1000 kg/m^3) (Yuan et al., 2017). Under virgin *in situ* conditions bitumen's shear viscosity can easily exceed 10^7 cP (Yang et al., 2014). As in the nearby and overlying oil sands, this viscosity of the bitumen saturating these carbonates must be reduced in order for it to be produced economically (Rassenfoss, 2013). In many cases this means the reservoir fluid will be sufficiently heated to more than 100°C as has now long been carried out in the oil sands using cyclic steam stimulation (CSS) or steam assisted gravity drainage (SAGD), although electrical technologies may play a role in heating or even initial in-situ upgrading (Butler, 1991; Jiang et al., 2010; Mohebati et al., 2014).

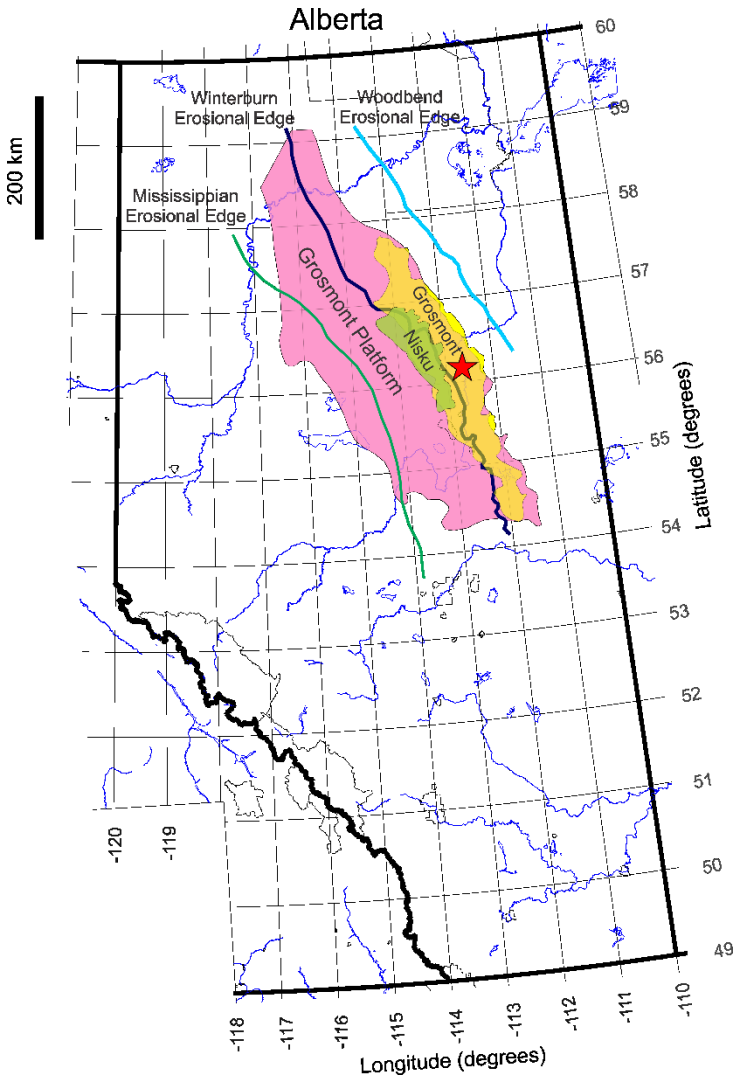

Figure 3.1. Map of Alberta showing the location of the buried Grosmont Formation in pink and the yellow areas indicative of the bitumen saturated Grosmont and the overlying Nisku Formations in green that lie unconformably beneath the Cretaceous deposits. The bitumen resides primarily in the secondary and tertiary porosities developed from karsting and dolomitization. The core sample was collected from a pilot project indicated by the red star.

It has been long known that elevated pressure and temperature of injected steam during in situ bitumen recovery processes such as SAGD lead to changes in seismic wave speeds and attenuation (Bianco et al., 2008; Kato et al., 2008). In bitumen saturated oil sands, the change in seismic reflectivity from a reservoir can be substantial due to the combined effects of increased temperature, pore pressure and effective stress, and the

substitution of bitumen with water and steam; and these physical property changes can be observed with time lapse seismic monitoring (Greaves and Fulp, 1987; Eastwood et al., 1994; Schmitt, 1999; Isaac and Lawton, 2006; Bianco et al., 2010; Zadeh et al., 2010). Understanding the seismic responses from such reservoirs requires knowledge of how the wave speeds and densities will evolve within the reservoir during the process; and there has already a great deal of laboratory work focussed on oil sands materials.

Nur (1982) first postulated a strong correlation between temperature increase and subsequent P-wave velocity decrease in oil sands. Wang and Nur (1990) later discussed the effects of temperature change in ultrasonic velocities in hydrocarbon liquids and rock sample saturated with liquids to monitor thermal enhanced oil recovery processes. They also found that the ultrasonic wave speeds in unconsolidated sands and rocks saturated with heavy oils decreased dramatically by between 15% and 40% over an increase in temperature of only 100°C. Daridon et al. (1998) came to similar conclusions in studies on a variety of oils of diverse densities. This temperature effects can be detected with high-resolution seismic methods to aid reservoir monitoring during production. Acoustic velocities in dead oils, refined petroleum hydrocarbons, and gas-saturated oil also strongly depend on the fluid pressure (Wang et al., 1990). Eastwood (1993) carried out ultrasonic P- and S-wave velocities measurements in Cold Lake oil sands and observed a good agreement with theoretical predictions of the velocities. While the S-wave velocity remains almost constant, the P velocity in the oil sands dropped by 15% over a temperature change of 22°C to 125°C. Eastwood (1993) predicted, based on modeling, that P-velocity drop was dominated by the change in fluid bulk modulus with temperature.

In more recent studies, Uvalde bitumen saturated carbonate rock exhibits shear relaxation at room temperature and Uvalde bitumen acts as solid at low temperature but transforms into liquid with zero shear modulus at higher temperatures (Batzle et al.,

2006; Behura et al., 2007). Strong temperature dependence of the bulk and shear moduli of unidentified extra heavy oil are also recently observed with ultrasonic measurements (Han et al., 2008). The rheological properties of bitumen are particularly complex. Zhao and Machel (2012) measured the rheological properties of Grosmont's bitumen extracted from archival core material, some of which were as much as 30 years old and found similar ranges of viscosities.

Kato et al. (2010) described a series of laboratory measurements from the Lower Cretaceous McMurray formation from about 300 m depth to assist in the interpretation of repeated seismic surveys collected earlier. Their experiments, carried out at relatively low effective pressures of only 1.37 MPa, showed that both the P- and S-wave speeds decreased by more than 40% with temperatures to 140°C. However, the rate of decline lessened above 30°C suggesting a change in the behaviour of the bitumen at this temperature. Spencer (2013) conducted low frequency measurements on samples of an Ells River oil sand and rheometer measurements on its produced bitumen. The saturated bulk- and shear- moduli in the bitumen sand drop by 30% and 6%, respectively with temperature change from 5°C to 49°C, while the pore pressure is maintained above bubble point. He also emphasizes that temperature dependent bulk modulus of bitumen causes the larger drop in P-wave velocity. Meanwhile, S-wave velocity he observed remained almost constant to justify smaller decrease of shear modulus. Most recently, Li et al. (2016) reaffirmed the strong influence of temperature of heavy oil-saturated sand rock.

There have also been parallel theoretical efforts to understand wave propagation, attenuation, and fluid substitutions in rocks containing highly viscous fluids. This is of great interest theoretically because the time scales of the response of bitumen, for example, will depend on viscosity (and hence temperature) (Gurevich et al., 2008; Makarynska et al., 2010; Mavko, 2013; Shamsa and Lines, 2015). Wang et al. (2015)

describe early attempts to numerically model the response of a bitumen-saturated carbonate at low frequencies. A few other attempts have also been made to study rock-physics models for heavy-oil and solid substitutions (Ciz and Shapiro, 2007; Saxena and Mavko, 2014). The presence of semi-solid bitumen in the compliant pores makes the rock very stiff, Saxena et al. (2016) have recently attempted to model this using a solid-squirt model.

Wave speeds and elastic properties in carbonate rocks have been studied under many different and combinations of pore and confining pressure and fluid saturations (Peselnick and Outerbridge, 1961; Wang et al., 1990; Anselmetti and Eberli, 1993; Kenter et al., 2002; Adam et al., 2006; Agosta et al., 2007; Verwer et al., 2008; Baechle et al., 2009; Bakhorji, 2010; Fabricius et al., 2010; Vanorio and Mavko, 2011; Melendez-Martinez and Schmitt, 2013; Njiekak et al., 2013; Mikhaltsevitch et al., 2016). The above information will be key to the proper interpretation of the variations in physical properties of Grosmont bitumen saturated carbonates under varying conditions expected during SAGD or CSS processes.

The structure and elastic properties of the bitumen saturated carbonates differ significantly from the highly compressible, siliclastic oil sands. Time lapse seismology could be an effective method for monitoring carbonate formations saturated with gas (Harris et al., 1995). However, the significant changes in acoustic impedance – density and velocity – over a period of time as demonstrated in the time-lapse seismic image, Figure 3.2, from repeated seismic surveys over a pilot steam injection project in the Grosmont carbonates of northeast Alberta could be quite difficult to interpret properly (Yang et al., 2014). More informed interpretations of the data of Figure 2 require additional knowledge of how fluid substitution and varying temperatures and pressures will influence the seismic properties of the rock.

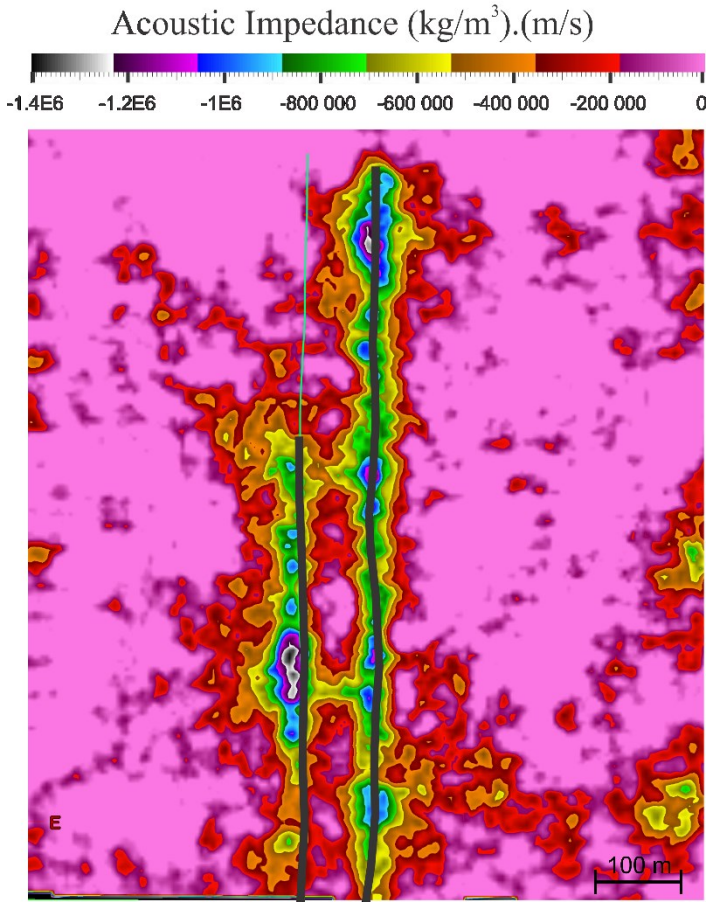

Figure 3.2. The effects of steam injection on a repeat-seismic survey are clearly visible in this map of the acoustic impedance difference between the monitor and baseline surveys over the time period from February 2011 to December 2012. Image is created by taking the volume of the joint prestack inverted P impedance of the monitor and subtracting the volume of the joint prestack inverted P impedance of the baseline. Shown above is the impedance difference slice at a level 2 m above the injector well in the eastern well pair. Black lines indicate the location of the horizontal CSS wellbores (Nycz et al., 2016).

To our knowledge, the only publicly available reports in the literature on the seismic properties of bitumen saturated carbonates under in situ conditions within such heated reservoirs is the recent example of Rabbani et al. (2014) and Yuan et al. (2017) and who measured the wave speeds and attenuation in a bitumen saturated dolomite and limestone. In this contribution we describe the development of a laboratory experiment that seeks to provide appropriate measures of seismic wave speeds and

attenuation in such rocks over the temperature range from 10°C to over 100°C subject to ranges of confining and pore pressures expected in such reservoirs. The peak temperature is less than that of the injected steam which will exceed 200°C but the lower range would still be representative of the larger volume of rock and reservoir fluid heated by the transfer of heat into the formation from the injection point and which would be detected in surface seismic surveys. Our purpose here is to first describe the experimental approach in which we take special care to deal with issues of effective pressure and then to report the results of our initial set of measurements on a porous sucrosic dolomite from the Grosmont formation. The paper begins with a brief overview of the target Grosmont formation followed by the characterization of the samples and fluids, describes our experimental approaches, and presents the results of the effects of temperature and pressure on the wave speeds through a saturated dolomite. We test a variety of theoretical models against these observations. The paper concludes with an exploration of how seismic responses might be expected to evolve during heating of the reservoir through simple modelling.

3.2 Geological background

As the main focus of this contribution is on the physical properties, we provide only a brief overview of the geology of the bitumen-bearing Grosmont formation. Recent discussions by Machel et al. (2012); Ardakani et al. (2014) and Russel-Houston and Gray (2014) and references therein provide more detailed background. The rock sample is taken from cores obtained at a pilot project site with details of the geology and geophysics given by Russel-Houston and Gray (2014), on petrophysics by MacNeil (2015), and on engineering by Mohebati et al. (2014) and Yang et al. (2014).

The Grosmont Formation itself is informally subdivided into 4 zones from oldest to youngest called A, B, C, D (or alternatively in the earlier literature the Lower Grosmont

(LGM) and Upper Grosmont 1, 2, and 3, respectively, e.g. Cutler (1982)). The deeper A and B units are mostly limestone but C and D are dolomitized. These upper units are bitumen bearing due to a combination of matrix porosity and karstification. Conveniently, the 'Grosmont Shale Breaks' are thin marl units that are more radioactive and allow these 4 units to be distinguished regionally in geophysical logs (see Ardakani et al, 2014 for an example). Figure 3.3 summarizes the average properties of the Grosmont C and D formation and indicates that the liquids within the pore spaces of the upper C are about 25% water and 75% bitumen.

Depth (m)	Formation	Porosity	Saturation Oil/Water
325	Upper D	0.25	0.82/0.18
332	Middle D	0.18	0.65/0.35
342	Lower C	0.30	0.80/0.30
354	C/D Marl	0.15	0.60/0.40
355	Upper C	0.16	0.75/0.25
362	Middle C	0.32	0.82/0.18
364	Middle C - Small vugs	0.18	0.80/0.20
370	Middle C - Larger vugs	0.14	0.65/0.35
375			

Figure 3.3. Average porosity and fluids saturation of Grosmont C and D formation (Mohebati et al., 2014).

This heterogeneity also complicates understanding of the details of the reservoir that cannot be obtained effectively by drilling, production testing, and geophysical

logging alone. These structural variations mandate the use of laboratory geophysical methods for better characterization of the reservoir.

3.3 Sample Characterization

The Grosmont formation core sample was preserved by deep refrigeration shortly after coring. Freezing these samples is necessary to avoid loss of the bitumen that, while still highly viscous, drains out of a sample under normal room storage conditions. The sample studied is a sucrosic dolomite representative of the Grosmont upper C formation (Figure 3.4) taken from a depth of 360.56 m.

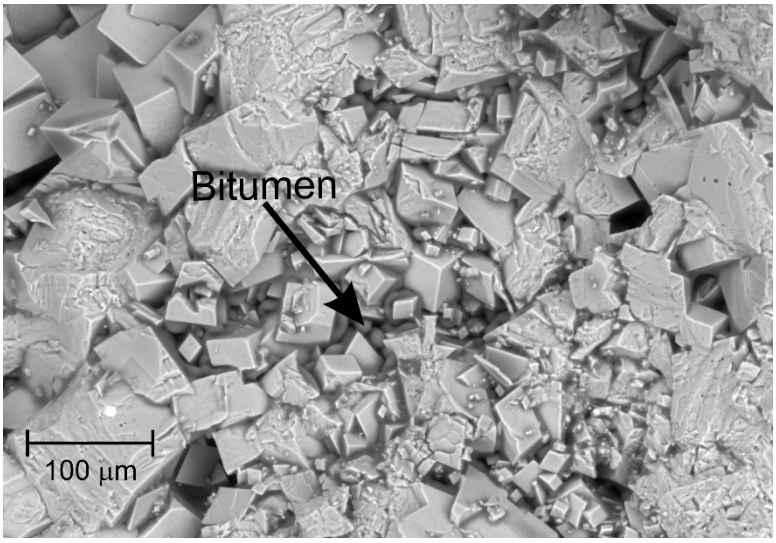

Figure 3.4. 550 X Scanning electron microscope image of the uncleaned sample illustrating the sucrosic dolomite structure. Bitumen saturation appears as grey zones filling pore space between the mineral grains.

Two suites of measurements were made on the core sample: the first with the original pore fluids in place as received (Figure 3.5a), and second on the 'dry' rock frame after the pore fluids had been displaced (Figure 3.5b) by over one week of soaking with toluene using a standard Soxhlet process. This cleaned solid porous frame was

characterized with standard petrophysical tests and details of the studies are described in Appendix 3.A and summarized in Table 3.1.

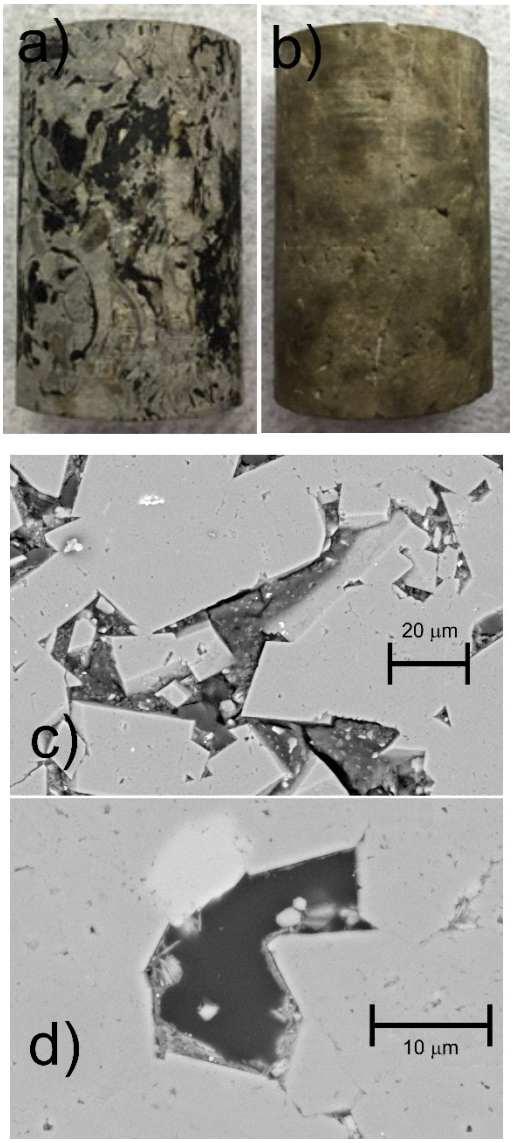

Figure 3.5. Images of saturated and cleaned sample. a) core sample in as received condition showing bitumen saturation. b) Sample after cleaning using Soxhlet process, note residual staining of bitumen remains. c) 885 X SEM image of material prior to cleaning showing pore spaced filled with bitumen mixed with some solids saturating the pore space. d) 2300 X SEM image of pore after Soxhlet cleaning showing removal of bitumen.

Table 3.1. Properties of the bitumen saturated carbonate at room condition

Grain density (kg/m^3)	2785 (Hg porosimetry)
Dry Bulk Density (kg/m^3)	2591 (Hg porosimetry) 2590 (From mass and envelope volume)
Porosity ϕ (%)	8 (Hg porosimetry) 7 (He pycnometry)
Permeability k (mD)	3 to 5
Mineral Bulk Modulus K_s (GPa)	94.9[a]
Mineral Shear Modulus μ_s (GPa)	45
Tortuosity τ	6.5
Dominant Pore Throat Radius	80 nm
Frame K_d (GPa)	37.5
Frame μ_d (GPa)	25.0

One of the tests is mercury injection porosimetry measurements which were made on a small portion taken from the cleaned sample. The Hg imbibition curve upon pressurization (Figure 3.6) suggests a continuous decrease in the dimensions of the pores with pressure that accelerates over the range of pore throats from 50 nm to 100 nm with the peak (solid line) near 80 nm. The drainage curve upon depressurization shows, however, that most of the Hg remains within the pore space of the sample. This can be interpreted to mean that the pore sizes exceed substantially that for the connecting pore throats. Once the Hg has entered a pore, it becomes trapped in what is often referred to as the ink well effect; the Hg cannot exit as there is insufficient pressure to push back out through the pore throats.

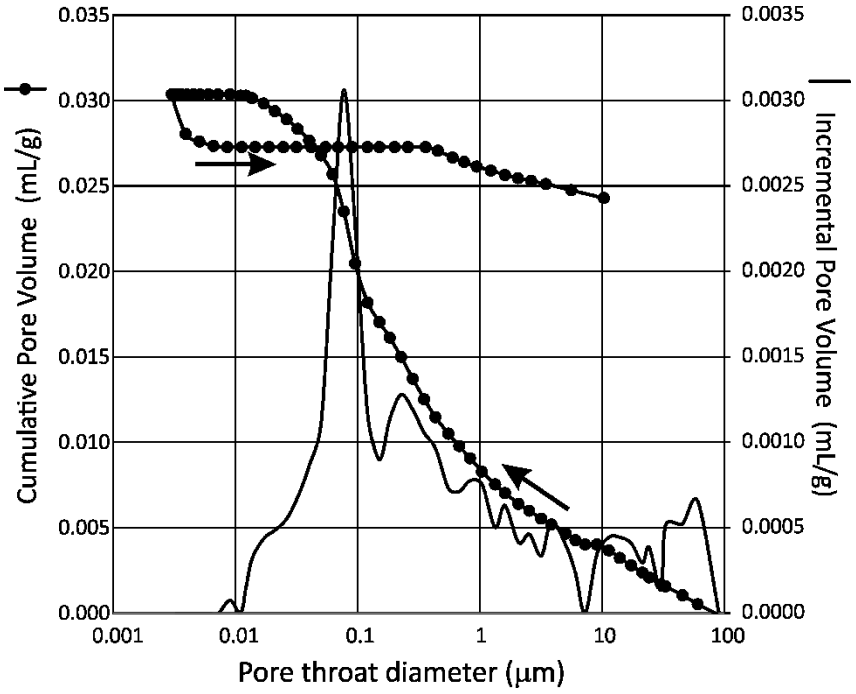

Figure 3.6. Results of mercury injection porosimetry on the sample. Line with data points is the cumulative pore volume of Hg imbibed per gram of material during pressurization (left pointing arrow) and depressurization (right arrow). Solid line is the corresponding increment of Hg imbibed.

3.4 Fluid characterization

The overall seismic responses can depend on various factors but are heavily influenced by the state of the fluid saturation within the rock. The proper interpretation of the observations on bitumen saturated carbonates, therefore, requires a solid understanding of the physical properties of saturating pore fluids under various conditions of pressure and temperature. The properties of bitumen, such as shear viscosity, density and bulk modulus, strongly depend on temperature and can dictate the observed seismic velocities and attenuation.

Measurements on bitumen extracted from cores (Figure 3.7a) shows that bitumen viscosity is 10 million times greater than that of water at 11°C but decreases rapidly with temperature with an exponential fit adequately describing the viscosity over the range of temperatures used here (Russel-Houston and Gray, 2014; Yang et al, 2014).

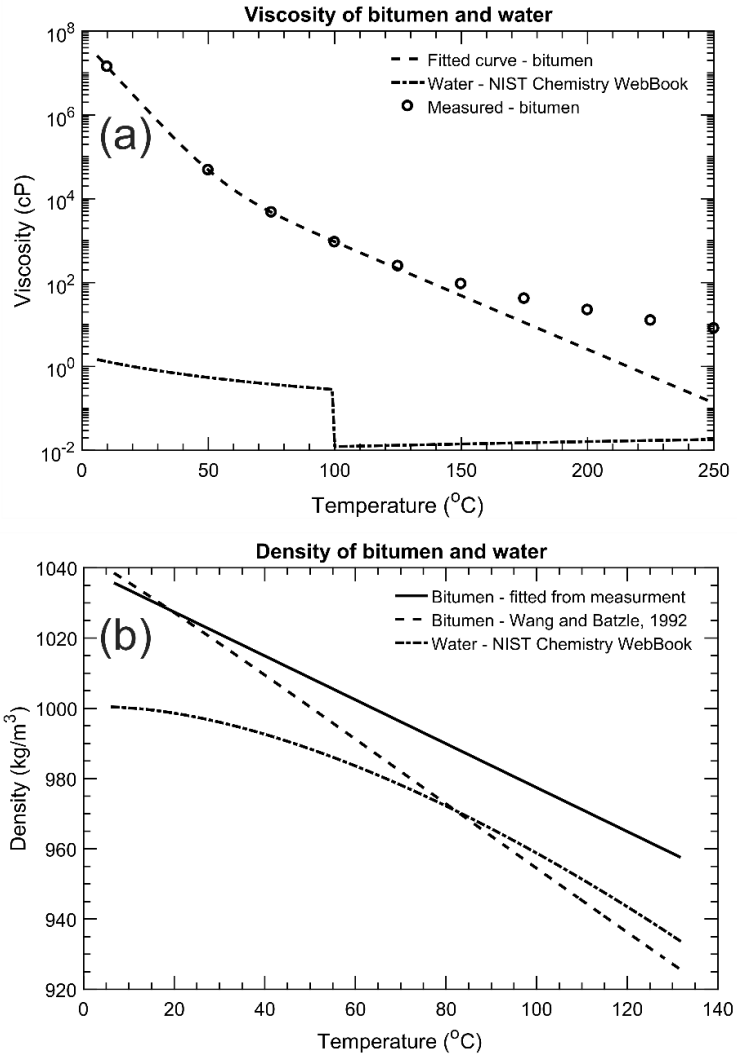

Figure 3.7. a) Dynamic viscosity of bitumen and water. b) Density of bitumen and water. Properties of saturating bitumen and water are from Yang et al. (2014) and NIST Chemistry WebBook, respectively.

We have additionally estimated the density of bitumen (ρ_f) at pressure (P) and temperature (T) from the well using known empirical relations from Batzle and Wang (1992). Initial density (ρ_0) for bitumen is 1020 kg/m^3 as standard ambient pressure and temperature. The saturated rock density, ρ_{sat} is calculated as,

$$\rho_{sat} = (1 - \varphi)\rho_s + \varphi\rho_f \quad (1)$$

where ρ_m = 2795 kg/m^3 is the matrix (dolomite) density and rock's porosity φ is 8%.

The measured density of bitumen (provided by our industry collaborator) is plotted in Figure 3.7b along with the values calculated from Wang and Batzle (1992). The empirical relation overstates the decrease in density at higher temperature.

The bulk modulus of the bitumen (Figure 3.8) is calculated using these temperature dependent densities and ultrasonic wave speeds measurements obtained from a parallel study (Rabbani et al, 2015; Rabbani and Schmitt, 2017).

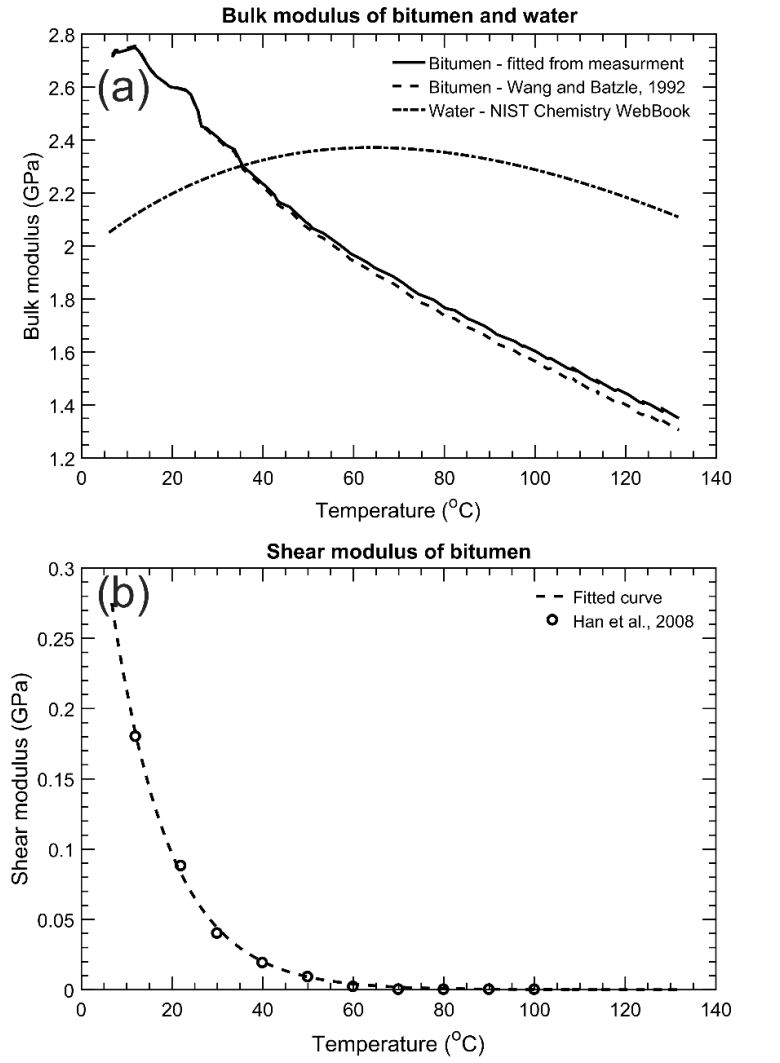

Figure 3.8. a) Adiabatic bulk modulus of bitumen and water as a function of temperature at 1 MPa pressure, b) Shear modulus of bitumen as a function of temperature as determined by Han et al. (2008).

These studies demonstrate that pressure only minimally influences the acoustic wave speed of bitumen. In contrast, the effect of temperature is significant. It is worthwhile noting that at low temperatures the density and bulk modulus of the bitumen exceeds that of water and that this is reversed before 40°C (Figure 3.8a).

An added complication is that the highly viscous bitumen possesses a small but measureable shear modulus at lower temperature (Batzle et al. 2006; Han et al. 2008). Measurements by Han et al. (2008) replicated in Figure 8b shows that the shear modulus of bitumen drops toward zero as temperatures reaches 60°C which also indicates that it transforms to liquid from the quasi solid state at lower temperature**.** Table 1 summarizes the physical properties of the sample.

3.5 Experimental details

In this study, we have adapted the well-known ultrasonic pulse transmission technique to the measurement of transit times, Δt through centimetre scale bitumen-saturated rock samples. The Δt are on the order of 20 μs, are then used with the sample's length dl to calculate the wave speed V = $dl/\Delta t$. Since the early studies, the ultrasonic pulse transmission method has perhaps become the most widely employed technique for estimating seismic or acoustic well log speeds in rocks subject to wide varieties of conditions (Mattaboni and Schreiber, 1967). Schmitt (2015) has recently reviewed the state of the art in this field.

One of the main purposes of this contribution is to describe the experimental measurements and in particular, the care that was taken in ensuring that we accurately understood the states of pore and confining pressure applied to sample. It is important to emphasize such aspects of the work because the elastic properties of the rock frame and correspondingly the compressional V_P and shear V_S wave speeds under saturated

conditions significantly depend on the differential pressure, $P_d = P_c - P_p$. It is important to note that differential pressure in this study is actually 'Terzaghi's effective stress' which is the correct effective stress for wave speed determinations, and we comment only that the Biot effective stress in which the pore pressure is modified by the Biot-Willis parameter applies only as a metric for volumetric strain. The confining pressure P_c equates in the earth to the overburden or tectonic stresses while the pore pressure P_p is what would normally be considered as the reservoir pressure in Petroleum Engineering calculations. Consequently, in order to properly understand the effects of the fluid on the seismic properties one should make the measurements at a constant differential pressure. This allows workers to minimize changes in the rock's frame properties during the tests in order to maximize the influence of the pore fluid (Schmitt et al., 2013).

Maintaining a state of constant differential pressure, however, is complicated in a rock saturated with a highly viscous fluid for two reasons. First, the high viscosity of the bitumen retards equilibration of the pore fluid pressure throughout the sample, consequently application of a confining pressure on the sample is expected to transiently increase the pore pressure due to a Skempton (1954) effect. Second, the bitumen has a relatively high thermal volumetric coefficient of thermal expansion ~0.001/°C which results if undrained in an increased pore pressure upon heating (e.g. Agar et al, 1986). As a result, sufficient time is required for equilibration to occur between changes. Zimmerman (1991) discusses the characteristic time t required for pore pressure equilibration with

$$t = \frac{\varphi \eta \beta L^2}{k} \tag{2}$$

where L = 5.9 cm is the sample length, k is the permeability (~5 mD), and the estimated total compressibility $\beta = \beta_{fluid} + \beta_{pore} \sim 5\ X\ 10^{-4}/MPa$. The pore pressure will equalize in ~0.1 seconds under water saturation. In contrast, however, at expected in situ

temperatures of 11°C over 80 hours may be required for the pore pressure excess to complete dissipate. This rapidly decreases with the decline in the bitumen viscosity to 3 hours at room temperature, about 20 minutes at 50°C, and less than 6 seconds at 100°C. The typical time allowed between measurements is about 20 minutes and this suggests that the true effective confining pressure P_d may be smaller than expected for temperatures below 50°C. Thus the maximum pressure error could be as much as 7% at low temperature and in turn the wave speeds would be slightly reduced.

Figure 3.9 summarizes the laboratory apparatus constructed featuring a cylindrical pressure vessel, an ultrasonic pulser-receiver, reservoir tanks, pumps, and temperature controller. The set-up independently controls both the confining pressure P_c of the hydraulic fluid that surrounding the jacketed sample and the pore fluid (i.e., reservoir) pressure P_p within the sample (Njiekak et al., 2013). Pressures are determined with an accuracy of better than 0.1 MPa.

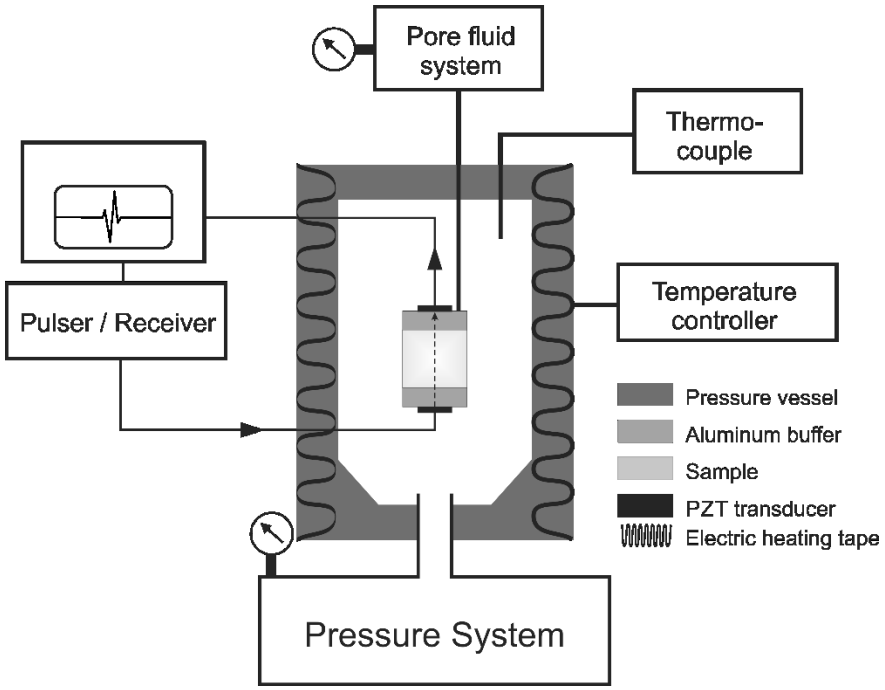

Figure 3.9. A schematic diagram of experimental set up that highlights both the confining and pore pressure controlling segments, and signal acquisition (Rabbani et al., 2016).

A chiller system (NESLAB Endocal Refrigerated Circulating Bath RTE-8DD) circulates fluid (mixture of water and glycol to prevent freezing) around the pressure vessel through a copper tubing system. The latter is wrapped directly around the pressure vessel and can control the temperature in pressure vessel from 0°C to 110°C with the stability of ±0.01°C. A 'K' type thermocouple is inserted into the pressure vessel to measure the inside temperature with an accuracy of ± 0.5°C. A hand driven pressure generator is used to control P_p during the tests. The pore pressure system is filled with silicone oil (Dow Corning Corp. 200 fluid) which applies back pressure to the bitumen within the sample. This silicone oil was employed because of its temperature stability and high immiscibility with bitumen.

Measurements were first conducted on the sample in as-received bitumen saturation (Figure 3.5a) and then on the same sample after the bitumen was removed (Figure 3.5b) and under dry and water-saturation with in-situ conditions preserved while adjusting factors such as confining pressure, pore pressure (using silicone oil pore fluid to provide back pressure), and temperature as prescribed in the results section below. The core sample is sandwiched between two aluminum end-caps, both of which include stacked 1 MHz laterally polarized shear-mode and axially polarized longitudinal-mode piezo-electric ceramics (APC International Ltd.) that, respectively, produce the S-wave and P-wave pulses. This arrangement is sealed with PVC tubing to prevent the confining fluid to enter the sample (Figure 3.10). Figure 3.11 gives examples of a suite P-wave and S-wave ultrasonic waveforms obtained using this system.

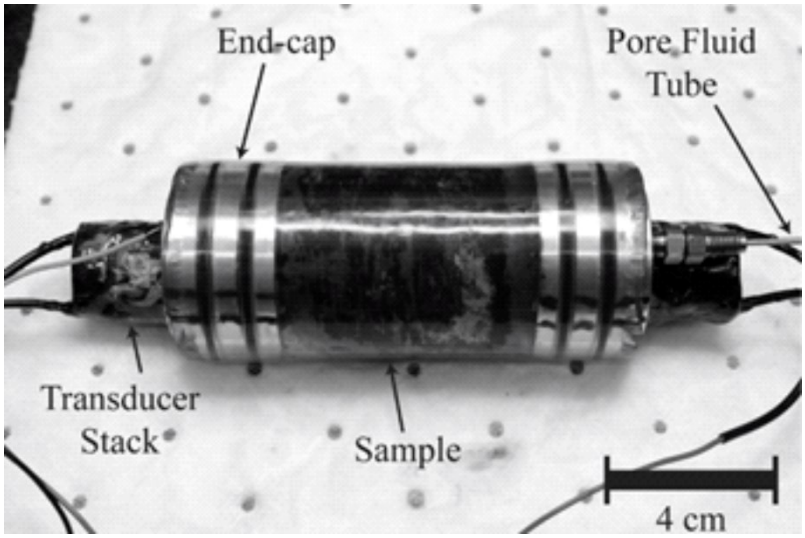

Figure 3.10. The sample assembly consisting of the core sample, aluminum end-caps and transducer stacks. A flexible PVC tube (Kuri Tec) covers the sample to isolate it from the confining fluid. The sample also shows the high saturation of bitumen.

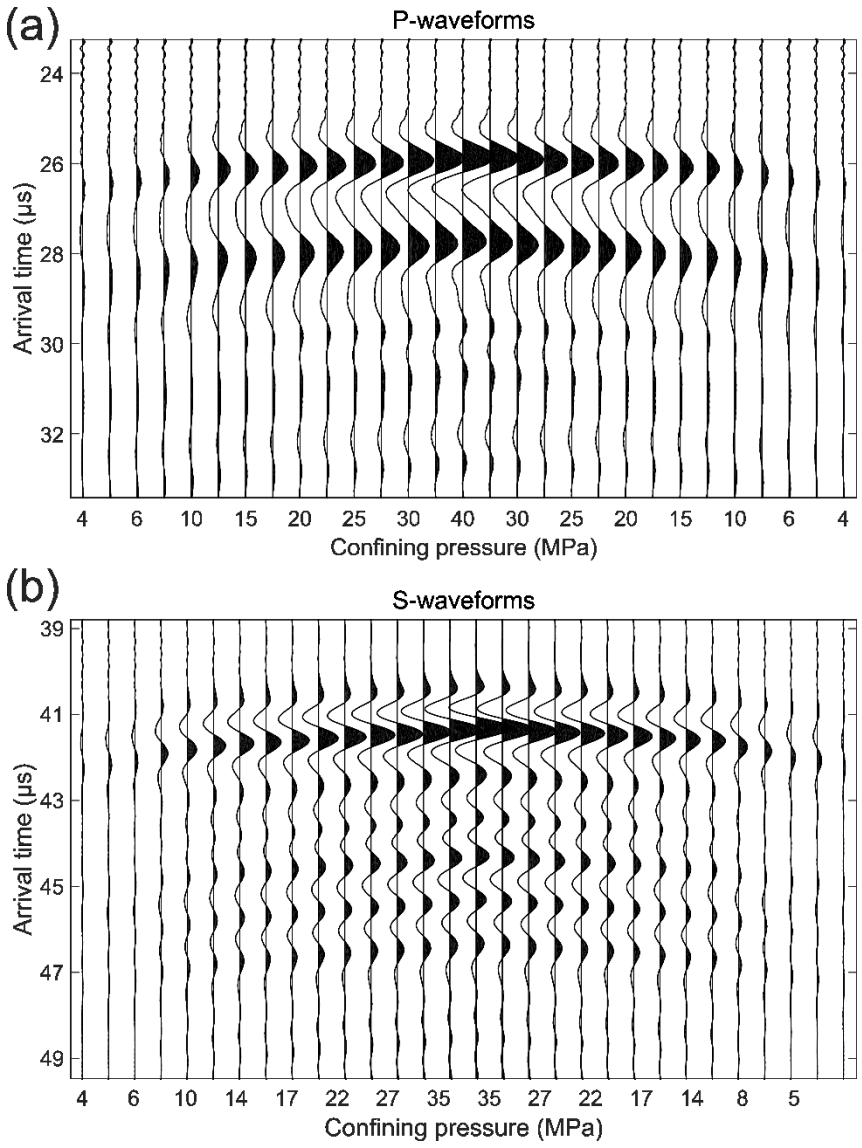

Figure 3.11. a) P- and b) S-waveforms as a function of confining pressure at room temperature (21.3ºC). Both the up and down cycle of pressure changes are shown in horizontal axis from left to right. The first breaks are actually the first extremum of the waveforms. This is particularly chosen for its clear appearance and consistency which provides us the phase velocity of the sample.

3.5.1 Velocity calculation and error analysis

The velocity measurements for a core sample are made by recording the total travel time of the P- and S-waves through both aluminum end-caps and the sample. The end-cap travel times are also recorded during separate calibration runs completed at the same confining pressures and temperatures; this value is subtracted from the total travel time recorded during a sample run to obtain the sample travel time to divide its known length to get velocity. The time of the first extremum amplitude of the waveform declares the transit time in both calibration and sample measurements (Molyneux and Schmitt, 2000).

The length of the sample measured at ambient condition is expected to vary with pressure and temperature. The path length difference (L) with pressure (p) and temperature (T) was obtained using the following equation in order to achieve satisfactory ultrasonic data (Lin and Trusler, 2012),

$$L(T,p) = L_0(T_0,p_0)\left\{1 + \alpha(T - T_0) - \frac{1}{3}\beta(p - p_0)\right\} \quad (3)$$

Here, α is the linear thermal expansion coefficient of carbonate (Yang et al. 2014) and β is the coefficient of bulk compressibility, i.e., the inverse of the samples measured dry bulk modulus. Another source of error in sample length is the error associated in flattening its faces for parallelism 20 μm (Njiekak et al. 2013). The 10 ns digitization sampling period contributes 10 ns to 30 ns uncertainty in picking of the transit times, these variations in this uncertainty mostly depend on the quality of the received signal which improves with P_c due to better coupling of the sample to the aluminum end-caps. Propagation of these errors suggests that the wave speeds are measured to better than 0.4%.

Bulk (K) and shear (G) moduli are then calculated from the measured compressional (V_p) and shear (V_p) velocities using the standard relations:

$$K = \rho {V_p}^2 - \frac{4}{3}\mu \tag{4}$$

and

$$G = \rho {V_s}^2 \tag{5}$$

where the density is calculated using equation (1) accounting for temperature and pressure.

3.5.2 Quality factor determination

The progressive loss of energy, or attenuation, of a seismic wave as it propagates into a material also contains a great deal of information about the state of fluids within a medium. This is especially true for bitumen filled rocks for which we expect the viscoelasticity of the bitumen will result in attenuation.

The spectral ratio method is used here for measuring the apparent quality factor Q of the P-wave over the entire temperature and pressure range (Molyneux and Schmitt, 2000; Subramaniyan et al., 2014). In this method, the amplitude spectra of the reference signal transmitted through the aluminum end caps *R(f)* and of the test signal passed through the rock sample *S(f)* were obtained with Fast Fourier transform (FFT) from their corresponding windowed time series. In the amplitude spectra the majority of the energy is spread between 0.7 MHz to 1.1 MHz.

The technique based on the assumption that, the ratio of two amplitude spectra is,

$$\frac{S(f)}{R(f)} = e^{-\frac{\pi \Delta t}{m} f} C \tag{6}$$

where Δt is the travel time difference between the test and reference signal, f is the frequency, m is the slope and C is the single constant value.

The natural logarithm of the ratio of the test and reference spectra yields,

$$\ln\left|\frac{S(f)}{R(f)}\right| = -\frac{\pi\Delta t}{m}f + C \tag{7}$$

The left hand side of the equation (7) is then plotted as a function of frequency, f in the dominant range of 0.7 to 1.1 MHz. The quality factor, Q is measured from the plot based on the slope of the best fit line,

$$Q = -\frac{\pi\Delta t}{m} \tag{8}$$

3.6 Results

The purpose of these measurements is to obtain information about the seismic properties of natural bitumen saturated samples under the varying pressure and temperature conditions expected during steam-assisted gravity drainage (SAGD) operation. As such one must consider the influence of temperature, confining pressure and pore fluid pressure as the elastic properties of both the fluid and rock frame depend on these variables (i.e., for the measurements to provide useful results all three must be known and controlled).

Further, one must be able to isolate the effects of each variable independently. To accomplish this, P- and S-waveforms were obtained during suites of measurements in which P_c, P_P, and T were varied first under the original bitumen saturation followed after cleaning by dry and water saturation as summarized in Table 3.2. The results are discussed as organized around Figures 3.12-3.14.

Table 3.2. Conditions of measurement suites

Suite	Saturation	Temperature °C	Pressures (MPa)			Assessment	Figures
			Confining P_c	Pore P_P	Effective P_d		
1a	Original	10	4 to 40	0	$= P_c$	Effect of T and P_c	Figure 3.12
1b		21.3					
2a		21.3	16 to 40	1 to 25	15	Effect of T and P_P	Figure 3.13
2b		70.0					
3a		10 to 70	15	0.5	14.5	Effect of T	Figure 3.14
3b		22 to 102	7.0	2.0	5.0		
4	Air	21.3	4 to 40	0	$= P_c$	Dry Frame	Figure 3.12
5	Water	23.5	16 to 40	1 to 25	15	Effect of saturant	Figure 3.13

3.6.1 Effect of confining pressure

The variations in onset time delay as a function of confining pressure can be observed in both the P-and S-waveforms (Figure 3.11). These waveforms display the influence of confining pressure on the wave speeds in such rocks with progressive closure of small aspect ratio porosity. These closures help more efficient transmission of acoustic stress and velocities along the sample to increase both the shear and bulk modulus.

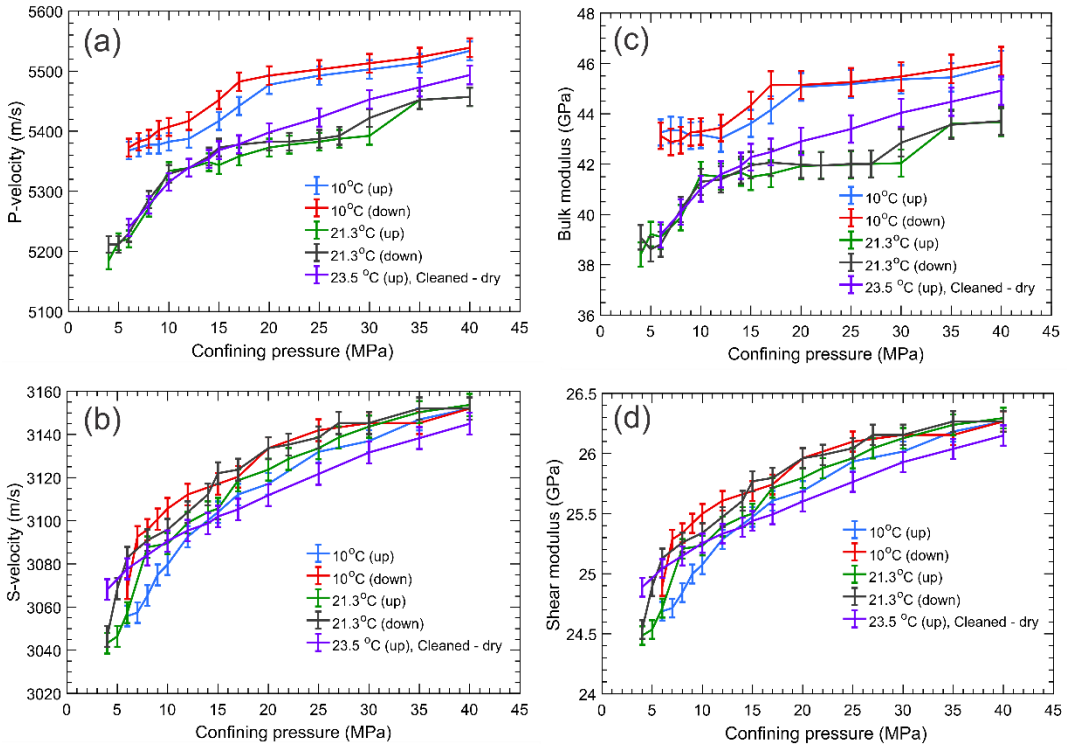

Figure 3.12. Effects of varying confining pressure under full drainage (Pp = atmospheric) in both bitumen saturated and dry on a) P-wave speeds, b) S-wave speeds, c) Bulk modulus, and d) Shear modulus for measurement suites #1 (bitumen saturated) and #4 (dry). 'Up' and 'down' in the legend represent the increase and decrease of pressure, respectively.

The purpose of suites #1 and #4 is to assess the P_c dependence of the material and to a lesser degree the effects of T (Figure 3.12). Both V_P and V_S (Figures 3.12a and 3.12b) increase nonlinearly with P_c regardless of the case. This behaviour is normal for most rocks resulting from the progressive closure of small aperture pores as just mentioned. The changes are relatively modest, being only about 4.8 % and 2.4% for the dry sample over the covered range of P_c. The effect of temperature on V_P is more noticeable on the saturated sample with a 2.7 % decrease with the small temperature rise of 11.3°C. The dry compressional wave speeds are close to those obtained at 21.3°C. In contrast, there seems to be little variation in the V_S between the different dry and saturated situations (Figure 3.12b).

3.6.2 Effect of pore pressure

The moduli for suites #2 and #5 (Figure 3.13) and wave speeds (Appendix 3.B) are all carried out at the same effective confining pressure P_d, assess the effects of the pore pressure P_P and temperature T dependent fluid properties on the wave speeds.

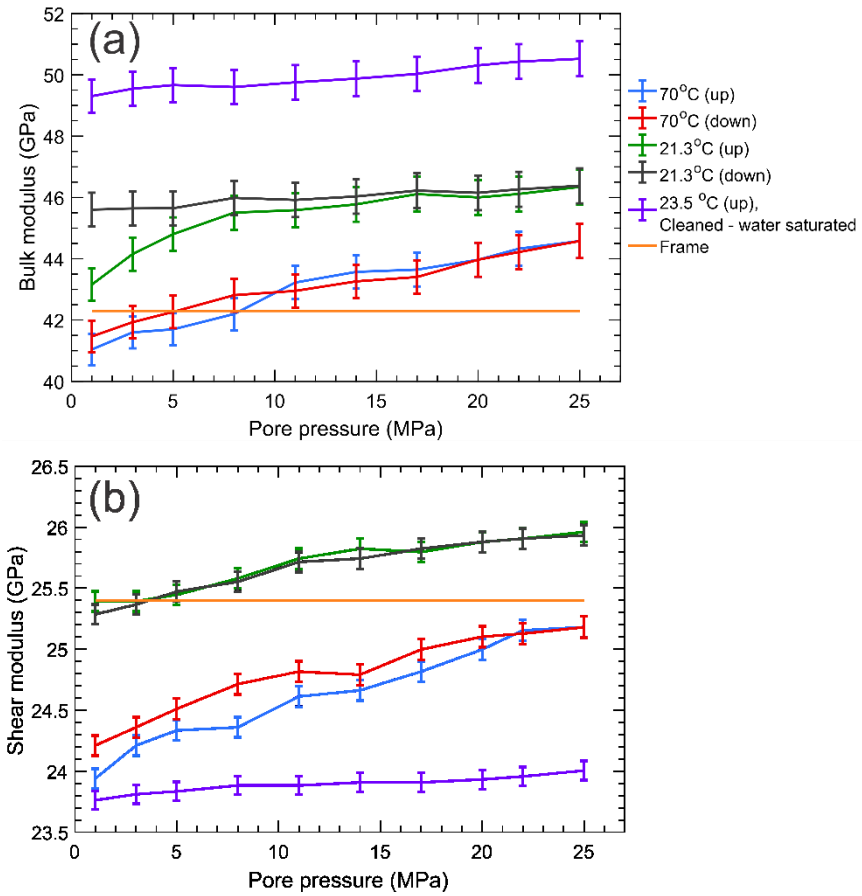

Figure 3.13. Effects of varying pore pressure at a constant effective pressure Pd = 15 MPa a) Bulk modulus, and b) Shear modulus for measurement suites #2 (bitumen saturated) and #5 (water saturated). Horizontal lines in a) and b) indicate the dry frame moduli as determined from Figures 12c and 12d at the same effective pressure.

For purposes of comparison, it is worth noting that at P_d = 15 MPa K_d = 42.3 GPa and G_d = 25.4 GPa (Figures 3.13a and 3.13b). It is first useful to consider the water saturated tests as the properties of water are well known, and for this situation K_{sat} and G_{sat} remain nearly constant over the range of P_P tested. This is expected, at least

qualitatively, by examination of the Gassmann relations Eqns. 13 and 14 above where the only variable K_f and subsequently K_{sat} will increase only weakly. Bakhorji (2010) made similar observations in water saturated carbonates.

3.6.3 Effect of temperature

The final set of comparisons shows the temperature dependence at two different effective pressures of P_d of 5 MPa and 14.5 MPa (Figure 3.14) from suite #3. Both V_P and V_S decline rapidly with temperature and this equates to large declines in the corresponding K_{sat} and G_{sat}. The two V_S and G_{sat} *remain* largely unaffected by the different P_d in agreement with the small changes seen in Figure 3.12b. In contrast the two V_P diverge from one another as the temperature rises.

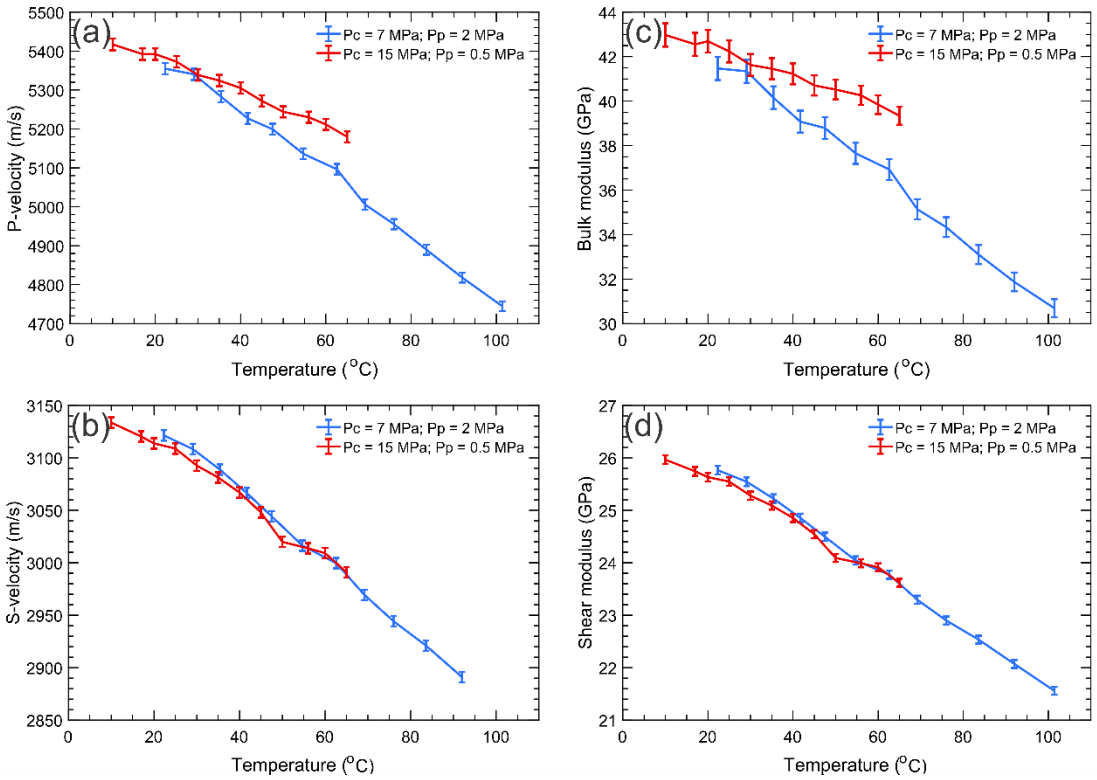

Figure 3.14. Effects of temperature change at constant effective pressures of 5 MPa (blue) and 14.5 MPa (red) on a) P-wave speeds, b) S-wave speeds, c) Bulk modulus, and d) Shear modulus from measurement suite #3.

The large declines are unexpected particularly given that the frame modulus K_d is quite stiff having values of 37.5 GPa and 39.5 GPa at the P_d of 2 MPa and 7 MPa, respectively.

3.6.4 Influence on Q-factor

Q factor or attenuation is calculated for the frequency range 0.7MHz to 1.1MHz (maximum amplitude), so we would expect a higher Q value at these frequencies, as shown in Figure 3.15.

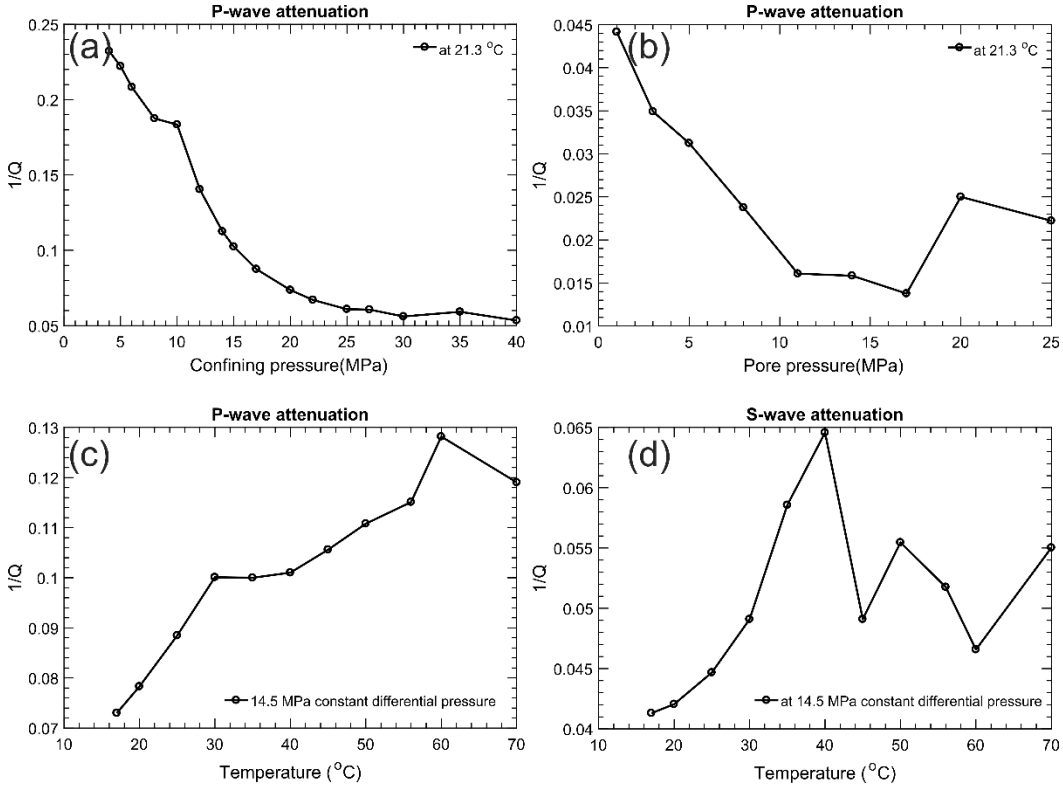

Figure 3.15. Ultrasonic wave attenuation for the P-wave under condtions of a) increasing effective pressure at 21.3 °C (suite #1), b) increasing pore pressure under constant effective pressure Pd of 15 MPa at 21.3 °C (suite #2), c) increasing temperature at constant effective pressure of 14.5 MPa (suite #3), and d) for the S-wave under the same conditions as (c).

However, the signal's quality is not always good enough to yield a better estimate of the Q-factor using the spectral ratio method and it is not uncommon for the uncertainty of such measurements to approach 100% in highly attenuating materials (e.g., Molyneux and Schmitt, 2000), formal uncertainties are not included in Figure 3.15 but the reader should keep this in mind. Some trends are apparent with both the P- and S-wave attenuations declining with effective confining pressure (Figures 3.15a and 3.15b) as the frame stiffens. In contrast, attenuation increases only weakly with temperature to 70°C (Figures 3.15c and 3.15d) and given the issues with uncertainty as noted it is not clear that these variations are significant.

3.7 Discussion

Density is one controlling factor on the observed wave speeds and this can be removed when the corresponding saturated (K_{sat} and G_{sat}) and dry (K_d and G_d) moduli are calculated (equations 9 and 10) and these follow largely the same pattern (Figure 3.12c-d). Significantly, K_{sat} decreases with temperature; as the sample has remained otherwise unchanged this variation must result from the decrease in K_f with T (Figure 8a) although the rapid decay in the bitumen shear modulus G_f (Figure 3.8b) may also contribute. At room temperature $K_{sat} \approx K_d$, this situation is unexpected as according to the well-known Gassmann relations the saturated sample should always be more incompressible according to

$$K_{sat} = K_d + \frac{\alpha^2}{\frac{\phi}{K_f} - \frac{\alpha - \phi}{K_s}} \tag{9}$$

where $a = (1 - K_d/K_s)$. The values of the G_f and G_d vary little over the range of P_c are nearly the same for all three cases in Figure 3.12d. This situation is as might be expected under Gassmann's relations for the shear modulus

$$G_{sat} = G_d \tag{10}$$

These relations are given here more to provide a point of reference against which the experimental observations may be compared. We will see substantial deviations of the experiments from these that go beyond the usual deviations seen in experiments that use less viscous saturants that are usually rationalized by the influence of microcracks (e.g., Bakhorji and Schmitt (2010)).

The behaviour under original saturation is somewhat different in Figure 13a. First, the K_{sat} for both temperatures is significantly less that for the water saturated case. This might be expected when T = 70°C where the bitumen K_f is much less than that for water but not when T= 23.5°C where the situation is reversed. One possible explanation for this discrepancy is that the original sample saturation includes some gas phase that results in an overall reduction in its effective K_f. The G_{sat} display the opposite trend with those observed for the bitumen saturation both exceeding and displaying greater pressure sensitivity that for water saturation (Figure 3.13b). There is also a strong temperature dependence with the overall value of G_{sat} decreasing with increasing T but showing increased control of P_P.

The observation, Figure 14, that the observed K_{sat} fall below K_d is particularly difficult to explain in light of the usual trends that would be suggested by Gassmann's equation 9 above that states that $K_{sat} \geq K_d$. This could be reconciled if the dry frame's moduli were also temperature dependent. We did not test the temperature dependence on the sample described here, but we note further measurements on similar samples we did not see any significant temperature dependence of the frame properties (Rabbani et al., 2016). Such large declines are also observed in oil sands as mentioned earlier but in those cases determining proper frame moduli is difficult or impossible.

3.7.1 Application of standard models

There have been many attempts to model the seismic and ultrasonic responses of oil sands. One lingering issue with this material is that it is difficult or impossible to obtain defensible measures of the dry frame moduli particularly if the material is heated. This is likely due to the fact that components of the bitumen contribute to cementing the mineral grains, and the material disaggregates to loose sand upon removal of the bitumen. The dolomite sample here, in contrast, retains its shape and the dry frame moduli are readily obtained. This consequently affords us a rare opportunity to test the validity of existing substitutional models when applied to a rock saturated with viscous bitumen. These tests are further motivated by the need to explain the unexpected observation above that $K_{sat} < K_d$ at higher temperatures. Such comparisons are important to practitioners who might hope to predict moduli and consequent seismic responses in real time lapse efforts.

We carried out calculations using a variety of classic bounds, inclusion, and poroelastic models and compared them to the observed temperature dependent moduli (Figures 3.14c and 3.14d). The calculations employed the petrophysical values of Table 1, the variable bitumen properties shown in Figures 3.7 and 3.8, and the frame moduli at the appropriate effective pressure extracted from Figure 12. Governing equations related to the models have been discussed in Appendix 3.C.

As there is uncertainty in the *as received* saturations the moduli are calculated assuming either a full liquid bitumen (S_b = 0.75) and water (S_w = 0.25) mixture, or by including a small methane gas saturation S_g. The bulk modulus of the fluid mixture was assumed to be adequately estimated using Wood's (1955) formula

$$K_f = \left(\frac{S_w}{K_w} + \frac{S_b}{K_b} + \frac{S_g}{K_g} \right)^{-1} \tag{11}$$

where the saturations sum to 1. In fact, in an early characterization of Grosmont reservoir by Jiang et al. (2009), NMR measurement indicates that the natural core from the formation contain about 14% initial gas saturation. The results from a cold solvent soak test done by our industry collaborator also show as much as 18% gas saturation in the natural sample. The presence of gas in the bitumen-saturated sample may be partially responsible for the lower response of P-wave velocity and bulk modulus than those of water saturation as seen earlier, but cannot entirely explain the observed responses.

The results of these calculations are compared to the observations in Figure 3.16 where the observed moduli for measurement suite #3b (Table 3.2) are shown by a thick dark line. The different bounds show large deviations and while it is comforting that the observations fall within these bounds they have little practical predictive value. It is worth pointing out in Figure 16a that K_d is only slightly less than the expected K_{sat} expected with some gas saturation (*G-Mixed*) and that the difference between the predicted G_{sat} and G_d in Figure 3.16b cannot be resolved as the fluid viscosity drops or if gas is included along the bottom of the zone labeled (*G-B Models – Mixed*).

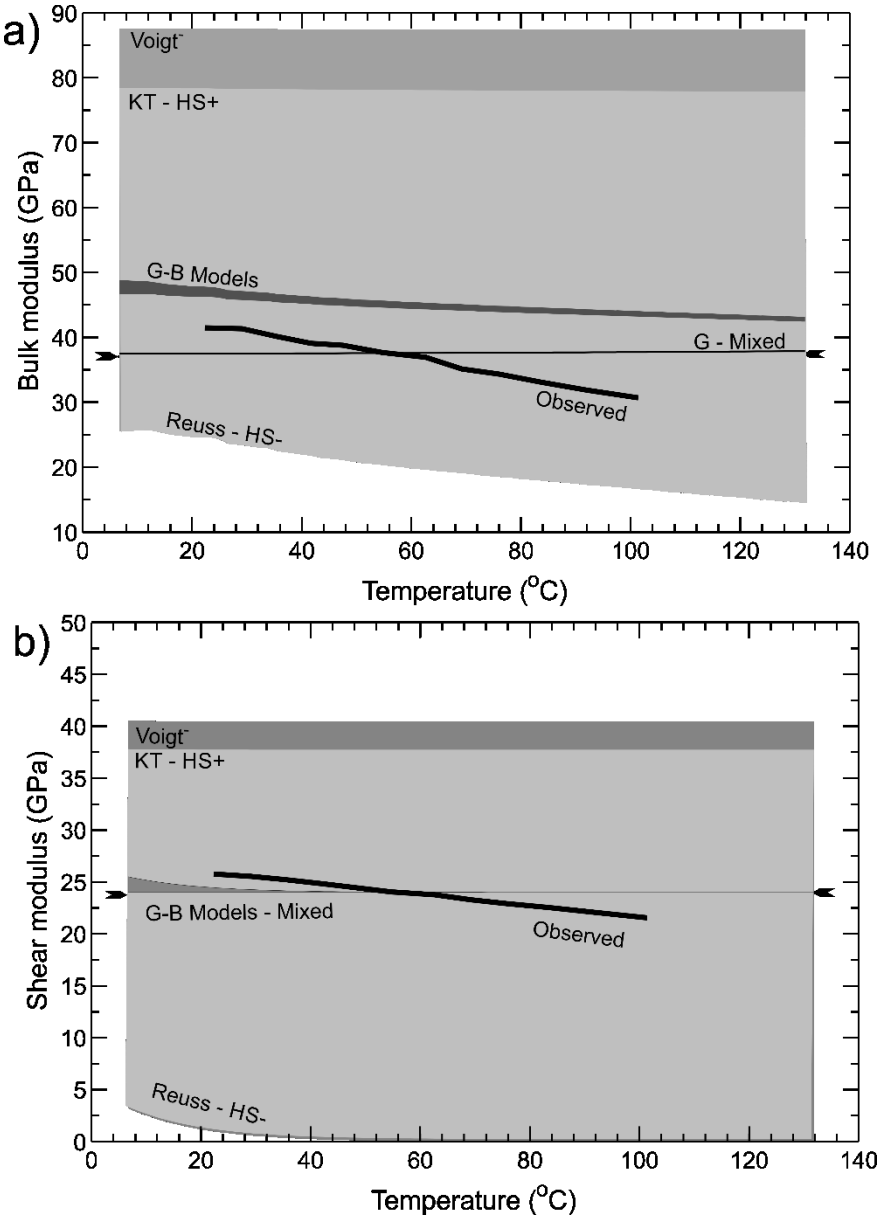

Figure 3.16. Comparison of calculated and observed (thick dark line) a) saturated bulk moduli and b) saturated shear moduli as a function of temperature. Inward pointing arrows indicate the corresponding dry moduli used in the calculations. Two ranges of bounds are the elementary Reuss-HS- to Voigt and the Hashin-Shtrickman (Reuss-HS- to KT-HS+) area shaded in dark and light gray. The range of Gassman-Biot models used fall within the darker gray bands for liquid (G-B Models) for liquid or (G-Mixed) if gas in included.

As described earlier, the sample is saturated with highly viscous fluid and the connecting pore throats are small as determined from Hg-injection permeametry. This

might suggest that the pores are essentially isolated from each other and act as independent inclusions. This is the situation that the Kuster-Toksoz model attempts to describe, but it too fails with predictions exceeding the observations by nearly 100%.

The family of Gassmann-Biot (G-B) models come closer to the observed but it is important to point out here some key differences from more normal observations. First, and as already noted, at temperatures above 50°C both observed moduli fall below those for the frame, this is particularly unexpected for K_{sat}. Second, the observed K_{sat} lie at only 11% to 28% of the G-B predictions.

Except for special cases of highly porous materials devoid of microcracks, disagreement between such models and ultrasonic observations is expected (Gist, 1994; Bakhorji, 2010) and is attributed to the influence of microcrack porosity (Diallo et al., 2003). The values seen under water saturation on the cleaned sample above, too, appear to agree with this expectation. However, the one key difference between these other examples and the current observations is that in the latter the observed ultrasonic values exceed those predicted using G-B models. Here, the situation is reversed with the observed values of bulk moduli always less than those estimated using G-B models even when the influence of the saturating fluid is minimized by including some gas saturation. The G-B models do seem able to capture some, but not all, of the decline of K_{sat} with temperature. The G-B values for the shear moduli are closer and actually cross, but they too do not adequately follow the dramatic declines in the observed shear moduli with temperature.

We currently do not understand the reasons for these discrepancies. One possibility is that they may be in part due to the actual effective pressure on the sample being lower than the stated value because of the aforementioned pore pressure diffusion time-scales. However, this explanation becomes less tenable at the higher temperatures where the time to reach equilibrium is only a few seconds. Biot's characteristic frequency,

$f_B = \frac{\eta\varphi}{2\pi\rho_f k}$ for the bitumen saturated sample depends heavily on the fluid properties and has a range from $5x10^{12}$ Hz to $2x10^{9}$ Hz over a temperature change from room temperature (23°C) to 100°C. Moreover, following Clearly (1978), the critical frequency for the drained or undrained transition, $f_c = \frac{4kK_d}{\eta L^2}$ is notably low at room temperature with the value of 0.4 mHz. Although the frequency (f_c) increases to 0.9 Hz at 100°C, it's still significantly lower than the ultrasonic wave. Therefore, it is very likely that the regime is neither the drained one nor the undrained one, but the unrelaxed regime and poroelasticity may not be applicable at ultrasonic frequency (Pimienta et al., 2015, 2016; Sarout, 2012).

Another could be that the frame properties are chemically influenced by the saturating fluids and, upon cleaning, the frame stiffened considerably from its natural saturations state. This situation is probably not likely as one might expect the frame to become more compressible and less rigid upon removal of some of the stiff bitumen components. On another note, thermal expansion coefficient ($6x10^{-4}$/K) for bitumen is higher than the host rock dolomite ($8x10^{-6}$/K) (Souraki et al., 2012; Yang et al., 2014). An increase of temperature of 50°C would lead to a volumetric expansion of $3x10^{-2}$ for the bitumen in the pore. Therefore, there is a possibility that microcracks induced by thermal expansion of the bitumen might appear in the bitumen saturated sample at higher temperature if excess pore pressures cannot drain sufficiently quickly. It is important to note in this context, however, that the manual pump for controlling pore pressure had to pull back with the increase of temperature in order to maintain the constant effective pressure. Essentially, the sample produced bitumen during heating. As such, we do not believe that new microcracks were introduced to the sample during the tests.

There could be other reasons for the discrepancies in saturated and dry measurements; for example, strong heterogeneity of the sample. Or, a slight difference in positions where the transducers are attached may influence the travel times of the propagated pulse. And, there may be experimental problems that are unknown and not adequately addressed. For example, the attenuations observed (Figures 3.15c and 3.15d) are quite high and this may influence the waveforms obtained.

Another possibility is the current theoretical G-B based models are not capturing all of the physical mechanisms operative as the ultrasonic waves pass through porous materials saturated with highly viscous fluid. It is certain, the Gassmann based models cannot describe frequency dependent behaviour. The Biot models used here do incorporate a simple rheology that includes a single value of the dynamic shear viscosity. The model has successfully predicted the speeds and attenuations of propagatory fast P, slow P, and S wave modes in highly porous and permeable porous media saturated with low viscosity fluids with largely Newtonian rheology (water, kerosene, CO_2). The rheologies of heavy hydrocarbons, in contrast, are much more complicated and still remain only poorly understood (Bazyleva et al., 2010; Mortazavi-Manesh and Shaw, 2016). An additional factor that may be important is the mostly ignored bulk, or volume, viscosity the contribution of which has only rarely been considered (e.g. Biot, 1962).

3.8 Implementation for time lapse seismic survey

Time lapse seismic is a method by which the dynamic reservoir can be monitored (Eastwood et al., 1994; Schmitt, 1999; Bianco et al., 2010). It measures dynamic changes in the reservoir due to stress changes, temperature variations, and fluid movement/replacement. However, the measured change in the PP or PS wave seismic is, based on the formulae for impedance, the overall change of all the above. In order to

better understand what exactly is changing within the reservoir due to (in the case of heavy oil thermal operations) steaming, a better understanding is required of which specific physical or elastic property changes within the rock are causing the observed differences in the time lapse data. It is the understanding of what specifically is changing that will allow for a more complete understanding of reservoir processes that will lead to more efficient and economical operational decisions. Time lapse (or 4-D) seismic monitoring can successfully assist in imaging the changes in bitumen saturated oil sand reservoirs during SAGD or CSS (Schmitt 1999; Kendall 2009; Zadeh et al. 2010).

The ultrasonic measurements of bitumen saturated core in this study show both the direct effects of pressure, and more importantly temperature on bitumen. The measured P- and S-wave velocities of saturated rock sample can be further implemented to demonstrate time lapse seismology for a simple layered 1-D world, where a pulse through a dolomite layer is reflected back from the underlying bitumen saturated layer (Figure 3.17).

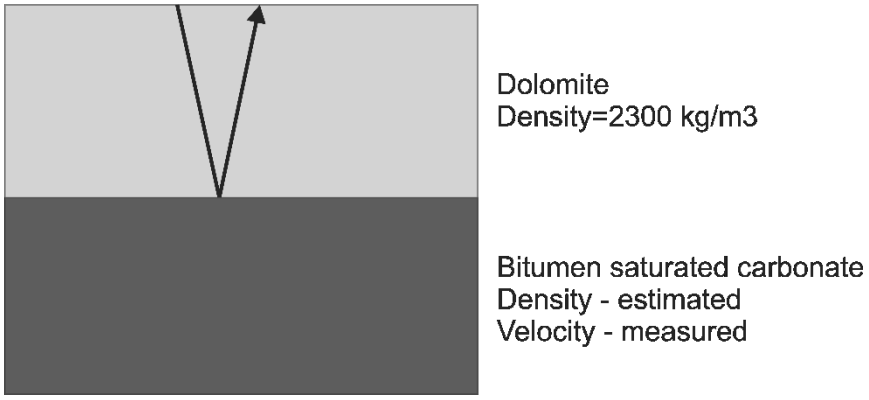

Figure 3.17. Illustration of a wave reflected from interface of a dolomite and bitumen saturated carbonate layer.

Finally, the simple normal incidence reflection coefficent (R) from the interface between the dolomite (d) and bitumen saturated (sat) carbonate is calculated from the corresponding impedances (Z's),

$$R = \frac{Z_{sat} - Z_d}{Z_{sat} + Z_d} \tag{12}$$

where, impedance (Z) = density ($\boldsymbol{\rho}$) * velocity (v).

We have seen in Figures 12 to 14 that confining and pore pressure, and temperature all affect the bitumen's velocities, therefore we attempt to carry out the reflection coefficient analysis for all three cases. Afterwards, in a simple convolutional model shown in Figure 3.18, a Ricker wavelet with 100 Hz central frequency is convolved with the reflection coefficients show the changes in root-mean-square, RMS value of the amplitude, where the amplitude peak is centered at zero time. RMS values essentially eliminate the negative amplitude.

Figure 3.18 shows amplitude stays somewhat same along with the increase of confining and pore pressure as corresponding velocities in Figures 3.12-3.14 do not significantly change to have great influence on reflection coefficients. There is, however, a noticeable decrease in amplitude with the increase of temperature. Both P- and S-wave reflection coefficients strongly depend on the temperature, as it decreases with increase of temperature, although not shown here. This decrease in amplitude also coincides with the fact in Figure 3.15c, that bitumen saturated samples have less attenuation of ultrasonic wave at low temperature. Attenuation increases with temperature and the corresponding amplitude decreases in the convolution model in Figure 3.18. This result demonstrates that studying the physical properties of bitumen at various conditions, particularly with the change in temperature is necessary in order to properly interpret observed 4-D seismic responses.

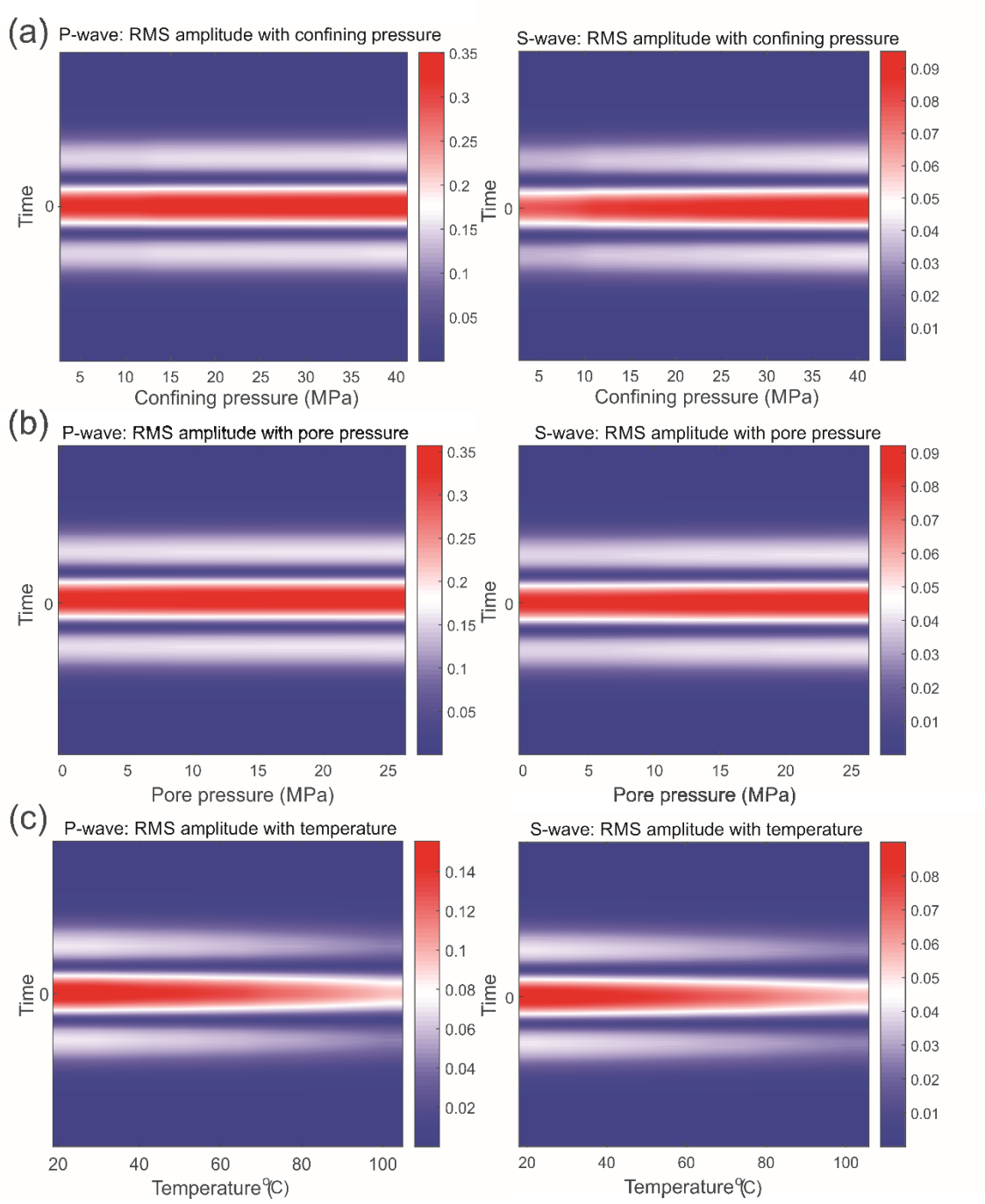

Figure 3.18. 1-D convolutional model with amplitude as background color. P-wave variations are in the left column and S-wave are on the right. (a) At varying confining pressure with atmospheric pore pressure at 21.3°C temperature, (b) Pore pressure change at 15 MPa constant differential pressure at 21.3°C and (c) Effects of change of temperature at 5 MPa differential pressure.

3.9 Conclusions

The P- and S- waves speeds were measured in a low porosity, bitumen-saturated carbonate rock sample cored from a bitumen saturated dolomite rock. Our existing laboratory high pressure system was modified to allow a greater range of temperature for both chilling and increased heating of the pressure vessel. Measurements were carried out under a variety of temperatures (10°C to 102°C) and under differing conditions of effective pressure in order to best isolate the effects of confining pressure, pore fluid pressure, and temperature. Despite the low porosity in this sample, substantial changes in the ultrasonic P- and S-wave speeds were observed particularly in relation to temperature variations. While no in-depth theoretical examinations of these changes have been carried out, it is likely that the strong temperature dependence of bitumen bulk modulus, density, and viscosity all contribute to these observations.

The observations of ultrasonic measurements in laboratory will help us to develop a time lapse model to monitor the reservoirs by relating seismic velocities to changes of bituminous formation with reservoir parameters (temperature, pressure and saturation). This study was done with one bitumen saturated sample which was later extracted through Soxhlet to study the effects of other fluid. In order to achieve a conclusive model, more studies are required with samples at different saturation levels and styles of porosity (i.e. fractures and vugs), at higher temperatures, and at different pore and confining pressures. Moreover, measurements with more 'cleaned' samples (after extracting the bitumen) would provide better characterization of fluid saturation.

Longer term work should include theoretical modeling of the observed responses using theories that will include the fluid properties more fully, but for this sample the standard range of Biot-Gassmann based models is incapable of describing the behaviour particularly with increasing temperature. Further, development of methodologies to

assess the dynamic moduli at seismic frequencies is necessary for both the saturated samples and the bitumen itself.

Appendix 3.A

Petrophysical characterization of the sample

Sample characterization with standard petrophysical tests includes:

i. Bulk dry density determined as the simple ratio of the mass to the sample volume using the cylinder's dimensions.

ii. Boyle's law Helium (He) pycnometry to determine the sample's grain density (Quantachrome™ Multipycnometer, Model MVP-D160-E) giving a value of 2785 kg/m^3 and porosity of 7%.

iii. Mercury (Hg) injection porosimetry employing injection capillary pressure curves for the estimation of the bulk density, porosity and pore size distribution (Micrometrics AutoPore IV 9510 with a peak pressure of 414 MPa). The reader may find descriptions of this method elsewhere (Wardlaw and McKellar, 1981; Giesche, 2006). Briefly, the premise of Hg injection porosimetry relies on Hg's nonwetting character with high wetting angle $\theta \approx 140°$ and surface tension $\lambda = 482.46\ mN/m$ (Iwata et al., 2016). Porous materials will not normally spontaneously imbibe Hg and increasing hydrostatic pressure is necessary to force it into the pore space. The Hg will not breach a pore throat aperture d until a pressure P through the Washburn equation

$$P = \frac{-4\lambda \cos\theta}{d} \tag{A1}$$

is exceeded. Consequently, measuring the amount of Hg imbibed by the material with pressure provides a distribution of the pore volume accessible through pore

throats of increasingly small diameters down to as small as 3.5 nm in principle. It provides the samples porosity of 8%.

iv. X-ray diffraction analysis to characterize the mineral compositions. The mineralogy of the sample was investigated by powder X-ray diffraction (XRD) analysis carried out using a Rigaku Geigerflex Power Diffractometer in the Department of Earth and Atmospheric Science at the University of Alberta. This analysis showed that the sample was primarily dolomite ($(CaMg)(CO3)_2$) but containing some quartz and a very minor amount of muscovite (probably illite clay).

v. The sample's formation factor F was determined from the ratio of the electrical conductivity σ_f of a saline brine to the conductivity σ_p of the rock sample saturated with the brine. Measurements were made at frequencies of 10, 100, and 1000 Hz in order to ensure there were no spurious electrode polarizations. Regrettably, measurements of dry and saturated masses together with knowledge of the porosity suggested an incomplete brine saturation of 85%; and consequently the $F = 77$ should be regarded as an upper bound.

Following Garrouch et al. (2001) the tortuosity (τ) may be estimated using the expression

$$\tau = \frac{\sigma_f}{\sigma_p}\varphi = F\varphi \tag{A2}$$

that here yields an upper bound $\tau = 6.2$. This information is not used here but is needed in following contributions that focus on efforts to predict the observed wave speeds and moduli.

vi. The permeability k was measured to be 3.0×10^{-15} m² (~3 mD) using a gas permeameter (Tiny Perm II made by New England Research Inc.), this was close

to the value of 5.0×10^{-15} m² (~5 mD) inferred from Hg injection porosimetry at confining pressure P_c = 68 MPa.

Appendix 3.B

Effects of pore pressure on the velocities

Figure 3.B-1 shows the effects of pore pressure on the P- and S-wave velocities of the bitumen- and water-saturated samples at constant effective pressure. The corresponding moduli are discussed in Figure 3.13.

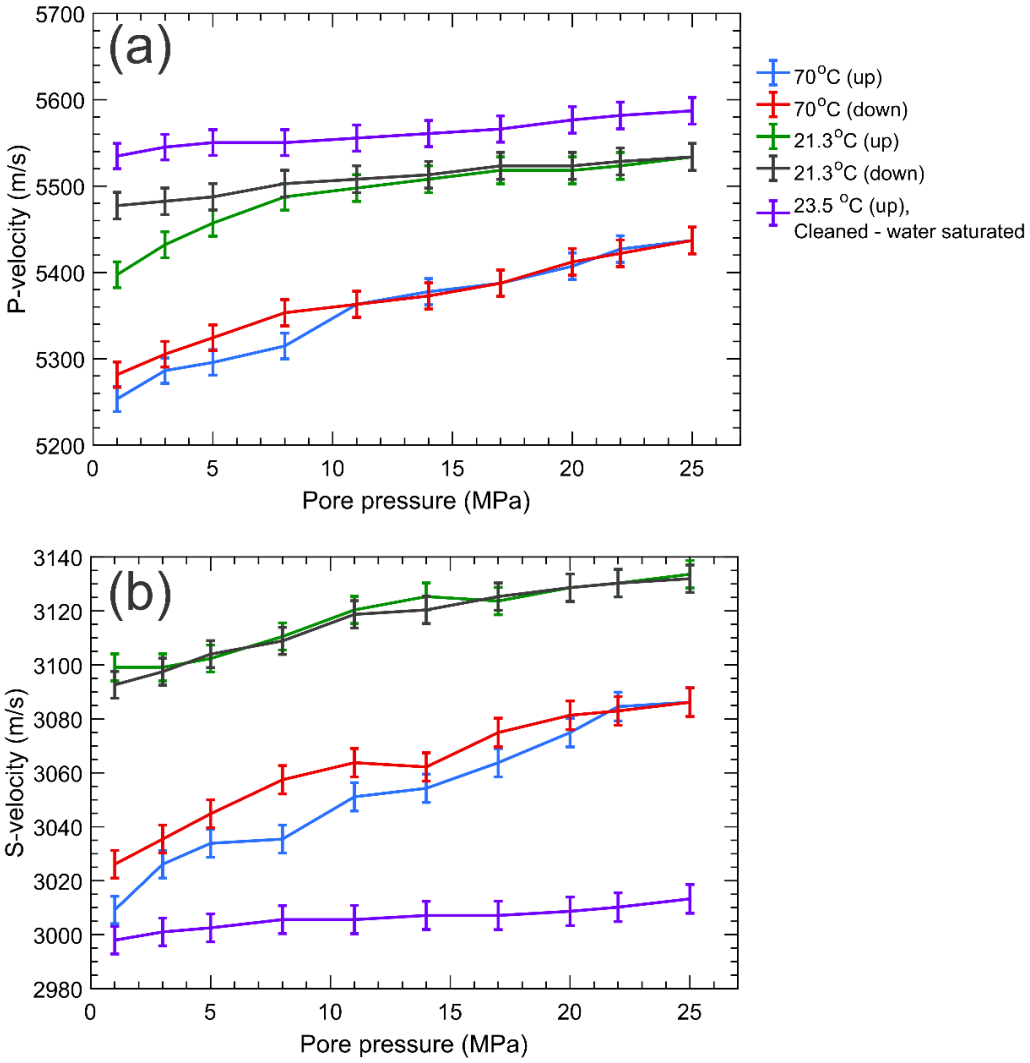

Figure 3.B1. Effects of varying pore pressure at a constant effective pressure of 15 MPa. a) P- and b) S- wave velocities.

Appendix 3.C

Governing equations related to the models

Fluid substitution models include:

i) the elementary Voigt-Reuss bounds where M can represent either the bulk K or the shear μ moduli:

$$M_V = (1-\phi)M_s + \phi M_f \geq M \geq \left[\frac{(1-\phi)}{M_s} + \frac{\phi}{M_f}\right]^{-1} = M_R \tag{C1}$$

ii) the Hashin and Shtrikman (1963) bounds for the bulk

$$K_{HS}^{+} = K_s + \frac{\phi}{(K_f - K_s)^{-1} + (1-\phi)\left(K_s + \frac{4}{3}G_s\right)^{-1}} \geq K \geq K_f + \frac{(1-\phi)}{(K_s - K_f)^{-1} + \phi\left(K_f + \frac{4}{3}G_f\right)} = K_{HS}^{-} \tag{C2}$$

and shear moduli:

$$G_{HS}^{+} = G_s + \frac{\phi}{(G_f - G_s)^{-1} + \frac{2(1-\phi)(K_s + 2G_s)}{5G_s\left(K_s + \frac{4}{3}G_s\right)}} \geq G \geq G_f + \frac{(1-\phi)}{(G_s - G_f)^{-1} + \frac{2\phi(K_f + 2G_f)}{5G_f\left(K_f + \frac{4}{3}G_f\right)}} = G_{HS}^{-} \tag{C3}$$

where it is important to note that when one of the materials is a liquid $K_{HS}^{-} \to K_R$ and $G_{HS}^{-} \to G_R$.

iii) the Kuster-Toksoz inclusion model assuming spherical pores with

$$(K_{KT} - K_s)\frac{(K_s + 4G_s/3)}{(K_{KT} + 4G_s/3)} = \phi\,(K_f - K_s)\frac{(K_s + 4G_s/3)}{(K_f + 4G_s/3)} \tag{C4}$$

and

$$(G^{KT} - G_s)\frac{(G_s + \zeta_s)}{(G^{KT} + \zeta_s)} = \phi\,(G_f - G_s)\frac{(G_s + \zeta_s)}{(G_f + \zeta_s)} \tag{C5}$$

where

$$\zeta_s = \frac{G_s\left(9K_s + 8G_s\right)}{6\left(K_s + 2G_s\right)}$$

Again, it is important to note here that $K_{HS}^{+} \to K_{KT}$ and $G_{HS}^{+} \to G_{KT}$.

iv) a variety of Gassmann-Biot based models including the zero-frequency Gassmann relations as already mentioned earlier (equations 9 and 10), the frequency dependent Biot (1956) model following the implementation of Mavko et al. (2009) and not repeated here for brevity, and the recent adaptations of Saxena et al (2016) in which the saturated bulk modulus (K_{sat}) of the bitumen saturated sample is calculated as,

$$K_{sat} = K_{bc} + \frac{\left(1 - \frac{K_{bc}}{K_s}\right)^2}{\frac{\varphi}{K_f} + \frac{1-\varphi}{K_s} - \frac{K_{bc}}{(K_s)^2}} \tag{C6}$$

where,

$$K_{bc} = \frac{(1-\varphi)\left(\frac{1}{K_s} - \frac{1}{K_d}\right) + \frac{3\varphi}{4}\left(\frac{1}{K_s} - \frac{1}{G_f}\right)}{\frac{1}{K_s}\left(\frac{1}{K_s} - \frac{1}{K_d}\right) + \frac{3\varphi}{4}\left(\frac{1}{G_s K_s} - \frac{1}{G_f K_d}\right)}$$

and saturated shear modulus (G_{sat}) is calculated as,

$$G_{sat} = G_{bc} + \frac{\left(1 - \frac{G_{bc}}{G_s}\right)^2}{\frac{\varphi}{G_f} + \frac{1-\varphi}{G_s} - \frac{G_{bc}}{(G_s)^2}} \tag{C7}$$

where,

$$G_{bc} = \frac{(1-\varphi)\left(\frac{1}{G_s} - \frac{1}{G_d}\right) + \varphi\left(\frac{1}{\zeta_s} - \frac{1}{\zeta_f}\right)}{\frac{1}{G_s}\left(\frac{1}{G_s} - \frac{1}{G_d}\right) + \varphi\left(\frac{1}{\zeta_s G_s} - \frac{1}{\zeta_f G_d}\right)}$$

with $$\zeta_f = \frac{G_f\left(9K_f + 8G_f\right)}{6\left(K_f + 2G_f\right)}$$

References

Adam, L., M. Batzle, and I. Brevik, 2006, Gassmann's fluid substitution and shear modulus variability in carbonates at laboratory seismic and ultrasonic frequencies: GEOPHYSICS, **71**, no. 6, F173-F183. doi: 10.1190/1.2358494.

Agar, J.G., N.R. Morgenstern, and J.D. Scott, Thermal expansion and pore pressure generation in oil sands, Can. Geotech. J., 23, 327-333, 1986.

Agosta, F., M. Prasad, and A. Aydin, 2007, Physical properties of carbonate fault rocks, fucino basin (Central Italy): implications for fault seal in platform carbonates: Geofluids, **7**, no. 1, 19-32.

Anselmetti, F. S., and G. P. Eberli, 1993, Controls on sonic velocity in carbonates: Pure and Applied Geophysics, **141**, no. 2-4, 287-323. doi: 10.1007/bf00998333.

Ardakani, E. P., D. R. Schmitt, and T. Bown, 2014, Detailed topography of the Devonian Grosmont Formation surface from legacy high-resolution seismic profiles, northeast Alberta: GEOPHYSICS, **79**, no. 4, B135-B149. doi: doi: 10.1190/geo2013-0268.1.

Baechle, G. T., G. P. Eberli, R. J. Weger, and J. L. Massaferro, 2009, Changes in dynamic shear moduli of carbonate rocks with fluid substitution: GEOPHYSICS, **74**, no. 3,E135-E147. doi: 10.1190/1.3111063.

Bakhorji A.M., 2010, Laboratory measurements of static and dynamic elastic properties in carbonate: PhD thesis. University of Alberta, Edmonton, Alberta, Canada.

Bass, J. D. 1995, Elasticity of minerals, glasses, and melts, in T.J. Ahrens, ed., Mineral Physics and Crystallography: A Handbook of Physical Constants: American Geophysical Union. 45-63.

Batzle, M. L., D. H. Han, and R. Hofmann, 2006, Fluid mobility and frequency-dependent seismic velocity - Direct measurements: GEOPHYSICS, **71**, no. 1, N1-N9. doi: 10.1190/1.2159053.

Batzle, M. L., and Z. Wang, 1992, Seismic properties of pore fluids: GEOPHYSICS, **57**, 1396-1408. doi: 10.1190/1.1443207.

Bazyleva, A. B., M. D. A. Hasan, M. Fulem, M. Becerra, and J. M. Shaw, 2010, Bitumen and Heavy Oil Rheological Properties: Reconciliation with Viscosity Measurements: Journal of Chemical & Engineering Data, **55**, no. 3, 1389-1397. doi: 10.1021/je900562u.

Behura, J., M. Batzle, R. Hofmann, and J. Dorgan, 2007, Heavy oils: Their shear story: GEOPHYSICS, **72**, no. 5, E175-E183. doi: 10.1190/1.2756600.

Bianco, E., S. Kaplan, and D. Schmitt, 2008, Seismic rock physics of steam injection in bituminous oil reservoirs: The Leading Edge, **27**, no. 9,1132-1137. doi: 10.1190/1.2978975.

Bianco, E., S., Kaplan, and D.R. Schmitt, 2010, Seismic rock physics of steam injection in bituminous-oil reservoirs – Chapter 6, in Heavy Oils: Reservoir Characterization and Production Monitoring, eds. Batzle, M., Chopra, S., Lines, L.R., and Schmitt, D.R.: Soc. Expl. Geophysicists, Tulsa, OK, **105-110**.

Biot, M.A., 1956, Theory of propagation of elastic waves in a fluid saturated porous solid. I. Low frequency range and II. Higher-frequency range: J. Acoust. Soc. Am., **28**, 168–191.

Biot, M.A., 1962, Mechanics of deformation and acoustic propagation in porous media: J. Appl. Phys., **33**, 1482–1498

Butler, R. 1991, Thermal recovery of oil and bitumen: Prentice Hall.

Cleary, M. P., 1978, Elastic and dynamic response regimes of fluid-impregnated solids with diverse microstructures: International Journal of Solids and Structures, 14, 795–819, doi: 10.1016/0020-7683(78) 90072-0.

Ciz, R., and S. A. Shapiro, 2007, Generalization of Gassmann equations for porous media saturated with a solid material: GEOPHYSICS, **72**, no. 6, A75-A79. doi: 10.1190/1.2772400.

Cutler, W. 1982, Stratigraphy and sedimentology of the Upper Devonian Grosmont Formation, Alberta: M.S. thesis, University of Calgary.

Daridon, J. L., A. Lagrabette, and B. Lagourette, 1998, Speed of sound, density, and compressibilities of heavy synthetic cuts from ultrasonic measurements under pressure: Journal of Chemical Thermodynamics, **30**, no. 5,607-623. doi: DOI 10.1006/jcht.1997.0330.

Diallo, M. S., M. Prasad, and E. Appel, 2003, Comparison between experimental results and theoretical predictions for P-wave velocity and attenuation at ultrasonic frequency: Wave Motion, **37**, no. 1, 1-16. doi: http://dx.doi.org/10.1016/S0165-2125(02)00018-5.

Eastwood, J., 1993, Temperature-Dependent Propagation of P-Waves and S-Waves in Cold Lake Oil Sands - Comparison of Theory and Experiment: GEOPHYSICS, **58**, 863-872. doi: Doi 10.1190/1.1443470.

Eastwood, J., P. Lebel, A. Dilay, and S. Blakeslee, 1994, Seismic monitoring of steam-based recovery of bitumen: The Leading Edge, **13**, no. 4, 242-251. doi: 10.1190/1.1437015.

Fabricius, I. L., G. T. Bächle, and G. P. Eberli, 2010, Elastic moduli of dry and water-saturated carbonates — Effect of depositional texture, porosity, and permeability: GEOPHYSICS, **75**, no. 3, N65-N78. doi: 10.1190/1.3374690.

Garrouch, A. A., Ali, L., and Qasem, F., 2001, Using diffusion and electrical measurements to access tortuosity of porous media: Ind. Eng. Chem. Res, **40**, 4363-4369.

Giesche, H., 2006, Mercury Porosimetry: A General (Practical) Overview: Particle & Particle Systems Characterization, **23**, no. 1,9-19. doi: 10.1002/ppsc.200601009.

Gist, G. A., 1994, Fluid effects on velocity and attenuation in sandstones: The Journal of the Acoustical Society of America, **96**, no. 2, 1158-1173.

Greaves, R. J., and T. J. Fulp, 1987, 3-Dimensional seismic monitoring of an enhanced oil-recovery process: GEOPHYSICS, **52**, 1175-1187. doi: 10.1190/1.1442381.

Gurevich, B., K. Osypov, R. Ciz, and D. Makarynska, 2008, Modeling elastic wave velocities and attenuation in rocks saturated with heavy oil: GEOPHYSICS, **73**, no. 4, E115-E122. doi: 10.1190/1.2940341.

Harris, J. M., R. C. Nolen-Hoeksema, R. T. Langan, M. V. Schaack, S. K. Lazaratos, and I. James W. Rector, 1995, High-resolution crosswell imaging of a west Texas carbonate reservoir: Part 1—Project summary and interpretation: GEOPHYSICS, 60, 667-681. doi: 10.1190/1.1443806.

Han, D. H., J. Liu, and M. Baztle, 2008, Seismic properties of heavy oils—measured data: The Leading Edge, **27**, no. 9, 1108-1115. doi: 10.1190/1.2978972.

Hashin, Z., and S. Shtrikman, 1963, A variational approach to the theory of the elastic behaviour of multiphase materials: Journal of the Mechanics and Physics of Solids, **11**, no. 2, 127-140. doi: http://dx.doi.org/10.1016/0022-5096(63)90060-7.

Isaac, J. H., and D. C. Lawton, 2006, A case history of time-lapse 3D seismic surveys at Cold Lake, Alberta, Canada: GEOPHYSICS, **71**, no. 4, B93-B99. doi: 10.1190/1.2211027.

Iwata, S., S. Yamauchi, Y. Yoshitake, R. Nagumo, H. Mori, and T. Kajiya, 2016, Measurement of dynamic surface tension by mechanically vibrated sessile

droplets: Review of Scientific Instruments, **87**, no. 4, 045106. doi: doi:http://dx.doi.org/10.1063/1.4944045.

Jiang, Q., J. Yuan, J. Russel-Houston, B. Thornton, and A. Squires, 2009, Evaluation of Recovery Technologies for the Grosmont Carbonate Reservoirs: Petroleum Society of Canada. doi:10.2118/137779-PA

Jiang, Q., B. Thornton, J. Russel-Houston, and S. Spence, 2010, Review of Thermal Recovery Technologies for the Clearwater and Lower Grand Rapids Formations in the Cold Lake Area in Alberta: Canadian J. Petroleum Technology, **49**, no. 9,57-68. doi: 10.2118/140118-PA.

Kato, A., S. Onozuka, and T. Nakayama, 2008, Elastic property changes in a bitumen reservoir during steam injection: The Leading Edge, **27**, no. 9, 1124-1131. doi: 10.1190/1.2978974.

Kato, A., O. S., and T. Nakayama. 2010, Elastic property changes in a bitumen reservoir during steam injection, in S Chopra, LR Lines, D. R. Schmitt and M.I. Batzle, eds., Heavy Oils: Reservoir Characterization and Production Monitoring: Society of Exploration Geophysicists. 121-127.

Kendall, R., 2009, Using Timelapse Seismic to Monitor the THAI TM Heavy Oil Production Process: *79th SEG meeting, Expanded Abstracts, 3954–3958*

Kenter, J. A. M., F. S. Anselmetti, P. H. Kramer, H. Westphal, and M. G. M. Vandamme, 2002, Acoustic properties of "young" carbonate rocks, ODP leg 166 and boreholes Clino and Unda, western Great Bahama Bank: Journal of Sedimentary Research, **72**, no. 1, 129-137. doi: 10.1306/041101720129.

Li, H., L. Zhao, D.-H. Han, M. Sun, and Y. Zhang, 2016, Elastic properties of heavy oil sands: Effects of temperature, pressure, and microstructure: GEOPHYSICS, **81**, no. 4, D453-D464. doi: 10.1190/geo2015-0351.1.

Lin, C.-W., and J. P. M. Trusler, 2012, The speed of sound and derived thermodynamic properties of pure water at temperatures between (253 and 473) K and at pressures up to 400 MPa: The Journal of Chemical Physics, **136**, no. 9,-. doi: doi:http://dx.doi.org/10.1063/1.3688054.

Lines, L. R., R. Jackson, and J. D. Covey, 1990, Seismic velocity models for heat zones in athabasca tar sands: GEOPHYSICS, **55**, 1108-1111. doi: 10.1190/1.1442924.

Machel, H. G., M. L. Borrero, E. Dembicki, H. Huebscher, L. Ping, and Y. Zhao, 2012, The Grosmont: the world's largest unconventional oil reservoir hosted in

carbonate rocks: Geological Society, London, Special Publications, **370**. doi: 10.1144/sp370.11.

MacNeil, A. J., 2015, Petrophysical Characterization of Bitumen-Saturated Karsted Carbonates: Case Study of the Multibillion Barrel Upper Devonian Grosmont Formation, Northern Alberta, Canada: Petrophysics, **56**, 592-614.

Makarynska, D., B. Gurevich, J. Behura, and M. Batzle, 2010, Fluid substitution in rocks saturated with viscoelastic fluids: GEOPHYSICS, **75**, no. 2, E115-E122. doi: 10.1190/1.3360313.

Mattaboni, P. and E. Schreiber, 1967, Method of pulse transmission measurements for determining sound velocities: *Journal of Geophysical Research* **72** (20): 5160-5163

Mavko, G., T. Mukerji, and J. Dvorkin, 2009, The rock physics handbook: Cambridge University Press.

Mavko, G., 2013, Relaxation shift in rocks containing viscoelastic pore fluids: GEOPHYSICS, **78**, no. 3, M19-M28. doi: doi:10.1190/geo2012-0272.1.

Melendez Martinez, J., and D. R. Schmitt, 2013, Anisotropic elastic moduli of carbonates and evaporites from the Weyburn-Midale reservoir and seal rocks: Geophysical Prospecting, **61**, no. 2, 363-379. doi: 10.1111/1365-2478.12032.

Meyer, R.F., Attanasi, E.D., and Freeman, P.A., 2007, Heavy oil and natural bitumen resources in geological basins of the world: U.S. Geological Survey Open-File Report 2007-1084, available online at https://pubs.usgs.gov/of/2007/1084/.

Mikhaltsevitch, V., M. Lebedev, and B. Gurevich, 2016, Laboratory measurements of the effect of fluid saturation on elastic properties of carbonates at seismic frequencies: Geophysical Prospecting, **64**, no. 4, 799-809. doi: 10.1111/1365-2478.12404.

Mohebati, M. H., D. Yang, and J. MacDonald, 2014, Thermal Recovery of Bitumen From the Grosmont Carbonate Formation-Part 1: The Saleski Pilot: Journal of Canadian Petroleum Technology, **53**, no. 4, 200-211.

Molyneux, J. B., and D. R. Schmitt, 2000, Compressional-wave velocities in attenuating media: A laboratory physical model study: GEOPHYSICS, **65**, 1162-1167. doi: 10.1190/1.1444809.

Mortazavi-Manesh, S., and J. M. Shaw, 2016, Effect of Pressure on the Rheological Properties of Maya Crude Oil: Energy & Fuels, **30**, no. 2, 759-765. doi: 10.1021/acs.energyfuels.5b02366.

Njiekak, G., D. R. Schmitt, H. Yam, and R. S. Kofman, 2013, CO2 rock physics as part of the Weyburn-Midale geological storage project: International Journal of Greenhouse Gas Control, **16, Supplement 1**, no. 0, S118-S133. doi: http://dx.doi.org/10.1016/j.ijggc.2013.02.007.

Nur, A. M., 1982, Seismic Imaging in Enhanced Recovery: Society of Petroleum Engineers, **SPE-10680-MS**. doi: 10.2118/10680-MS.

Nycz, J., D. Yang, and D. Schmitt. 2016, Analysis of 4D time-lapse seismic responses integrated with 3D data products, production information, and laboratory data to characterize a bitumen-bearing carbonate reservoir, SEG Technical Program Expanded Abstracts, 2951-2955.

Peselnick, L., and W. F. Outerbridge, 1961, Internal friction in shear and shear modulus of solenhofen limestone over a frequency range of 10 to seventh power cycles per second: Journal of Geophysical Research, **66**, no. 2, 581-&. doi: 10.1029/JZ066i002p00581.

Pimienta, L., J. Fortin, and Y. Guéguen, 2015, Bulk modulus dispersion and attenuation in sandstones: GEOPHYSICS, 80, no. 2,D111-D127. doi: 10.1190/geo2014-0335.1.

Pimienta, L., J. Fortin, and Y. Guéguen, 2016, Effect of fluids and frequencies on Poisson's ratio of sandstone samples: GEOPHYSICS, 81, no. 2,D183-D195. doi: 10.1190/geo2015-0310.1.

Rabbani, A., D. R. Schmitt, R. Kofman, and J. Nycz, 2014, Laboratory studies of the seismic properties of bitumen saturated grosmont carbonates: Geoconvention Abstracts.

Rabbani, A., D. R. Schmitt, J. Nycz, and K. Gray, 2015, Velocity measurements of pore fluids at pressure and temperature: application to bitumen: Geoconvention Abstracts.

Rabbani, A., O. Ong*, X. Chen, D. Schmitt, J. Nycz, and K. Gray. 2016, Rock physics laboratory experiments on bitumen-saturated carbonates from the Grosmont Formation, Alberta: SEG Technical Program Expanded Abstracts 2016. 3464-3467.

Rabbani, A. and D. R. Schmitt, 2017 : Ultrasonic properties of bitumen: Influence of bulk viscosity, In preperation.

Rassenfoss, S., 2013, Finding Pathways to Produce Heavy Oil From Canadian Carbonates: JPT, **65**, no. 08.

Russel-Houston, J., and K. Gray, 2014, Paleokarst in the Grosmont Formation and reservoir implications, Saleski, Alberta, Canada: Interpretation, **2**, no. 3, SF29-SF50. doi: 10.1190/int-2013-0187.1.

Sarout, J., 2012, Impact of pore space topology on permeability, cut-off frequencies and validity of wave propagation theories: Geophysical Journal International, 189, no. 1,481-492. doi: 10.1111/j.1365-246X.2011.05329.x.

Saxena, N., and G. Mavko, 2014, Exact equations for fluid and solid substitution: GEOPHYSICS, **79**, no. 3, L21-L32. doi: 10.1190/geo2013-0187.1.

Saxena, N., G. Mavko, R. Hofmann, B. Gurevich, S. Glubokovskikh, S. Aliyeva, and P. Dutta, 2016, Rock-physics models for heavy-oil and organic-solid substitution: The Leading Edge, **35**, no. 6, 506-510. doi: 10.1190/tle35060506.1.

Schmitt, D. R., 1999, Seismic attributes for monitoring of a shallow heated heavy oil reservoir: A case study: GEOPHYSICS, **64**, 368-377. doi: 10.1190/1.1444541.

Schmitt, D. R. 2015, 11.03 - Geophysical Properties of the Near Surface Earth: Seismic Properties A2 - Schubert, Gerald, Treatise on Geophysics (Second Edition): Elsevier, 43-87.

Schmitt, D. R., G. Njiekak, M. Chowdhury, R. Kofman, A. Rabbani, and H. Yam. 2013, Use of CO2 as a Fluid in Fundamental Studies of Wave Propagation through Porous Media, Poromechanics V. 209-216.

Shamsa, A., and L. Lines, 2015, Effect of oil composition on fluid substitution in heavy oil reservoirs: Geophysical Prospecting, **63**, no. 2,422-441. doi: 10.1111/1365-2478.12147.

Skempton, A. W., 1954, The Pore-Pressure Coefficients A and B: Géotechnique, **4**, no. 4, 143-147. doi: 10.1680/geot.1954.4.4.143.

Spencer, J. W., 2013, Viscoelasticity of Ells River bitumen sand and 4D monitoring of thermal enhanced oil recovery processes: GEOPHYSICS, **78**, no. 6, D419-D428. doi: 10.1190/geo2012-0535.1.

Souraki, Y., M. Ashrafi, and O. Torsaeter, 2013, A comparative field-scale simulation study on feasibility of SAGD and ES-SAGD processes in naturally fractured bitumen reservoirs: Energy Environ. Res., 3(1), doi:10.5539/eer.v3n1p49.

Subramaniyan, S., B. Quintal, N. Tisato, E. H. Saenger, and C. Madonna, 2014, An overview of laboratory apparatuses to measure seismic attenuation in reservoir rocks: Geophysical Prospecting, **62**, no. 6, 1211-1223. doi: 10.1111/1365-2478.12171.

Teare M., S. Miller, S. Overland, and R. Marsh, 2015, in ST98-2015: Alberta's Energy Reserves 2014 and Supply/Demand Outlook 2015–2024: Alberta Energy Regulator.

Vanorio, T., and G. Mavko, 2011, Laboratory measurements of the acoustic and transport properties of carbonate rocks and their link with the amount of microcrystalline matrix: GEOPHYSICS, **76**, no. 4, E105-E115. doi: 10.1190/1.3580632.

Verwer, K., H. Braaksma, and J. A. Kenter, 2008, Acoustic properties of carbonates: Effects of rock texture and implications for fluid substitution: GEOPHYSICS, **73**, no. 2, B51-B65. doi: 10.1190/1.2831935.

Wang, Z., and A. Nur, 1990, WAVE VELOCITIES IN HYDROCARBON-SATURATED ROCKS - EXPERIMENTAL RESULTS: GEOPHYSICS, **55**, 723-733. doi: 10.1190/1.1442884.

Wang, Z., R. Wang, and D.R. Schmitt, 2015, The elastic moduli of velocities of artificial carbonate rocks with known pore structure at different saturation conditions: Geoconvention Abstract, CSEG/CSPG/CWLA.

Wang, Z. J., A. M. Nur, and M. L. Batzle, 1990, Acoustic velocities in petroleum oils: Journal of Petroleum Technology, **42**, no. 2, 192-200.

Wardlaw, N. C., and M. McKellar, 1981, Mercury porosimetry and the interpretation of pore geometry in sedimentary rocks and artificial models: Powder Technology, **29**, no. 1, 127-143. doi: http://dx.doi.org/10.1016/0032-5910(81)85011-5.

Wood, A.W., 1955, A Textbook of Sound: New York: McMillan Co.

Yang, D., M. H. Mohebati, S. Brand, and C. Bennett, 2014, Thermal Recovery of Bitumen From the Grosmont Carbonate Formation-Part 2: Pilot Interpretation and Development Strategy: Journal of Canadian Petroleum Technology, **53**, no. 4, 212-223.

Yuan, H., D.-h. Han, H. Li, and W. Zhang, 2017, A comparison of bitumen sands and bitumen carbonates: Measured data: GEOPHYSICS, **82**, no. 1, MR39-MR50. doi: 10.1190/geo2015-0657.1.

Zadeh, H. M., R. P. Srivastava, N. Vedanti, and M. Landro, 2010, Seismic monitoring of in situ combustion process in a heavy oil field: Journal of Geophysics and Engineering, **7**, no. 1, 16-29. doi: 10.1088/1742-2132/7/1/002.

Zhao, Y., and H. G. Machel, 2012, Viscosity and other rheological properties of bitumen from the Upper Devonian Grosmont reservoir, Alberta, Canada: Aapg Bulletin, **96**, no. 1, 133-153. doi: 10.1306/04261110180.

Zimmerman, R. W. 1991, Chapter 6. Undrained Compression, Developments in Petroleum Science: Elsevier. 57-65.

Chapter 4: The Longitudinal Modulus of Bitumen: Pressure and Temperature Dependencies*

*A version of this chapter is submitted to Geophysics. Rabbani and Schmitt, Geophysics, 2018

Bitumen retains significant solid-like behaviour even to temperatures in excess of 50°C, although traditional ultrasonic wave propagation studies largely ignore the existence of shear modulus in such materials. These non vanishing complex shear moduli doubt the conventional determination of bulk moduli that fail to consider the imaginary part or equivalently its bulk viscosity. Therefore, we study the ultrasonic longitudinal (P) wave transmission through viscous bitumen at pressure and temperature using an adapted version of the technique that consist two piezoelectric receivers placed at unequal lengths from the transmitter. As such, we are able to calculate the P-wave attenuation and velocity that is used to derive the material's complex longitudinal modulus, which differ from the bulk modulus particularly at lower (reservoirs) temperature. The results, with the knowledge of the various phase transition in bitumen through the compositional and thermophysical characteristics, can be implemented to improve fluid substitutions analyses.

4.1. Introduction

Recovery of highly viscous hydrocarbons (e.g., bitumen) using methods such as steam assisted gravity drainage (SAGD) or cyclic steam stimulation (CSS) from oil sands and/or carbonates necessitates that the reservoirs are heated to more than 100°C in order to lower the viscosity so that it can flow for production (Butler, 1991; Yang et al., 2014). The elevated temperature and pressure in the reservoirs during thermal recovery also influence the seismic wave speeds and attenuation which can be observed with time lapse seismic monitoring (Eastwood et al., 1994; Schmitt, 1999; Isaac and Lawton, 2006;

Kato et al., 2008; Bianco, 2010; Zadeh et al., 2010). Many workers, (Eastwood, 1993; Spencer, 2013) have observed significant drops in the longitudinal (P-wave) velocities in bitumen saturated sands with increasing temperature at both high and low frequencies, respectively. They both attribute this drop in P-velocity to the change in fluid's bulk modulus with temperature. Recent ultrasonic measurements with bitumen saturated carbonate from the Grosmont formation of northern Alberta show that its P- and S-wave velocities, too, decrease with temperature, and changes in the bitumen's properties are expected to be the dominating factor (Rabbani et al., 2017; Yuan et al., 2017). In lower frequency experiments, Das and Batzle (2008) report even larger temperature dependent changes in a Uvalde carbonate from Texas.

Prediction of this behaviour consequently requires knowledge of the bitumen's mechanical properties and how they vary with temperature, pressure, and even frequency e.g., (Rodrigues and Batzle, 2015). Although single component hydrocarbons have been extensively interrogated with ultrasonic acoustic techniques as reviewed in Tahani (2011) exhaustive bibliography, only a handful of studies are publicly available particularly with regards to very heavy oils or their components. Wang et al. (1990) describe 1 MHz ultrasonic P-wave pulse transmission tests on a series of heavy oils with API° as low as 5 over the ranges in temperature from 24°C to 114°C and in pressure from 0 MPa to 44.2 MPa over which the wave speeds declined by ~20% and increased by ~13%, respectively. Similar behaviour was seen in at 3 MHz in simpler single component heavy n-alkanes (Dutour et al., 2001; Dashti and Riazi, 2014), synthetic high-boiling point distillation products (Daridon et al., 1998) above 20°C and n-paraffins (Dutour et al., 2002) above 70°C, and on heavy natural oils from 20°C to 100°C up to 20 MPa (Plantier et al., 2008). Further reports of P-wave velocity measurements on natural heavy oils with temperature at different pressures (Eastwood, 1993; Verrall et al., 1994; Arafin et al., 2006; Batzle et al., 2006; George et al., 2008; Han et al., 2006; Han, Liu,

and Batzle, 2008; Mochinaga et al., 2006; Plantier et al., 2008; Khelladi et al., 2010; Tahani, 2011) have also appeared periodically and generally confirm the trends. Fazelabdolabadi and Bahramian (2012) show how such data may be used to derive a host of thermophysical parameters from acoustic measurements in heavy oil.

Our recent research has focused on issues related to production of bitumen from the Grosmont Formation of NE Alberta (Rabbani et al., 2017) and modelling associated with this work requires knowledge of the behaviour of the saturating bitumen (Wang et al., 2017b) beyond that necessary for conventional fluid substation calculations employing Gassmann's relation or later ones derived from it. Finding appropriate analog values is further complicated by the fact that the virgin in situ temperatures in this reservoir are only about 10°C to 14°C; this is colder than most of the earlier studies which typically begin at room temperature. As far as we are aware, the only P-wave ultrasonic velocity measurements through bitumen at lower temperatures are those of Mochinaga et al. (2006) from -20°C to 60°C on Athabasca bitumen, by Batzle et al., (2006) on an API° 5 heavy oil above 10°C, and by Han et al, (2006, 2008) from ~-50°C to 40°C on a very stiff heavy oil with API° -5. Regrettably, to our knowledge none of these data are generally available. The interesting aspect of these lower temperature studies is that the bitumen velocity increases rapidly and nonlinearly with decreasing temperature below about 50°C. On the basis of these observations, Han et al., (2006, 2008) characterize the bitumen velocity behaviour within temperature ranges as being either a glass, a quasi-solid, or a fluid oil at well defined 'phase transition' temperatures. This is a useful construct, but evidence from other disciplines shows that the sequence of transitions is more complicated and as yet poorly understood in bitumen and as such is worthy of further investigation.

Here we build on this earlier work by carrying out P-wave pulse transmission measurements on bitumen produced by steam injection methods in the Grosmont pilot

project of our industrial partners. We first review the literature as to knowledge of the constituents of bitumen and how temperature dependent phase transitions of these various components influence bitumen's microscopic colloidal structure. We then describe the composition and thermophysical characteristics of our particular bitumen sample using a variety of different techniques. This leads to the description of the P-wave pulse transmission tests of the wave speed temperature and pressure dependencies. We diverge from common practice in that we interpret the results in terms of the P-wave, or longitudinal modulus instead of assuming that the bulk modulus is obtained and incorporate parallel measurements of the bitumen's shear modulus to this analysis. We discuss the results in light of current knowledge of the complex phase transition behaviour in bitumen and what implications this may have to time lapse seismic investigations.

4.2 Theoretical background

In the tests here we are confident that we are able to obtain accurate values of the longitudinal, P-wave phase speed $V(P,T)$ through the bitumen as a function of pressure P, temperature T, at the dominant frequency of the waveforms. In the context of ultrasonic wave propagation through heavy hydrocarbons in the geophysical literature, studies have largely ignored the existence of the shear modulus in such materials and assumed that the bulk modulus $K = \rho V^2$ is determined, which conveniently may be used for Gassmann fluid substitution analysis. Following earlier work on 'simpler' polymers e.g., (Verdier et al., 1998; Alig et al., 1991; Lionetto and Maffezzoli, 2008), however, we instead carry out this analysis in terms of the complex longitudinal, or P-wave, modulus M^*. This is necessary because the complex shear modulus G^* of our bitumen does not vanish over much of the temperature range used in the experiments (Rabbani and Schmitt, 2018); and as such the bitumen retains significant solid-like behaviour. Ideally,

we too would have frequency dependent measures of the P-wave attenuation $\alpha(P,T,\omega)$ and velocity $V(P,T,\omega)$ that may be used to determine the material's complex moduli.

It is useful to review a number of the longstanding relationships between our observations and the various mechanical descriptions for the material available (Herzfeld and Litovitz, 1959; Bhatia, 1967). Consider a longitudinal-mode plane wave of angular frequency (ω) propagating with a real observable phase speed $V_P(\omega)$ and whose amplitude $A(x,t,\omega)$ decays according to an observable attenuation coefficient $\alpha(\omega)$, Following O'connell and Budiansky (1978),the wave equation describing this propagation

$$\frac{\partial^2 A}{\partial t^2} = \frac{M^*}{\rho}\frac{\partial^2 A}{\partial x^2} \tag{1}$$

where $M^*(\omega) = M'(\omega) + iM''(\omega)$ is the adiabatic complex longitudinal, or P-wave, modulus has the well-known solution.

$$A(x,t) = A_o e^{\alpha x} e^{-i\omega(t-x/V)} \tag{2}$$

M' and M'' are referred to as the storage and loss moduli, respectively. M^* is related to α and V through (Marvin and McKinney, 1965)

$$M^* = \frac{\rho V^2}{\left(1 - i\alpha V/\omega\right)^2} \tag{3}$$

which can be manipulated into its real M',

$$M' = \frac{\rho V^2\left(1 - \alpha^2 V^2/\omega^2\right)}{\left(1 + \alpha^2 V^2/\omega^2\right)^2} \tag{4}$$

and imaginary M''components

$$M'' = \frac{2\rho V^2\left(\alpha V/\omega\right)}{\left(1 + \alpha^2 V^2/\omega^2\right)^2} \tag{5}$$

Often, it is assumed that the attenuation is small with $aV/\omega << 1$ whereby researchers often make the approximations $M' = \rho V^2$ and $M'' = 2\rho\alpha V^3/\omega$ (e.g., Alig et al 1991).

It is important to further note that M^* is related to the complex bulk $K^*(\omega) = K'(\omega) + iK''(\omega)$ and shear $G^*(\omega) = G'(\omega) + iG''(\omega)$ by direct analogy to the purely elastic case

$$M^* = M' + iM'' = K' + \frac{4}{3}G' + i\left(K'' + \frac{4}{3}G''\right) \quad (6)$$

Others in the context of fluids more familiar expressions arise if $K' >> K''$, G', and G'' such that the latter can be ignored and $|M^*| \rightarrow |K^*|$ such that the measurements serve to determine the purely elastic bulk modulus K that, again, conveniently may be used in fluid substitution analyses.

The bitumen sample here is, in contrast, highly attenuative to the longitudinal waves and has a complex shear modulus with $|G^*| \rightarrow 0.5$ GPa (Rabbani and Schmitt, 2018) at lower temperatures that cannot be ignored. As such, the more general Eqn. 6 holds and this means that measurements of the longitudinal and shear wave speeds and attenuations, that in principle can provide both M^* and G^* are required should K^* be sought.

It may also be useful to consider the above expressions instead in terms of the complex dynamic shear $\eta_S^* = \eta_S' + i\eta_S''$ and volume $\eta_V^* = \eta_V' + i\eta_V''$ viscosities, respectively which are related to the moduli via

$$K' + iK'' = K' + i\omega\eta_V' \quad (7)$$

and

$$G' + iG'' = G' + i\omega\eta_S' \quad (8)$$

These formula, in principal, allow calculation of the frequency dependent dynamic bulk η_V' and shear η_S' viscosity from knowledge of K'' and G'', respectively. Some authors (e.g. Bhatia, 1967; Alig et al., 1991) examine the viscosities in terms of the attenuation of the P-wave

$$\alpha = \frac{4}{3}\eta_{eff}\left(\frac{\omega^2}{\rho V^3}\right) \tag{9}$$

where the effective viscosity $\eta_{eff} = \eta'_S + 3\eta'_V/4$. It is worth commenting that in the middle of the last century studies of wave speed and attenuation through fluids provided important fundamental information used to test theories related to the observation that ultrasonic waves propagating through fluids much simpler than bitumen e.g., (Singer, 1969) are attenuated more than it can be explained from the classic mechanisms. In these cases, the observed P-wave attenuation was then used with knowledge of η'_S independently determined to calculate η'_V using Eqn. 9. We could in principle carry out these bulk viscosity calculations but retreat from this in part because it is likely that other mechanisms, such as scattering within the colloidal bitumen, area also contributing to the observed attenuation, and because of the expected uncertainties of our current methodology.

4.3 Bitumen characterization: Chemistry and structure

In this section we review some of the techniques used in characterizing the properties, chemistry, phase state, and structure of bitumen that together may impact the wave speed observations. While doing so the corresponding factors for our bitumen sample are provided for illustration. Additional complementary information may be found in Rabbani and Schmitt (2018). Hinkle et al. (2008) also employ similar methods in their characterization of a number of heavy oils.

Briefly, the bitumen sample was provided to us *as produced* during steam injection to the Grosmont Formation of NE Alberta at the Saleski Pilot project (Yang et al, 2014). The Devonian carbonate Grosmont Formation hosts a globally important, but as yet essentially untapped, bituminous reservoir estimated to contain upwards of 64.5

X 10^9 m^3 (406 bbl) of bitumen (AER, 2016). The reservoir subcrops at an unconformity between the platform Devonian limestones and dolomites and the Cretaceous siliclastic rocks that contain the more recognized Athabasca oil sands. While the geology and structure will of course influence the seismic response e.g., (Russel-Houston and Gray, 2014) this contribution focuses on the study of the bitumen itself and the reader may find further geological descriptions reviewed elsewhere recently (e.g., Ardakani et al., 2014).

Bitumen is a somewhat ambiguous term describing very heavy oils occurring either naturally (where it may then be called asphalt) or more often as an end product of petroleum distillation. The American Petroleum Institute designates bitumen as an 'extra heavy oil' with a specific gravity of 1 at 15.56°C (60°F) such that its API° value is less than 10° and generally with a steady state shear viscosity exceeding 10,000 cP at room condition. Here bitumen density was determined with temperature (Figure 4.1a) using the oscillating U-tube method (automatic density meter DDM 2910, Rudolph Research Analytical), and converting to API° 6 or lower. This is in good agreement with earlier measurements conducted by our industrial partners using an undisclosed method on oil produced or extracted directly from the core by high speed centrifugation (Rabbani et al., 2017). The dynamic shear viscosity of the bitumen is measured with temperature using the Searle rotating spindle method (Brookfield viscometer DV2T viscometer, Brookfield Engineering), as shown in Fig.1b. The instrument operates at increasing shear rate while ramping the temperature and is limited to measure viscosity smaller than 10^5 cP. This also compares well with the determinations by (Yang et al., 2014), Figure 4.1b. The shear viscosity decreases by 4 orders of magnitude with temperatures ranging from 10°C to 100°C. Ultrasonic techniques can also be used to measure the viscosity of bitumen which yields lower numbers than the spindle method, mostly due to the shear thinning effects (Rabbani and Schmitt, 2018).

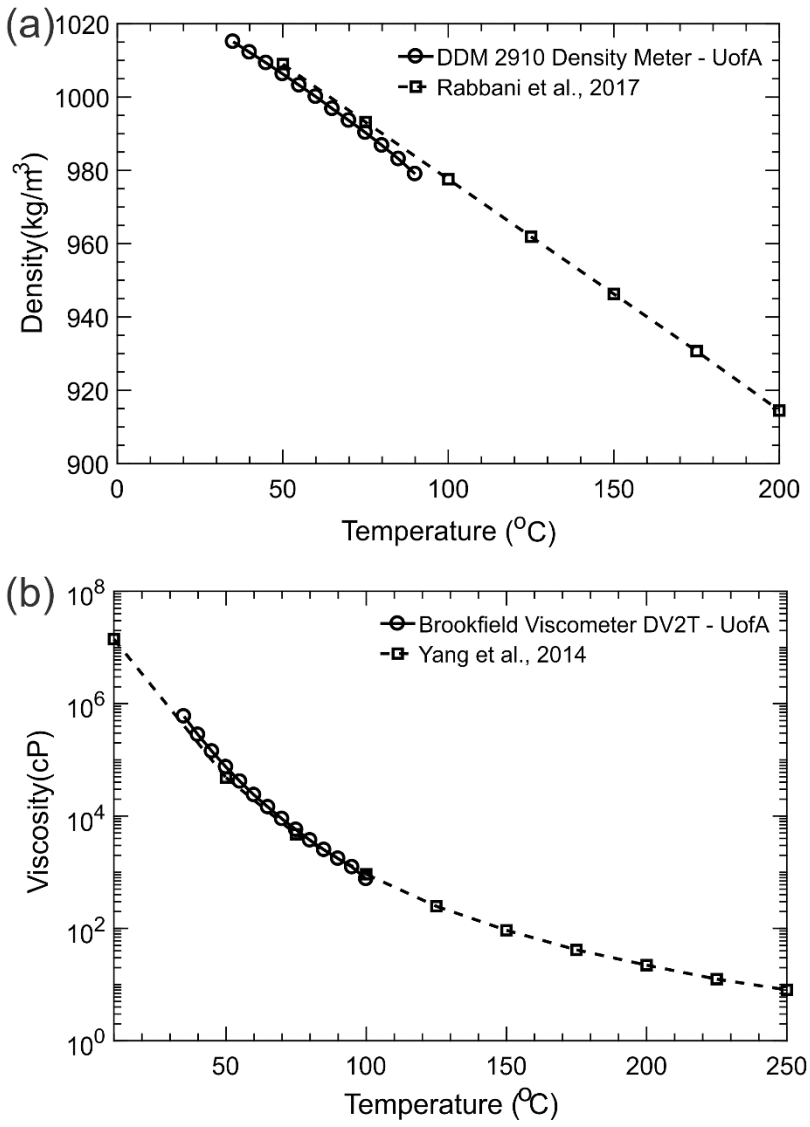

Figure 4.1. (a) Density of bitumen versus temperature at room pressure on the sample of produced bitumen used (open circles) and at 1.5 MPa on Grosmont bitumen obtained by centrifugation (square markers). The sample density is well described by the linear fit $\rho(T) = 1037.5 - 0.0634T$ in kg/m^3 with T°C. (b) Dynamic viscosity of bitumen decreases exponentially with temperature. Brookfield viscometer provides data plotted as the solid line (circle), and dashed line (square) is from Yang et al. (Yang et al., 2014).

Any given bitumen is a complex mixture of numerous hydrocarbons and the composition and physical properties can vary widely between and within reservoirs (e.g., (Larter et al., 2008). As such, accurately chemically characterizing bitumen is challenging and a

number of strategies can be employed. Elementally, bitumen primarily consists of from 90% to 98% by weight of C and H atoms with a H/C ratio of ~1.5. It's worth to note that hydrogen-to-carbon molar ratio is 1 for aromatic structures (e.g., benzene) and ~2 for saturated alkanes (e.g., ethane) (Read and Whiteoak, 2003; Lesueur, 2009). This suggests that the structure of bitumen is in between that of aromatic and long chain polymers.

Bitumen composition is most often described in terms of the saturates-aromatics-resins-asphaltenes (SARA) separation technique (ASTM, 2003) that, first, on the basis of solubility or insolublity in n-heptane divides the sample into 'maltenes' and 'asphaltenes', respectively. The maltane portion is then further separated into saturates, aromatics, and resins. There is a large literature on these components, see reviews in (Masson et al., 2005; Lesueur, 2009) and here we attempt to extract the salient aspects of these components to this study.

At room temperature, the asphaltene portion is a dark solid powder with a grain density ~1150 kg/m^3 (Corbett, 1969). Their number-average molecular weights lie in the range from 800 to 3500 g/mol consistent with their large planar molecules with nanometer scale dimensions (Zhao et al., 2001) that are stackable in analogy to graphite sheets. The asphaltenes molecules, too, are polar carrying permanent electrical charges on their surface that contribute to the microscopic colloidal structure of the bitumen and appear to result in different temperature dependent phase transitions below 150°C (Evdokimov and Losev, 2010). The resin portion primarily consists of polar aromatic rings that exist as a black solid at room temperature with an elemental composition similar to the asphaltenes but with a lower molecular mass of ~1100 g/mol and a higher H/C ratio.

At room temperature, the aromatic fraction is a viscous yellow-red liquid with a number-average molecular weight ~800 g/mol. They undergo a phase transition from liquid to glass near -20°C. Finally, the saturates are a low density (~900 kg/m^3) lightly colored

liquid with a number average molecular weight ~600 g/mol. Their glass transition temperature is ~ -70°C. As already reported (Rabbani and Schmitt, 2018), SARA analysis for our sample yields 13.84% asphaltenes, 27.17% saturates, 26.28% aromatics, and 32.68% resins.

Complementary descriptions instead employ the distributions of the molecular weights of the hydrocarbons constituting the natural oil with bitumen's distribution centered near C28 (Mansoori, 2009). Gas chromatography (Kariznovi et al., 2014) and mass spectroscopy (Silva et al., 2011)) provide additional complementary information to further characterize the hydrocarbon chemistry of the sample, as shown Figure 4.2. A compositional analysis of the sample using a high temperature gas chromatography method yields it as a large asphatlene molecule with a distribution of carbon number up to C_{100} and total boiling temperature as high 700 ºC, when, the component $n\text{-}C_{100}$ is eluted, Figs. 4.2a-4.2b (Kariznovi et al., 2014). The spectrum, Fig. 4.2c, provides a number-average molecular weight of 652 g/mol and weight - average molecular weight of 970 g/mol, (Fenistein and Barré, 2001).

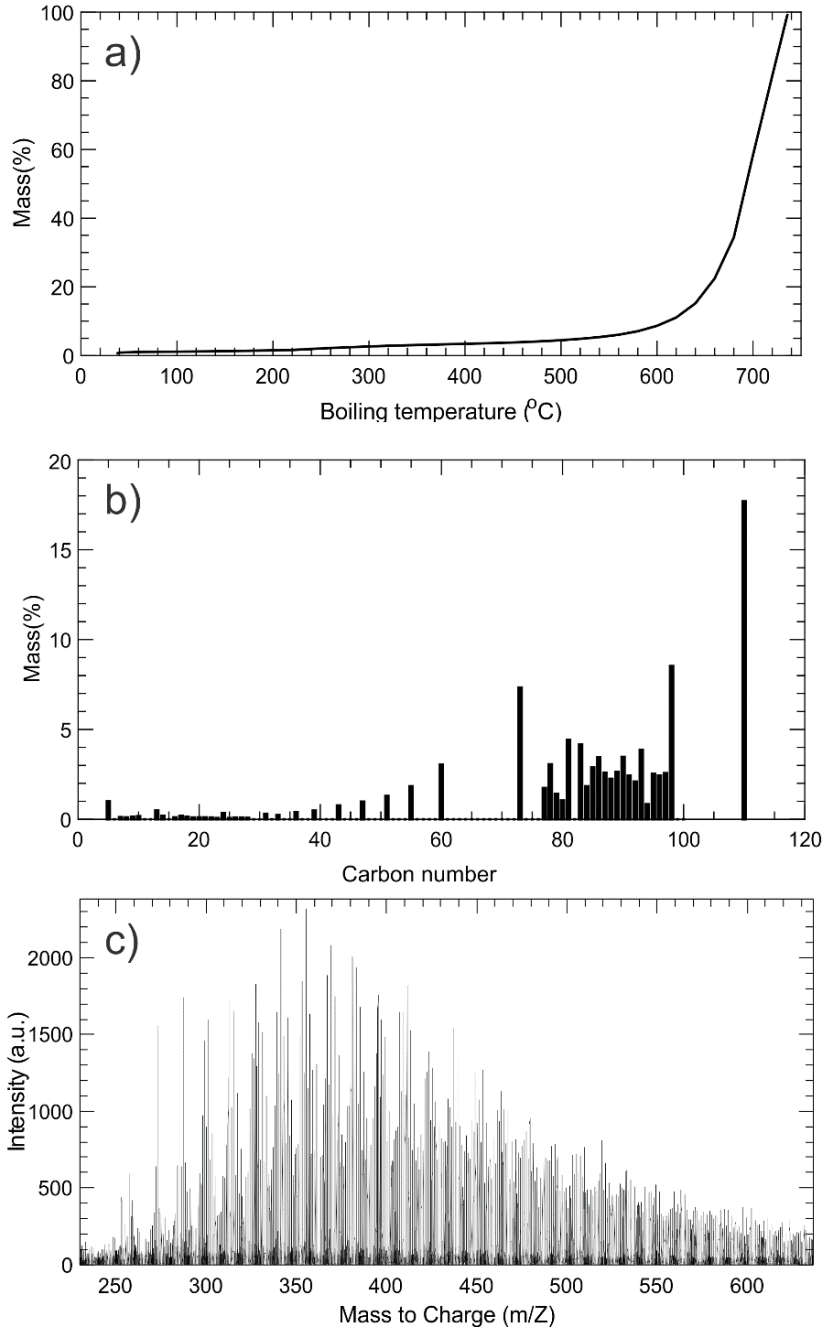

Figure 4.2. (a) Gas chromatography analyses yields the boiling curves for bitumen. It requires the temperature to reach as high as 700 ºC to elute the total fraction of the sample b) the sample consists of compounds containing carbon number up to 110, c) the relative intensity (current produced by ions) of varying mass-charge ratio from the mass spectroscopy analyses illustrates a distributed molecular spectrum of bitumen.

The exact molecular weight or molecular weight distribution is difficult properties to measure (Redelius and Soenen, 2015). Among several techniques such as Vapour Phase Osmometry (VPO) and Gel Permeation Chromotography (GPC), Mass Spectroscopy provides the most reliable molecular weight distribution (Boduszynski et al., 1980). A matrix-assisted laser desorption/ionization (MALDI) technique is used for the mass spectrocopy of the bitumen sample.

This particular sample, however, also contains water possibly derived in part from the natural water in the formation but almost certainly from the steam injection process itself. Evidence for this water was found first from thermogravimetric analysis (TGA), whereby the mass of the sample is measured with increasing temperature (Mettler Toledo TGA/DSC 1 STAR System) on the bitumen sample Over the range from room temperature to 150°C the sample lost ~16% of its mass before 100°C likely indicating evaporation of some lighter hydrocarbon portions and water, as shown in Figure 4.3. The total drop of its weight as the temperature reaches around 100°C. The onset temperature (70°C) of this 25% weight loss, however, may imply that it is due to the evaporation of lighter hydrocarbon molecules as well as water. An additional Karl Fisher e.g., (Giles, 2016) analysis using a titrator (Mettler Toledo T70 Autotitrator) later confirms that that the sample possesses 22% of water content. Finally, optical microscopy of the sample further reveals the existence of the water in micron scale spherical droplets dispersed within the hydrocarbon mixture (Figure 4.4). The water droplets in the bitumen sample, with a diameter from 1-10 μm, indicate a bitumen-water emulsion (Figure 4.4). Tausk and Wilson (1981) observe a reduction of viscosity in such a bitumen-in-water emulsion due to the absorption of water in the bitumen droplets.

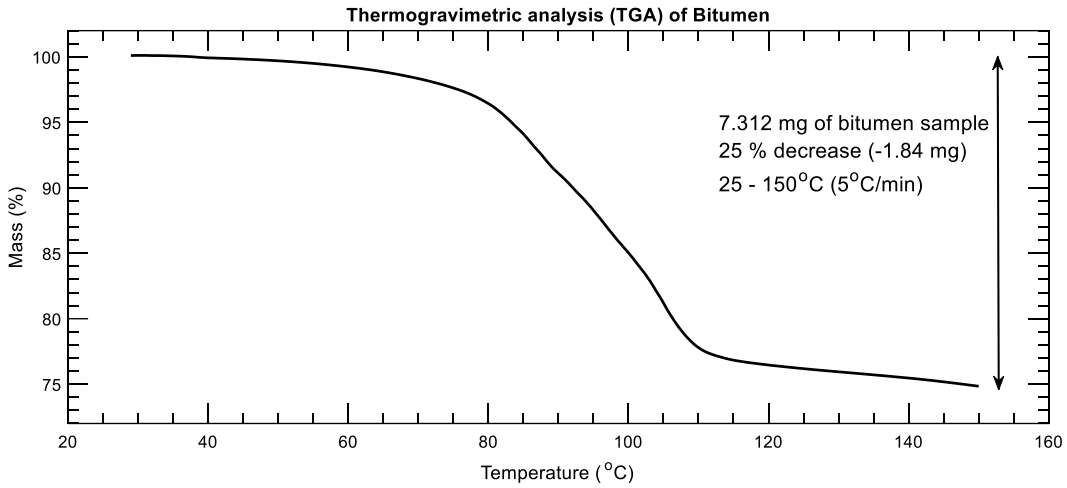

Figure 4.3. The bitumen sample loses as much as 25% of its weight over a temperature change from 70°C to 150°C in the thermographic analysis.

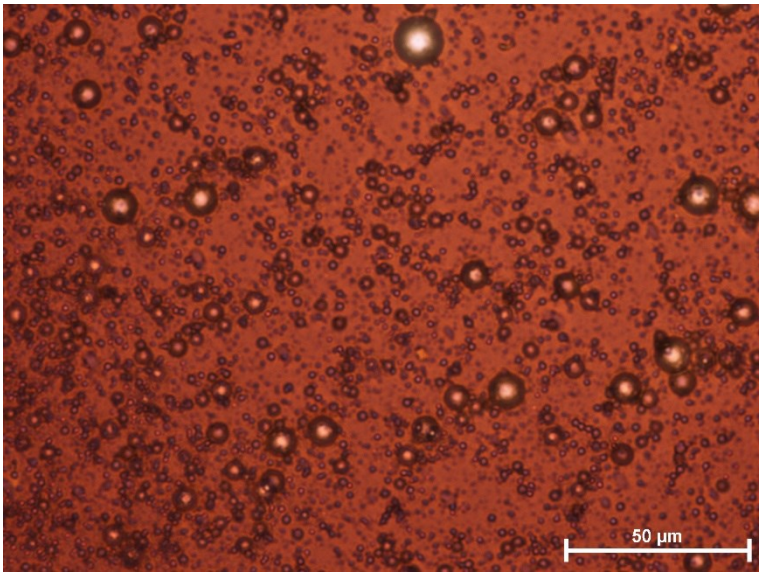

Figure 4.4. Microscopic image exhibits the existence of water droplets as big as ~10 μm within the raw bitumen sample.

Bitumen's complicated composition also leads to a complex microscopic architecture that is influenced by a number of factors, many of which likely remain unknown, but do include phase transformations within the bitumen's components

together with its colloidal nature. Bitumen shares some characteristics with manmade polymer plastics for which a glass transition is well understood.

Phase transitions are often studied using differential scanning calorimetry (DSC) whereby the subtle differences in heat flows between the sample of interest and a suitable standard are carefully monitored as the temperature of the system is progressively changed. Briefly, the sample will release or consume heat energy as it experiences a phase transformation that is, respectively, exothermic or endothermic and this small variance in heat energy is sensed. Too, some phase changes are manifest by variations in heat capacities that affect the rate of energy consumption or release as temperature is varied. There are different types of phase transitions that can occur within bitumen that are

i) First order phase changes that include the solid-liquid-gas transitions such as the melting of ice and boiling of water that most readers will be familiar with. They are associated with a latent heat that must be exchanged with the surroundings before the transitions can be complete, and occur only at specific set of pressures and temperatures. The material's properties (e.g. density, sound velocity) are discontinuous across these phase boundaries.

ii) Second order, or continuous, phase transformations that do not require transfer of a latent heat energy but are associated with a change in the material's physical properties (Wada et al., 1959) such as the heat capacity, the thermal expansivity, the complex rigidity (which incorporates the viscosity), or the P-wave velocity, e.g.,(Lionetto and Maffezzoli, 2008; Nguyen et al., 1995). In the context of bitumen and by analogy to the much studied and well understood behaviour of 'simpler' man-made polymers e.g., (Wada and Hirose, 1960; Kriz et al., 2008), the glass transition whereby a supercooled liquid freezes into a 'solid' sufficiently quickly that crystallization cannot occur. In other words, the transition exists if the time required for structural arrangement of the

molecules is longer than the time of the experiment; this is often stated in terms of the rapid increase in the shear viscosity to values ~10^{13} Pa•s as a rule of thumb. A glass transition temperature T_g is often arbitrarily assigned to indicate a range of temperatures over which the transition occurs, and its value will depend on the method used to determine it. T_g further rises with increasing pressures (e.g. (Wang et al., 1982). The situation in bitumen, that is composed of many different molecular compounds, further confuses its behaviour such that it has been classified as a *complex glass forming liquid* that has not much been studied (e.g. (Laukkanen et al., 2018). Indeed, depending on its chemistry, any given bitumen may have a number of different T_g's although one might question the use of the term 'glass transition' for all of them. For example, using DSC, Masson et al. (2005) detect four T_g's at ~-70°C, ~-20°C, ~0°C, and +70°C that they associate with different amorphous components. Abivin et al. (2012) describe broad glass transitions centered near -50°C in two bitumens. Bazyleva et al. (2011) describe finding a number of first and second order phase transitions within an Athabasca bitumen from about -80° to 300°C. A number of studies have focussed on the separated heavy asphaltenes with glass transitions with ranges of 70°-130°C and 130°-170°C (Ganeeva et al., 2014), 35°-40°C (Evdokimov and Losev, 2010), 186°-307°C (Mansoori, 2009), and from 100° to 180°C (Zhang et al., 2004). Bazyleva et al (2011) report a glass transition in the maltene separate from -60° to -45°C. However, it is important to note that it may not always be clear what is actually occurring within the material through these 'glass' transitions; and those seen in the bitumen may differ at both microscopic and molecular scales from the glass transition in a less compositionally complex polymer. Mansoori (2009), for example, lists 5 different phase transitions in heavy oils containing asphaltenes an resins that are related to the precipitation, the deposition, the colloidal formation, the micellization, and the micelle coacervation of the asphaltenes all

of which results in structural rearrangement that one might expect to affect the mechanical properties.

Further, bitumen is considered to have a colloidal structure (Van Nellensteyn, 1923; Lesueur, 2009). Moreover, in a rheological standpoint, the colloidal bitumen is also attributed with a 'sol - gel' type feature. The 'sol' bitumen behaves as a Newtonian fluid with the dispersed asphaltenes micelles. Whereas, the 'gel' structure exhibits as non-Newtonian behaviour with a interconnecting asphaltene micelles (Lesueur, 2009; Pfeiffer and Saal, 1940). As a non-Newtonian fluid, it possesses complex and frequency dependent shear viscosities (Bazyleva et al., 2010b) (Rabbani and Schmitt, 2018). However, Lesueur (2009) adverted that 'sol-gel' concept of bitumen has its limitation and emphasized on 'colloidal model' as the standout model to explain the features in bitumen. Results from various experiments on bitumen, e.g., wave scattering, rheological measurements, kinetic and thermal properties, diffusion and also polymer modifications can only be explained considering it possesses colloidal structure. There are various evidences in literature that confirms the colloidal structure of bitumen (Espinat et al., 1998; Yen, 1992) and crude oil (Bardon et al., 1996).

An exploratory DSC run with our sample, Figure 4.5, shows distinctly the melting and boiling of water within the sample; this is particularly evident in examining the DSC curve's derivative that emphasizes any changes in rate indicative of the phase transformation. A smaller but significant transition occurs near -25°C and, possibly, a second near 70°C, most likely due to the degassing of the sample. The experimental setup of P-wave propagation through bitumen operates at the temperature range from 5°C to 130°C which would not allow us to observe the glass transition behaviors below 0°C but the phase transitions at higher temperature (~70°C) are expected to leave a footprint on the observed waveforms.

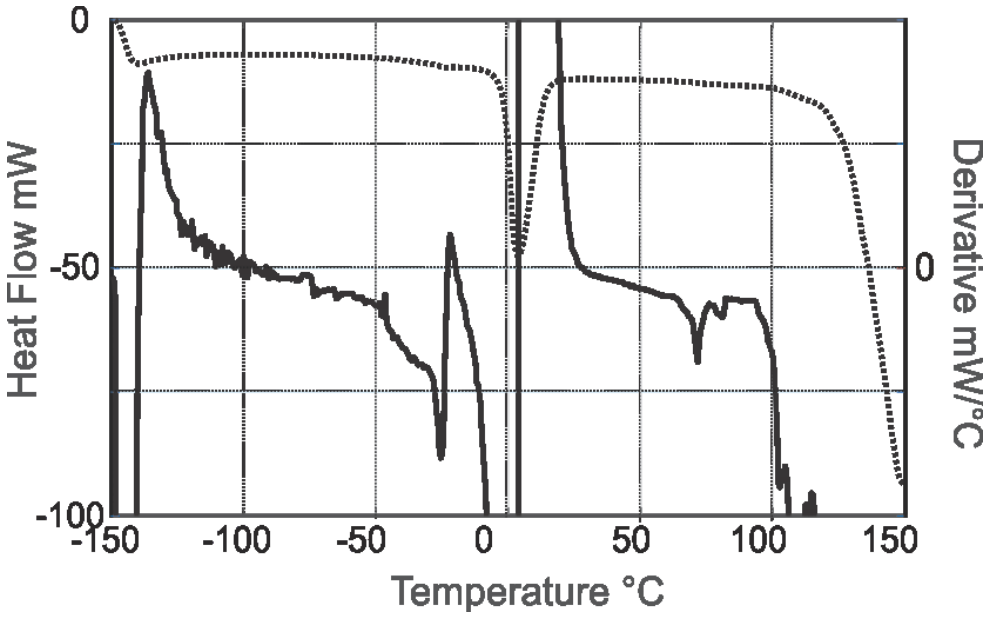

Figure 4.5. DSC analysis of bitumen sample carried out from 150-°C to 150°C at a heating rate of 30°C/min using a Mettler Toledo Polymer DSC. Observed differential heat flow (left axis, dashed line) and its derivative with respect to temperature (right axis, solid line) highlight melting of ice and boiling of the water in the sample at 0°C and ~100°C. a glass transition near -25°C, and another possible transition near 70°, mostly related to degassing.

The above review emphasizes the complexity in the temperature dependent phase behaviour of bitumen. We will attempt to interpret our observations in light of these findings, but we emphasize that our knowledge of the behaviour of the bitumen sample studied here is incomplete and further complicated by the water emulsion. As such, while it is possible that we are able to detect temperature driven changes in the observed wave speeds, it is impossible at this juncture to associate these with any specific phase transition at the molecular level in our material.

4.4 Experimental technique

The experimental configuration was constructed to measure the sound speed in fluids subject to varied pressure and temperature following, at least initially, the double pulse-echo technique first developed by Ball and Trusler (2001) and subsequently adapted by

numerous researchers. This geometry consists simply of a single longitudinal-mode PZT that both sends an ultrasonic pulse outwards from both of its faces into the studied fluid. Both pulses are then reflected back from acoustic 'mirrors' (i.e. polished flat reflectors constructed of steel or other high impedance material) to be received by the PZT. The great advantage of this approach is that the echo transit times along two different paths may be obtained from a single activation of the PZT reducing errors introduced by the calibrations necessary in pulse transmission. Indeed, in our first implementation of this technique we were able to reproduce published standards for water with pressure and temperature to better than 0.1% (Rabbani et al. 2014).

These advantages, however, disappear should the fluid be highly attenuating to the ultrasonic pulse as was subsequently found to be the case when the instrument was immersed within the bitumen and we were unable to obtain interpretable waveforms due to the large increase in attenuation at lower temperatures, a problem experienced by other workers e.g., (Khelladi et al., 2010).

To overcome the high attenuation, we reverted to a direct pulse transmission geometry with two independent receiver PZTs placed at different distances on opposite sides of the central transmitting PZT (Figure 4.6a). The PZTs with 0.2 cm thickness and 2 cm diameter are axially polarized longitudinal-mode piezoelectric ceramics resonant at 1 MHz (APC international Ltd). The far and near receivers were placed at 4.27 cm and 2.78 cm, respectively, from the transmitter. This allowed us to determine wave speeds accurately but we could not obtain satisfactory measures of attenuation due to unresolved problems related to the temperature sensitive response of the receivers particularly that did not allow for the acquisition of waveforms with sufficiently consistent amplitude spectra to be used high-fidelity quantitative analysis.

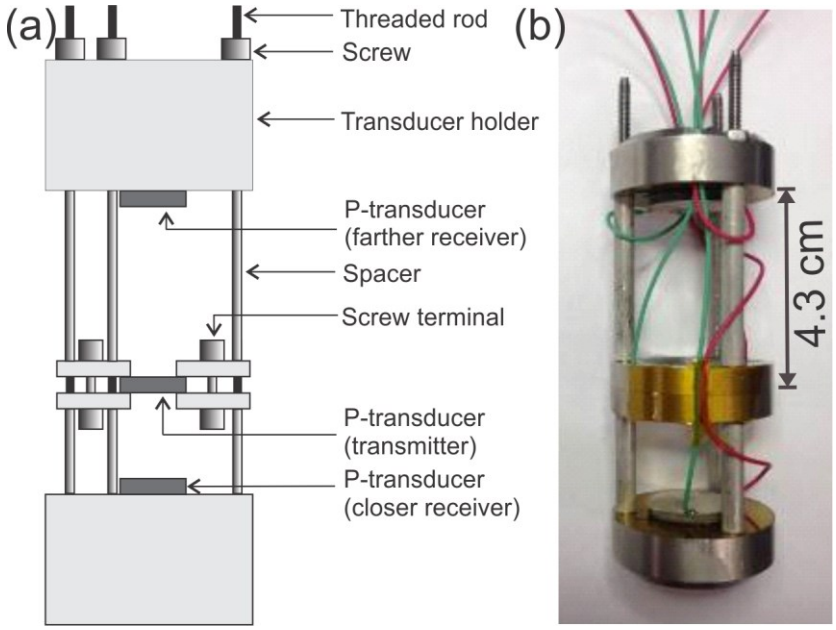

Figure 4.6. Pulse-transmission approach for highly attenuating fluids consisting of a central single transmitter with a far and near receivers. (a) the schematic of the cell and (b) picture shows the actual cell made with stainless steel.

This measurement cell as shown in Figure 4.6b is placed in a sealed pressure vessel that is then filled with bitumen. Bitumen is warmed on a hot plate to pour in the pressure vessel. We use a pressure transducer (Tecsis, model 99-6308-0001) with an accuracy of 0.05% to measure and a manual pressure accumulator (HiP 62 6-10) to control the pressure. A chiller system (NESLAB Endocal Refrigerated Circulating Bath RTE-8DD) circulates fluid a mixture of water and around the pressure vessel through a copper tubing system to control the temperature, mainly to cool the system. Another heating tape wrapped the vessel is used for the high temperature application. Temperature is measured to ±0.1°C accuracy using a K-type thermocouple with a temperature controller (OMEGA® - CNi16D44-C24). Rabbani et al. (2017) include a schematic of the experimental set up that also highlights the other technical details.

The PZT element is activated using an ultrasonic pulser (Panametrics pulser/receiver, model 5800) and the signal or waveform is recorded at a sampling period of 20 *ns* (NI 8-bit digitizer, model PXI-5114). Each final record is the average of 300 pulses. The time

of the first extremum amplitude of the waveform declare the transit time, which with the known distance is then used to calculate the velocity. The velocities measured with the far and near receivers are usually differed by 0.5%. Therefore, for the first phase of measurements (at constant temperature), we calculate the velocities from the travel time and length difference of the receivers. This technique usually provides more accuracy and undermines the issues related to the first break picking in an attenuative fluid (Molyneux and Schmitt, 2000).

As already noted the temperature sensitivity of the transducers did not allow for a proper estimate of the attenuation using a spectral ratio method e.g., (Molyneux and Schmitt, 2000). Instead a more direct method that employed the waveform amplitudes *A(x)* was used according to

$$\alpha(T,P,\omega) = -\frac{\ln\left(A(x_2)/A(x_1)\right)}{(x_2 - x_1)} \tag{10}$$

where x_1 and x_2 are the one-way propagation distances through the bitumen from the central transmitter to the near and far receivers, respectively. Following Bouzidi and Schmitt (2006) we used the peak magnitude of the analytic signal, often called the amplitude envelope, as calculated using the Hilbert transform to provide representative values of the amplitudes to employ in Eqn. 10. The advantage of our experimental geometry is that the source signal to both receivers is exactly the same, but the failure of the far receiver in the later stages of the tests precluded more complete calibration to account for beam diffraction (e.g., (Li et al., 2018)) and the response functions for both receivers. As such, we consider our calculated values of α to be apparent attenuation coefficients.

4.5 Results and Discussion

4.5.1 Observed waveforms

Two different ensembles of measurements were made in bitumen as summarized in Table 4.1. The first consisted of 6 constant temperature suites with measurements made while pressure increased from room conditions to 15 MPa. Both the near and far receivers functioned during this suite and the full set of waveforms (Figure 4.7) clearly show that the pulses arrive earlier as pressure increases. The differences in the amplitudes between the near and the far receivers illustrate the strong attenuative behaviour of the bitumen that decreases with temperature at least till 71°C.

Table 4.1. Conditions for the two different ensembles of measurements

	Pressure (MPa)	Temperature (°C)	Figures
Ensemble 1 (Constant temperature)	0.1 to 15	23	4.7a
	0.08 to 15	37	4.7b
	0.1 to 15	51	4.7c
	0.5 to 15	63	4.7d
	0.1 to 15	71	4.7e
	0.1 to 15	88	4.7f
Ensemble 2 (Constant pressure)	1	7 to 132	4.8a
	2	10 to 85	4.8b
	5	9 to 102	4.8c

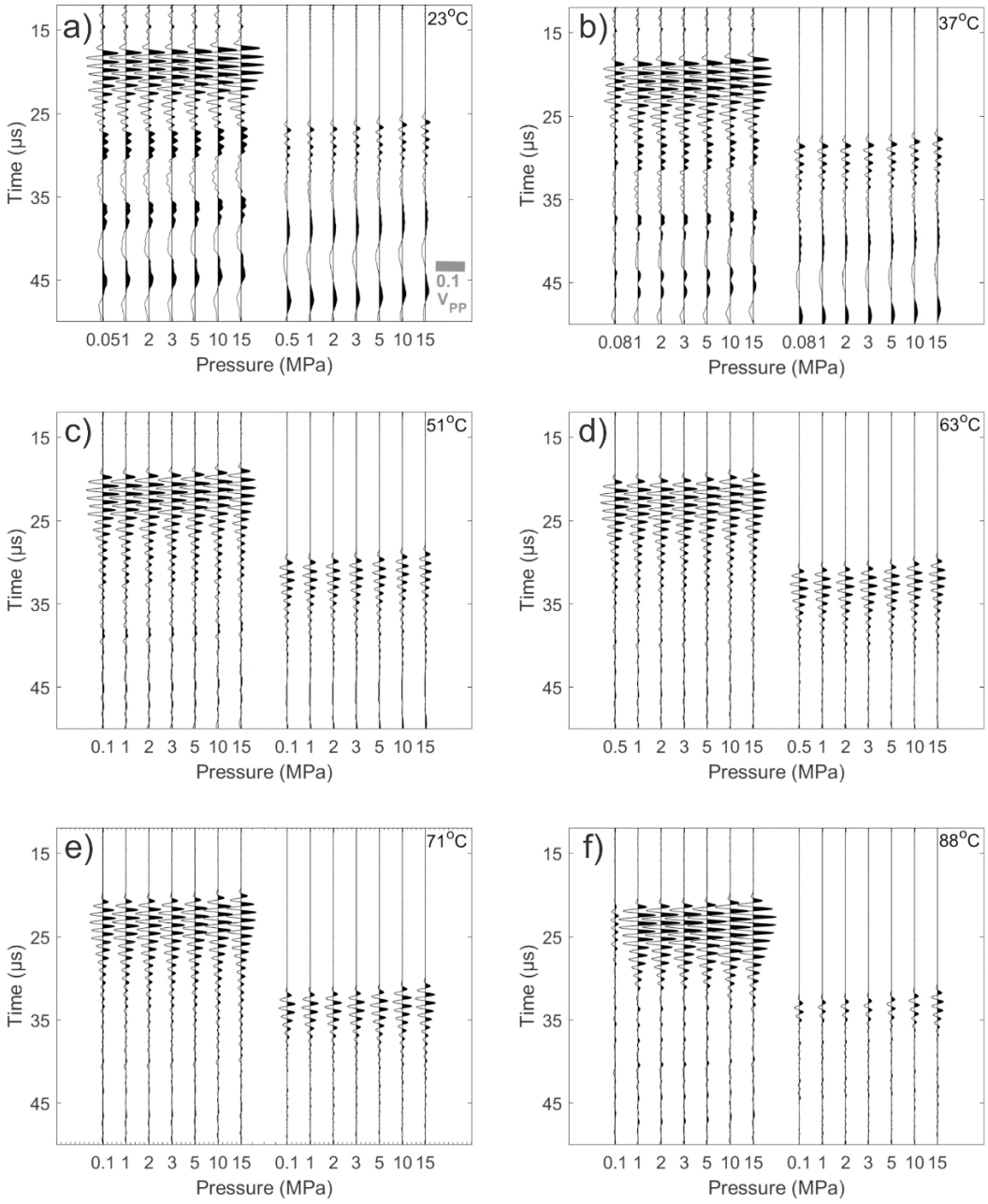

Figure 4.7. Full set of waveforms observed for the constant temperature measurement ensemble. The scale bar of 0.1 V_{PP} in the first panel is the peak to peak voltage and applied to the waveforms in all the panels. The first set of six waveforms with higher amplitude in a panel are recorded at the near receiver and the next six with smaller amplitude are measured at the far receiver.

The second ensemble consisted of suites at constant pressures of 1 MPa, 2 MPa, and 5 MPa over temperatures from as low as 7°C to as high as 132°C (Figure 4.8).

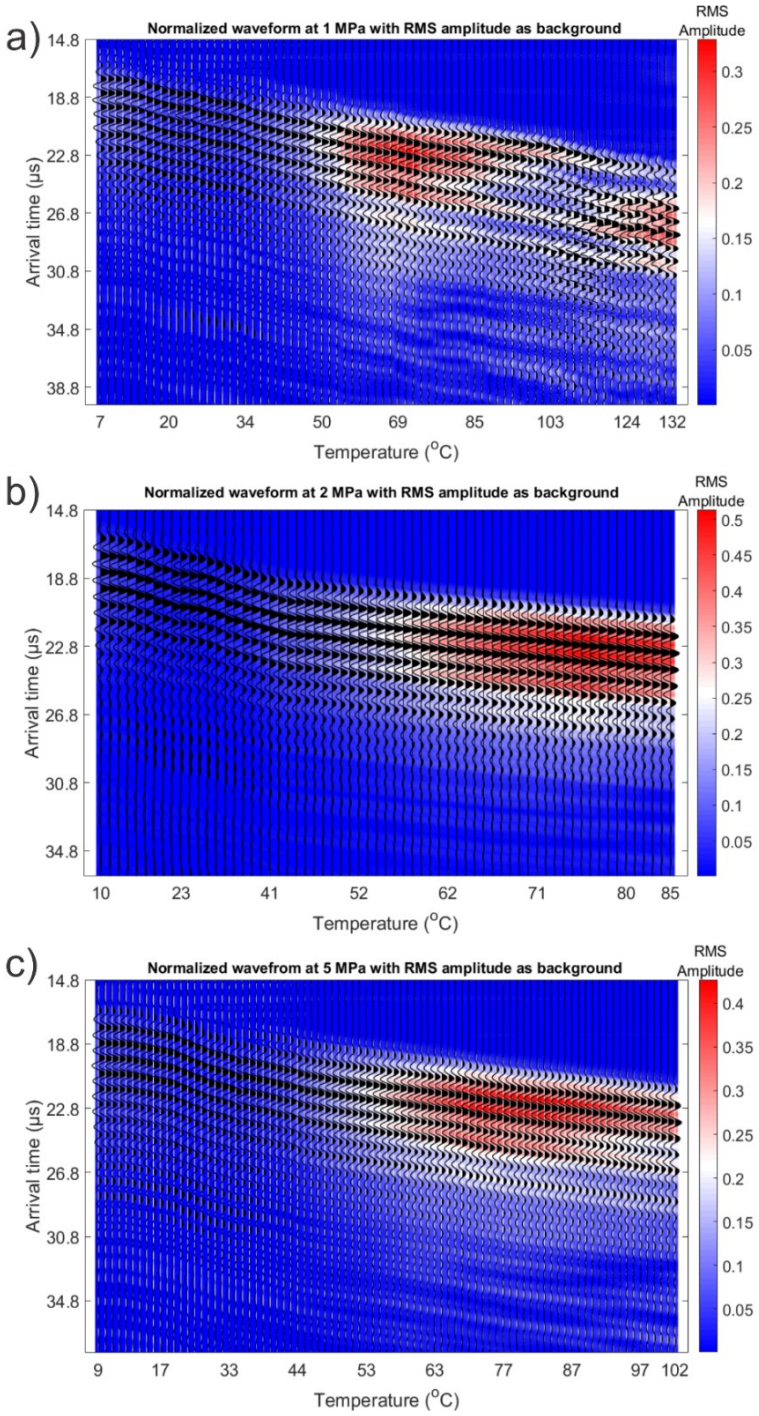

Figure 4.8. Normalized ultrasonic waveforms to the maximum amplitude shown in variable area mode observed for constant pressures suites at a) 1 MPa 7°C to 132°C, b) 2 MPa 10 °C to 85°C, and c) 5 MPa 9°C to 102°C. Background colors indicate the moving root-mean-square (RMS) amplitude calculated for each 10 samples along a trace at each temperature.

The inconsistent temperature range at various pressure are due to technical limitation related to the heating/cooling systems. Unfortunately, the far receiver failed at the beginning of this ensemble and the only waveforms available in Figure 4.8 are for the near receiver.

4.5.2 Constant Temperature Ensemble and Complex Moduli

The wave speeds observed in the first constant temperature ensemble (Figure 4.9a) illustrate their dramatic changes with temperature and, less so, with pressure; these results are in good agreement with earlier observations of many researchers mentioned earlier. As the waveforms of Figure 4.7 suggest, there is also considerable variability in the observed amplitude ratios with temperature but at constant temperature the ratio between the far $A(x_2)$ and near $A(x_1)$ amplitudes remain nearly unchanged across the range of pressures (Figure 4.9b). This consistency provides some confidence of the consistency of the amplitude measurements although we remain concerned with their accuracy. $A(x_2)/A(x_1)$ initially increases rapidly with temperature with the rate of change decreasing above 51°C and with values for the 63°C and 71°C suites being nearly the same. The ratio drops substantially by 81°C suggesting that the attenuation may again increase. The constant pressure waveforms (Figure 4.8), too, show decreased received amplitudes at the higher temperatures that may be consistent with increased attenuation at greater temperatures. The attenuation coefficients calculated directly using the amplitude ratios (Figure 4.9c) fall between 20 m^{-1} and 100 m^{-1} further indicating the attenuating nature of the bitumen. For purposes of comparison, the attenuation of water at 20°C is $\alpha \sim 0.025$ m^{-1} at 1 MHz (Krautkrämer and Krautkrämer, 1990).

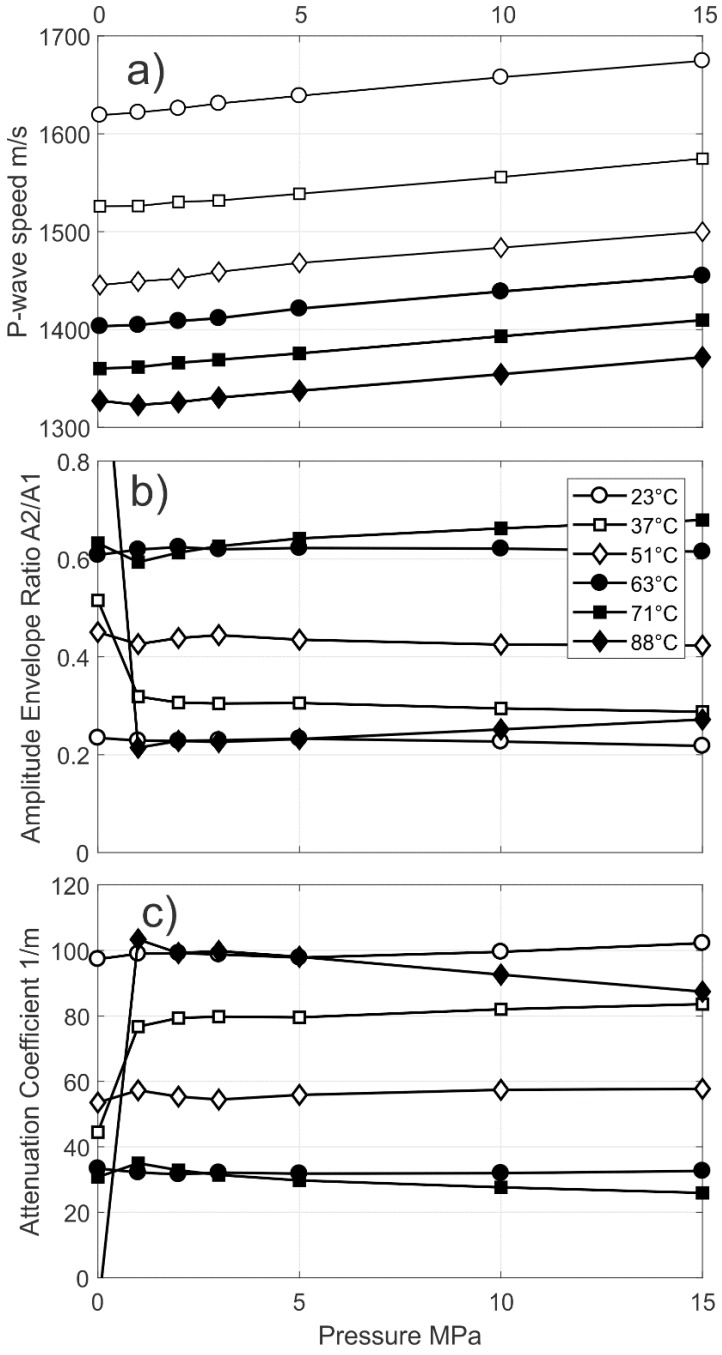

Figure 4.9. Constant temperature ensemble results versus pressure. a) Average of the wave speeds determined using the far and near receivers. Typically, the wave speeds obtained from the two receivers differed by a maximum of 0.5% such that the uncertainty of the measurements is much smaller than the height of the symbols. b) Ratio of the far to the near receiver amplitudes A_2/A_1. c) Attenuation coefficient α calculated using amplitude ratios of b). Symbols have same meaning in all of the panels as defined by the legend in b).

The real *M'* and imaginary *M"* parts of the longitudinal moduli are then calculated using Eqn. 4 and Eqn. 5, respectively, and the values for the 1 MPa measurements shown in Figure 4.10a. The corresponding values for *G'* (in GPa) are calculated using the empirically derived expressions for the storage

$$G'(T) = \exp\left[\frac{6900}{T + 273.15} - 24.36\right] \tag{11}$$

and loss

$$G''(T) = \exp\left[\frac{8133}{T + 273.15} - 29.55\right] \tag{12}$$

shear moduli where T is in °C both produced from the fits of an Arrhenius-like function to the observed values obtained from ultrasonic (~1 MHz) shear reflectivity reported on this same bitumen in Rabbani and Schmitt, 2018. The bulk moduli are then simply the differences $K' = M' - 4G'/3$ and $K'' = M'' - 4G''/3$ as indicated in Eqn. 6. *G'* is a significant component of *M'* at the lowest temperatures but its effect is substantially diminished by 70°C above which the bitumen likely could be considered to be a viscous liquid. It is interesting to further note in Figure 4.10b that *K"* is the dominant component of *M"* above 50°C; if these results are valid it means that the bulk viscosity η_V may be the most important component of the P-wave attenuation through the bitumen.

The results of Figure 4.10 clearly demonstrate the P-wave modulus *M** retains a nonnegligible shear component even to temperatures in excess of 50°C. One implication of this is that assuming measurement of the P-wave velocity together with the mass density of the 'fluid' can be used to directly calculate the fluid bulk modulus K_f is not always valid. Strictly, it is the longitudinal modulus M_f that is determined and K_f can only be calculated if the appropriate value for G_f is available. Otherwise ignoring this means that the value of K_f used may be too large.

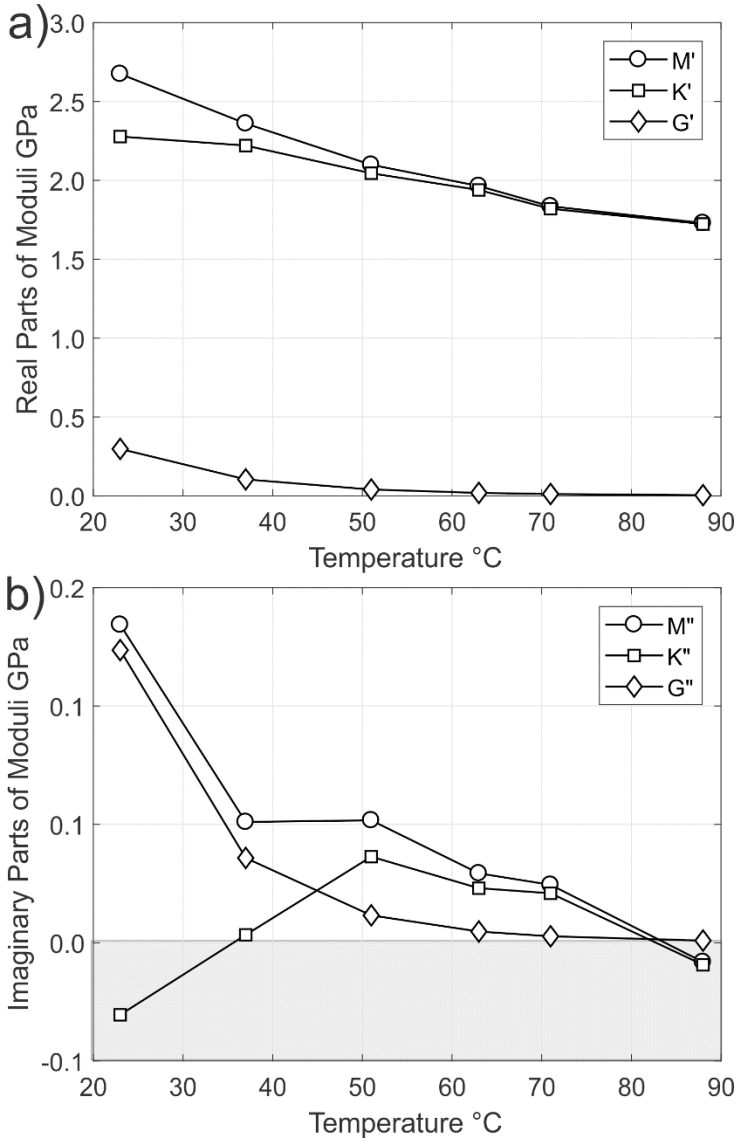

Figure 4.10. Temperature dependence at 1 MPa pressure of a) the real components *M',* *K',* and *G',* and b) the imaginary components *M", K", and G".* Gray shaded area represents physically disallowed values.

As noted we deferred from calculating the bulk viscosity η_V' directly from *K"* but examination of Figure 4.10b may provide some indication of its temperature dependent behaviour relative to the shear viscosity η_S'. Ignoring the nonphysical results at lower temperature, *K"* is higher than *G"* indicating that their ratio $\eta_V'/\ \eta_S' > 1$ particularly for temperature from 50°C to 70°C. Although he was not able to obtain measures of attenuation α that are necessary in ultimately calculating $\eta_V'/\ \eta_S'$, Eastwood (1993)

inferred from assumptions about the frequency dispersion relations that $\eta_V' / \eta_S' > 1$ with values increasing from about 2.6 to 36 from 22°C to 57°C.

4.5.3 Constant Pressure Ensemble and Empirical Curves

The second ensemble consists of three suites of velocity measurements each of which was carried out at a constant pressure as temperature was varied. The sampling interval of about 1°C allows the temperature dependent wave speeds *V(T)* to be tracked in some detail (Figure 4.11a).

As might be expected from the above results, the P-wave speed declines rapidly over the range of temperatures studied decreasing, at a constant pressure of 1 MPa, by 28% from 7°C to 132°C. We further calculate an apparent longitudinal modulus $M(T) = \rho(T)V^2(T)$ that is deficient in that we have no knowledge of the attenuation for this ensemble of measurements (Figure 4.11b). This clearly demonstrates a strong thermal control to the wave speeds and moduli of the bitumen; and for purposes of predicting seismic responses it would be useful to have an appropriate description of the bitumen's behaviour.

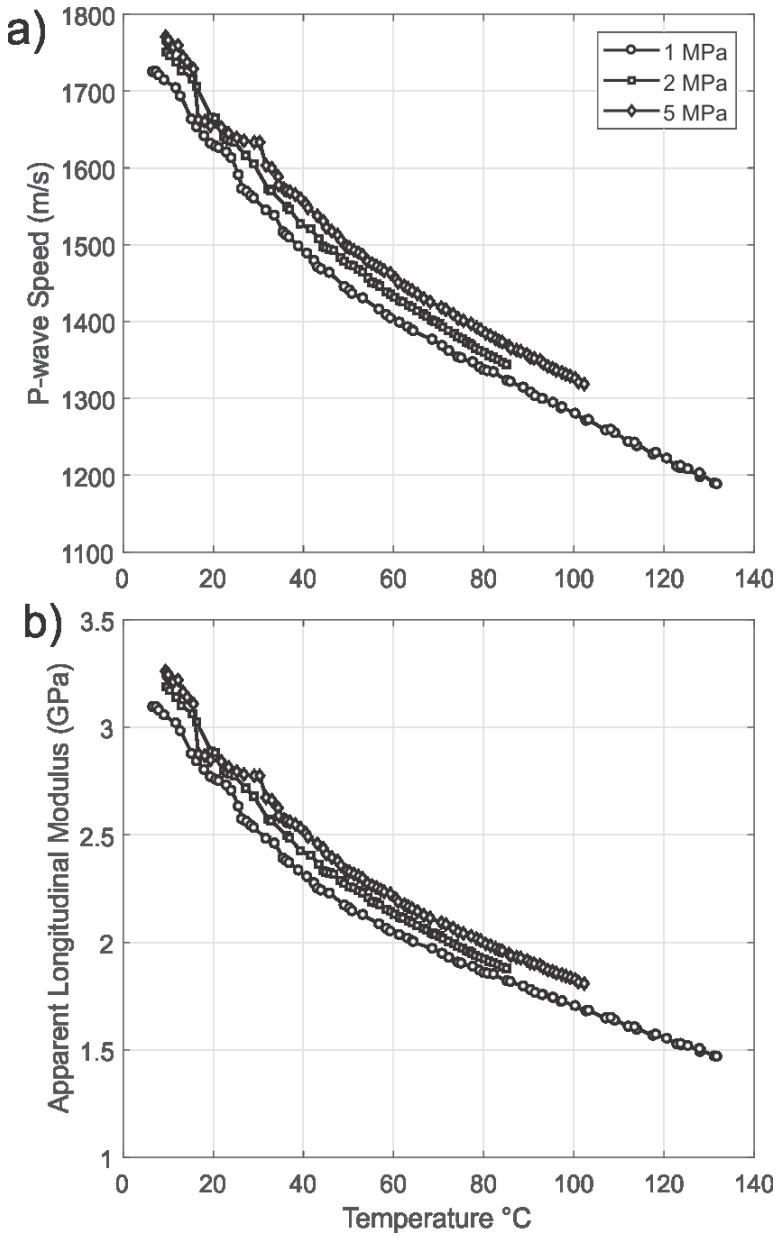

Figure 4.11. a) Observed wave speeds V(T) versus temperature, and b) apparent longitudinal modulus *M(T)* versus 1/T (°K) for the suites of data collected at the constant pressures of 1 MPa (circles), 2 MPa (squares), and 5 MPa (diamonds).

When studying such thermally modulated kinetic processes, workers in many disciplines will assume that the thermal dependence of the physical property being studied is controlled by kinetic processes at the molecular level. This is perhaps most obvious in describing a fluid's viscosity which depends essentially on the thermal speed

that a given molecule on average moves and the time before it interacts with another molecule which is related to its mean free path, e.g., (Falkovich, 2011) and such concepts have been applied reasonably successfully to the viscosity of heavy oils (e.g. Hinkle et al, 2008). It remains challenging to know the nature of these processes at this scale, and in practice empirical curves are usually employed. There are many alternatives that range from a simple exponential that decays with temperature to more sophisticated formulae used in more homogeneous polymer melts that rely on knowledge of glass transition temperatures such as the Williams-Landel-Ferry model (Williams et al., 1955). Arrhenius-like equations are popular as a base for such empirical descriptions where the temperature is given in °K of the form:

$$M(T) = Ae^{-K/T} \tag{13}$$

with two constants K controlling the processes rate and A controlling the magnitude. It is important to note that Arrhenius equation mainly represents a transport phenomenon (e.g., viscosity), where the constant K is more usually given in terms of the ratio of an activation energy E_a to the universal gas constant R. But in the interests of simplicity we retain here only the constant K as a positive number as we are interested primarily in finding an appropriate fitting function. We chose this model as it provided a better, but still imperfect, fit to *M(T)* than a decaying exponential and because the complexity of the bitumen phase behaviour (i.e. with multiple phase transformations) relative to polymers does not warrant use of the more complicated equations. However, we remind the readers that modulus is an equilibrium function not a diffusion phenomenon. Although, there is relation between the modulus and the viscosity (transport function), one might not find much of a physical sense by Arrhenius fitting to *M(T)*. The Arrhenius-like Eqn. 13 is readily linearized

$$\ln\left[M(T)\right] = \ln(A) + K/T \tag{14}$$

that when plotted in *ln(M(T))* vs *1/T* space can be fit by a line with slope *K* and intercept *ln(A)* allowing these constants to be found. This is done in for each of the three suites at different constant pressures (Figure 4.12) together with their corresponding linear fits with the resulting values of *A* and *K* in Table 4.2 for the three different pressures. Each of the fits appears with a high value of the correlation coefficient r^2 but examination of the resulting fits in Figure 4.12 suggest that some care may need to be taken when interpreting these fits as the actual data diverge from the trend. Such deviations should not be surprising particularly as use of Eqn. 14 assumes that the behaviour of the system is controlled by a single process in contrast to bitumen where a number of different processes compete with one another. Although additional work would be necessary, these deviations that oscillate around the Arrhenius-like fit indicate distinct variations in the bitumen's physical properties that might provide an additional tool to study the bitumen's subtle and complex phase transformation behaviour. The rationale for this is, as mentioned earlier, a phase transition in the material will be manifest by changes in the physical properties of which the moduli would be included. Deviations from the thermally controlled Arrhenius-like function could consequently be indicative of such changes and supplement the standard and difficult to interpret DSC methods described earlier. This may not be crucial to finding from the point of view of arriving at values that may be appropriate for fluid substitution analyses, however, the Arrhenius-like equation is one predictor for bitumen's temperature dependent modulus.

Table 4.2. Arrhenius fit constants for the three constant pressure suites for *M(T)*.

Pressure (MPa)	Pre-exponential *A* (GPa)	Slope *K* (K)	Correlation Coefficient r^2
1	0.289	657.6	0.998
2	0.257	706.9	0.997
5	0.310	657.3	0.996

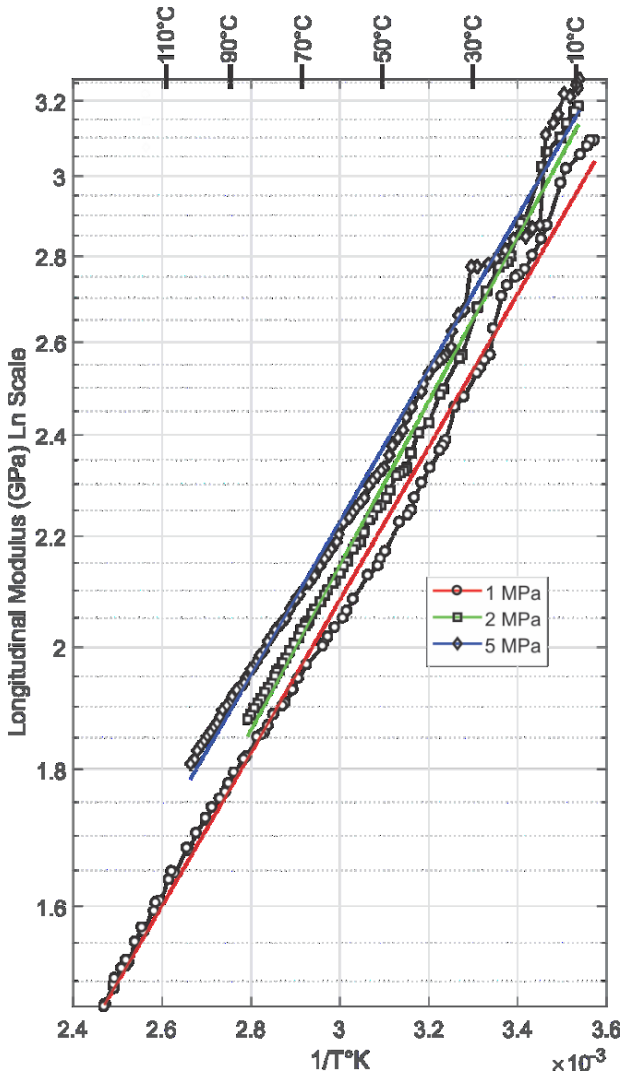

Figure 4.12. Arrhenius plot of the apparent longitudinal modulus (see Fig. Yb) versus the reciprocal absolute temperature (1/°K) for the three suites of data obtained at constant pressures of 1 MPa (circles), 2 MPa (squares), and 5 MPa (diamonds) with

respective linear fits represented by red, green, and blue lines, respectively. Equivalent temperatures in °C shown at the top axis for comparison.

4.5.4 Implications for Modelling of Seismic Responses

Due to their relative simplicity, Gassmann (1951) relations are widely employed in fluid substitution studies for the saturated bulk modulus K_{sat} of a rock with porosity ϕ with drained frame modulus K_d composed of a mineral with bulk modulus K_s filled with an inviscid fluid of bulk modulus K_f

$$K_{sat} = K_d + \frac{\alpha^2}{\frac{\phi}{K_f} - \frac{\alpha - \phi}{K_s}} \tag{15}$$

where $\alpha = 1 - K_d/K_s$, and saturated shear modulus G_{sat}

$$G_{sat} = G_d \tag{16}$$

where G_d is the drained frame's shear modulus. K_{sat} as given by Eqn. 15 is derived assuming static loading (i.e. zero frequency) and is assumed in practice to adequately represent the behaviour at the frequencies used (<200 Hz) in seismic exploration.

In addition to this, many authors have noted that the popular Eqn. 16 fails in many cases and in particular with viscous heavy oils. Illustrating with examples from the literature, Gibiansky and Torquato (1998) have noted, however, that Eqns. 15-16 require the pore fluid pressure to remain uniform but since this is usually not the case in the pore networks of real rocks that often contain compressible microcrack porosity the Gassmann relations should only be considered as providing a lower bound estimate. This limitation of real rocks also constrains the applicability of Biot's (1956) equations that incorporate particle motion of the fluid relative to the solid as modulated by a number of factors including the fluid's shear viscosity. More germane to this discussion, many authors have noted that the semi-solid nature of the bitumen itself disqualifies

Eqn. 15-16 and the related Biot relations as appropriate predictors of that saturated material moduli.

Other workers, too, have remarked that these equations strictly do not apply for a viscoelastic 'fluid' or a 'quasi-solid' and, usually in the context of heavy oils, have developed alternative descriptions. Ciz and Shapiro (2007) extended Brown and Korringa (1975) theory to the case where the pore fluid is replaced by a elastic solid 'infill' of bulk K_{if} and shear G_{if} moduli whereupon

$$K_{sat} = \left[\frac{1}{K_d} - \frac{\left(\alpha / K_d\right)^2}{\frac{\phi}{K_{if}}\left(1 - K_{if}/K_\phi\right) + \frac{\alpha}{K_d}} \right]^{-1} \tag{17}$$

and

$$G_{sat} = \left[\frac{1}{G_d} - \frac{\left(1/G_d - 1/G_s\right)^2}{\phi\left(1/G_{if} - 1/G_\phi\right) + 1/G_d - 1/G_s} \right]^{-1} \tag{18}$$

which requires the Brown and Korringa's penalty of additional knowledge of the bulk K_ϕ and shear G_ϕ moduli of the pore space of the frame. These latter moduli are still rarely measured and in practice workers usually assume $K_\phi \rightarrow K_s$ and $G_\phi \rightarrow G_s$ which is the limiting case achieved only for an micro-homogeneous monomineralic rock frame (Brown and Korringa, 1975). Some limitations on the applicability of Eqns. 17-18 are noted in the literature. Ke et al. (2012) suggest that it applies only to cases in which the contrast between the frame and infill solids are less than 40%. Saxena et al. (2013) point out that these equations apply to a particular case of stiff ellipsoidal pores and may in some cases fall outside of the Hashin-Shtrikhman bounds.

Saxena et al. (2016) developed an alternative description with (see also Chapter 3)

$$K_{sat} = K_{bc} + \frac{\left(1 - \frac{K_{bc}}{K_s}\right)^2}{\frac{\varphi}{K_f} + \frac{1-\varphi}{K_s} - \frac{K_{bc}}{(K_s)^2}} \tag{19}$$

where,

$$K_{bc} = \frac{(1-\varphi)\left(\frac{1}{K_s} - \frac{1}{K_d}\right) + \frac{3\varphi}{4}\left(\frac{1}{K_s} - \frac{1}{G_f}\right)}{\frac{1}{K_s}\left(\frac{1}{K_s} - \frac{1}{K_d}\right) + \frac{3\varphi}{4}\left(\frac{1}{G_s K_s} - \frac{1}{G_f K_d}\right)}$$

and

$$G_{sat} = G_{bc} + \frac{\left(1 - \frac{G_{bc}}{G_s}\right)^2}{\frac{\varphi}{G_f} + \frac{1-\varphi}{G_s} - \frac{G_{bc}}{(G_s)^2}} \tag{20}$$

where,

$$G_{bc} = \frac{(1-\varphi)\left(\frac{1}{G_s} - \frac{1}{G_d}\right) + \varphi\left(\frac{1}{\zeta_s} - \frac{1}{\zeta_f}\right)}{\frac{1}{G_s}\left(\frac{1}{G} - \frac{1}{G_d}\right) + \varphi\left(\frac{1}{\zeta_s G_s} - \frac{1}{\zeta_f G_d}\right)}$$

with

$$\zeta_f = \frac{G_f\left(9K_f + 8G_f\right)}{6\left(K_f + 2G_f\right)}$$

Numerous workers have attempted to address this issue using different calculation strategies that, for the most part, attempt to incorporate knowledge of the heavy oil's shear modulus and shear viscosity. Some attempts have used adaptations of Biot's (1956) models (e.g. (Carcione and QuirogaGoode, 1996; Tsiklauri and Beresnev, 2003) ignoring the frequency dependencies in the fluid moduli and viscosity. The coherent-potential approximation method (Berryman, 1980) has been used by a number of authors (Gurevich et al., 2008; Bown and Schmitt, 2010; Makarynska et al., 2010;

Shamsa and Lines, 2015) calculate dispersion using knowledge of shear viscosity dispersion curves from experiments or as predicted using expected models for dispersion (e.g. Cole-Cole). Numerical schemes at different scales (e.g. (Saenger et al., 2011; Wang et al., 2017b) have used frequency dispersive shear viscosities based on a Maxwell-type dispersive model. Using estimates of the real part of the shear modulus obtained from difficult shear wave propagation measurements through heavy oils discussed in Hinkle et al. (2008), Das and Batzle (2008) tested empirical combinations of the Hashin-Shtrikman bounds and the Ciz and Shapiro (2007) relations above, after adjusting several of their input variables they were able to obtain velocity versus frequency dispersion curves that mimicked those observed. Yuan et al. (2017) apply both Eqns. 15-18 to Athabasca oil sands incorporating temperature dependent values of K_f and G_f estimated from a proprietary model, the lack of knowledge of frame moduli complicated these analyses. Ke et al (2010, 2012) use low frequency complex rheological determinations of the shear viscosity and ultrasonic velocities in what they refer to as a fractional gradient model that allows them to predict the frequency dependent shear modulus of bitumen, this data is then used within an iterative implementation of the Hashin-Shtrikman bounds to fit geophysical log and laboratory data.

A theme common to all of the above studies is that they use knowledge of the shear viscosity or the complex shear modulus either directly or in the construction of a model the bitumen's modulus dispersion. To our knowledge, only Eastwood (1993) incorporated at ultrasonic frequencies a complex bulk modulus K^* which would accordingly include a bulk viscosity η_V'. Given the evidence above and in Eastwood (1993) that η_V' is nonnegligible suggests that it may be just as if not more important that the shear viscosity η_S' in controlling the attenuation of seismic waves.

4.7 Conclusions

The longitudinal P-wave speeds and attenuations were measured through a bitumen sample produced from the Grosmont Formation at temperatures from 10°C to 130 °C and pressures from 0.1 MPa to 15 MPa using a specially developed dual receiver system. Significant declines in the wave speeds over this temperature range were observed in agreement with earlier studies. The P-wave attenuation, too, declined monotonically with temperature although this trend appeared to reverse at the highest temperatures. Changes in pressure weakly affect the wave speeds but do not appear to influence the attenuation. Combining these results with complex shear modulus measurements from a parallel study suggest that the shear modulus is a significant portion of the P-wave modulus at temperatures below ~60°C and reinforces that the P-wave speed cannot be used in isolation to provide the bitumen bulk modulus. A corollary issue is that the bulk modulus determined from the complex longitudinal P-wave modulus M^* and the shear modulus G^* is also complex; this suggests that proper modelling of seismic responses through heavy oil saturated formations may require consideration of the bitumen's *K"* or equivalently its bulk viscosity η_V'.

The temperature dependent wave speeds were also densely measured at constant pressures. These data largely, but not perfectly, can be fit by an Arrhenius-like function. Deviations from the Arrhenius function might be sensitive indicators of various complicated phase transitions taking place within the bitumen. From the perspective of providing empirical measures of the bitumen moduli in seismic fluid substitution analyses, however, the Arrhenius-like function would be adequate in providing measures for substitutional analysis.

Working with a complicated 'fluid' such as bitumen is challenging; and future work will endeavour to improve the reliability of the experimental apparatus. Another key issue that cannot be addressed in this study is the influence of dispersion of the complex

moduli with frequency. Indeed, as reiterated by Spencer (2013), at frequencies around ~100 Hz using standard rheometers $|G^*|$ ~ 1 MPa which is orders of magnitude lower than values ~0.5 GPa obtained from ultrasonic methods, although part of this discrepancy may be due to large differences in total strains and strain rates between rheometers and ultrasonic techniques (e.g. Rodriques and Batzle, 2015). Towards this end, having independent measurements of the complex bulk modulus of bitumen at seismic frequencies may be necessary to resolve this issue.

References

Abivin, P., S. D. Taylor, and D. Freed. 2012, Thermal Behavior and Viscoelasticity of Heavy Oils. Energy & Fuels, **26**, no. 6,3448-3461. doi: 10.1021/ef300065h.

AER. 2018, ST98-2016: Alberta's Energy Reserves 20156 and Supply/Demand Outlook 2016-2025. Alberta Energy Regulator 2016 [cited February 21, 2018 2018]. Available from http://www.aer.ca/documents/sts/ST98/ST98-2016_Executive_Summary.pdf.

Alig, I., F. Stieber, and S. Wartewig. 1991, Analysis of temperature-dependent longitudinal ultrasonic properties of amorphous polymers. Polymer, **32**, no. 12,2146-2149. doi: 10.1016/0032-3861(91)90038-k.

Arafin, S., A. K. George, and R. N. Singh. 2006, Equation of state of crude oil through temperature dependent ultrasonic measurements. Journal of Geophysics and Engineering, **3**, no. 4,307-313. doi: 10.1088/1742-2132/3/4/002.

Ardakani, E. P., D. R. Schmitt, and T. Bown. 2014, Detailed topography of the Devonian Grosmont Formation surface from legacy high-resolution seismic profiles, northeast Alberta. Geophysics, **79**, no. 4,B135-B149. doi: doi: 10.1190/geo2013-0268.1.

ASTM. 2003, ASTM D2007-03, Standard Test Method for Characteristic Groups in Rubber Extender and Processing Oils and Other Petroleum-Derived Oils by the Clay-Gel Absorption Chromatographic Method. West Conshohocken, PA,: ASTM International.

Bardon, C., L. Barre, D. Espinat, V. Guille, M. H. Li, J. Lambard, J. C. Ravey, E. Rosenberg, and T. Zemb. 1996, The Colloidal Structure of Crude Oils and Suspensions of Asphaltenes And Resins. Fuel Science and Technology International, **14**, no. 1-2,203-242. doi: 10.1080/08843759608947569.

Batzle, M., R. Hofmann, and D.-H. Han. 2006, Heavy oils - seismic properties. The Leading Edge, **25**, no. 6,750-756.

Bazyleva, A., M. Fulem, M. Becerra, B. Zhao, and J. M. Shaw. 2011, Phase Behavior of Athabasca Bitumen. Journal of Chemical and Engineering Data, **56**, no. 7,3242-3253. doi: 10.1021/je200355f.

Bazyleva, A. B., M. D. A. Hasan, M. Fulem, M. Becerra, and J. M. Shaw. 2010, Bitumen and Heavy Oil Rheological Properties: Reconciliation with Viscosity

Measurements. Journal of Chemical & Engineering Data, **55**, no. 3,1389-1397. doi: 10.1021/je900562u.

Berryman, J. G. 1980, Long- wavelength propagation in composite elastic media I. Spherical inclusions. The Journal of the Acoustical Society of America, **68**, no. 6,1809-1819. doi: 10.1121/1.385171.

Bhatia, A. 1967, Ultrasonic absorption. An introduction to the theory of sound absorption and dispersion in gases, liquids, and solids: Oxford University Press.

Bianco, E., S., Kaplan, and D.R. Schmitt. 2010, Seismic rock physics of steam injection in bituminous-oil reservoirs – Chapter 6,in Heavy Oils: Reservoir Characterization and Production Monitoring, eds. Batzle, M., Chopra, S., Lines, L.R., and Schmitt, D.R.: Soc. Expl. Geophysicists, Tulsa, OK, **105-110**.

Boduszynski, M. M., J. F. McKay, and D. R. Latham. 1980, Asphaltenes, where are you? : Proc. Assoc. Asphalt Paving Technol., **49**,123-143.

Bouzidi, Y., and D. R. Schmitt. 2006, A large ultrasonic bounded acoustic pulse transducer for acoustic transmission goniometry: Modeling and calibration. Journal of the Acoustical Society of America, **119**, no. 1,54-64. doi: 10.1121/1.2133683.

Bown, T., and D. R. Schmitt. 2010, Seismic Dispersion in Extra-Heavy Oil Saturated Rock. In GeoCanada 2010. Calgary Canadian Society of Exploration Geophysicists

Brown, R. J. S., and J. Korringa. 1975, Dependence of Elastic Properties of a Porous Rock on Compressibility of Pore Fluid. Geophysics, **40**, no. 4,608-616. doi: 10.1190/1.1440551.

Butler, R. 1991, Thermal recovery of oil and bitumen: Prentice Hall.

Carcione, J. M., and G. QuirogaGoode. 1996, Full frequency-range transient solution for compressional waves in a fluid-saturated viscoacoustic porous medium. Geophysical Prospecting, **44**, no. 1,99-129. doi: 10.1111/j.1365-2478.1996.tb00141.x.

Ciz, R., and S. A. Shapiro. 2007, Generalization of Gassmann equations for porous media saturated with a solid material. GEOPHYSICS, **72**, no. 6,A75-A79. doi: 10.1190/1.2772400.

Corbett, L. W. 1969, Composition Of Asphalt Based On Generic Fractionation Using Solvent Deasphaltening Elution-Adsorption Chromatography And Densimetric

Characterization. Analytical Chemistry, **41**, no. 4,576-&. doi: 10.1021/ac60273a004.

Daridon, J. L., A. Lagrabette, and B. Lagourette. 1998, Speed of sound, density, and compressibilities of heavy synthetic cuts from ultrasonic measurements under pressure. Journal of Chemical Thermodynamics, **30**, no. 5,607-623. doi: DOI 10.1006/jcht.1997.0330.

Das, A., and M. Batzle. 2008, Modeling studies of heavy oil—in between solid and fluid properties. The Leading Edge, **27**, no. 9,1116-1123. doi: 10.1190/1.2978973.

Dashti, H. H., and M. R. Riazi. 2014, Acoustic velocities in petroleum fluids: Measurement and prediction. Journal of Petroleum Science and Engineering, **124**,94-104. doi: 10.1016/j.petrol.2014.10.013.

Dutour, S., B. Lagourette, and J. L. Daridon. 2001, High-pressure speed of sound and compressibilities in heavy normal hydrocarbons: n-C23H48 and n-C24H50. Journal of Chemical Thermodynamics, **33**, no. 7,765-774. doi: 10.1006/jcht.2000.0793.

Dutour, S., B. Lagourette, and J. L. Daridon. 2002, High-pressure speed of sound, density and compressibility of heavy normal paraffins: C28H58 and C36H74. Journal of Chemical Thermodynamics, **34**, no. 4,475-484. doi: 10.1006/jcht.2001.0922.

Eastwood, J. 1993, Temperature-Dependent Propagation Of P-Waves And S-Waves In Cold Lake Oil Sands - Comparison Of Theory And Experiment. Geophysics, **58**, no. 6,863-872. doi: 10.1190/1.1443470.

Eastwood, J., P. Lebel, A. Dilay, and S. Blakeslee. 1994, Seismic monitoring of steam-based recovery of bitumen. The Leading Edge, **13**, no. 4,242-251. doi: 10.1190/1.1437015.

Espinat, D., E. Rosenberg, M. Scarsella, L. Barre, D. Fenistein, and D. Broseta. 1998, Colloidal Structural Evolution from Stable to Flocculated State of Asphaltene Solutions and Heavy Crudes, in Oliver C. Mullins and Eric Y. Sheu, eds., Structures and Dynamics of Asphaltenes: Springer US. 145-201.

Evdokimov, I. N., and A. P. Losev. 2010, Electrical Conductivity and Dielectric Properties of Solid Asphaltenes. Energy & Fuels, **24**, no. 7,3959-3969. doi: 10.1021/ef1001887.

Falkovich, G. 2011, Fluid Mechanics: A short course for physicists: Cambrige University Press.

Fazelabdolabadi, B., and A. Bahramian. 2012, Acoustic determination of the heavy oil thermophysical properties: Thermodynamic consistency revisited. Fuel, **102**,49-53. doi: 10.1016/j.fuel.2012.06.106.

Fenistein, D., and L. Barré. 2001, Experimental measurement of the mass distribution of petroleum asphaltene aggregates using ultracentrifugation and small-angle X-ray scattering. Fuel, **80**, no. 2,283-287. doi: https://doi.org/10.1016/S0016-2361(00)00072-7.

Ganeeva, Y. M., T. N. Yusupova, G. V. Romanov, and N. Y. Bashkirtseva. 2014, Phase composition of asphaltenes. Journal of Thermal Analysis and Calorimetry, **115**, no. 2,1593-1600. doi: 10.1007/s10973-013-3442-3.

Gassmann, F. 1951, Über die Elastizität poroser Medien. Vierteljahrsschrift der Naturforschenden Gesellschaft in Zürich, **96**,1-23.

George, A. K., N. Al-Majrafi, R. N. Singh, and S. Arafin. 2008, Thermo-elastic and thermodynamic properties of light and heavy crude oil. Physics and Chemistry of Liquids, **46**, no. 3,328-341. doi: 10.1080/00319100701458931.

Gibiansky, L., and S. Torquato. 1998, Rigorous connection between physical properties of porous rocks. Journal of Geophysical Research-Solid Earth, **103**, no. B10,23911-23923. doi: 10.1029/98jb02340.

Giles, H. N. 2016, Crude Oil Analysis: History and Development of Test Methods From 1854 to 2016. Materials Performance and Characterization, **5**, no. 2,1-169. doi: 10.1520/mpc20160056.

Gurevich, B., K. Osypov, R. Ciz, and D. Makarynska. 2008, Modeling elastic wave velocities and attenuation in rocks saturated with heavy oil. Geophysics, **73**, no. 4,E115-E122. doi: 10.1190/1.2940341.

Han, D. h., J. Liu, and M. Batzle. 2006, Acoustic property of heavy oils - measured data. In SEG Technical Program Expanded Abstracts 2006. New Orleans: Socieity of Exploration Geophysicists.

Han, D. h., J. Liu, and M. Batzle. 2008, Velocity and dispersion of heavy oils. In SEG Technical Program Expanded Abstracts 2008.

Herzfeld, K. F., and T. A. A. Litovitz. 1959, Absorption and dispersion of ultrasonic waves.: Academic Press.

Hinkle, A., E. J. Shin, M. W. Liberatore, A. M. Herring, and M. Batzle. 2008, Correlating the chemical and physical properties of a set of heavy oils from around the world. Fuel, **87**, no. 13-14,3065-3070. doi: 10.1016/j.fuel.2008.04.018.

Isaac, J. H., and D. C. Lawton. 2006, A case history of time-lapse 3D seismic surveys at Cold Lake, Alberta, Canada. Geophysics, **71**, no. 4,B93-B99. doi: 10.1190/1.2211027.

Kariznovi, M., H. Nourozieh, and J. Abedi. 2014, Measurement and Correlation of Viscosity and Density for Compressed Athabasca Bitumen at Temperatures Up to 200 degrees C. Journal of Canadian Petroleum Technology, **53**, no. 6,330-338.

Kato, A., S. Onozuka, and T. Nakayama. 2008, Elastic property changes in a bitumen reservoir during steam injection. The Leading Edge, **27**, no. 9,1124-1131. doi: 10.1190/1.2978974.

Ke, G., M. Johnston, and H. Dong. 2012, Rock-physics models for bitumen-saturated sands: Fractional gradient model and Hashin-Shtrikman iterative model. GEOPHYSICS, **77**, no. 2,D7-D15. doi: 10.1190/geo2011-0338.1.

Khelladi, H., F. Plantier, and J. L. Daridon. 2010, A phase comparison technique for sound velocity measurement in strongly dissipative liquids under pressure. Journal of the Acoustical Society of America, **128**, no. 2,672-678. doi: 10.1121/1.3455857.

Krautkrämer, J., and H. Krautkrämer. 1990, Ultrasonic testing of materials: Springer-Verlag.

Kriz, P., J. Stastna, and L. Zanzotto. 2008, Glass Transition and Phase Stability in Asphalt Binders. Road Materials and Pavement Design, **9**, no. sup1,37-65. doi: 10.1080/14680629.2008.9690158.

Larter, S., J. Adams, I. D. Gates, B. Bennett, and H. Huang. 2008, The origin, prediction and impact of oil viscosity heterogeneity on the production characteristics of tar sand and heavy oil reservoirs. Journal of Canadian Petroleum Technology, **47**, no. 1,52-61. doi: 10.2118/08-01-52.

Laukkanen, O. V., H. H. Winter, H. Soenen, and J. Seppala. 2018, An empirical constitutive model for complex glass-forming liquids using bitumen as a model material. Rheologica Acta, **57**, no. 1,57-70. doi: 10.1007/s00397-017-1056-6.

Lesueur, D. 2009, The colloidal structure of bitumen: Consequences on the rheology and on the mechanisms of bitumen modification. Advances in Colloid and Interface Science, **145**, no. 1-2,42-82. doi: 10.1016/j.cis.2008.08.011.

Li, W., D. R. Schmitt, C. Zou, and X. Chen. 2018, A program to calculate pulse transmission responses through transversely isotropic media. Computers & Geosciences, **114**,59-72. doi: https://doi.org/10.1016/j.cageo.2018.02.002.

Lionetto, F., and A. Maffezzoli. 2008, Polymer Characterization by Ultrasonic Wave Propagation. Advances in Polymer Technology, **27**, no. 2,63-73. doi: 10.1002/adv.20124.

Makarynska, D., B. Gurevich, J. Behura, and M. Batzle. 2010, Fluid substitution in rocks saturated with viscoelastic fluids. Geophysics, **75**, no. 2,E115-E122. doi: 10.1190/1.3360313.

Mansoori, G. A. 2009, A unified perspective on the phase behaviour of petroleum fluids. International Journal of Oil Gas and Coal Technology, **2**, no. 2,141-167. doi: 10.1504/ijogct.2009.024884.

Marvin, R. S., and J. E. McKinney. 1965, 9 - Volume Relaxations in Amorphous Polymers, in Warren P. Mason, ed., Physical Acoustics: Academic Press. 165-229.

Masson, J. F., G. Polomark, and P. Collins. 2005, Glass transitions and amorphous phases in SBS-bitumen blends. Thermochimica Acta, **436**, no. 1-2,96-100. doi: 10.1016/j.tca.2005.02.017.

Mochinaga, H., S. Onozuka, F. Kono, T. Ogawa, A. Takahashi, and T. Torigoe. 2006, Properties of Oil sands and Bitumen in Athabasca. In 2006 CSPG-CSEG-CWLS Convention. Calgary.

Molyneux, J. B., and D. R. Schmitt. 2000, Compressional-wave velocities in attenuating media: A laboratory physical model study. Geophysics, **65**, no. 4,1162-1167. doi: 10.1190/1.1444809.

Nguyen, N. T., M. Lethiecq, and J. F. Gerard. 1995, Glass-Transition Characterization Of Homogeneous And Heterogeneous Polymers By An Ultrasonic Method. Ultrasonics, **33**, no. 4,323-329. doi: 10.1016/0041-624x(95)98709-l.

Oconnell, R. J., and B. Budiansky. 1978, MEASURES OF DISSIPATION IN VISCOELASTIC MEDIA. Geophysical Research Letters, **5**, no. 1,5-8. doi: 10.1029/GL005i001p00005.

Pfeiffer, J. P., and R. N. J. Saal. 1940, Asphaltic Bitumen as Colloid System. The Journal of Physical Chemistry, **44**, no. 2,139-149. doi: 10.1021/j150398a001.

Plantier, F., D. Bessieres, J. L. Daridon, and F. Montel. 2008, Structure and thermodynamic consistency of heavy oils: A study on the basis of acoustic measurements. Fuel, **87**, no. 2,196-201. doi: 10.1016/j.fuel.2007.04.008.

Read, J., and D. Whiteoak. 2003, The Shell Bitumen Handbook, The Shell Bitumen Handbook: Thomas Telford Ltd: London.

Rabbani, A., D. R. Schmitt. 2014, A laboratory procedure of measuring ultrasonic properties of CO2 saturated fluids, SEG abstract.

Rabbani, A., D. R. Schmitt, J. Nycz, and K. Gray. 2017, Pressure and temperature dependence of acoustic wave speeds in bitumen-saturated carbonates: Implications for seismic monitoring of the Grosmont Formation. GEOPHYSICS, **82**, no. 5,MR133-MR151. doi: 10.1190/geo2016-0667.1.

Rabbani, A. and D. R. Schmitt. 2018, Ultrasonic Shear Wave Reflectometry Applied to the Determination of the Shear Moduli and Viscosity of a Viscoelastic Bitumen. FUEL (accepted).

Redelius, P., and H. Soenen. 2015, Relation between bitumen chemistry and performance. Fuel, **140**,34-43. doi: https://doi.org/10.1016/j.fuel.2014.09.044.

Rodrigues, P. E., and M. L. Batzle. 2015, Strain amplitude dependence of shear modulus in heavy oils: Rheometer versus tension/compression technique. Geophysics, **80**, no. 4,L35-L43. doi: 10.1190/geo2014-0354.1.

Russel-Houston, J., and K. Gray. 2014, Paleokarst in the Grosmont Formation and reservoir implications, Saleski, Alberta, Canada. Interpretation, **2**, no. 3,SF29-SF50. doi: 10.1190/int-2013-0187.1.

Saenger, E. H., F. Enzmann, Y. Keehm, and H. Steeb. 2011, Digital rock physics: Effect of fluid viscosity on effective elastic properties. Journal of Applied Geophysics, **74**, no. 4,236-241. doi: 10.1016/j.jappgeo.2011.06.001.

Saxena, N., G. Mavko, R. Hofmann, B. Gurevich, S. Glubokovskikh, S. Aliyeva, and P. Dutta. 2016, Rock-physics models for heavy-oil and organic-solid substitution. The Leading Edge, **35**, no. 6,506-510. doi: 10.1190/tle35060506.1.

Saxena, N., G. Mavko, and T. Mukerji. 2013, Change in effective bulk modulus upon fluid or solid substitution. Geophysics, **78**, no. 4,L45-L56. doi: 10.1190/geo2012-0065.1.

Schmitt, D. R. 1999, Seismic attributes for monitoring of a shallow heated heavy oil reservoir: A case study. Geophysics, **64**, no. 2,368-377. doi: 10.1190/1.1444541.

Shamsa, A., and L. Lines. 2015, Effect of oil composition on fluid substitution in heavy oil reservoirs. Geophysical Prospecting, **63**, no. 2,422-441. doi: 10.1111/1365-2478.12147.

Silva, S. L., A. M. S. Silva, J. C. Ribeiro, F. G. Martins, F. A. Da Silva, and C. M. Silva. 2011, Chromatographic and spectroscopic analysis of heavy crude oil mixtures

with emphasis in nuclear magnetic resonance spectroscopy: A review. Analytica Chimica Acta, **707**, no. 1,18-37. doi: 10.1016/j.aca.2011.09.010.

Singer, J. R. 1969, Excess Ultrasonic Attenuation And Volume Viscosity In Liquid Methane. Journal of Chemical Physics, **51**, no. 11,4729-&. doi: 10.1063/1.1671860.

Spencer, J. W. 2013, Viscoelasticity of Ells River bitumen sand and 4D monitoring of thermal enhanced oil recovery processes. Geophysics, **78**, no. 6,D419-D428. doi: 10.1190/geo2012-0535.1.

Tahani, H. 2011, Determination of the velocity of sound in reservoir fluids using an equation of state, Heriot-Watt University.

Tausk, R. J. M., and P. N. Wilson. 1981, Colloid chemical studies on bitumen-in-water emulsions part I. absorption of water in the bitumen droplets and other factors affecting emulsion viscosity. Colloids and Surfaces, **2**, no. 1,71-80. doi: https://doi.org/10.1016/0166-6622(81)80054-6.

Tsiklauri, D., and I. Beresnev. 2003, Properties of elastic waves in a non-Newtonian (Maxwell) fluid-saturated porous medium. Transport in Porous Media, **53**, no. 1,39-50. doi: 10.1023/a:1023559008269.

Van Nellensteyn, F. J. 1923, Bereiding en constitutie van asphalt.

Verdier, C., P. Y. Longin, and M. Piau. 1998, Dynamic shear and compressional behavior of polydimethylsiloxanes: Ultrasonic and low frequency characterization. Rheologica Acta, **37**, no. 3,234-244. doi: 10.1007/s003970050111.

Verrall, R. E., G. A. Heal, and K. L. Dyer. 1994, Sound-velocity studies of pipeline oils as a function of viscosity, density and water-content. Journal of Canadian Petroleum Technology, **33**, no. 2,51-57.

Wada, Y., and H. Hirose. 1960, Glass transition phenomena and rheological properties of petroleum asphalt. Journal of the Physical Society of Japan, **15**, no. 10,1885-1894. doi: 10.1143/jpsj.15.1885.

Wada, Y., H. Hirose, T. Asano, and S. Fukutomi. 1959, On the dynamic mechanical properties of polymers at ultrasonic frequencies in relation to their glass transition phenomena. Journal of the Physical Society of Japan, **14**, no. 8,1064-1072. doi: 10.1143/jpsj.14.1064.

Wang, W. C. V., E. J. Kramer, and W. H. Sachse. 1982, Effects of high-pressure co2 on the glass-transition temperature and mechanical-properties of polystyrene.

Journal of Polymer Science Part B-Polymer Physics, **20**, no. 8,1371-1384. doi: 10.1002/pol.1982.180200804.

Wang, Z. J., A. M. Nur, and M. L. Batzle. 1990, Acoustic velocities in petroleum oils. Journal of Petroleum Technology, **42**, no. 2,192-200.

Wang, Z. Z., D. R. Schmitt, and R. H. Wang. 2017, Modeling of viscoelastic properties of nonpermeable porous rocks saturated with highly viscous fluid at seismic frequencies at the core scale. Journal of Geophysical Research-Solid Earth, **122**, no. 8,6067-6086. doi: 10.1002/2017jb013979.

Williams, M. L., R. F. Landel, and J. D. Ferry. 1955, Mechanical properties of substances of high molecular weight .19. The temperature dependence of relaxation mechanisms in amorphous polymers and other glass-forming liquids. Journal of the American Chemical Society, **77**, no. 14,3701-3707. doi: 10.1021/ja01619a008.

Yang, D., M. H. Mohebati, S. Brand, and C. Bennett. 2014, Thermal recovery of bitumen from the grosmont carbonate formation - Part 2: Pilot interpretation and development strategy. Journal of Canadian Petroleum Technology, **53**, no. 4,212-223. doi: 10.2118/171561-PA.

Yen, T. F. 1992, The colloidal aspect of a macrostructure of petroleum asphalt. Fuel Science and Technology International, **10**, no. 4-6,723-733. doi: 10.1080/08843759208916018.

Yuan, H., D.-h. Han, H. Li, and W. Zhang. 2017, A comparison of bitumen sands and bitumen carbonates: Measured data. GEOPHYSICS, **82**, no. 1,MR39-MR50. doi: 10.1190/geo2015-0657.1.

Zadeh, H. M., R. P. Srivastava, N. Vedanti, and M. Landro. 2010, Seismic monitoring of in situ combustion process in a heavy oil field. Journal of Geophysics and Engineering, **7**, no. 1,16-29. doi: 10.1088/1742-2132/7/1/002.

Zhang, Y., T. Takanohashi, S. Sato, I. Saito, and R. Tanaka. 2004, Observation of glass transition in asphaltenes. Energy & Fuels, **18**, no. 1,283-284. doi: 10.1021/ef0301147.

Zhao, S. Q., L. S. Kotlyar, B. D. Sparks, J. R. Woods, J. S. Gao, and K. H. Chung. 2001, Solids contents, properties and molecular structures of asphaltenes from different oilsands. Fuel, **80**, no. 13,1907-1914. doi: 10.1016/s0016-2361(01)00044-8.

Chapter 5: Ultrasonic Shear Wave Reflectometry Applied to the Determination of the Shear Moduli and Viscosity of a Viscoelastic Bitumen*

*A version of this chapter is accepted for the publication in FUEL. Rabbani A. and Schmitt D. R., 2018 (Accepted on May 31, 2018).

Ultrasonic shear wave reflectometry is widely used in process control to measure the dynamic shear viscosities of Newtonian liquids. We apply the technique to study the temperature dependence of produced bitumen: a non-Newtonian ultra-heavy 6° API hydrocarbon with a room temperature viscosity of ~10^3 Pa•s. The experimental apparatus employs a delay line made of polyetheretherketone (PEEK) whose shear impedance more closely matches that of the bitumen allowing for greater sensitivity but at the cost of long equilibration wait times. The temperature dependent values of the complex shear modulus and consequent estimates of the steady flow shear viscosity both follow close to an Arrhenius behaviour over the range of 10°C to 50°C, but there are significant discrepancies between the ultrasonic and more conventional spindle viscosities. These may reflect differences between the particle displacements, the strains, and the strain rates associated with each measurement technique. Regardless, these measurements do show that the shear wave reflectometry does provide information on the changes in the viscoelastic bitumen with temperature that may be useful in for purposes of its monitoring during production and processing.

5.1. Introduction

In a Newtonian fluid, the shear stress is linearly proportional to the strain rate via the proportionality constant of the dynamic viscosity. Many low molecular weight liquids and gases, such a molten metals and inorganic salts, and organic and inorganic

liquids and gases, exhibit Newtonian viscous behavior (Chhabra and Richardson, 2008). In contrast, the stress observed in most foams, emulsions, colloidal suspensions and polymeric solutions depend nonlinearly on strain rate; and these are known as non-Newtonian fluids. The apparent viscosity in these depends on the strain being manifest as the phenomena of shear thinning (apparent viscosity decreases with shear rate) or shear thickening (apparent viscosity increases with shear rate).

Bitumen is the generic term used by the American Petroleum Institute to collectively describe ultra-heavy hydrocarbon oils with densities higher than 1000 kg/m^3 and dynamic shear viscosities at the in situ temperature (11°C) as high as ~10^4 Pa•s (Yang et al., 2014; Hamida and Roberts, 2014). The extreme viscosities of bitumen make economic extraction difficult as it cannot flow easily through permeable rock or pipelines. The bitumen used in this study, for example, is natural sample produced from the Grosmont Formation of northern Alberta, Canada where thermal recovery processes are used to reduce the natural oil's viscosity allowing it to flow. Understanding the rheological behavior of these oils and how it changes with temperature (Batzle et al., 2006; Behura et al., 2007; Schmitt, 2004; Bazyleva et al., 2010a; Shamsa and Lines, 2015; Abivin et al., 2012; Svrcek and Mehrotra, 1982; Behzadfar and Hatzikiriakos, 2013) and pressure (Mortazavi-Manesh and Shaw, 2016; Behzadfar and Hatzikiriakos, 2014) is key to the design of efficient extraction processes. Therefore, having advance knowledge of these changes in viscosity is of practical importance in the design of efficient recovery techniques, among other needs.

Knowledge of bitumen's rheological behavior, too, is necessary to properly interpret surface time-lapse geophysical data (Schmitt, 1999; Rojas Luces, 2010) where the changes in seismic wave speeds will for the most part depend on the fluid properties (Rabbani et al., 2017). When considering seismic wave propagation at sufficiently low temperatures (<~50°C), the bitumen may have a nonnegligible shear

modulus (Han, Liu, and Baztle, 2008) that will contribute to the overall frequency-dependent rock elastic properties (Wang et al., 2017a). This information could be vital to the proper interpretation of the angle of incidence variations in seismic reflectivity in attempts to measure in situ attenuation directed towards pore fluid identification e.g., (Chapman et al., 2006; Bouzidi and Schmitt, 2012; Innanen, 2011) although a great deal of care must be taken to properly define this problem e.g., (Krebes, 1984; Krebes and Daley, 2007; Deng and Morozov, 2017).

Reliable determination of bitumen viscosity alone remains problematic for many reasons. Round-robin blind measurements from differing laboratories on carefully collected and presumably uniform samples of the same bitumen have given values differing by more than a factor of two from 36 Pa•s to 72 Pa•s at 20°C (Zhao and Machel, 2012; Miller et al., 2006). Considering only shear viscosity, however, likely masks more complex rheological behavior.

Bazyleva et al. (Bazyleva et al., 2010a) emphasized three critical issues on the viscosity data for such complex multicomponent and multiphase fluid bitumen: the geographical origin of the sample, the environment of the experiments, and the awareness of the limitation or associated error of the techniques. They noted that shear rate has the most substantial impact on the rheological measurements. The complex viscosity of non-Newtonian Athabasca bitumen at the low-temperature is reported to vary as much as three orders or magnitude with shear rate.

Bitumen possesses a small but measurable shear modulus at the lowered temperatures where it has been referred to a quasi-solid (Batzle et al., 2006; Han, Liu, and Baztle, 2008). By examining the changes in shear wave reflectivity from a bitumen over a range of temperatures, Han et al. (Han, Liu, and Baztle, 2008) showed that a measurable shear modulus vanished in their sample at about 60°C. Besides, Bitumen tends to have a broad range of relaxation spectrum due to the presence of various sizes

of molecules (Baumgaertel and Winter, 1989; Gurevich et al., 2008; Behzadfar and Hatzikiriakos, 2013). Hence, the relaxation time, the ratio of viscosity and shear modulus (real) of the medium at high frequency, also depends on the temperature (Nava et al., 1994).

These issues highlight the need to better understand the mechanical behavior of bitumen and to estimate viscosity and shear modulus. Towards this end, we describe the further development of an ultrasonic shear wave reflectometer. This method, first described by Mason et al. (Mason et al., 1949), has been used quantitatively and qualitatively to measure the dynamic shear properties of a variety of complex fluids with applications to the setting of concrete (Popovics and Subramaniam, 2015) and asphalt (Zavrtanik et al., 2017), foodstuffs such as honey (Gasparoux et al., 2008) and bread doughs (Letang et al., 2001), polymers (Lellinger et al., 2002), silicate melt (Balasubramaniam et al., 1999), and various other compounds (Shah and Balasubramaniam, 2000; Greenwood et al., 2006; Franco et al., 2010; Greenwood and Bamberger, 2002; Schirru et al., 2015; Schirru and Dwyer-Joyce, 2015) including hydrocarbon oils ((Barlow and Lamb, 1959) (Rabani et al., 2011)). Aside from Han et al.'s (Han et al.; Han et al., 2007; Han, Liu, and Baztle, 2008) measurements, to our knowledge this technique has not been applied to bitumen although there have recently been attempts to model similar responses using vegetable oil shortening with compressional wave reflectivity (Lines et al., 2014).

This paper begins with a brief overview of the theory of extracting shear properties from the complex shear wave reflection coefficient. We describe the construction of an ultrasonic shear wave reflectometer and its testing at modest temperatures using well known fluids. This is followed a detailed description of our bitumen sample and measurements that incorporate a novel signal processing scheme. We interpret the observed complex shear wave reflection coefficients and comment on

the meaning of the measurements given that the analysis relies on the assumed rheological behaviour of the material.

5.2. Theory

The ultimate goal of our measurements is to constrain the rheological behaviour of bitumen using shear wave reflectometry. This is accomplished in two stages by first experimentally determining the fluid's shear modulus G^* that, second, must then be interpreted using an appropriate rheological model.Here only simple models are discussed given the preliminary nature of this study the intent of which is to develop the methodology.

5.2.1. Physical property relationships

In general, the shear properties of any material of known density ρ may be described equivalently by the complex shear modulus G^*, velocity c*, the viscosity η^*, or impedance Z^*. Here we will employ measurements of Z^* to provide information on the other parameters; and it is instructive to review these relationships that are summarized in Table 5.1.

The shear modulus for any material may be written as a complex number $G^* = G' + iG''$ where G' and G'' are real numbers respectively referred to as the storage and loss moduli. Their values are generally frequency dependent. They are constants only for the bounding cases of a perfect Hookean elastic solid with $G'' \equiv 0$ on one hand and a Newtonian fluid with $G' \equiv 0$ on the other.

Table 5.1: Shear properties of a material with known density ρ can be described equivalently by the complex shear modulus G^*, the viscosity η^*, velocity c^*, impedance Z^*, and wave number (k^*) (Litovitz and Davis, 1965; Dixon et al., 2004)

	Complex Shear Modulus G*	Complex Viscosity $\eta*$	Complex Velocity $c*$	Complex Impedance Z*	Complex Wavenumber $k*$
Complex Shear Modulus G*	$G^* = G' + i\,G''$	$G' = \omega\eta''$ $G'' = \omega\eta'$	$G' = \rho(c'^2 - c''^2)$ $G'' = 2\rho c' c''$	$G' = \frac{R^2 - X^2}{\rho}$ $G'' = \frac{2RX}{\rho}$	$G' = \rho\omega^2 \frac{k'^2 - k''^2}{k'^4 + k''^4 + 2k'^2 k''^2}$ $G'' = -\rho\omega^2 \frac{2k'k''}{k'^4 + k''^4 + 2k'^2 k''^2}$
Complex Viscosity $\eta*$	$\eta' = G''/\omega$ $\eta'' = G'/\omega$	$\eta^* = \eta' + i\,\eta''$	$\eta' = \frac{2\rho c' c''}{\omega}$ $\eta'' = \frac{\rho(c'^2 - c''^2)}{\omega}$	$\eta' = \frac{2RX}{\rho\omega}$ $\eta'' = \frac{R^2 - X^2}{\rho\omega}$	$\eta' = \rho\omega \frac{k'^2 - k''^2}{k'^4 + k''^4 + 2k'^2 k''^2}$ $\eta'' = -\rho\omega \frac{2k'k''}{k'^4 + k''^4 + 2k'^2 k''^2}$
Complex Velocity $c*$	$c^* = \sqrt{\frac{G^*}{\rho}}$ $c' = \left[\frac{1}{2\rho}\left(\sqrt{G'^2 + G''^2} + G'\right)\right]^{1/2}$ $c'' = \left[\frac{1}{2\rho}\left(\sqrt{G'^2 + G''^2} - G'\right)\right]^{1/2}$	$c^* = \sqrt{\frac{\omega\eta^*}{\rho}}$ $c' = \left[\frac{\omega}{2\rho}\left(\sqrt{\eta'^2 + \eta''^2} + \eta'\right)\right]^{1/2}$ $c'' = \left[\frac{\omega}{2\rho}\left(\sqrt{\eta'^2 + \eta''^2} - \eta'\right)\right]^{1/2}$	$c^* = c' + i\,c''$	$c' = \frac{R}{\rho}$ $c'' = \frac{X}{\rho}$	$c^* = \frac{\omega}{k^*}$ $c' = \frac{\omega k'}{k'^2 + k''^2}$ $c'' = \frac{-\omega k''}{k'^2 + k''^2}$
Complex Impedance Z*	$Z^* = \sqrt{\rho G^*}$ $R = \left[\frac{\rho}{2}\left(\sqrt{G'^2 + G''^2} + G'\right)\right]^{1/2}$ $X = \left[\frac{\rho}{2}\left(\sqrt{G'^2 + G''^2} - G'\right)\right]^{1/2}$	$Z^* = \sqrt{\rho\omega\eta^*}$ $R = \left[\frac{\rho\omega}{2}\left(\sqrt{\eta'^2 + \eta''^2} + \eta'\right)\right]^{1/2}$ $X = \left[\frac{\rho\omega}{2}\left(\sqrt{\eta'^2 + \eta''^2} - \eta'\right)\right]^{1/2}$	$Z^* = \rho c^*$ $R = \rho c'$ $X = \rho c''$	$Z^* = R + iX$	$Z^* = \frac{\rho\omega}{k^*}$ $R = \rho\omega \frac{k'}{k'^2 + k''^2}$ $X = -\rho\omega \frac{k''}{k'^2 + k''^2}$
Complex Wavenumber $k*$	$k^* = \sqrt{\frac{\rho\omega^2}{G^*}}$ $k' = \left[\frac{\rho\omega^2}{2(G'^2 + G''^2)}\left(\sqrt{G'^2 + G''^2} + G'\right)\right]^{1/2}$ $k'' = \left[\frac{\rho\omega^2}{2(G'^2 + G''^2)}\left(\sqrt{G'^2 + G''^2} - G'\right)\right]^{1/2}$	$k^* = \sqrt{\frac{\rho\omega}{\eta^*}}$ $k' = \left[\frac{\rho\omega}{2(\eta'^2 + \eta''^2)}\left(\sqrt{\eta'^2 + \eta''^2} + \eta'\right)\right]^{1/2}$ $k'' = \left[\frac{\rho\omega}{2(\eta'^2 + \eta''^2)}\left(\sqrt{\eta'^2 + \eta''^2} - \eta'\right)\right]^{1/2}$	$k' = \frac{\omega c'}{c'^2 + c''^2}$ $k'' = \frac{-\omega c''}{c'^2 + c''^2}$	$k' = \rho\omega \frac{R}{R^2 + X^2}$ $k'' = -\rho\omega \frac{X}{R^2 + X^2}$	$k^* = k' + i\,k''$

In the following we implicitly assume that all parameters are frequency dependent. Following Dixon et al. (Dixon et al., 2004), if the material has density ρ, one can similarly describe a complex shear phase velocity $c^*=c' + ic''$ and the relationship

$$G' + iG'' = \rho\left[\left(c'^2 - c''^2\right) + 2ic'c''\right] \quad (1)$$

Alternatively, the phase velocity $c^* = \omega/k^*$ where $k^* = k' + ik''$ is the complex wavenumber with

$$k' = \frac{\omega c'}{c'^2 + c''^2} \text{ and } k'' = \frac{-\omega c''}{c'^2 + c''^2} \quad (2)$$

through solution of the wave equation allows the wave displacement amplitude $A(x,t)$ to be described through its propagation

$$A(x,t) = A_o \exp(-k''x)\exp(i(k'x - \omega t)) \quad (3)$$

where A_o is the initial amplitude, that will have a measurable wave speed $v = \omega/k'$ and attenuation k''. The subsequent concept of the skin or penetration depth $\delta = 1/k''$ that is in studies of electromagnetic wave propagation a measure of the distance from the surface of the material at which the amplitude has decayed to $A(\delta,t)/A_o = 1/e$ (~36.79%) and the intensity to $1/e^2$ (~13.53%). The quality factor $Q = G'/G''$ is a normalized measure of the wave's attenuation that is also often useful (Oconnell and Budiansky, 1978).

In principle, G^* could be determined by direct measurement of v and k'' (e.g., Barlow and Subramanian, (Barlow and Subramanian, 1966)) but due to difficulties in propagating shear waves into fluids this is usually not practical. To overcome this difficulty, it is important to note that a material's mechanical properties, independent of any assumed rheology, may also be expressed in terms of its complex impedance $Z^* = \rho c^* = R + iX$, where R and X are respectively the shear resistance and reactance in mechanical Ohm units of $N \cdot s/m^3$. The complex shear impedance is related to the complex shear modulus as,

$$Z^* = (\rho G^*)^{1/2} \tag{4}$$

or rearranging

$$G^* = \frac{(Z^*)^2}{\rho} = (R + iX)^2/\rho \tag{5}$$

Hence, in principle G^* may be determined from knowledge of the density and complex impedance with real

$$G'(\omega) = \frac{R^2 - X^2}{\rho} \tag{6}$$

and imaginary components

$$G''(\omega) = \frac{2RX}{\rho} \tag{7}$$

with these equations being applicable for any rheology (Barlow and Subramanian, 1966). These relations are exploited using shear wave reflectometry as described below.

Alternatively, the material can be considered in terms of its complex viscosity $\eta^* = \eta' + i\eta''$ ((Macosko, 1994; Stastna et al., 1994)) with the frequency dependent dynamic viscosity $\eta' = G''/\omega$, which collapses to the static or steady-flow viscosity η at the lowest frequencies, and an elastic component $\eta'' = G'/\omega$ with

$$|\eta^*| = \frac{|G^*|}{\omega} \tag{8}$$

Exploration of these relationships for a simple Maxwell rheology discussed later but constructed with an instantaneous shear modulus G_∞ and steady flow viscosity η illustrates the expected changes in the components of G^* and η' with increasing normalized frequency (Figure 5.1a) and in the mechanical shear resistance R and reactance X (Figure 5.1b) leading to a wave propagation speed v and the attenuation in terms of the quality factor $Q = G'/G''$ (Oconnell and Budiansky, 1978), (Figure 5.1c).

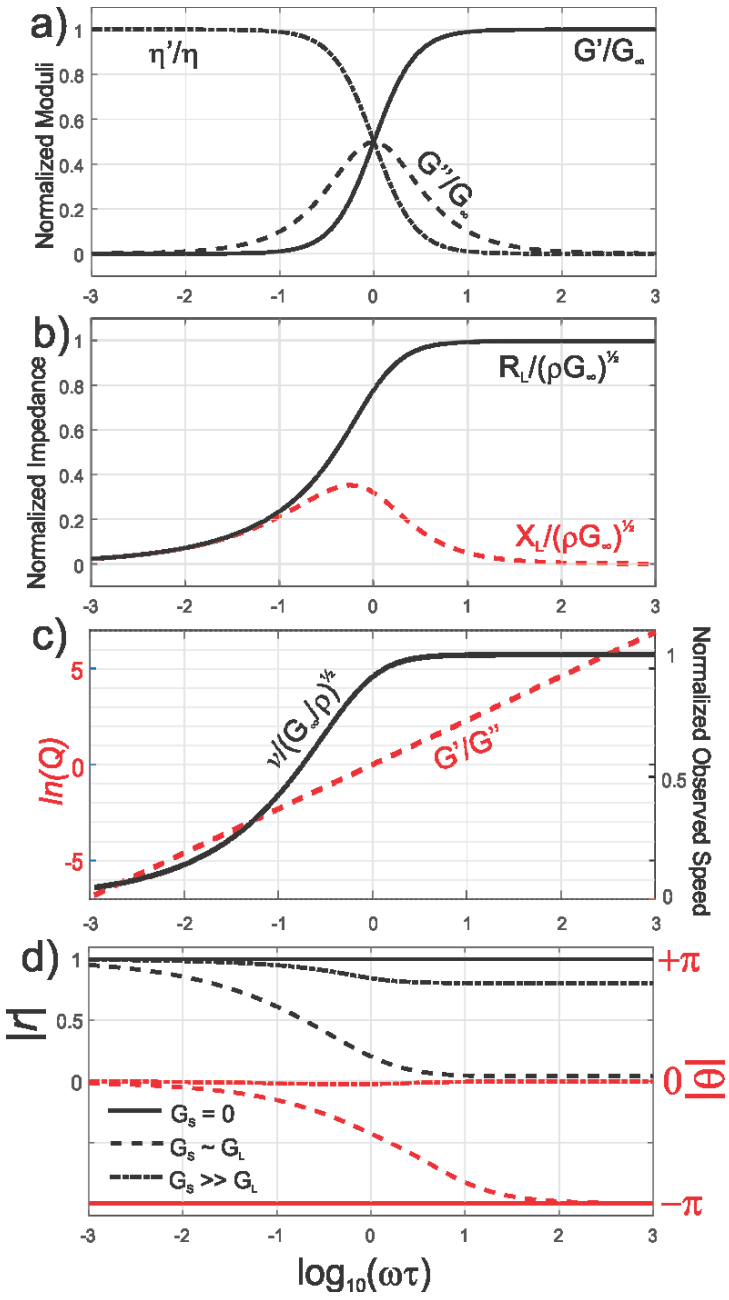

Figure 5.1. Illustration of frequency dispersion for a simple Maxwell material of instantaneous shear modulus $\mathbf{G}_\infty$ and steady flow viscosity η giving a shear relaxation time τ_S on a) dynamic viscosity η' and the real G' and imaginary components G'' of the complex shear modulus, b) the corresponding real resistive R and imaginary reactive X components of the complex shear impedance, c) the observed phase speed v and quality factor Q, and d) on the reflection coefficient r (black) and phase θ (red) for a wave incident on the fluid from an elastic delay line with impedance vanishing (solid lines), similar (dashed lines), or much greater (dash-dot lines) than the material.

5.2.2. Relationships to shear wave reflectivity

O'Neil (Oneil, 1949) first derived the principle of shear waves reflection and refraction in viscoelastic materials. In the same year, Mason et al. (Mason et al., 1949) exploited Eq. 5 to first determine the shear viscosity and modulus of liquids by measuring Z^* in a shear wave reflection experiment.

The normal-incidence complex reflection coefficient r^* for a shear wave propagating within a perfectly elastic solid of shear impedance Z_S and reflected from the contact interface of the solid with a lossy medium with shear impedance Z_l^* is

$$r^* = \frac{Z_S - Z_l^*}{Z_S + Z_l^*} \tag{9}$$

that may alternatively be expressed in terms of measurable reflection coefficient modulus r (real and positive valued) and phase θ

$$r^* = re^{-i\omega\theta} \quad . \tag{10}$$

It is important to note that Eq. 9 is taken from the perspective in which the particle motions are with respect to a fixed co-ordinate frame reference. This is opposed to the more usual wave propagation frame used in much of the Geophysical literature with the numerator of $Z_l^* - Z_s$. This difference is immaterial to the final results but care needs to be taken with the sign of the phase.

It is worthwhile to consider some simple bounding cases for r^*. If the second medium is a vacuum then $Z_l^* \equiv 0$ leading to $r = 1$ and $\theta = 0$. If the second medium is a perfectly elastic solid then both Z_l^* and r^* are real valued and $\theta = 0$ or $-\pi$ depending respectively on whether $Z_l < Z_S$ or $Z_l > Z_S$. Finally, if Z_l^* is only complex valued (e.g., a perfect Newtonian fluid) then $r = 1$ always but θ will be frequency dependent equaling 0 or $-\pi$ for, respectively, low and high frequency regimes with a transition range of frequencies that depends on the contrasts, Figure 5.1d.

The dispersion of r and θ is not as straightforward once the fluid G^* has both real and imaginary components as illustrated by three cases in which the shear modulus G_S is much less than, is approximately equal to, or is much greater than the real part G_L of the complex shear modulus of the fluid under study. In the first case with $G_S \rightarrow 0$, r $\rightarrow 1$ and $\theta \rightarrow -\pi$. In the last case with $G_S >> G_L$ the reflectivity is unity at low frequencies but at high frequencies behaves as if produced by two welded solids. At low frequencies the reflected phase $\theta = o$ but displays a small positive for higher frequencies. In contrast, if $G_S \sim G_L$ both r and θ show considerable variations with frequency. This highlights the need to minimize the contrast between Z_L and Z_S in order to maximize the sensitivity in determining Z_L^* and motivated us to construct the delay line from a low impedance material as described later.

Manipulation of the above equations allows Z_l^* to be given in terms of the r and θ (McSkimin and Andreatch, 1967),

$$Z_l^* = \frac{Z_s(1-r^2)}{1+r^2+2r\cos\theta} + i\frac{2Z_s r\ \sin\theta}{1+r^2+2r\cos\theta} \tag{11}$$

with by analogy explicitly

$$R_l = \frac{Z_s(1-r^2)}{1+r^2+2\mathrm{r}\cos\theta} \quad and\ X_l = \frac{2Z_s r\ \sin\theta}{1+r^2+2\mathrm{r}\cos\theta} \tag{12}$$

Manipulation of equations (6), (7) and (12) help in defining the storage and loss modulus as,

$$G'(\omega) = \frac{R_l^2 - X_l^2}{\rho_l} = Z_s{}^2\,\frac{(1-r^2) - 4r^2\sin^2\theta}{\rho_l(1+r^2+2\mathrm{r}\cos\theta)^2} \tag{13}$$

$$G''(\omega) = \frac{2R_l X_l}{\rho_l} = Z_s{}^2\,\frac{4r(1-r^2)\ \sin\theta}{\rho_l(1+r^2+2\mathrm{r}\cos\theta)^2} \tag{14}$$

Therefore, G' and G'' of a fluid with a known density may be found using the measured values of r and θ.

In a practical experimental situation this is accomplished differentially with respect to, first, a reference measurement of the reflected amplitude $A_r(\omega)$ and phase $\theta_r(\omega)$taken from the solid-N_2 interface, and second of the amplitude $A_l(\omega)$ and phase $\theta_l(\omega)$ taken from the solid-liquid interface that in the frequency domain is (Voigt, 2005),

$$r(\omega) = \frac{A_l(\omega)}{A_r(\omega)} \tag{15}$$

$$\theta(\omega) = \theta_l(\omega) - \theta_r(\omega) \tag{16}$$

The behaviour of r and θ depends strongly on the contrasts between Z_S and Z_L as illustrated in Figure. 1d which shows the evolution of the reflectivity from $|Z_S| << |Z_L|$ to $|Z_S| >> |Z_L|$.

5.2.3. Rheological models

The section above provides the essential details to finding the complex shear modulus in the shear wave reflectometry experiment. Usually, however, one desires knowledge of the fluid's viscosity. To do this requires knowledge of an appropriate rheological model, that in practice may or many not be known. In the following we provide the relationships for the determination a shear viscosity using the standard fluid-like Maxwell and solid-like Kelvin-Voigt models but emphasizing that the values obtained will depend on the model employed. More sophisticated descriptions, derived from extensions of the Maxwell model that, for example, combine a number of relaxation times and instantaneous viscosities may be preferred (Baumgaertel and Winter, 1989), but cannot be determined here because of the relatively small frequency band used.

5.2.3.1. Newtonian Fluid

As noted earlier, in a perfectly Newtonian fluid $G' \equiv 0$ (and equivalently $\eta'' = 0$)

and hence the dynamic viscosity follows from Eqs. (8) and (14),

$$\eta' = \frac{G''}{\omega} = {Z_s}^2 \frac{4r(1-r^2)\,\sin\theta}{\rho_l \omega (1+r^2+2r\cos\theta)^2} \tag{17}$$

which for a given temperature is presumed independent of frequency.

Only for this Newtonian case, r and θ are functionally related and Eq. (17) could be recast in terms of either (Shah and Balasubramaniam, 2000; Franco et al., 2010) as it can be shown that

$$\theta(r) = \frac{1}{2}\cos^{-1}\left[1 - \frac{\left(1-r^2\right)^2}{2r^2}\right] \tag{18}$$

That when combined with Eq. 17 allows the dynamic viscosity to be written full in terms of the observed reflectivity

$$\eta' = \frac{2{Z_s}^2}{\rho_l \omega}\left[\frac{1-r^2}{1+r^2+\sqrt{r^2(6-r^2)-1}}\right]^2 \approx \frac{2{Z_s}^2}{\rho_l \omega}\left[\frac{1-r}{1+r}\right]^2 \tag{19}$$

where the approximation of the last term holds if $cos(\theta) \rightarrow 1$ for small θ.

5.2.3.2. Maxwell model

At low temperatures bitumen is exhibits complex and frequency dependent shear viscosities indicating that it behaves as a non-Newtonian fluid. To examine the effects of relaxation time, one can start with the simple Maxwell model which describes a Debye-type relaxation in a system to yield the frequency dependence of the viscosity as (Maxwell, 1867),

$$\eta' = \frac{\eta_M}{1+\omega^2 {\tau_s}^2} \tag{20}$$

where η_M is the asymptotic low-frequency or steady-flow viscosity.

In more details, under Maxwell's series spring-dashpot model the fluid has a single shear relaxation time $\tau_s = \eta_M / G_\infty$ where G_∞ is the infinite-frequency (instantaneous) shear modulus (i.e., the spring) and Maxwell apparent viscosity η_M is

the steady flow or low frequency viscosity (i.e., the dashpot) which is a frequency independent constant, or alternatively $\eta'(\omega) \rightarrow \eta_M$ as $\omega \rightarrow 0$. For the sinusoidal variation of shear stress and shear rate with angular frequency, Maxwell model describes the storage and loss modulus in terms of this relaxation time (Sheen et al., 1996; Litovitz and Davis, 1965; Barlow and Subramanian, 1966),

$$G' = \frac{\omega^2 G_\infty \tau_S^2}{1+\omega^2 {\tau_s}^2} = \frac{\omega^2 \eta_M \tau_s}{1+\omega^2 {\tau_s}^2} \tag{21}$$

and

$$G'' = \frac{\omega G_\infty \tau_s}{1+\omega^2 {\tau_s}^2} = \frac{\omega \eta_M}{1+\omega^2 {\tau_s}^2} \tag{22}$$

from which follows

$$\omega \tau_s = \frac{G'}{G''} \tag{23}$$

Combining Eqs. (14) and (22) and rearranging gives the low frequency dynamic viscosity

$$\eta_M = {Z_s}^2 \left(\frac{4(1-r^2) r \sin\theta}{\rho_l (1+r^2+2r\cos\theta)^2}\right) \frac{(1+\omega^2 {\tau_s}^2)}{\omega} \tag{24}$$

that upon substitution of Eq. 23 is

$$\eta_M = \frac{{Z_s}^2}{\omega \rho_l} \left(\frac{4(1-r^2) r \sin\theta}{(1+r^2+2r\cos\theta)^2}\right) \left(1 + \left(\frac{G'}{G''}\right)^2\right), \tag{25}$$

which can be expanded fully in terms of r and θ.

5.2.3.3. Kelvin-Voigt Model

We mention briefly the Kelvin-Voigt model that arranges the viscous dashpot with apparent viscosity η_{KV} and 'relaxed' elastic rigidity G_o in parallel. The complex shear modulus for this case is more simply (e.g., Vernon-Carter et al. (Vernon-Carter et al., 2016)),

$$G^* = G' + iG'' = G_0 + i\eta_{KV}\omega \tag{26}$$

with the straightforward results that the relaxed modulus G_o = G' and η_{KV} = G''/ω, allowing that η_{KV} is calculated using Eq. (19) above as would be done if the fluid had an ideal Newtonian viscosity.

5.3. Sample characterization

Natural heavy hydrocarbon oils are a mixture of a wide variety of hyrocarbons of differing molecular weights with organic molecules containing nitrogen, oxygen, and sulphur, that may be further contaminated with compounds incorporating copper, iron, nickle, and vanadium (e.g., Speight (Speight, 1999)). The mix of compounds directly affects the physical properties, which are also somewhat dependent on pressure but highly dependent on temperature (Kariznovi et al., 2014). Given this complexity even knowing how to fully characterize such materials alone can be a challenge. Here we chose to broadly characterize the bitumen's composition of satruates, aromatics, resins, and asphaltenes (SARA) by fractionation supplemented by measures of the distributions of molecular weights followed by dynamic viscosity η and density ρ_l. The bitumen used in the measurements was produced during a field pilot test in which steam was injected to the carbonate Grosmont Formation in NE Alberta. As such the sample is essentially a colloidal suspension of water in oil with the water content measured to be 22% by weight using the Karl Fischer titration method (Mettler Toledo T70 Autotitrator. SARA

(saturates, aromatics, resins and asphaltenes) component analysis (Table 5.2) was carried out on the hydrocarbon portions using the clay-gel chromatographic method according to ASTM 2007-03 and IP 143 (Castro and Vazquez, 2009; Moreno Arciniegas). It reveals a high percentage of asphaltene/resin concentration in the sample which leads to having higher rigidity and elasticity (Loeber et al., 1998).

Table 5.2: SARA Analysis: in percent (weight)

Asphaltenes	Saturates	Aromatics	Resins
13.84	27.17	26.28	32.68

Thermogravimetric analysis (TGA) using Mettler Toledo TGA/DSC 1 STAR System, Figure 5.2, shows that the bitumen sample exhibits significant weight loss, as much as 25%, by about 90°C. Although, the onset temperature (70°C) of the weight loss, in Figure 5.2, may infer that it is due to the evaporation of lighter hydrocarbon molecules as well as water.

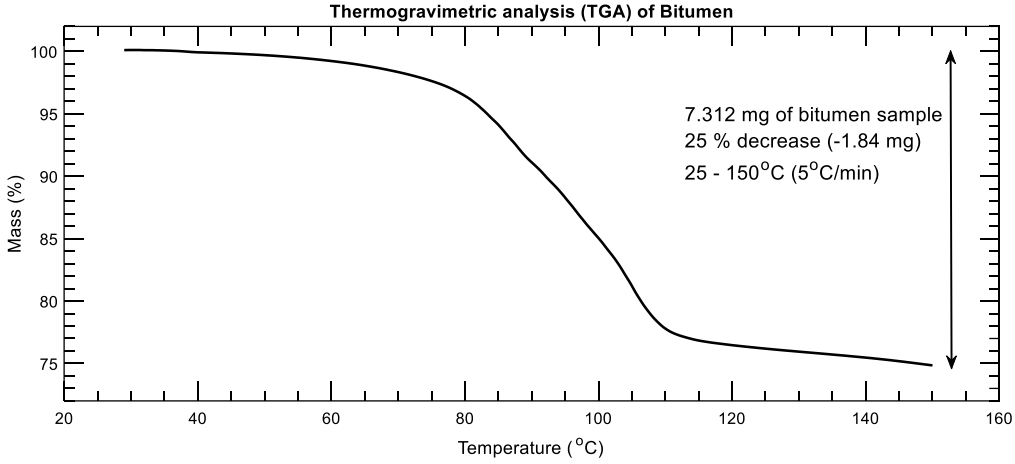

Figure 5. 2 The bitumen sample loses as much as 25% of its weight over a temperature change from 70°C to 150°C in the thermographic analysis.

Mass spectroscopy on the bitumen dissolved in chloroform was measured by using matrix-assisted laser desorption/ionization (MALDI) at the mass spectrometry facility, University of Alberta. Figure 5.3 shows the relative intensity (current produced by ions) of varying mass/charge ratio where it is assumed that the ions all have a charge of 1+. The most abundant ion in the spectrum, Figure 5.3, indicates an molecular weight of 355 g/mol with the spectra giving a number average molecular weight of 652 g/mol and weight average molecular weight of 970 g/mol, following (Fenistein and Barré, 2001).

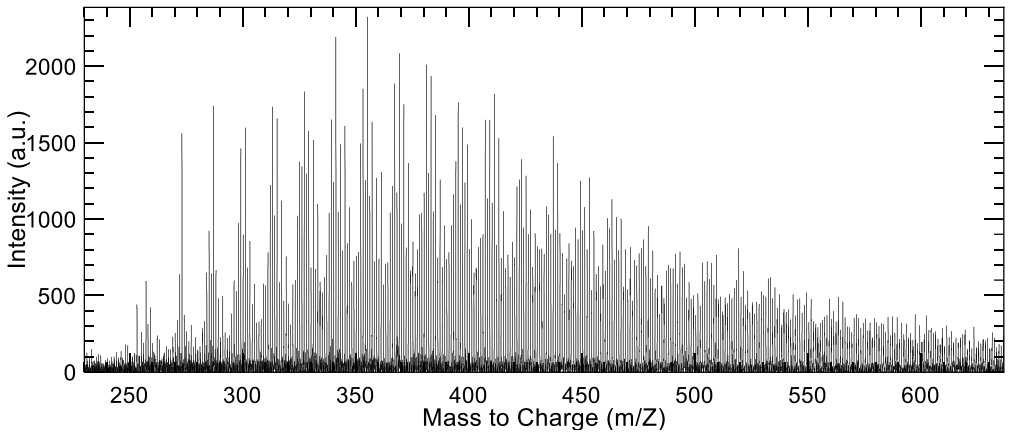

Figure 5. 3 The relative intensity with varying mass-charge ratio from mass spectroscopy analysis indicates the average molecular weight. If the compound is ionized such that it has a net charge of +1 then the mass to charge ratio is the same as the molecular weight in g/mol.

The bitumen density was determined with temperature (Figure 5.4) using the oscillating U-tube method (automatic density meter DDM 2910, Rudolph Research Analytical) and converting to API° 6. This is in good agreement with earlier measurements conducted by our industrial partners using an undisclosed method on oil produced or extracted directly from the core by high speed centrifugation (Rabbani et al., 2017). Our sample is expected to contain more water because it was produced by the steam-assisted gravity drainage (SAGD) process.

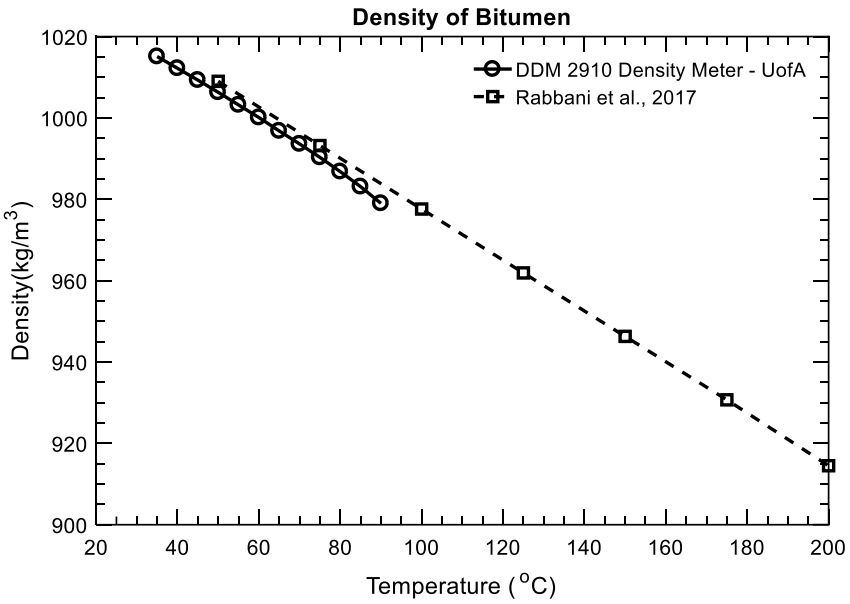

Figure 5. 4 he density of bitumen decreases with temperature. Densities measured at a pressure of 1.5 MPa (square markers) are heavily comparable to that measured at atmospheric pressure (circular markers).

The dynamic shear viscosity of the bitumen is measured with temperature using the Searle rotating spindle method (Brookfield viscometer DV2T viscometer, Brookfield Engineering). The measurement conditions including shear rate and accuracy are shown in Table 5.3. The instrument is limited to measure viscosity smaller than 10^5 cP only, hence cannot operate at lower temperature than 35°C. This also compares well with the determinations by Yang et al. (Yang et al., 2014), as shown in Figure 5.5.

Table 5.3: Conditions for viscosity measurement of bitumen using Brookfield DV2T viscometer

Temperature (°C)	Speed (rpm)	Torque	Shear Stress	Shear Rate (1/s)	Viscosity (cP)	Accuracy
35	0.1	59.9	1189	0.2	594300	9922
40	0.3	84.7	1681	0.6	280100	3307
45	0.6	85.5	1697	1.2	141400	1654
50	1.2	89.9	1784	2.4	74330	826.8
55	2.2	91.3	1812	4.4	41180	451
60	4	95.5	1895	8	23690	248.1
65	6	87	1726	12	14390	165.4
70	10	89.4	1774	20	8870	99.22
75	16	91.8	1822	32	5693	62.01
80	25	93.1	1847	50	3695	39.69
85	35	88.1	1748	70	2498	28.35
90	50	87.8	1742	100	1742	19.84
95	70	86.9	1724	140	1232	14.17
100	100	76.5	1518	200	759	9.92

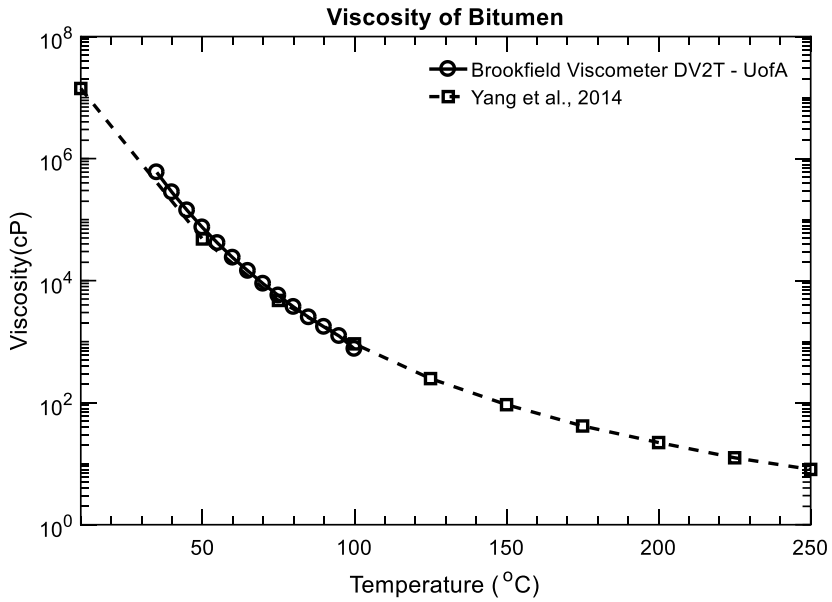

Figure 5. 5 Dynamic viscosity of bitumen decreases significantly with temperature. Brookfield viscometer provides data plotted as the solid line (circle), and dashed line (square) is from Yang et al. (Yang et al., 2014).

5.4. Experimental details and signal processing

An adapted version of the pulse-echo technique is used to measure the shear properties of liquids at ultrasonic frequency (Greenwood et al., 2006; Shah and Balasubramaniam, 2000; Franco et al., 2010; Dixon and Lanyon, 2005; Schirru and Dwyer-Joyce, 2015). A schematic of the experimental details is shown in Figure 5.6.

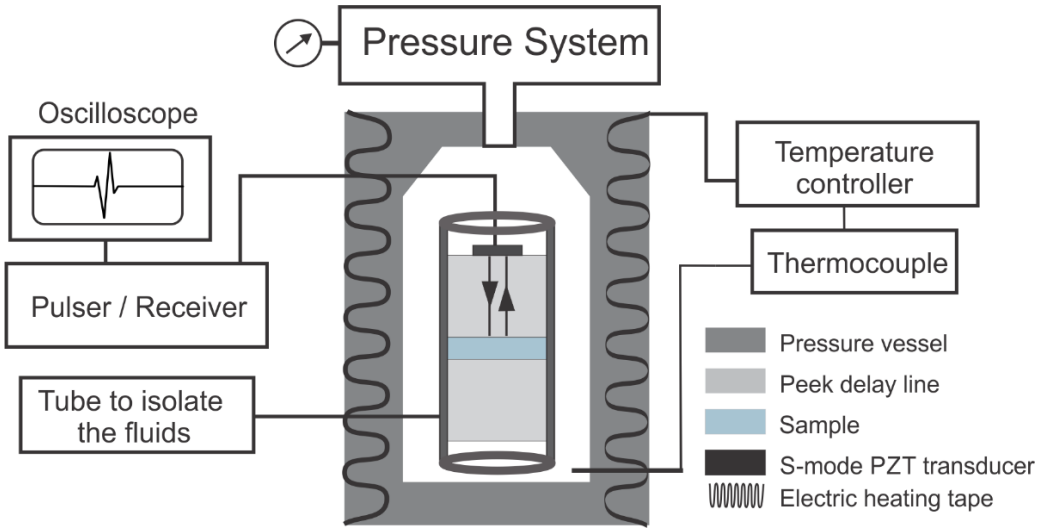

Figure 5. 6 The schematic of the experimental set up that highlights the pressure and temperature control segments, and signal acquisition. The measurement cell inside the vessel consists a shear wave transducer glued into the PEEK delay line and is wrapped with a plastic tube to isolate the fluids of interest from Nitrogen used to create the back pressure.

5.4.1. Technical details

A square (15mm × 15mm × 1mm) transversely-poled shear-mode PZT piezoelectric ceramic (APC international Ltd) resonant at 600 kHz is mounted on one end of the PEEK delay line (Figure 5.6). The transducer is carefully covered with a thick layer of damping material that, first, damps and broadens the bandwidth of the transmitted pulse and, second, isolates the PZT material from direct contact with the pressurizing fluid in the vessel. The PZT element is activated in a pulse-echo mode using an ultrasonic pulser (Panametrics pulser/receiver, model 5800) with the returned signal digitally recorded (NI 8-bit digitizer, model PXI-5114) at a sampling period of 20 *ns* for 600 μs. The final record is the average of 500 pulses.

A lower second cylinder of PEEK allows for the volume of test fluid to be isolated from the pressure chamber using flexible plastic tubing. We filled the gap between the

buffer and reflector with the reference- and test- fluids through hole in the tube. The hole is then sealed with a flexible urethane putty.

This prepared cell is then placed in a sealed pressure vessel that is filled with N_2 that acts as the pressure transmitting medium and held at a desired pressure and temperature. We use a pressure transducer (Tecsis, model 99-6308-0001) with an accuracy of 0.05% to measure and a manual pressure accumulator (HiP 62 6-10) to control the pressure. A chiller system (NESLAB Endocal Refrigerated Circulating Bath RTE-8DD) circulates fluid a mixture of water and around the pressure vessel through a copper tubing system to control the temperature. Temperature is measured to ±0.1°C accuracy using a K-type thermocouple with a temperature controller (OMEGA® - CNi16D44-C24).

The observed reflection coefficient r depends on the contrast between the acoustic impedances of the delay line and the fluid of interest. Many workers have constructed their solid buffer (i.e. delay-line) from thermally stable, low-loss materials, such as fused quartz (Deblock et al., 1998; Camara and Laux, 2010). Their large contrast in shear impedance relative to that for the test fluid leading to significant reductions in sensitivity in reflected amplitudes and phases to changes in the fluid is one disadvantage to the use of fused quartz, however (Fig. 1d). To overcome this difficulty, we constructed the delay line from unfilled Poly ether ether ketone (PEEK) that is chosen for its low density, velocity and stability. The Beige PEEK rod (FDA listed material, UL94V0, McMaster-Carr, meets specification ASTM D6262). The density of the PEEK used here is 1304 kg/m^3 at 21°C as measured with a Helium pycnometer, this agrees well a reported range from 1286 kg/m^3 to 1310 kg/m^3 (Fitch et al., 2010). Our measured shear speed at 23°C is 1125 m/s again is within two values reported in the literature of 1086.1 m/s (Fitch et al., 2010) to 1130 m/s (Rae et al., 2007). We estimated the temperature dependent variations (ΔT in sample length (ΔL) and density ($\Delta \rho$) assuming a co-efficient of thermal

expansivity (α) of 34 μm/m°C (Lu et al., 1996) constant over the range of temperatures encountered, using the relations $\Delta L=\alpha L\Delta T$ and $\Delta\rho=3\alpha\rho\Delta T$ (Peleties et al., 2010). We finally calculated the shear wave speed in PEEK at different pressure and temperature directly using the transit times of the reflected pulses (e.g., Fig. 5a) and the temperature corrected lengths. Table 5.4 includes the properties of the delay line (PEEK) at 2 MPa pressure as determined in these measurements.

Table 5.4: Physical properties of PEEK delay line

Temperature (°C)	10	30	40	50
Shear wave speed (m/s)	1140.7	1119.7	1110.9	1102.5
Density (kg/m3)	1306	1302	1300	1298
Shear Impedance (kg/m^3).(m/s)	1.49×10^6	1.46×10^6	1.44×10^6	1.43×10^6

The PEEK also has a number of disadvantages, however. Its physical properties depend on pressure and temperature. Like many polymers, its properties will vary by the batch and each piece must be fully characterized. Finally, it has a low thermal diffusivity meaning that it takes a substantial amount of time for the test piece to come into thermal equilibrium, this lengthens the time required between measurements when changing temperature; fused quartz also has a low thermal diffusivity and suffers as a material in the same way. Deblock et al. (Deblock et al., 1998) also mention the importance of the temperature stability in the delay line. A variation of 0.01°C in temperature produces an uncertainty of 0.01° on the reflection coefficient phase in the fused quartz delay line which influences the viscosity measurement. As a polymer it also has a measurable, but low, attenuation and should, strictly, also be considered to have a complex impedance. We chose to ignore this here as these effects are automatically compensated by the differential measurements of Eqs. 15 and 16, and were careful to achieve maximum

temperature stability by waiting enough time even after reaching the target temperature but cannot confirm the stability inside the delay line.

5.4.2. Waveform analysis procedures

Figure 5.7 details the steps taken to obtain the phase from the two recorded time series (Fig. 5a) for the waveforms reflected from the reference (N_2) and sample (bitumen) with the corresponding amplitude spectra (Figure 5.7b) calculated using the FFT. The waveforms were further processed by i) debiasing, ii) applying a 10 μs hanning tapered window over the pulse to remove any early trigger noise or later reverberations, iii) shifting of times 89 μs towards t=0 such that the magnitude of the phases smaller, iv) padding with zeros to extend the time series to 2^{14} samples to allow for denser sampling of frequencies by the FFT. The FFT of these revised time series are then taken and those values between 490 kHz to 650 kHz containing the greatest energy of the reflected pulses was selected for further analysis such as calculation of the ratio $A_t(\omega)/A_r(\omega)$ (Figure 5.7c) which gives the reflectivity according to Eq. (15). Phases are more difficult to deal with as it is often not clear that the phase unwrapping procedure is correct with a potential for large errors. As we are interested only in the phase difference, Eq. (16), and because both the direct unwrapped phases $\theta_r(\omega)$ and $\theta_t(\omega)$ are well behaved over range of analysis frequencies chosen, we first determined the intercepts and slopes $d\theta_r(\omega)/d\omega$ and $d\theta_t(\omega)/d\omega$ of the unwrapped phases by linear least-squares regression. Each curve is then shifted according to the intercept such that the phase at $\omega = 0$ vanishes from which the differential phase $\theta(\omega)$ (Figure 5.7d) of Eq. (16) is calculated. After accounting for the sign of the phase, the shear reactance and resistance are or $G'(\omega)$ and $G''(\omega)$, (Figure 5.7e) may be determined using Eqs. (12) through (14). Equations (17) and (25) are then used to calculate the Newtonian and Maxwell viscosity.

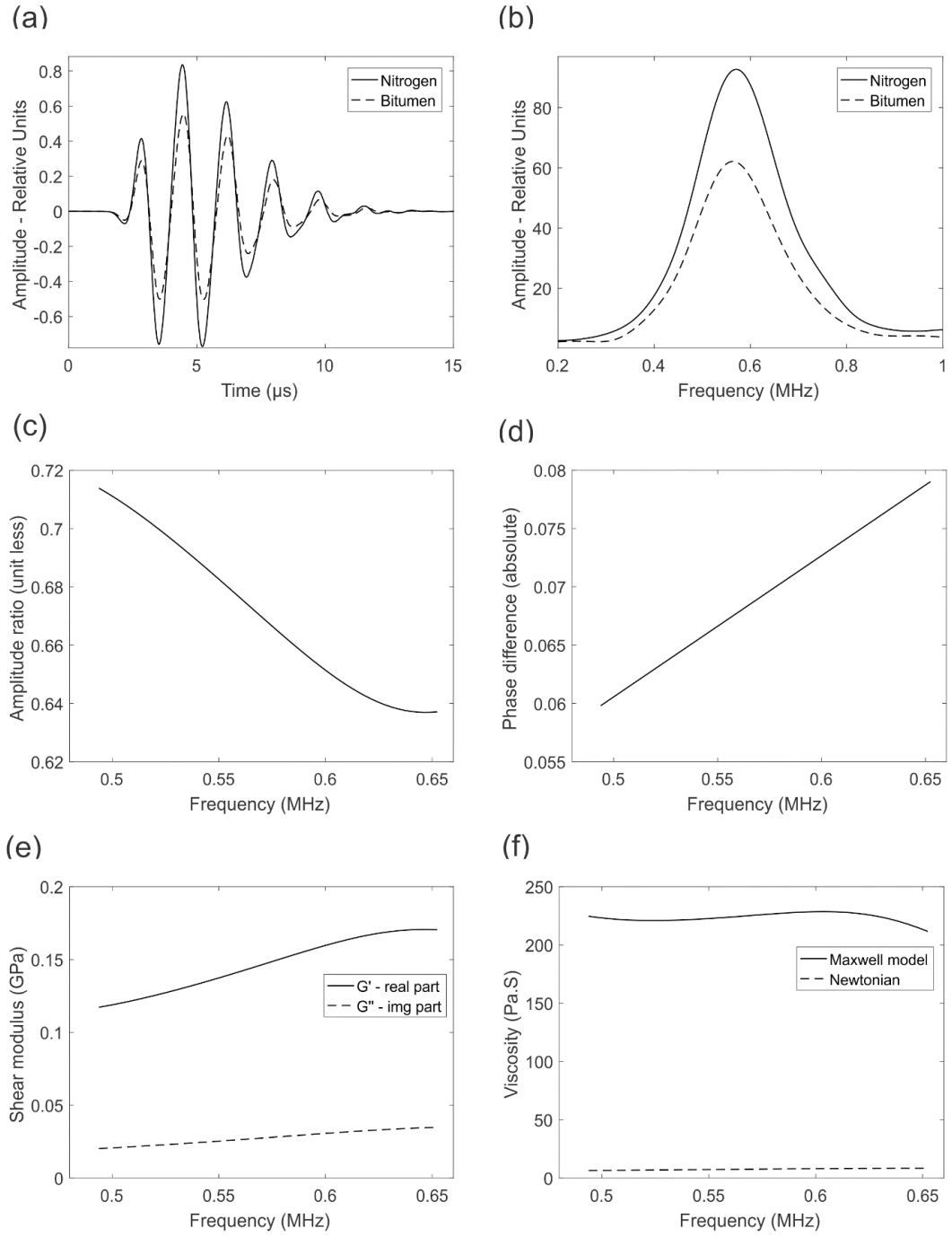

Figure 5.7. An example of the workflow of processing the time domain signals to derive the phase difference of the reflected pulses from the bitumen sample at 30°C and the subsequent calculations of shear modulus to be used to calculate dynamic viscosity of the liquid.

We note that the peak of the amplitude spectra in Figure 5.7b are near 555 kHz. In the following, we report values determined as being the average over the range of

frequencies used.

5.5. Results and discussion

5.5.1. Calibration curves and water tests

Nitrogen (N_2) gas is used for the reference fluid, so the shear wave reflected pulses from the PEEK-N_2 interface were first acquired with details of one reflected wave form given in Fig. 6a, and the full suite of waveforms from 10°C to 50°C is displayed later to compare with reflections from PEEK – bitumen interface. These provide references necessary for the determination of $r(\omega)$ and $\theta(\omega)$, and the changes seen with temperature highlight the need for such a calibration procedure. The variations stem from the combination of temperature dependent variations in the output and sensitivity of the PZT element and in the physical properties of the PEEK.

The time domain waveforms reflected from the PEEK – N_2 interface and that from the PEEK – water interface are nearly identical (Figure 5.8a). This similarity further appears in the Fourier domain with their corresponding amplitude spectra (Figure 5.8b) and vanishing phase θ (Figure 5.8c) that translates to small values for G' and G" (Figure 5.8d). This is as expected for these Newtonian fluids that at ~ 500 kHz remain well within their low frequency ranges as structural transitions in water, for example, are not expected until THz (10^{12}) frequencies (Slie et al., 1966; Kaatze, 2017; Greenwood and Bamberger, 2002) and this is largely confirmed by the phase of the reflected waveform (Figure 5.8a). With the technique here we are unable to obtain sufficient sensitivity in either r or θ to make an accurate determination of η' for water. Indeed, Han et al. (Han et al.) took advantage of this and used water as the reference fluid in their measurements.

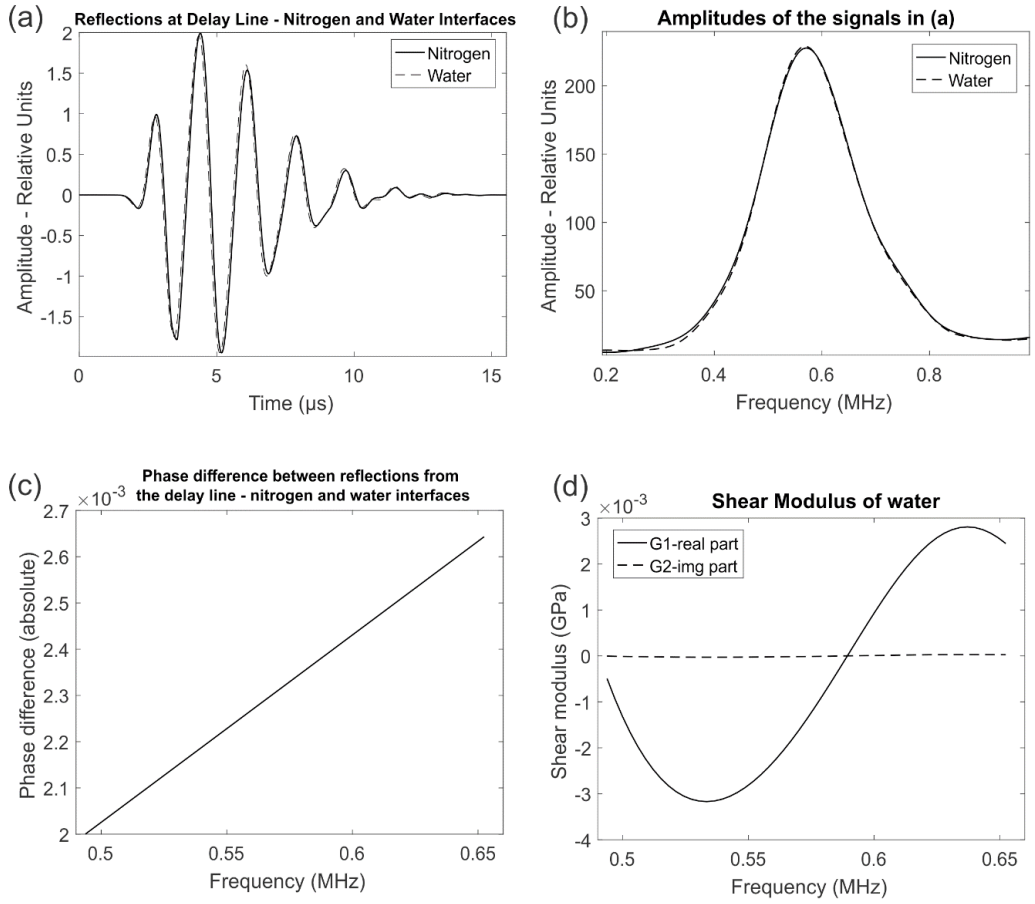

Figure 5.8. (a) Observed ultrasonic waveforms reflected from the delay line – nitrogen (solid line) and delay line – water (dash line) interfaces at 30°C and 2 MPa of pressure. (b) the corresponding amplitudes with minimal variation, (c) significantly low phase shift in the reflected waveforms, and (d) the negative and extremely low moduli indicate the insensitivity of the technique for liquid such as water.

5.5.2. Glycerol Test

Reagent grade glycerol (99.9% $C_3H_8O_3$, Sigma-Aldrich) was selected for a second test fluid primarily because of it can be obtained in highly purified form, it is relatively viscous at the temperatures employed, and it is well studied (Slie et al., 1966; Fergusson et al., 1954). Tests were run at three temperatures but all with the fluid at 1 MPa. At a given temperature, the waveforms reflected from the PEEK – water and PEEK

– glycerol interfaces amplitude scaled versions of one another, as shown in Figure 5.9; this indicates that there is little relative phase θ shift between the two again in agreement with the glycerol also largely being characterized as a Newtonian fluid. The relative amplitudes between the two, however, are readily determined to provide the reflection coefficient r (Table 5.4) and indicates the variations in viscosity. The differences in the amplitudes of the water and the glycerol waveforms become smaller as temperature increases as correspondingly the viscosity of the glycerol decreases.

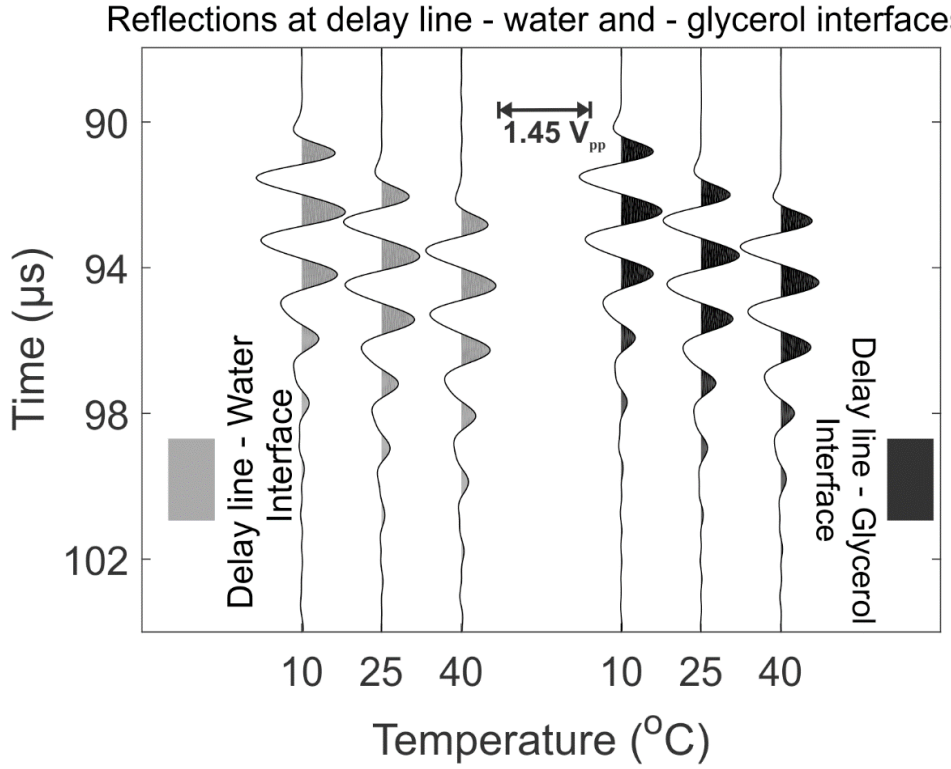

Figure 5.9. Observed waveforms reflected from the PEEK – water interface (light shade) and the PEEK – glycerol interface (dark shade) at 1 MPa pressure and at various temperature

Again, the phase shifts θ were too small to be adequately determined but values for these (Table 5.4) are calculated using the reflection coefficient r in Eqs. (18) (Franco et al., 2010), for an assumed Newtonian fluid glycerol are given in Table 5.5. The shear moduli of glycerol are also calculated using Eqs. (13) and (14). Table 5.4 also displays the

deviations of the measured viscosities (using equation 17) from values found in the literature (Cheng, 2008; sheely, 1932) under the assumption that the influence of pressure may be ignored. The deviations are small (4%) at the low temperatures where the viscosity of glycerol is also higher. However, the error is up to 37.2% at 40°C. This high percentage of error could be induced by various reasons, including calibration error or the insensitivity of the current system to measure lower viscosity (Figure 5.8d).

Table. 5.5. The viscosity of glycerol (99.5%) as the function of temperature at 1 MPa of pressure compared with atmospheric data from Cheng (Cheng, 2008) and Sheely (sheely, 1932).

Temperature (°C)	10	25	40
Density (kg/m^3) (Cheng, 2008)	1266.9	1257.4	1248.5
Reflection coefficient (at 570 kHz)	0.8854	0.9409	0.96
Calculated phase shift (Dixon and Lanyon, 2005; Franco et al., 2010), (radian)	0.1228	0.061	0.0408
Real part of the shear modulus G' (MPa)	23.7	12.3	8.14
Real part of the shear modulus G" (MPa)	13.14	3.19	1.38
Dynamic Viscosity (Pa.S)	3.67	0.892	0.386
Reported Viscosities (99.5%), η_0' (Pa.S) (sheely, 1932; Cheng, 2008)	3.82	0.856	0.282
Deviation $\left\|\frac{\eta_0'-\eta'}{\eta_0'}\right\| \times 100$ (%)	3.9	4.2	37.2

5.5.3. Bitumen test

The strengths of observed waveforms from the PEEK-bitumen interface (Figure 5.10) increase with temperature with the *r* determined in the comparison of these to their corresponding reference waveforms rising from 0.24 to 0.82 from 10°C to 50°C (Table 5.6) indicating significant changes in the bitumen's shear impedance and viscosity.

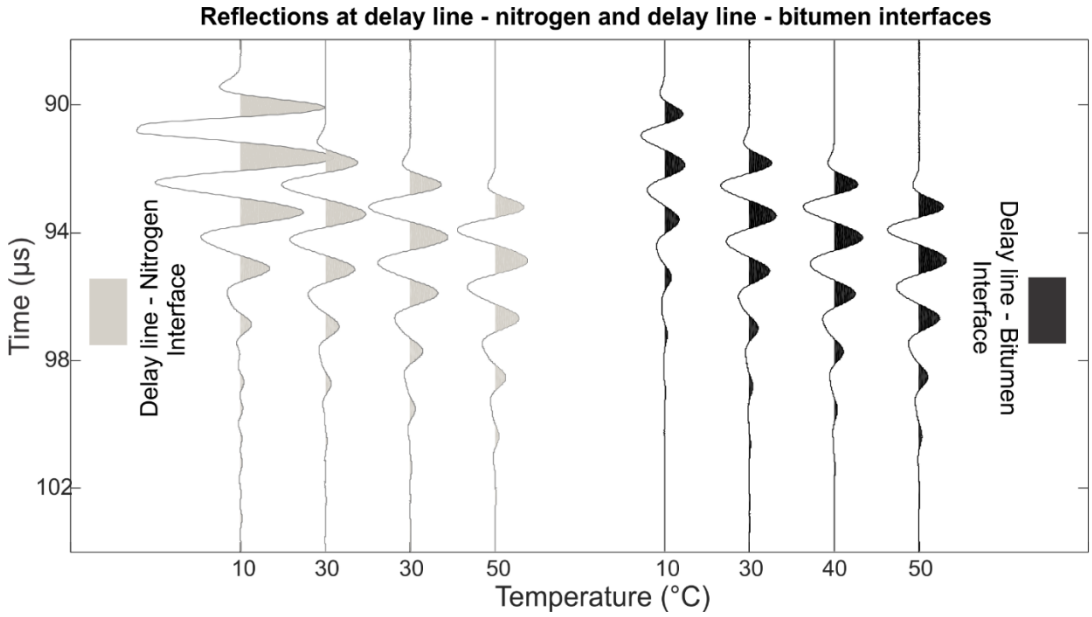

Figure 5. 10 The waveforms during the calibration and measurements with liquid, at different temperature and 2 MPa pressure. Observed ultrasonic waveforms reflected from the delay line – N_2 interface (light shade) and the delay line – bitumen interface (dark shade).

Table 5.6: Measured shear properties of bitumen at various temperature at 555 KHz, a middle frequency over the short bandwidth of the pulse (490 KHz to 650 KHz)

Temperature (°C)		10	30	40	50
Density (kg/m^3)		1033	1020	1015	1008
Reflection coefficient modulus, r		0.2395	0.6678	0.7533	0.8386
Phase θ (radian)		0.7094	0.0694	0.1041	0.109
Real part of the impedance R_l (kg/m^3).(m/s)		1.00×10^6	2.91×10^5	2.02×10^5	1.51×10^6
Imaginary part the impedance X_l (kg/m^3).(m/s)		3.32×10^5	4.87×10^4	7.30×10^4	1.51×10^6
Real part of the shear modulus G' (GPa)		0.924	0.148	0.087	0.046
Imaginary part of the shear modulus G" (GPa)		0.643	0.028	0.029	0.019
Shear wave speed v (m/s)		1094.1	386	304.5	226.5
Relaxation time τ_S (s)		4.0×10^{-7}	1.48×10^{-6}	8.46×10^{-7}	6.94×10^{-7}
Dynamic Viscosity η *(Pa.s)*	Newtonian	179.6	7.7	8.2	5.4
	Maxwell	550.5	225.71	82	37
	Brookfield DV2T	1.4×10^4	770	280	74

The phase shift θ is nontrivial and indicates that the shear properties in this bitumen cannot be determined by simple comparison of the reflected reference and

sample waveforms as was possible for the glycerol above and as applied by earlier workers (Han et al.; Greenwood and Bamberger, 2002). Variations in θ (Table 5.5) are not monotonic although this may reflect more uncertainty in its determination. Regardless, these results show that the bitumen studied retains substantial shear impedance over this range of temperatures as shown in the corresponding *G'* and *G"* calculated using Eqs. (13) and (14). Under the presumption that temperature controls *G'* and *G"* behave according to an empirical Arrhenius equation with a form:

$$G = Ae^{-K/T} \tag{27}$$

where the temperature is given in °K, the pre-exponential term *A* is the value of G at absolute zero, and the constant *K* related to the activation energy of the process being studied controls the rate of change with temperature. *G'* and *G"* are displayed in an Arrhenius plot (Figure 5.11) of *ln(G)* vs *1/T* within which properties behaving according the Arrhenius Eq. (27) will plot along a line. *G'* appears to follow Arrhenius behavior well, while *G"* shows considerable scatter.

We note that many authors, e.g., Abivin et al. (Abivin et al., 2012), have discussed the deviation of bitumen behavior from Eq. (25) but the preliminary nature of the current study does not warrant more detailed interpretation. That said, it is worthwhile to compare the moduli observed here with the lower frequency rheometer measurements on similar heavy oils by other workers. Behzadfar and Hatzikiriakos (Behzadfar and Hatzikiriakos, 2013) measured both *G'* and *G"* using a plate and cone rheometer at 6 temperatures from -30°C to 90°C over the range of frequencies from ~0.3 Hz to 3.2 kHz on an Athabasca bitumen. Their peak values for *G'* and *G"* are respectively only ~ 32 MPa and ~ 10 MPa at the coldest temperature. Abivin et al. (Abivin et al., 2012) found similar values in their heaviest oils. Hasan et al. (Hasan et al., 2009) report only values for *G"* (their viscous modulus) that attain peak values slightly greater than 1 MPa at ~50°C and 100 Hz. All of these are substantially lower than the values given by the ultrasonic

method here. It must further be noted that the rheometric equipment typically operates at maximum frequencies of a few 100 Hz. However, in polymer research it is common practice to extend these data into the MHz range by applying the time-temperature superposition principle (Markovitz, 1975); but this does not change the magnitudes of *G'* and *G"* further highlighting the differences with the ultrasonic observations here. Direct comparisons of ultrasonic and rheometric shear modulus measurements on polymers are rare with the only example of which we are aware being that of Longin et al. (Longin et al., 1998), on a series of heavy polydimethylsiloxanes ('silicone oils'). They were able to fit their data using different relaxation spectra models, inspection of their *G'* and *G"* versus frequency plots may display a change in behavior of the ultrasonic values.

Conversely, however, Behura et al. (Behura et al., 2007) obtain peak values of *G'* ~ 1 GPa at room temperature on an asphaltene rich heavy oil extracted from core samples at frequencies less than 100 Hz, this value is more comparable to our observations. Preliminary studies by Rodriques and Batzle (Rodrigues and Batzle, 2015) show that the magnitude of *G'* depended on strains encountered between ultrasonic pulse transmission, forced compressional oscillations, and parallel plate rheometry that they suggest may be due to breaking of weak bonds within the material in the latter test. Their ultrasonic values of *G'* are ~ 0.8 GPa at room temperature are similar to those found here. Batzle et al. (Batzle et al., 2006), too, in difficult shear wave pulse transmission tests on a Venezuelan heavy oil estimate *G'* to range from ~1 GPa at °C to ~0.4 GPa at 50°C also comparable to our observations.

Part of these discrepancies may be due to differences in the levels of strain and/or strain rate applied in the differing tests. Zhao and Machel (Zhao and Machel, 2012) develop a similar hypothesis based on their observations at constant temperature of the dependence of viscosity, determined from parallel plate rheometry, on shear rate.

Finally, Han et al. (Han, Liu, and Baztle, 2008) describe similar ultrasonic shear reflection measurements with the primary goal of obtaining the shear wave speed in the bitumen as a function of temperature. They obtain the bitumen's shear impedance, wave speed, and modulus using reflected amplitudes only and show values possibly representative of *G'* of about 0.5 GPa at low temperatures again comparable to the current measurements.

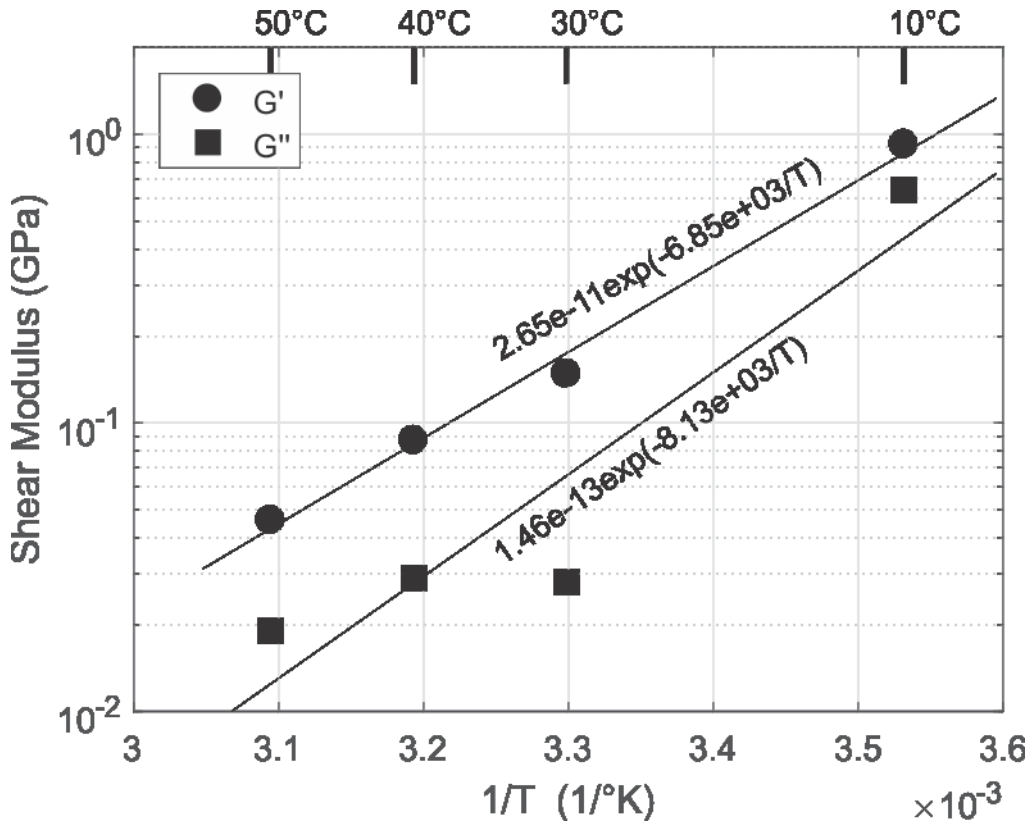

Figure 5. 11 Arrhenius plot of the Real *G'* and imaginary *G"* components for bitumen versus *1/T*. The equations shown correspond to the parameters fit to Eq. (27). Corresponding temperatures in °C shown at top.

The shear wave speed of bitumen as indirectly determined from ultrasonic shear wave reflectometry (Han et al.) or by direct pulse transmission (Batzle et al., 2006) has been provided in the geophysical literature. Our calculated values for this velocity (Table 5.5) are plotted (Figure 5.12) and display a significant variation with temperature. These

values, too, are comparable to the earlier observations. We have also calculated the penetration depth δ for these waves as this give some indication as to how far from the delay line – fluid interface the waves sense into the fluid. The values here at the 555 kHz also decrease rapidly with temperature but suggest that the waves sense distances on the order of 1 mm or less. This is important as we expect this to exceed the dimensions of the complex colloidal nature of bitumen (Bagheri et al., 2012; Loeber et al., 1996) particularly given the existence of water droplets within our material (~10 μm), as observed under microscope.

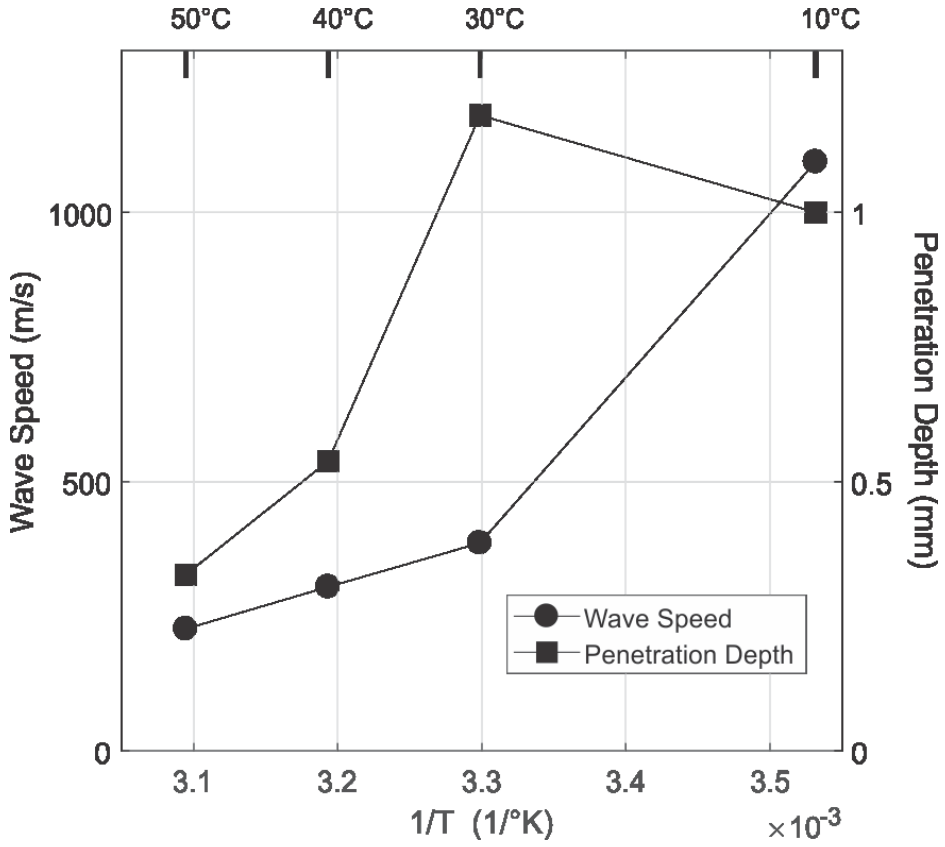

Figure 5. 12 Arrhenius plot of hypothetical shear wave speeds ($v = \omega/k'$) and penetration depth ($\delta = 1/k''$)

The viscosities measured by the Searle spindle method (Table 5.5) at low frequencies are compared against those calculated using the Newtonian (Eq. 17) and the

Maxwell (Eq. 25) models in an Arrhenius plot (Figure 5.13). The Newtonian values are substantially less than the others, but this should not be unexpected as within the temperature range studied the bitumen is expected to clearly behave as a non-Newtonian fluid. The values calculated assuming a single Maxwell relaxation, too, are all lower than those measured using the spindle but at the highest temperature they differ only by a factor of 2.

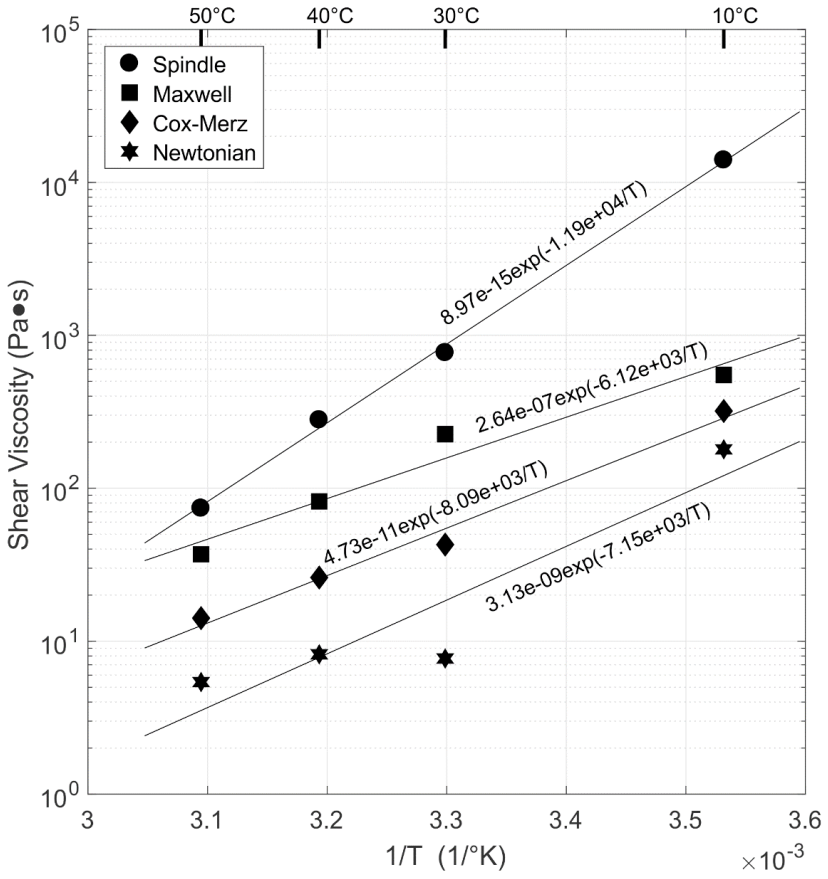

Figure 5. 13. Dynamic shear viscosity of bitumen calculated using the Newtonian, the Maxwell models, and the Cox-Merz rule in an Arrhenius plot, compared with the Searle spindle method at low frequencies.

There are a number of possible reasons for this discrepancy which has also been observed by a number of other works that employ high frequencies. Using an immersed torsional waveguide method operating at frequencies ~ 50 kHz, Shephard et al. (Shepard et al., 1999) obtained a good match for a variety of fluids (water, hydrocarbon motor oils, and glycerol) with viscosities < 0.3 Pa•s, but poor agreement for three silicone oil viscosity standards in which the ultrasonic values were generally significantly less than those measured using a similar rotational instrument. They suggested that this difference arose from the degree of polymerization within the silicone oils. More recently, Rabani et al., (2011) obtained similar results with ultrasonic (~625 kHz) torsional wave guide viscosities significantly lower than those provided by the rotational viscometer for a series of viscous non-Newtonian fluids and two multi-phase slurries. They estimated their shear rates to be ~5000 s^{-1} for water which are much larger than the rotational viscometer values near100 s^{-1} (Table 5.1).

Briefly, the differences are likely due to combination of i) inappropriate use of Maxwell equation with single relaxation, ii) significant differences in the methods with displacements, strains, strain rates, and duration – suggesting that high frequency methods do not really see the entanglements in the polymers as they have not pushed the material far enough that it becomes important, and iii) the shear thinning discussion which may be part of the same phenomena as (ii).

(i) Maxwell model as in equation (19) is rather too simple to characterize the viscoelastic behaviour of bitumen. Bitumen is a mixture of different components and can be considered as a long chain polymer (Vasiljevic-Shikaleska et al., 2010; Read and Whiteoak, 2003; Zhu et al., 2014). This model with single relaxation may fail to account for the distributions of molecular weight and the relaxation spectra. In a more mature model that reckons the molecular weight distributions, Barlow et al. (Barlow et al., 1964)

showed that in a long chain polymer many relaxation times occur and their summation over segments of different length results in a broad frequency response. He expressed the viscosity of a polymer liquid with N equal segments in the chain as (Rabani et al., 2011; Rouse, 1953),

$$\eta' = \frac{6\eta}{\pi^2}\sum_{p=1}^{N}\frac{1}{p^2+\omega^2\frac{\tau'}{p^2}} \tag{28}$$

$$\tau' = \frac{3\eta\overline{M_n}}{\pi^2\rho_l RT} \tag{29}$$

where $\tau'$is the effective relaxation time of the molecule, $\overline{M_n}$ represents the number average molecular weight (calculated from the mass spectroscopy, Figure 5.3), R is the gas constant and T is the absolute temperature. The summation occurs over p = 1 to N, where p = 1 represents the whole molecule, and $p = N$ stands for the shortest segment of the polymer chain (Rouse, 1953; Rabani et al., 2011; Barlow et al., 1964). The use of the static viscosity (η) measured with the conventional rheometer and relaxation time of Eq. (29), we can calculate the expected frequency dependent shear viscosity through Eq. (28). At $T = 303.15\ K$, for $\overline{M_n} = 0.652\ kg/mol$, $R = 8.3145\ Pa.m^3/K.mol$, $T = 303.15\ K$, $\rho_l = 1020\ kg/m^3$, $\eta = 770$ Pa•s, and N = 212992 (total number of molecule from the mass spectra, Figure 5.3), the viscosity η'=35.7 Pa•s, which is still significantly lower than the rheometer value. It's important to note that this formulation is for a mono-disperse polymer, whereas bitumen is poly-dispersed (Barlow et al., 1964).

(ii) The principles of operation between the ultrasonic and the rotational techniques, too, may contribute to the differences in G and η. Rotational viscometers operate by continuously shearing the fluid at low shear rates while measuring torque; during the course of the measurement the fluid essentially experiences infinite shear strain at timescale of seconds. In contrast, in the ultrasonic method here the fluid is

perturbed by small amplitude (< 1 μm), short duration (~ 13 μs) pulses with higher strain rates of ~12 s^{-1} (Appendix 5.A), whereas, for the Brookfield viscometer the strain is significantly smaller at 0.6 s^{-1} (Table 5.1).

We suggest that the significant discrepancies in bitumen's viscosity among the ultrasonic and rheometer techniques are due to the considerable variations in their shear/strain rate rather the viscoelastic relaxation effects in the polymer molecule. Bazyleva et al. (Bazyleva et al., 2010a), and Zhao and Machel (Zhao and Machel, 2012) showed that viscosity of bitumen - particularly from Athabasca and Grosmont formation – drops noticeably with increasing shear rate. Rodrigues and Batzle (Rodrigues and Batzle, 2015) also doubted the validity of conventional rheometer operating at the higher strain amplitude. The shear properties (moduli) of heavy oil measured by their tension/compression technique at low amplitude are much larger than the rheometer results.

6. Conclusions

An adapted version of the ultrasonic pulse echo method is used to measure the shear properties of a viscoelastic hydrocarbon. Although the shear moduli are comparable to some similar measurements, the measured values of dynamic shear viscosity are noticeably smaller than the results from conventional rheometer. We have shown that viscoelastic relaxation and shear thinning phenomena in a highly viscous material significantly influence the high-frequency viscosity results. The application of shear wave reflection technique for the extremely viscous material might not be the best approach to study the complex rheology but it is certainly the simplest method to examine the overall response of the shear behavior of the fluid over a period of temperature, pressure, and frequency.

On a more practical note, regardless of the disagreements between rheometer and ultrasonic shear reflectivity the latter method does display a good sensitivity to variations in the shear properties of highly viscous bitumen. While a thorough theoretical understanding of these differences remains elusive, this work does show that the shear wave reflectometry can provide quantitative measures of changes in the material; this information alone may be useful for empirically based monitoring of fluid conditions.

Appendix 5.A

Calculation of Shear rate

The strain rate is calculated from the displacement amplitude, Eq. (3), by first differentiating it with respect to the propagation distance (x) to get an estimate of the strain. The strain is then differentiated with respect to the propagation time (t) to get the strain rate. This yields a strain rate of $A_o\omega k'$. At 40°C, for example, the frequency ($\omega = 3.52\times10^6$ s^{-1}) and real part of the wave number ($k' = 1.15\times10^4$ m^{-1}) are already known. The initial amplitude (A_o) can be calculated using the shear displacement of the PZT element. The electric field on the element = applied voltage / thickness of the element = 300 V / 0.001 m = 3.0×10^5 V/m = E_1. The shear strain on the sample is then $\varepsilon_5 = d_{15}E_1$ = $(480\times10^{-12}$ m/V) × (200000 V/m) ~ 1.44×10^{-4}, where d_{15} the piezoelectric charge constant for the PZT element is taken from the manufacturer (APC International Ltd). The displacement of the element should be = thickness × strain = $(1.0\times10^{-3}$ m) *(1.44×10^{-4}) =144 *nm*. However, due to the signal attenuation through the delay line, the observed displacement would be scaled down by a factor of about 400-500 (estimated from the observed amplitude). Therefore, the initial displacement (A_o) would be on the order of 0.3 *nm*. Therefore, the strain rate ($A_o\omega k'$) in the ultrasonic technique is ~ 12 s^{-1}, whereas, for the Brookfield viscometer the strain is significantly smaller at 0.6 s^{-1} (Table 5.1).

References

Abivin, P., S. D. Taylor, and D. Freed. 2012, Thermal Behavior and Viscoelasticity of Heavy Oils. Energy & Fuels, **26**, no. 6,3448-3461. doi: 10.1021/ef300065h.

Bagheri, S. R., B. Masik, P. Arboleda, Q. Wen, K. H. Michaelian, and J. M. Shaw. 2012, Physical Properties of Liquid Crystals in Athabasca Bitumen Fractions. Energy & Fuels, **26**, no. 8,4978-4987. doi: 10.1021/ef300339v.

Barlow, A. J., G. Harrison, and J. Lamb. 1964, Viscoelastic relaxation of polydimethylsiloxane liquids. Proceedings of the Royal Society of London Series a-Mathematical and Physical Sciences, **282**, no. 1388,228-+. doi: 10.1098/rspa.1964.0229.

Barlow, A. J., and S. Subramanian. 1966, EXPERIMENTAL TECHNIQUE FOR DETERMINATION OF VISCOELASTIC PROPERTIES OF LIQUIDS IN FREQUENCY RANGE 5-75 MC/S. British Journal of Applied Physics, **17**, no. 9,1201-+. doi: 10.1088/0508-3443/17/9/313.

Batzle, M., R. Hofmann, and D.-H. Han. 2006, Heavy oils - seismic properties. The Leading Edge, **25**, no. 6,750-756.

Baumgaertel, M., and H. H. Winter. 1989, Determination of discrete relaxation and retardation time spectra from dynamic mechanical data. Rheologica Acta, **28**, no. 6,511-519. doi: 10.1007/bf01332922.

Bazyleva, A. B., A. Hasan, M. Fulem, M. Becerra, and J. M. Shaw. 2010, Bitumen and Heavy Oil Rheological Properties: Reconciliation with Viscosity Measurements. Journal of Chemical and Engineering Data, **55**, no. 3,1389-1397. doi: 10.1021/je900562u.

Behura, J., M. Batzle, R. Hofmann, and J. Dorgan. 2007, Heavy oils: Their shear story. Geophysics, **72**, no. 5,E175-E183. doi: 10.1190/1.2756600.

Behzadfar, E., and S. G. Hatzikiriakos. 2013, Viscoelastic properties and constitutive modelling of bitumen. Fuel, **108**, no. Supplement C,391-399. doi: https://doi.org/10.1016/j.fuel.2012.12.035.

Camara, V. C., and D. Laux. 2010, High frequency shear ultrasonic properties of water/sorbitol solutions. Ultrasonics, **50**, no. 1,6-8. doi: 10.1016/j.ultras.2009.08.002.

Castro, L. V., and F. Vazquez. 2009, Fractionation and Characterization of Mexican Crude Oils. Energy & Fuels, **23**, no. 3,1603-1609. doi: 10.1021/ef8008508.

Cheng, N.-S. 2008, Formula for the Viscosity of a Glycerol–Water Mixture. Industrial & Engineering Chemistry Research, **47**, no. 9,3285-3288. doi: 10.1021/ie071349z.

Deblock, Y., F. Lefebvre, E. Radziszewski, and B. Nongaillard. 1998, The determination of the viscoelastic properties of liquid materials at ultrasonic frequencies by CW mode impedance measurements. IEEE Transactions on Instrumentation and Measurement, **47**, no. 3,680-685. doi: 10.1109/19.744324.

Dixon, S., and B. Lanyon. 2005, Phase change measurement of ultrasonic shear waves on reflection from a curing epoxy system. Journal of Physics D-Applied Physics, **38**, no. 22,4115-4125. doi: 10.1088/0022-3727/38/22/016.

Fenistein, D., and L. Barré. 2001, Experimental measurement of the mass distribution of petroleum asphaltene aggregates using ultracentrifugation and small-angle X-ray scattering. Fuel, **80**, no. 2,283-287. doi: https://doi.org/10.1016/S0016-2361(00)00072-7.

Fergusson, F. A. A., E. W. Guptill, and A. D. Macdonald. 1954, Velocity of sound in glycerol. Journal of the Acoustical Society of America, **26**, no. 1,67-69. doi: 10.1121/1.1907292.

Fitch, D. A., B. K. Hoffmeister, and J. de Ana. 2010, Ultrasonic evaluation of polyether ether ketone and carbon fiber-reinforced PEEK. Journal of Materials Science, **45**, no. 14,3768-3777. doi: 10.1007/s10853-010-4428-1.

Franco, E. E., J. C. Adamowski, and F. Buiochi. 2010, Ultrasonic Viscosity Measurement Using the Shear-Wave Reflection Coefficient with a Novel Signal Processing Technique. Ieee Transactions on Ultrasonics Ferroelectrics and Frequency Control, **57**, no. 5,1133-1139. doi: 10.1109/tuffc.2010.1524.

Greenwood, M. S., J. D. Adamson, and L. J. Bond. 2006, Measurement of the viscosity-density product using multiple reflections of ultrasonic shear horizontal waves. Ultrasonics, **44**, no. SUPPL. doi: 10.1016/j.ultras.2006.05.093.

Greenwood, M. S., and J. A. Bamberger. 2002, Measurement of viscosity and shear wave velocity of a liquid or slurry for on-line process control. Ultrasonics, **39**, no. 9,623-630. doi: 10.1016/S0041-624X(02)00372-4.

Han, D.-h., J. Liu, and M. Baztle. 2008, Seismic properties of heavy oils—measured data. The Leading Edge, **27**, no. 9,1108-1115. doi: 10.1190/1.2978972.

Han, D. h., J. Liu, and M. Batzle. Measurement of shear wave velocity of heavy oil, SEG Technical Program Expanded Abstracts 2005. 1513-1516.

Hasan, M. D. A., M. Fulem, A. Bazyleva, and J. M. Shaw. 2009, Rheological Properties of Nanofiltered Athabasca Bitumen and Maya Crude Oil. Energy & Fuels, **23**,5012-5021. doi: 10.1021/ef900313r.

Kaatze, U. 2017, Dielectric and structural relaxation in water and some monohydric alcohols. Journal of Chemical Physics, **147**, no. 2,9. doi: 10.1063/1.4991850.

Kariznovi, M., H. Nourozieh, and J. Abedi. 2014, Measurement and Correlation of Viscosity and Density for Compressed Athabasca Bitumen at Temperatures Up to 200 degrees C. Journal of Canadian Petroleum Technology, **53**, no. 6,330-338.

Litovitz, T. A., and C. M. Davis. 1965, Structural and Shear Relaxation in Liquids. Vol. 2: ACADEMIC PRESS INC.

Loeber, L., G. Muller, J. Morel, and O. Sutton. 1998, Bitumen in colloid science: a chemical, structural and rheological approach. Fuel, **77**, no. 13,1443-1450. doi: https://doi.org/10.1016/S0016-2361(98)00054-4.

Loeber, L., O. Sutton, J. Morel, J. M. Valleton, and G. Muller. 1996, New direct observations of asphalts and asphalt binders by scanning electron microscopy and atomic force microscopy. Journal of Microscopy-Oxford, **182**,32-39. doi: 10.1046/j.1365-2818.1996.134416.x.

Longin, P. Y., C. Verdier, and M. Piau. 1998, Dynamic shear rheology of high molecular weight polydimethylsiloxanes: comparison of rheometry and ultrasound. Journal of Non-Newtonian Fluid Mechanics, **76**, no. 1-3,213-232. doi: 10.1016/s0377-0257(97)00119-5.

Lu, S. X., P. Cebe, and M. Capel. 1996, Thermal stability and thermal expansion studies of PEEK and related polyimides. Polymer, **37**, no. 14,2999-3009. doi: https://doi.org/10.1016/0032-3861(96)89397-9.

Macosko, C. W. 1994, Rheology : principles, measurements, and applications Wiley-VCH.

Markovitz, H. 1975, Superposition in rheology. Journal of Polymer Science Part C-Polymer Symposium, no. 50,431-456.

Mason, W. P., W. O. Baker, H. J. McSkimin, and J. H. Heiss. 1949, Measurement of shear elasticity and viscosity of liquids at ultrasonic frequencies. Physical Review, **75**, no. 6,936-946. doi: 10.1103/PhysRev.75.936.

Maxwell, J. C. 1867, On the Dynamical Theory of Gases. Philosophical Transactions of the Royal Society of London, **157**,49-88.

McSkimin, H. J., and P. Andreatch. 1967, Measurement of dynamic shear impedance of low viscosity liquids at ultrasonic frequencies. Journal of the Acoustical Society of America, **42**, no. 1,248-+. doi: 10.1121/1.1910560.

Moreno Arciniegas, L. S., Asphaltene Precipitation During Solvent Injection at Different Reservoir Conditions and Its Effects on Heavy-Oil Recovery from Oilsands.

Oconnell, R. J., and B. Budiansky. 1978, Measures of dissipation in viscoelastic media. Geophysical Research Letters, **5**, no. 1,5-8. doi: 10.1029/GL005i001p00005.

Oneil, H. T. 1949, Reflection and refraction of plane shear waves in viscoelastic media. Physical Review, **75**, no. 6,928-935. doi: 10.1103/PhysRev.75.928.

Peleties, F., J. J. Segovia, J. P. M. Trusler, and D. Vega-Maza. 2010, Thermodynamic properties and equation of state of liquid di-isodecyl phthalate at temperature between (273 and 423)K and at pressures up to 140MPa. The Journal of Chemical Thermodynamics, **42**, no. 5,631-639. doi: https://doi.org/10.1016/j.jct.2009.12.002.

Rabani, A., R. E. Challis, and V. J. Pinfield. 2011, The torsional waveguide viscosity probe: Design and anomalous behavior. IEEE Transactions on Ultrasonics, Ferroelectrics, and Frequency Control, **58**, no. 8,1628-1640. doi: 10.1109/TUFFC.2011.1990.

Rabbani, A., D. R. Schmitt, J. Nycz, and K. Gray. 2017, Pressure and temperature dependence of acoustic wave speeds in bitumen-saturated carbonates: Implications for seismic monitoring of the Grosmont Formation. GEOPHYSICS, **82**, no. 5,MR133-MR151. doi: 10.1190/geo2016-0667.1.

Rae, P. J., E. N. Brown, and E. B. Orler. 2007, The mechanical properties of poly(ether-ether-ketone) (PEEK) with emphasis on the large compressive strain response. Polymer, **48**, no. 2,598-615. doi: 10.1016/j.polymer.2006.11.032.

Read, J., and D. Whiteoak. 2003, The Shell Bitumen Handbook, The Shell Bitumen Handbook: Thomas Telford Ltd: London.

Rodrigues, P. E., and M. L. Batzle. 2015, Strain amplitude dependence of shear modulus in heavy oils: Rheometer versus tension/compression technique. Geophysics, **80**, no. 4,L35-L43. doi: 10.1190/geo2014-0354.1.

Rouse, P. E. 1953, A Theory of the Linear Viscoelastic Properties of Dilute Solutions of Coiling Polymers. The Journal of Chemical Physics, **21**, no. 7,1272-1280. doi: 10.1063/1.1699180.

Schirru, M. M., and R. S. Dwyer-Joyce. 2015, A model for the reflection of shear ultrasonic waves at a thin liquid film and its application to viscometry in a journal bearing. Proceedings of the Institution of Mechanical Engineers, Part J: Journal of Engineering Tribology, **0**, no. 0,1-13. doi: 10.1177/1350650115610357.

Shah, V. V., and K. Balasubramaniam. 2000, Measuring Newtonian viscosity from the phase of reflected ultrasonic shear wave. Ultrasonics, **38**, no. 9,921-927. doi: 10.1016/s0041-624x(00)00033-0.

sheely, M. L. 1932, Glycerol Viscosity Tables. Industrial & Engineering Chemistry, **24**, no. 9,1060-1064. doi: 10.1021/ie50273a022.

Sheen, S.-H., H.-T. Chien, and A. Raptis. 1996, Measurement of shear impedances of viscoelastic fluids. In 1996 IEEE Ultrasonics Sympoisum. San Antonio: IEEE.

Shepard, C. L., B. J. Burghard, L. A. Friesel, B. P. Hildebrand, M. Xang, A. A. Diaz, and C. W. Enderlin. 1999, Measurements of density and viscosity of one- and two-phase fluids with torsional waveguides. Ieee Transactions on Ultrasonics Ferroelectrics and Frequency Control, **46**, no. 3,536-548. doi: 10.1109/58.764840.

Slie, W. M., A. R. Donfor, and T. A. Litovitz. 1966, Ultrasonic shear and longitudinal measurements in aqueous glycerol. Journal of Chemical Physics, **44**, no. 10,3712-&. doi: 10.1063/1.1726524.

Speight, J. G. 1999, The chemical and physical structure of petroleum: effects on recovery operations. Journal of Petroleum Science and Engineering, **22**, no. 1,3-15. doi: https://doi.org/10.1016/S0920-4105(98)00051-5.

Stastna, J., L. Zanzotto, and K. Ho. 1994, Fractional complex modulus manifested in asphalts. Rheologica Acta, **33**, no. 4,344-354. doi: 10.1007/bf00366961.

Vasiljevic-Shikaleska, A., F. Popovska-Pavlovska, S. Cimmino, D. Duraccio, and C. Silvestre. 2010, Viscoelastic properties and morphological characteristics of polymer-modified bitumen blends. Journal of Applied Polymer Science, **118**, no. 3,1320-1330. doi: 10.1002/app.32317.

Vernon-Carter, E. J., G. Avila-de la Rosa, H. Carrillo-Navas, Y. Carrera, and J. Alvarez-Ramirez. 2016, Cox-Merz rules from phenomenological Kelvin-Voigt and Maxwell models. Journal of Food Engineering, **169**,18-26. doi: 10.1016/j.jfoodeng.2015.08.005.

Voigt, T. 2005, The application of an ultrasonic shear wave reflection method for nondestructive testing of cement-based materials at early ages.

Yang, D., M. H. Mohebati, S. Brand, and C. Bennett. 2014, Thermal recovery of bitumen from the grosmont carbonate formation - Part 2: Pilot interpretation and development strategy. Journal of Canadian Petroleum Technology, **53**, no. 4,212-223. doi: 10.2118/171561-PA.

Zhao, Y., and H. G. Machel. 2012, Viscosity and other rheological properties of bitumen from the Upper Devonian Grosmont reservoir, Alberta, Canada. Aapg Bulletin, **96**, no. 1,133-153. doi: 10.1306/04261110180.

Zhu, J., B. Birgisson, and N. Kringos. 2014, Polymer modification of bitumen: Advances and challenges. European Polymer Journal, **54**,18-38. doi: https://doi.org/10.1016/j.eurpolymj.2014.02.005.

Chapter 6: Conclusions

The Grosmont carbonate formation in Northern Alberta holds a significant amount of bitumen in place. Thermal recovery processes are necessary for this formation, like any other bitumen saturated reserves, to reduce its extremely high viscosity to make it mobile for the production. In doing so, the physical properties of the reservoir change due to the combined effects of increased temperature, pressure, and the substitution of bitumen with water and steam. The changes can be observed with time lapse seismic monitoring. However, seismic surveys are attributed to many factors such as velocities, densities, attenuation, and shear properties of the host rock and saturating fluids and it is not straightforward to isolate their effects. Therefore, we started this thesis with pointing out two interests – how one can disintegrate fluid's or rock's properties as the most influential factor causing the changes in seismic surveys, and how the fluid substitutions models can be improved?

To address these issues, we have studied physical properties of carbonates saturated with bitumen and later with water, and produced raw bitumen over various temperature, pressure, and saturation. For all the cases, we have implemented various ultrasonic techniques for its ease of use and to compare the observations with the previous related studies.

6.1 Contributions

First, we observed significant drops in the measured longitudinal and shear wave speeds in bitumen saturated carbonates from Grosmont formation with the increase of temperature. We, then, carried out validity tests of the standard fluid substitution models using a variety of classic bounds, inclusion, and poroelastic models, such as Voigt

– Reuss, Hashin – Shtrikman, and Biot – Gassmann family. The standard range of Biot-Gassmann based models come only closer to the observed temperature dependent moduli but still incapable of describing the behavior particularly with the increasing temperature. This study was done with one bitumen-saturated sample, but more studies with samples at different saturation levels, porosity, permeability, and compositions are required to achieve a conclusive model. However, we expect, as with other researchers, that the complex properties of bitumen are the dominating factors that influence the experimental observations most.

The complex shear moduli of bitumen do not vanish until the temperature reaches to ~60°C and as such the bitumen retains significant solid-like behaviour. This led us to calculate complex longitudinal moduli from the measured P-wave speed and attenuation at various temperatures and pressures. We observed significant declines in the wave speeds with the increase in temperature but weak influence from the changes in pressure. The P-wave attenuation also declined monotonically with temperature, although they had a reverse trend at the higher temperature. The change in pressure does not appear to influence the attenuation. Combining these results with parallel complex shear modulus measurements from a parallel study, in chapter 5, suggests that the shear modulus is a significant portion of the P-wave modulus at temperatures below ~60°C and reinforces that the P-wave speed cannot be used in isolation to provide the bitumen bulk modulus. The discrepancies among the bulk moduli and longitudinal moduli suggests that proper modelling of seismic responses through heavy oil saturated formations may require consideration of the imaginary part of the bulk moduli or equivalently its bulk viscosity.

The shear properties studies in the last chapter reveal that bitumen possesses substantial shear moduli, both the storage and loss moduli, over the range of temperatures from 10°C to 50°C. The shear wave speeds also display a significant

variation in this temperature. In fact, the virgin in situ temperatures in this reservoir is only about 10°C to 14°C; this is colder than most of the earlier studies which typically begin at room temperature. Therefore, these studies provide us a chance to look how bitumen's shear properties behave at the lower temperature and to implement fluid substitutions models accurately which require concrete information of the fluid's shear moduli. Moreover, the ultrasonic shear reflection technique was never been used for the non-Newtonian bitumen to measure the viscosity. We found that the viscosity obtained with this technique is lower than the standard Spindle method. We have shown that viscoelastic relaxation and, most importantly, the shear thinning phenomena in a highly viscous material significantly influence the high-frequency viscosity results. Despite the discrepancies, the ultrasonic shear reflection technique with a proper delay line for the low impedance bitumen can provide quantitative measures of its shear properties, which are useful information for monitoring purposes during its processing and production.

6.2 Suggested future works

The overall seismic responses can depend on various factors but are heavily influenced by the state of the fluid saturation within the rock. Viscoelastic properties of a viscous fluid-saturated rock are predominantly dependent on the frequency, the fluid's bulk and shear properties, and the rock frame stiffness. While the suites of measurements discussed in this thesis should help us characterizing the seismic behavior of bitumen and bitumen saturated carbonates, the proper interpretation of the seismic survey can undoubtedly be improved with a detailed understanding of the dynamic bulk properties of bitumen and –saturated rock at the seismic frequency.

Bulk relaxation type processes, e.g., bulk viscosity, can have as much influence as the shear viscosity for seismic dispersion and attenuation of rocks containing highly viscous liquids. In a viscoelastic material, applied hydrostatic stress can create a bulk

deformation like shear stress creates shear deformation and there will be a phase lag between the stress and strain. Ultrasonic compressional wave reflection from bitumen, using similar approach or formulation of the shear wave reflection technique described in chapter 5, can provide valuable information on the bulk properties of bitumen. However, this measurement is still limited to a higher frequency (~1 MHz), whereas seismic frequencies are in the range of ~100 Hz. Therefore, low-frequency measurements of bulk properties are necessary to interpret the survey results. There are a couple of ways in the literature to create the oscillating hydrostatic stress such as using a pump. However, a pure form can involve a pressure vessel filled with fluid through which a sinusoidal pressure is generated using piezoelectric ceramics (PZT). This pressure change affects the sample contained within the vessel. Another set of PZT's observes the volumetric change inside the cell, which may lag behind the pulses initially applied to the fluid due to the elastic response of the sample. The idea was recently employed by Guillot and Trivett (2011), but in order to implement this for samples with such strong viscoelastic properties (e.g., bitumen); one needs to improve the technique. Firstly, the reference fluid needs to be studied extensively, e.g., its compressibility. An additional challenge for this technique lies within the theoretical understanding of the properties of piezoelectric ceramics at the desired experimental conditions.

The low frequency measurements can be used to measure dynamic properties of rock samples with any shape and characteristic. This could save resources when working with particular dimensions and types of core samples. Overall, reservoir's rocks properties at a seismic frequency can be implemented for any time-lapse seismic monitoring of geothermal and hydrocarbon reservoirs, CO_2 and nuclear waste storage sites etc.

Bibliography

Abivin, P., S. D. Taylor, and D. Freed. 2012, Thermal Behavior and Viscoelasticity of Heavy Oils. Energy & Fuels, **26**, no. 6,3448-3461. doi: 10.1021/ef300065h.

Adam, L., M. Batzle, and I. Brevik, 2006, Gassmann's fluid substitution and shear modulus variability in carbonates at laboratory seismic and ultrasonic frequencies: GEOPHYSICS, **71**, no. 6, F173-F183. doi: 10.1190/1.2358494.

Agar, J.G., N.R. Morgenstern, and J.D. Scott, Thermal expansion and pore pressure generation in oil sands, Can. Geotech. J., 23, 327-333, 1986.

Agosta, F., M. Prasad, and A. Aydin, 2007, Physical properties of carbonate fault rocks, fucino basin (Central Italy): implications for fault seal in platform carbonates: Geofluids, **7**, no. 1, 19-32.

Anselmetti, F. S., and G. P. Eberli, 1993, Controls on sonic velocity in carbonates: Pure and Applied Geophysics, **141**, no. 2-4, 287-323. doi: 10.1007/bf00998333.

Ardakani, E. P., D. R. Schmitt, and T. Bown. 2014, Detailed topography of the Devonian Grosmont Formation surface from legacy high-resolution seismic profiles, northeast Alberta. Geophysics, **79**, no. 4,B135-B149. doi: doi: 10.1190/geo2013-0268.1.

Baechle, G. T., G. P. Eberli, R. J. Weger, and J. L. Massaferro, 2009, Changes in dynamic shear moduli of carbonate rocks with fluid substitution: GEOPHYSICS, **74**, no. 3,E135-E147. doi: 10.1190/1.3111063.

Bakhorji A.M., 2010, Laboratory measurements of static and dynamic elastic properties in carbonate: PhD thesis. University of Alberta, Edmonton, Alberta, Canada.

Bagheri, S. R., B. Masik, P. Arboleda, Q. Wen, K. H. Michaelian, and J. M. Shaw. 2012, Physical Properties of Liquid Crystals in Athabasca Bitumen Fractions. Energy & Fuels, **26**, no. 8,4978-4987. doi: 10.1021/ef300339v.

Balasubramaniam, K., V. V. Shah, R. D. Costley, G. Boudreaux, and J. P. Singh. 1999, High temperature ultrasonic sensor for the simultaneous measurement of viscosity and temperature of melts. Review of Scientific Instruments, **70**, no. 12,4618-4623. doi: 10.1063/1.1150123.

Barlow, A. J., G. Harrison, and J. Lamb. 1964, Viscoelastic relaxation of polydimethylsiloxane liquids. Proceedings of the Royal Society of London Series a-Mathematical and Physical Sciences, **282**, no. 1388,228-+. doi: 10.1098/rspa.1964.0229.

Barlow, A. J., and J. Lamb. 1959, The visco-elastic behaviour of lubricating oils under cyclic shearing stress. Proceedings of the Royal Society of London Series a-Mathematical and Physical Sciences, **253**, no. 1272,52-69. doi: 10.1098/rspa.1959.0178.

Barlow, A. J., and S. Subramanian. 1966, Experimental technique for determination of viscoelastic properties of liquids in frequency range 5-75 mc/s. British Journal of Applied Physics, **17**, no. 9,1201-+. doi: 10.1088/0508-3443/17/9/313.

Bass, J. D. 1995, Elasticity of minerals, glasses, and melts, in T.J. Ahrens, ed., Mineral Physics and Crystallography: A Handbook of Physical Constants: American Geophysical Union. 45-63.

Batzle, M., R. Hofmann, and D.-H. Han. 2006, Heavy oils - seismic properties. The Leading Edge, **25**, no. 6,750-756.

Batzle, M. L., D. H. Han, and R. Hofmann, 2006, Fluid mobility and frequency-dependent seismic velocity - Direct measurements: GEOPHYSICS, **71**, no. 1, N1-N9. doi: 10.1190/1.2159053.

Batzle, M. L., and Z. Wang, 1992, Seismic properties of pore fluids: GEOPHYSICS, **57**, 1396-1408. doi: 10.1190/1.1443207.

Baumgaertel, M., and H. H. Winter. 1989, Determination of discrete relaxation and retardation time spectra from dynamic mechanical data. Rheologica Acta, **28**, no. 6,511-519. doi: 10.1007/bf01332922.

Bazyleva, A. B., A. Hasan, M. Fulem, M. Becerra, and J. M. Shaw. 2010, Bitumen and Heavy Oil Rheological Properties: Reconciliation with Viscosity Measurements. Journal of Chemical and Engineering Data, **55**, no. 3,1389-1397. doi: 10.1021/je900562u.

Behura, J., M. Batzle, R. Hofmann, and J. Dorgan. 2007, Heavy oils: Their shear story. Geophysics, **72**, no. 5,E175-E183. doi: 10.1190/1.2756600.

Behzadfar, E., and S. G. Hatzikiriakos. 2013, Viscoelastic properties and constitutive modelling of bitumen. Fuel, **108**, no. Supplement C,391-399. doi: https://doi.org/10.1016/j.fuel.2012.12.035.

Behzadfar, E., and S. G. Hatzikiriakos. 2014, Rheology of bitumen: Effects of temperature, pressure, CO2 concentration and shear rate. Fuel, **116**,578-587. doi: https://doi.org/10.1016/j.fuel.2013.08.024.

Bhatia, A. B. 1985, Ultrasonic absorption : an introduction to the theory of sound absorption and dispersion in gases, liquids and solids: New York : Dover Publications, 1985, c1967.

Bhatia, A. B., and R. N. Singh. 1986, Mechanics of deformable media, Graduate student series in physics: Bristol : Hilger, c1986.

Bianco, E., S. Kaplan, and D. Schmitt. 2008, Seismic rock physics of steam injection in bituminous oil reservoirs. The Leading Edge, **27**, no. 9,1132-1137. doi: 10.1190/1.2978975.

Bianco, E., S., Kaplan, and D.R. Schmitt, 2010, Seismic rock physics of steam injection in bituminous-oil reservoirs – Chapter 6, in Heavy Oils: Reservoir Characterization and Production Monitoring, eds. Batzle, M., Chopra, S., Lines, L.R., and Schmitt, D.R.: Soc. Expl. Geophysicists, Tulsa, OK, **105-110**.

Biot, M.A., 1956, Theory of propagation of elastic waves in a fluid saturated porous solid. I. Low frequency range and II. Higher-frequency range: J. Acoust. Soc. Am., **28**, 168–191.

Biot, M.A., 1962, Mechanics of deformation and acoustic propagation in porous media: J. Appl. Phys., **33**, 1482–1498

Bouzidi, Y. 2003, The acoustic reflectivity and transmissivity of liquid saturated porous media : experimental tests of theoretical concepts: 2003.

Bouzidi, Y., and D. R. Schmitt. 2012, Incidence-angle-dependent acoustic reflections from liquid-saturated porous solids. Geophysical Journal International, **191**, no. 3,1427-1440. doi: 10.1111/j.1365-246X.2012.05695.x.

Burrowes, A., M. Teare, R. Marsh, and AAA. 2011, Alberta's Energy Reserves 2011 and Supply/Demand Outlook 2012-2021. . Annual Report ST98-2011, Energy Resources Conservation Board, Calgary, Alberta (June 2011).

Butler, R. 1991, Thermal recovery of oil and bitumen: Prentice Hall.

Camara, V. C., and D. Laux. 2010, High frequency shear ultrasonic properties of water/sorbitol solutions. Ultrasonics, **50**, no. 1,6-8. doi: 10.1016/j.ultras.2009.08.002.

Castro, L. V., and F. Vazquez. 2009, Fractionation and Characterization of Mexican Crude Oils. Energy & Fuels, **23**, no. 3,1603-1609. doi: 10.1021/ef8008508.

Chapman, M., E. R. Liu, and X. Y. Li. 2006, The influence of fluid-sensitive dispersion and attenuation on AVO analysis. Geophysical Journal International, **167**, no. 1,89-105. doi: 10.1111/j.1365-246X.2006.02919.x.

Cheng, N.-S. 2008, Formula for the Viscosity of a Glycerol–Water Mixture. Industrial & Engineering Chemistry Research, **47**, no. 9,3285-3288. doi: 10.1021/ie071349z.

Chhabra, R. P., and J. F. Richardson. 2008, Chapter 1 - Non-Newtonian Fluid Behaviour, Non-Newtonian Flow and Applied Rheology (Second Edition): Butterworth-Heinemann. 1-55.

Chowdhury, M. M. H. 2014, Effects of CO2 on seismic wave speed in Fontainebleau sandstone.

Cleary, M. P., 1978, Elastic and dynamic response regimes of fluid-impregnated solids with diverse microstructures: International Journal of Solids and Structures, 14, 795–819, doi: 10.1016/0020-7683(78) 90072-0.

Ciz, R., and S. A. Shapiro, 2007, Generalization of Gassmann equations for porous media saturated with a solid material: GEOPHYSICS, **72**, no. 6, A75-A79. doi: 10.1190/1.2772400.

Cutler, W. 1982, Stratigraphy and sedimentology of the Upper Devonian Grosmont Formation, Alberta: M.S. thesis, University of Calgary.

Daridon, J. L., A. Lagrabette, and B. Lagourette, 1998, Speed of sound, density, and compressibilities of heavy synthetic cuts from ultrasonic measurements under pressure: Journal of Chemical Thermodynamics, **30**, no. 5,607-623. doi: DOI 10.1006/jcht.1997.0330.

Deblock, Y., F. Lefebvre, E. Radziszewski, and B. Nongaillard. 1998, The determination of the viscoelastic properties of liquid materials at ultrasonic frequencies by CW mode impedance measurements. IEEE Transactions on Instrumentation and Measurement, **47**, no. 3,680-685. doi: 10.1109/19.744324.

Deng, W. B., and I. B. Morozov. 2017, Trade-off of Elastic Structure and Q in Interpretations of Seismic Attenuation. Pure and Applied Geophysics, **174**, no. 10,3853-3867. doi: 10.1007/s00024-017-1581-3.

Diallo, M. S., M. Prasad, and E. Appel, 2003, Comparison between experimental results and theoretical predictions for P-wave velocity and attenuation at ultrasonic frequency: Wave Motion, **37**, no. 1, 1-16. doi: http://dx.doi.org/10.1016/S0165-2125(02)00018-5.

Dixon, S., D. Jaques, S. B. Palmer, and G. Rowlands. 2004, The measurement of shear and compression waves in curing epoxy adhesives using ultrasonic reflection and transmission techniques simultaneously. Measurement Science and Technology, **15**, no. 5,939-947. doi: 10.1088/0957-0233/15/5/023.

Dixon, S., and B. Lanyon. 2005, Phase change measurement of ultrasonic shear waves on reflection from a curing epoxy system. Journal of Physics D-Applied Physics, **38**, no. 22,4115-4125. doi: 10.1088/0022-3727/38/22/016.

Dukhin, A. S., and P. J. Goetz. 2009, Bulk viscosity and compressibility measurement using acoustic spectroscopy. The Journal of Chemical Physics, **130**, no. 12,124519. doi: doi:http://dx.doi.org/10.1063/1.3095471.

Eastwood, J. 1993, emperature-dependent propagation of p-waves and s-waves in cold lake oil sands - comparison of theory and experiment. Geophysics, **58**, no. 6,863-872. doi: 10.1190/1.1443470.

Eastwood, J., P. Lebel, A. Dilay, and S. Blakeslee, 1994, Seismic monitoring of steam-based recovery of bitumen: The Leading Edge, **13**, no. 4, 242-251. doi: 10.1190/1.1437015.

Fabricius, I. L., G. T. Bächle, and G. P. Eberli, 2010, Elastic moduli of dry and water-saturated carbonates — Effect of depositional texture, porosity, and permeability: GEOPHYSICS, **75**, no. 3, N65-N78. doi: 10.1190/1.3374690.

Fenistein, D., and L. Barré. 2001, Experimental measurement of the mass distribution of petroleum asphaltene aggregates using ultracentrifugation and small-angle X-ray scattering. Fuel, **80**, no. 2,283-287. doi: https://doi.org/10.1016/S0016-2361(00)00072-7.

Fergusson, F. A. A., E. W. Guptill, and A. D. Macdonald. 1954, Velocity of sound in glycerol. Journal of the Acoustical Society of America, **26**, no. 1,67-69. doi: 10.1121/1.1907292.

Ferry, J. D. 1980, Viscoelastic Properties of Polymers. 3rd ed: Wiley, New York.

Fitch, D. A., B. K. Hoffmeister, and J. de Ana. 2010, Ultrasonic evaluation of polyether ether ketone and carbon fiber-reinforced PEEK. Journal of Materials Science, **45**, no. 14,3768-3777. doi: 10.1007/s10853-010-4428-1.

Franco, E. E., J. C. Adamowski, and F. Buiochi. 2010, Ultrasonic Viscosity Measurement Using the Shear-Wave Reflection Coefficient with a Novel Signal Processing Technique. Ieee Transactions on Ultrasonics Ferroelectrics and Frequency Control, **57**, no. 5,1133-1139. doi: 10.1109/tuffc.2010.1524.

Garrouch, A. A., Ali, L., and Qasem, F., 2001, Using diffusion and electrical measurements to access tortuosity of porous media: Ind. Eng. Chem. Res, **40**, 4363-4369.

Gasparoux, J., D. Laux, J. Y. Ferrandis, J. Attal, and P. Tordjeman. 2008, Large frequency bands viscoelastic properties of honey. Journal of Non-Newtonian Fluid Mechanics, **153**, no. 1,46-52. doi: 10.1016/j.jnnfm.2007.11.007.

Giesche, H., 2006, Mercury Porosimetry: A General (Practical) Overview: Particle & Particle Systems Characterization, **23**, no. 1,9-19. doi: 10.1002/ppsc.200601009.

Gist, G. A., 1994, Fluid effects on velocity and attenuation in sandstones: The Journal of the Acoustical Society of America, **96**, no. 2, 1158-1173.

Greaves, R. J., and T. J. Fulp, 1987, 3-Dimensional seismic monitoring of an enhanced oil-recovery process: GEOPHYSICS, **52**, 1175-1187. doi: 10.1190/1.1442381.

Greenwood, M. S., J. D. Adamson, and L. J. Bond. 2006, Measurement of the viscosity-density product using multiple reflections of ultrasonic shear horizontal waves. Ultrasonics, **44**, no. SUPPL. doi: 10.1016/j.ultras.2006.05.093.

Greenwood, M. S., and J. A. Bamberger. 2002, Measurement of viscosity and shear wave velocity of a liquid or slurry for on-line process control. Ultrasonics, **39**, no. 9,623-630. doi: 10.1016/S0041-624X(02)00372-4.

Guillot, F. M., and D. H. Trivett. 2011, Complete elastic characterization of viscoelastic materials by dynamic measurements of the complex bulk and Young's moduli as a function of temperature and hydrostatic pressure. Journal of Sound and Vibration, **330**, no. 14,3334-3351. doi: http://dx.doi.org/10.1016/j.jsv.2011.02.003.

Gurevich, B., K. Osypov, R. Ciz, and D. Makarynska. 2008, Modeling elastic wave velocities and attenuation in rocks saturated with heavy oil. Geophysics, **73**, no. 4,E115-E122. doi: 10.1190/1.2940341.

Gutierrez-Lemini, D. 2014, Fundamental Aspects of Viscoelastic Response, Engineering Viscoelasticity: Springer US. 1-21.

Haddadi, S., E. Ghorbel, and N. Laradi. 2008, Effects of the manufacturing process on the performances of the bituminous binders modified with EVA. Construction and Building Materials, **22**, no. 6,1212-1219. doi: https://doi.org/10.1016/j.conbuildmat.2007.01.028.

Hamida, T., and B. Roberts. 2014, Recovery of Bitumen From a Carbonate Reservoir by Thermal-Assisted Gravity Drainage (TAGD). Journal of Canadian Petroleum Technology, **53**, no. 4,224-232.

Han, D. h., J. Liu, and M. Batzle. 2005. Measurement of shear wave velocity of heavy oil, SEG Technical Program Expanded Abstracts. 1513-1516.

Han, D. h., J. Liu, and M. Batzle. 2007, Shear velocity as a function of frequency in heavy oils. In Society of Exploration Geophysicists Annual Meeting

Han, D.-h., J. Liu, and M. Baztle. 2008, Seismic properties of heavy oils—measured data. The Leading Edge, **27**, no. 9,1108-1115. doi: 10.1190/1.2978972.

Hasan, M. D. A., M. Fulem, A. Bazyleva, and J. M. Shaw. 2009, Rheological Properties of Nanofiltered Athabasca Bitumen and Maya Crude Oil. Energy & Fuels, **23**,5012-5021. doi: 10.1021/ef900313r.

Hashin, Z., and S. Shtrikman, 1963, A variational approach to the theory of the elastic behaviour of multiphase materials: Journal of the Mechanics and Physics of Solids, **11**, no. 2, 127-140. doi: http://dx.doi.org/10.1016/0022-5096(63)90060-7.

Innanen, K. A. 2011, Inversion of the seismic AVF/AVA signatures of highly attenuative targets. Geophysics, **76**, no. 1,R1-R14. doi: 10.1190/1.3518816.

Isaac, J. H., and D. C. Lawton. 2006, A case history of time-lapse 3D seismic surveys at Cold Lake, Alberta, Canada. Geophysics, **71**, no. 4,B93-B99. doi: 10.1190/1.2211027.

Iwata, S., S. Yamauchi, Y. Yoshitake, R. Nagumo, H. Mori, and T. Kajiya, 2016, Measurement of dynamic surface tension by mechanically vibrated sessile droplets: Review of Scientific Instruments, **87**, no. 4, 045106. doi: doi:http://dx.doi.org/10.1063/1.4944045.

Jiang, Q., J. Yuan, J. Russel-Houston, B. Thornton, and A. Squires, 2009, Evaluation of Recovery Technologies for the Grosmont Carbonate Reservoirs: Petroleum Society of Canada. doi:10.2118/137779-PA

Jiang, Q., B. Thornton, J. Russel-Houston, and S. Spence. 2010, Review of Thermal Recovery Technologies for the Clearwater and Lower Grand Rapids Formations in the Cold Lake Area in Alberta. Canadian J. Petroleum Technology, **49**, no. 9,57-68. doi: 10.2118/140118-PA.

Kaatze, U. 2017, Dielectric and structural relaxation in water and some monohydric alcohols. Journal of Chemical Physics, **147**, no. 2,9. doi: 10.1063/1.4991850.

Kariznovi, M., H. Nourozieh, and J. Abedi. 2014, Measurement and Correlation of Viscosity and Density for Compressed Athabasca Bitumen at Temperatures Up to 200 degrees C. Journal of Canadian Petroleum Technology, **53**, no. 6,330-338.

Kato, A., S. Onozuka, and T. Nakayama. 2008, Elastic property changes in a bitumen reservoir during steam injection. The Leading Edge, **27**, no. 9,1124-1131. doi: 10.1190/1.2978974.

Kelly, B., and D. C. Lawton. 2012, Processing and interpretation of time-lapse seismic data from a heavy oil field , Alberta , Canada (a) (b) 4D Processing and Interpretation (a) (b).1-5.

Kendall, R., 2009, Using Timelapse Seismic to Monitor the THAI TM Heavy Oil Production Process: *79th SEG meeting, Expanded Abstracts, 3954–3958*

Kenter, J. A. M., F. S. Anselmetti, P. H. Kramer, H. Westphal, and M. G. M. Vandamme, 2002, Acoustic properties of "young" carbonate rocks, ODP leg 166 and boreholes Clino and Unda, western Great Bahama Bank: Journal of Sedimentary Research, **72**, no. 1, 129-137. doi: 10.1306/041101720129.

Kinsler, L. E. 1982, Fundamentals of acoustics: New York : Wiley, 1982. 3rd ed.

Kono, R. 1961, The Dynamic Bulk and Shear Viscosity of High Polymers, 1. Journal of the Physical Society of Japan, **16**, no. 8,1580-1586. doi: 10.1143/JPSJ.16.1580.

Krebes, E. S. 1984, On the reflection and transmission of viscoelastic waves - some numerical results. Geophysics, **49**, no. 8,1374-1380. doi: 10.1190/1.1441765.

Krebes, E. S., and P. F. Daley. 2007, Difficulties with computing anelastic plane-wave reflection and transmission coefficients. Geophysical Journal International, **170**, no. 1,205-216. doi: 10.1111/j.1365-246X.2007.03349.x.

Lakes, R. 2009, Viscoelastic Materials: Cambridge University Press.

Lellinger, D., S. Tadjbach, and I. Alig. 2002, Determination of the elastic moduli of polymer films by a new ultrasonic reflection method. Macromolecular Symposia, **184**,203-213. doi: 10.1002/1521-3900(200208)184:1<203::aid-masy203>3.0.co;2-8.

Letang, C., M. Piau, C. Verdier, and L. Lefebvre. 2001, Characterization of wheat-flour-water doughs: a new method using ultrasound. Ultrasonics, **39**, no. 2,133-141. doi: 10.1016/s0041-624x(00)00058-5.

Li, H., L. Zhao, D.-H. Han, M. Sun, and Y. Zhang, 2016, Elastic properties of heavy oil sands: Effects of temperature, pressure, and microstructure: GEOPHYSICS, **81**, no. 4, D453-D464. doi: 10.1190/geo2015-0351.1.

Lin, C.-W., and J. P. M. Trusler, 2012, The speed of sound and derived thermodynamic properties of pure water at temperatures between (253 and 473) K and at

pressures up to 400 MPa: The Journal of Chemical Physics, **136**, no. 9,-. doi: doi:http://dx.doi.org/10.1063/1.3688054.

Lines, L. R., R. Jackson, and J. D. Covey, 1990, Seismic velocity models for heat zones in athabasca tar sands: GEOPHYSICS, **55**, 1108-1111. doi: 10.1190/1.1442924.

Lines, L., J. Wong, K. Innanen, F. Vasheghani, C. Sondergeld, S. Trietel, and T. Ulrych. 2014, Research Note: Experimental measurements of Q-contrast reflections. Geophysical Prospecting, **62**,190-195.

Litovitz, T. A., and C. M. Davis. 1965, Structural and Shear Relaxation in Liquids. Vol. 2: ACADEMIC PRESS INC.

Loeber, L., G. Muller, J. Morel, and O. Sutton. 1998, Bitumen in colloid science: a chemical, structural and rheological approach. Fuel, **77**, no. 13,1443-1450. doi: https://doi.org/10.1016/S0016-2361(98)00054-4.

Loeber, L., O. Sutton, J. Morel, J. M. Valleton, and G. Muller. 1996, New direct observations of asphalts and asphalt binders by scanning electron microscopy and atomic force microscopy. Journal of Microscopy-Oxford, **182**,32-39. doi: 10.1046/j.1365-2818.1996.134416.x.

Longin, P. Y., C. Verdier, and M. Piau. 1998, Dynamic shear rheology of high molecular weight polydimethylsiloxanes: comparison of rheometry and ultrasound. Journal of Non-Newtonian Fluid Mechanics, **76**, no. 1-3,213-232. doi: 10.1016/s0377-0257(97)00119-5.

Lu, S. X., P. Cebe, and M. Capel. 1996, Thermal stability and thermal expansion studies of PEEK and related polyimides. Polymer, **37**, no. 14,2999-3009. doi: https://doi.org/10.1016/0032-3861(96)89397-9.

Machel, H. G., M. L. Borrero, E. Dembicki, H. Huebscher, L. Ping, and Y. Zhao, 2012, The Grosmont: the world's largest unconventional oil reservoir hosted in carbonate rocks: Geological Society, London, Special Publications, **370**. doi: 10.1144/sp370.11.

MacNeil, A. J., 2015, Petrophysical Characterization of Bitumen-Saturated Karsted Carbonates: Case Study of the Multibillion Barrel Upper Devonian Grosmont Formation, Northern Alberta, Canada: Petrophysics, **56**, 592-614.

Macosko, C. W. 1994, Rheology : principles, measurements, and applications Wiley-VCH.

Makarynska, D., B. Gurevich, J. Behura, and M. Batzle, 2010, Fluid substitution in rocks saturated with viscoelastic fluids: GEOPHYSICS, **75**, no. 2, E115-E122. doi: 10.1190/1.3360313.

Markovitz, H. 1975, Superposition in rheology. Journal of Polymer Science Part C-Polymer Symposium, no. 50,431-456.

Mason, W. P., W. O. Baker, H. J. McSkimin, and J. H. Heiss. 1949, Measurement of shear elasticity and viscosity of liquids at ultrasonic frequencies. Physical Review, **75**, no. 6,936-946. doi: 10.1103/PhysRev.75.936.

Mattaboni, P. and E. Schreiber, 1967, Method of pulse transmission measurements for determining sound velocities: *Journal of Geophysical Research* **72** (20): 5160-5163

Mavko, G., T. Mukerji, and J. Dvorkin, 2009, The rock physics handbook: Cambridge University Press.

Mavko, G., 2013, Relaxation shift in rocks containing viscoelastic pore fluids: GEOPHYSICS, **78**, no. 3, M19-M28. doi: doi:10.1190/geo2012-0272.1.

Maxwell, J. C. 1867, On the Dynamical Theory of Gases. Philosophical Transactions of the Royal Society of London, **157**,49-88.

McSkimin, H. J., and P. Andreatch. 1967, Measurement of dynamic shear impedance of low viscosity liquids at ultrasonic frequencies. Journal of the Acoustical Society of America, **42**, no. 1,248-+. doi: 10.1121/1.1910560.

Melendez Martinez, J., and D. R. Schmitt, 2013, Anisotropic elastic moduli of carbonates and evaporites from the Weyburn-Midale reservoir and seal rocks: Geophysical Prospecting, **61**, no. 2, 363-379. doi: 10.1111/1365-2478.12032.

Meyer, R.F., Attanasi, E.D., and Freeman, P.A., 2007, Heavy oil and natural bitumen resources in geological basins of the world: U.S. Geological Survey Open-File Report 2007-1084, available online at https://pubs.usgs.gov/of/2007/1084/.

Mikhaltsevitch, V., M. Lebedev, and B. Gurevich, 2016, Laboratory measurements of the effect of fluid saturation on elastic properties of carbonates at seismic frequencies: Geophysical Prospecting, **64**, no. 4, 799-809. doi: 10.1111/1365-2478.12404.

Miller, K. A., L. A. Nelson, and R. M. Almond. 2006, Should you trust your heavy oil viscosity measurement? : Journal of Canadian Petroleum Technology, **45**, no. 4,42-48. doi: 10.2118/06-04-02.

Mohebati, M. H., D. Yang, and J. MacDonald. 2014, Thermal Recovery of Bitumen From the Grosmont Carbonate Formation-Part 1: The Saleski Pilot. Journal of Canadian Petroleum Technology, **53**, no. 4,200-211.

Molyneux, J. B., and D. R. Schmitt, 2000, Compressional-wave velocities in attenuating media: A laboratory physical model study: GEOPHYSICS, **65**, 1162-1167. doi: 10.1190/1.1444809.

Moreno Arciniegas, L. S., Asphaltene Precipitation During Solvent Injection at Different Reservoir Conditions and Its Effects on Heavy-Oil Recovery from Oilsands.

Mortazavi-Manesh, S., and J. M. Shaw. 2016, Effect of Pressure on the Rheological Properties of Maya Crude Oil. Energy & Fuels, **30**, no. 2,759-765. doi: 10.1021/acs.energyfuels.5b02366.

Nava, R., L. Amorer, and D. Pereira. 1994, Viscoelastic relaxation at megahertz frequencies in a Guasare (Venezuela) coal. Fuel, **73**, no. 1,51-55. doi: https://doi.org/10.1016/0016-2361(94)90187-2.

Njiekak, G., D. R. Schmitt, H. Yam, and R. S. Kofman, 2013, CO2 rock physics as part of the Weyburn-Midale geological storage project: International Journal of Greenhouse Gas Control, **16, Supplement 1**, no. 0, S118-S133. doi: http://dx.doi.org/10.1016/j.ijggc.2013.02.007.

Nur, A. M., 1982, Seismic Imaging in Enhanced Recovery: Society of Petroleum Engineers, **SPE-10680-MS**. doi: 10.2118/10680-MS.

Nycz, J., D. Yang, and D. Schmitt. 2016, Analysis of 4D time-lapse seismic responses integrated with 3D data products, production information, and laboratory data to characterize a bitumen-bearing carbonate reservoir, SEG Technical Program Expanded Abstracts 2016. 2951-2955.

Oconnell, R. J., and B. Budiansky. 1978, measures of dissipation in viscoelastic media. Geophysical Research Letters, **5**, no. 1,5-8. doi: 10.1029/GL005i001p00005.

Oneil, H. T. 1949, Reflection and refraction of plane shear waves in viscoelastic media. Physical Review, **75**, no. 6,928-935. doi: 10.1103/PhysRev.75.928.

Özkaya, N., D. Leger, D. Goldsheyder, and M. Nordin. 2017, Mechanical Properties of Biological Tissues, Fundamentals of Biomechanics: Equilibrium, Motion, and Deformation: Springer International Publishing. 361-387.

Peleties, F., J. J. Segovia, J. P. M. Trusler, and D. Vega-Maza. 2010, Thermodynamic properties and equation of state of liquid di-isodecyl phthalate at temperature between (273 and 423)K and at pressures up to 140MPa. The Journal of Chemical

Thermodynamics, **42**, no. 5,631-639. doi: https://doi.org/10.1016/j.jct.2009.12.002.

Peselnick, L., and W. F. Outerbridge, 1961, Internal friction in shear and shear modulus of solenhofen limestone over a frequency range of 10 to seventh power cycles per second: Journal of Geophysical Research, **66**, no. 2, 581-&. doi: 10.1029/JZ066i002p00581.

Pimienta, L., J. Fortin, and Y. Guéguen, 2015, Bulk modulus dispersion and attenuation in sandstones: GEOPHYSICS, 80, no. 2,D111-D127. doi: 10.1190/geo2014-0335.1.

Pimienta, L., J. Fortin, and Y. Guéguen, 2016, Effect of fluids and frequencies on Poisson's ratio of sandstone samples: GEOPHYSICS, 81, no. 2,D183-D195. doi: 10.1190/geo2015-0310.1.

Popovics, J. S., and K. V. L. Subramaniam. 2015, Review of Ultrasonic Wave Reflection Applied to Early-Age Concrete and Cementitious Materials. Journal of Nondestructive Evaluation, **34**, no. 1,12. doi: 10.1007/s10921-014-0267-3.

Rabani, A., R. E. Challis, and V. J. Pinfield. 2011, The torsional waveguide viscosity probe: Design and anomalous behavior. IEEE Transactions on Ultrasonics, Ferroelectrics, and Frequency Control, **58**, no. 8,1628-1640. doi: 10.1109/TUFFC.2011.1990.

Rabbani, A., D. R. Schmitt, R. Kofman, and J. Nycz, 2014, Laboratory studies of the seismic properties of bitumen saturated grosmont carbonates: Geoconvention Abstracts.

Rabbani, A., D. R. Schmitt, J. Nycz, and K. Gray, 2015, Velocity measurements of pore fluids at pressure and temperature: application to bitumen: Geoconvention Abstracts.

Rabbani, A., O. Ong*, X. Chen, D. Schmitt, J. Nycz, and K. Gray. 2016, Rock physics laboratory experiments on bitumen-saturated carbonates from the Grosmont Formation, Alberta, SEG Technical Program Expanded Abstracts 2016. 3464-3467.

Rabbani, A., D. R. Schmitt, J. Nycz, and K. Gray. 2017, Pressure and temperature dependence of acoustic wave speeds in bitumen-saturated carbonates: Implications for seismic monitoring of the Grosmont Formation. GEOPHYSICS, **82**, no. 5,MR133-MR151. doi: 10.1190/geo2016-0667.1.

Rabbani, A. and D. R. Schmitt. 2018, Ultrasonic Shear Wave Reflectometry Applied to the Determination of the Shear Moduli and Viscosity of a Viscoelastic Bitumen. FUEL (accepted).

Rae, P. J., E. N. Brown, and E. B. Orler. 2007, The mechanical properties of poly(ether-ether-ketone) (PEEK) with emphasis on the large compressive strain response. Polymer, **48**, no. 2,598-615. doi: 10.1016/j.polymer.2006.11.032.

Rassenfoss, S. 2013, Finding Pathways to Produce Heavy Oil From Canadian Carbonates. JPT, **65**, no. 08.

Read, J., and D. Whiteoak. 2003, The Shell Bitumen Handbook, The Shell Bitumen Handbook: Thomas Telford Ltd: London.

Rodrigues, P. E., and M. L. Batzle. 2015, Strain amplitude dependence of shear modulus in heavy oils: Rheometer versus tension/compression technique. Geophysics, **80**, no. 4,L35-L43. doi: 10.1190/geo2014-0354.1.

Rojas Luces, M. 2010, Viscoelastic properties of heavy oils, University of Houston.

Rouse, P. E. 1953, A Theory of the Linear Viscoelastic Properties of Dilute Solutions of Coiling Polymers. The Journal of Chemical Physics, **21**, no. 7,1272-1280. doi: 10.1063/1.1699180.

Russel-Houston, J., and K. Gray, 2014, Paleokarst in the Grosmont Formation and reservoir implications, Saleski, Alberta, Canada: Interpretation, **2**, no. 3, SF29-SF50. doi: 10.1190/int-2013-0187.1.

Sarout, J., 2012, Impact of pore space topology on permeability, cut-off frequencies and validity of wave propagation theories: Geophysical Journal International, 189, no. 1,481-492. doi: 10.1111/j.1365-246X.2011.05329.x.

Saxena, N., and G. Mavko, 2014, Exact equations for fluid and solid substitution: GEOPHYSICS, **79**, no. 3, L21-L32. doi: 10.1190/geo2013-0187.1.

Saxena, N., G. Mavko, R. Hofmann, B. Gurevich, S. Glubokovskikh, S. Aliyeva, and P. Dutta, 2016, Rock-physics models for heavy-oil and organic-solid substitution: The Leading Edge, **35**, no. 6, 506-510. doi: 10.1190/tle35060506.1.

Schirru, M., R. Mills, R. Dwyer-Joyce, O. Smith, and M. Sutton. 2015, Viscosity Measurement in a Lubricant Film Using an Ultrasonically Resonating Matching Layer. Tribology Letters, **60**, no. 3,1-11. doi: 10.1007/s11249-015-0619-x.

Schirru, M. M., and R. S. Dwyer-Joyce. 2015, A model for the reflection of shear ultrasonic waves at a thin liquid film and its application to viscometry in a journal

bearing. Proceedings of the Institution of Mechanical Engineers, Part J: Journal of Engineering Tribology, **0**, no. 0,1-13. doi: 10.1177/1350650115610357.

Schmitt, D. R. 1999, Seismic attributes for monitoring of a shallow heated heavy oil reservoir: A case study. Geophysics, **64**, no. 2,368-377. doi: 10.1190/1.1444541.

Schmitt, D. 2004, Rock Physics of Heavy Oil Deposits. CSEG National Convention - Great Explorations - Canada and Beyond,1-4.

Schmitt, D. R., G. Njiekak, M. Chowdhury, R. Kofman, A. Rabbani, and H. Yam. 2013, Use of CO2 as a Fluid in Fundamental Studies of Wave Propagation through Porous Media, Poromechanics V. 209-216.

Schmitt, D. R. 2015, 11.03 - Geophysical Properties of the Near Surface Earth: Seismic Properties A2 - Schubert, Gerald, Treatise on Geophysics (Second Edition): Elsevier, 43-87.

Shah, V. V., and K. Balasubramaniam. 2000, Measuring Newtonian viscosity from the phase of reflected ultrasonic shear wave. Ultrasonics, **38**, no. 9,921-927. doi: 10.1016/s0041-624x(00)00033-0.

Shamsa, A., and L. Lines. 2015, Effect of oil composition on fluid substitution in heavy oil reservoirs. Geophysical Prospecting, **63**, no. 2,422-441. doi: 10.1111/1365-2478.12147.

Sheely, M. L. 1932, Glycerol Viscosity Tables. Industrial & Engineering Chemistry, **24**, no. 9,1060-1064. doi: 10.1021/ie50273a022.

Sheen, S.-H., H.-T. Chien, and A. Raptis. 1996, Measurement of shear impedances of viscoelastic fluids. In 1996 IEEE Ultrasonics Sympoisum. San Antonio: IEEE.

Shepard, C. L., B. J. Burghard, L. A. Friesel, B. P. Hildebrand, M. Xang, A. A. Diaz, and C. W. Enderlin. 1999, Measurements of density and viscosity of one- and two-phase fluids with torsional waveguides. Ieee Transactions on Ultrasonics Ferroelectrics and Frequency Control, **46**, no. 3,536-548. doi: 10.1109/58.764840.

Skempton, A. W., 1954, The Pore-Pressure Coefficients A and B: Géotechnique, **4**, no. 4, 143-147. doi: 10.1680/geot.1954.4.4.143.

Slie, W. M., A. R. Donfor, and T. A. Litovitz. 1966, Ultrasonic shear and longitudinal measurements in aqueous glycerol. Journal of Chemical Physics, **44**, no. 10,3712-&. doi: 10.1063/1.1726524.

Speight, J. G. 1999, The chemical and physical structure of petroleum: effects on recovery operations. Journal of Petroleum Science and Engineering, **22**, no. 1,3-15. doi: https://doi.org/10.1016/S0920-4105(98)00051-5.

Spencer, J. W. 2013, Viscoelasticity of Ells River bitumen sand and 4D monitoring of thermal enhanced oil recovery processes. Geophysics, **78**, no. 6,D419-D428. doi: 10.1190/geo2012-0535.1.

Stastna, J., L. Zanzotto, and K. Ho. 1994, Fractional complex modulus manifested in asphalts. Rheologica Acta, **33**, no. 4,344-354. doi: 10.1007/bf00366961.

Souraki, Y., M. Ashrafi, and O. Torsaeter, 2013, A comparative field-scale simulation study on feasibility of SAGD and ES-SAGD processes in naturally fractured bitumen reservoirs: Energy Environ. Res., 3(1), doi:10.5539/eer.v3n1p49.

Subramaniyan, S., B. Quintal, N. Tisato, E. H. Saenger, and C. Madonna, 2014, An overview of laboratory apparatuses to measure seismic attenuation in reservoir rocks: Geophysical Prospecting, **62**, no. 6, 1211-1223. doi: 10.1111/1365-2478.12171.

Svrcek, W. Y., and A. K. Mehrotra. 1982, Gas solubility, viscosity and density-measurements for athabasca bitumen. Journal of Canadian Petroleum Technology, **21**, no. 4,31-38.

Teare M., S. Miller, S. Overland, and R. Marsh, 2015, in ST98-2015: Alberta's Energy Reserves 2014 and Supply/Demand Outlook 2015–2024: Alberta Energy Regulator.

Trusler, J. P. M. 1991, Physical Acoustics and Metrology of Fluids, The Adam Hilger Series on Measurement Science and Technology: Adam Hilger.

Vanorio, T., and G. Mavko, 2011, Laboratory measurements of the acoustic and transport properties of carbonate rocks and their link with the amount of microcrystalline matrix: GEOPHYSICS, **76**, no. 4, E105-E115. doi: 10.1190/1.3580632.

Vasiljevic-Shikaleska, A., F. Popovska-Pavlovska, S. Cimmino, D. Duraccio, and C. Silvestre. 2010, Viscoelastic properties and morphological characteristics of polymer-modified bitumen blends. Journal of Applied Polymer Science, **118**, no. 3,1320-1330. doi: 10.1002/app.32317.

Vernon-Carter, E. J., G. Avila-de la Rosa, H. Carrillo-Navas, Y. Carrera, and J. Alvarez-Ramirez. 2016, Cox-Merz rules from phenomenological Kelvin-Voigt and Maxwell models. Journal of Food Engineering, **169**,18-26. doi: 10.1016/j.jfoodeng.2015.08.005.

Verwer, K., H. Braaksma, and J. A. Kenter, 2008, Acoustic properties of carbonates: Effects of rock texture and implications for fluid substitution: GEOPHYSICS, **73**, no. 2, B51-B65. doi: 10.1190/1.2831935.

Voigt, T. 2005, The application of an ultrasonic shear wave reflection method for nondestructive testing of cement-based materials at early ages.

Wang, Z., and A. Nur, 1990, Wave velocities in hydrocarbon-saturated rocks - experimental results: geophysics, **55**, 723-733. doi: 10.1190/1.1442884.

Wang, Z., R. Wang, and D.R. Schmitt, 2015, The elastic moduli of velocities of artificial carbonate rocks with known pore structure at different saturation conditions: Geoconvention Abstract, CSEG/CSPG/CWLA.

Wang, Z. J., A. M. Nur, and M. L. Batzle, 1990, Acoustic velocities in petroleum oils: Journal of Petroleum Technology, **42**, no. 2, 192-200.

Wang, Z., D. R. Schmitt, and R. Wang. 2017, Modeling of viscoelastic properties of nonpermeable porous rocks saturated with highly viscous fluid at seismic frequencies at the core scale. Journal of Geophysical Research: Solid Earth, **122**, no. 8,6067-6086. doi: 10.1002/2017JB013979.

Ward, I. M., and D. W. Hadley. 1993, An introduction to the mechanical properties of solid polymers: John Wiley and Sons Ltd, New York.

Wardlaw, N. C., and M. McKellar, 1981, Mercury porosimetry and the interpretation of pore geometry in sedimentary rocks and artificial models: Powder Technology, **29**, no. 1, 127-143. doi: http://dx.doi.org/10.1016/0032-5910(81)85011-5.

Whorlow, R. W. 1980, Rheological techniques, Ellis Horwood physics in medicine and biology series: Chichester [Eng.] : E. Horwood ; New York : Wiley, 1980.

Wolf, K., T. Vanorio, and G. Mavko. 2008, Measuring and monitoring heavy-oil reservoir properties. The Leading Edge, **27**, no. 9,1138-1147. doi: 10.1190/1.2978976.

Wood, A.W., 1955, A Textbook of Sound: New York: McMillan Co.

Yam, H. 2011, CO2 rock physics: a laboratory study. University of Alberta

Yang, D., M. H. Mohebati, S. Brand, and C. Bennett. 2014, Thermal recovery of bitumen from the grosmont carbonate formation - Part 2: Pilot interpretation and development strategy. Journal of Canadian Petroleum Technology, **53**, no. 4,212-223. doi: 10.2118/171561-PA.

Yuan, H., D.-h. Han, H. Li, and W. Zhang. 2017, A comparison of bitumen sands and bitumen carbonates: Measured data. GEOPHYSICS, **82**, no. 1,MR39-MR50. doi: 10.1190/geo2015-0657.1.

Zadeh, H. M., R. P. Srivastava, N. Vedanti, and M. Landro. 2010, Seismic monitoring of in situ combustion process in a heavy oil field. Journal of Geophysics and Engineering, **7**, no. 1,16-29. doi: 10.1088/1742-2132/7/1/002.

Zavrtanik, N., G. Turk, M. Tušar, and G. Trtnik. 2017, Monitoring of bitumen hardening with a non-destructive ultrasonic shear wave reflection technique. International Journal of Pavement Engineering, **18**, no. 6,560-566. doi: 10.1080/10298436.2016.1138110.

Zhao, Y., and H. G. Machel. 2012, Viscosity and other rheological properties of bitumen from the Upper Devonian Grosmont reservoir, Alberta, Canada. Aapg Bulletin, **96**, no. 1,133-153. doi: 10.1306/04261110180.

Zhu, J., B. Birgisson, and N. Kringos. 2014, Polymer modification of bitumen: Advances and challenges. European Polymer Journal, **54**,18-38. doi: https://doi.org/10.1016/j.eurpolymj.2014.02.005.

Zimmerman, R. W. 1991, Chapter 6. Undrained Compression, Developments in Petroleum Science: Elsevier. 57-65.